Semiaromatic Polyamides and Copolyamides Comprising Kinked Repeating Units

THÈSE N^{O} 8633 (2018)

PRÉSENTÉE LE 8 JUIN 2018

À LA FACULTÉ DES SCIENCES ET TECHNIQUES DE L'INGÉNIEUR
LABORATOIRE DES MATÉRIAUX ORGANIQUES ET MACROMOLÉCULAIRES
PROGRAMME DOCTORAL EN SCIENCE ET GÉNIE DES MATÉRIAUX

ÉCOLE POLYTECHNIQUE FÉDÉRALE DE LAUSANNE

POUR L'OBTENTION DU GRADE DE DOCTEUR ÈS SCIENCES

PAR

Julien Philippe CRETENOUD

acceptée sur proposition du jury:

Prof. D. Damjanovic, président du jury
Prof. H. Frauenrath, directeur de thèse
Prof. S. Mecking, rapporteur
Prof. W. Caseri, rapporteur
Prof. K. Sivula, rapporteur

ÉCOLE POLYTECHNIQUE
FÉDÉRALE DE LAUSANNE

Suisse
2018

“Sois comme le roseau : plie mais ne romps pas !”

Un père à son fils

Acknowledgments

I would like to sincerely thank all the people that helped me scientifically and/or made me stay strong and confident over the almost five years that lasted my PhD thesis.

First of all, I would like to thank my supervisor, Prof. Holger Frauenrath, for having trusted me, a food and analytic chemist who had barely heard about polymers before, when this polyamide project started in 2013, as well as for teaching me how to make figures that look amazing. I am equally grateful to my collaborators, Dr. Chris Plummer and Dr. Sylvain Galland, who produced enormous amounts of thermal, mechanical and X-ray data to support this work. I am particularly thankful to Chris, who additionally spent countless hours correcting my various drafts. My dear friend Bilal Özen also deserves a special mention, simply for hanging around with me, sharing food and always being this "smiling buddy" that everyone needs on sad days. I would also like to thank Cindy Känel and Jacques Morisod, from the LP lab, for their help with GPC measurements, Dr. Rosario Scopelliti and Dr. Farzaneh Fadaei Tirani, my crystal magicians, Emilie Baudat for the NMR support as well as Prof. Pierre Vogel for the fruitful discussions. All the former and current LMOM group members should of course not be forgotten, because they were always ready for good fun, drinks, ski weekends or BBQs, with special thanks to Bjoern, Dragana, Manu, Emmanuel, Bastien, Roman, Damien, Su, Jan, Giuseppe, Nicolas, Regina, Enzo, Thomas and Daniel.

On a more personal point of view, I would like to thank my good old friends Sylvain, Vincent, Fabian, Claudio and Matia for having always been present for crazy vacations all around the world as well as cinema sessions, drinks or burgers in the city. My ex-flatmates, Aurélien and Paul, as well as the current ones, Thomas and Jérémy also deserve to be part of this list, for their never-ending kindness and desire to party. Sport also helped a lot releasing pressure; this is why I need to thank all my dear friends from the Tennis Club Bussigny and from the LUC badminton team for all these wonderful (and sweaty) moments spent together.

Last but far from least, I really want to thank my family in general but more specifically my "little" sister and my parents, for their love, mental support, guidance and advice every time I needed it during my studies, that are now finally concluded with this PhD thesis. Un grand merci à vous, du plus profond de mon coeur, je vous aime !

Summary

The replacement of metals with polymer-based materials is considered to be key to reducing weight, cost, and cycle times in different technological applications, including the automotive and aerospace industries. Semiaromatic polyamides are particularly attractive engineering polymers due to their balanced mechanical properties and processability. They combine high strength and stiffness due to the rigid aromatic repeating units with greater ductility and better processability than those of polyaramids, owing to the presence of flexible aliphatic repeating units. However, the challenge remains to find ways to improve the strain at break and toughness of semiaromatic polyamides and their composites, without inducing adverse consequences for their strength and stiffness.

The present thesis addresses this challenge following two complementary approaches. In an engineering-driven approach suitable to industrial scale-up, we produced random copolyamides by high-temperature melt-blending of a strong and stiff semiaromatic polyamide with more ductile aliphatic polyamides. The blending of up to 30 *wt*% of PA66 or PA610 in PA6TI resulted in a five-fold increase of the strain at break compared to that of pure PA6TI, with almost no change in stiffness and only minor losses in strength.

In a second, chemistry-driven approach inspired by the crucial role of polymer chain in silk materials, we designed and synthesized monomers that induce the formation of "U-turn folds" in attempt to induce re-entrant chain folding in the crystalline lamellae of semiaromatic polyamides. Contrary to polyamides with kinked repeating units that are usually amorphous, the use of such monomers did not impede crystallization. Acridine-based polyamides were shown to adopt a folded structure in the solid state that was structurally related to the β-serpentine folds in amyloids. They also exhibited a modulus comparable to other semiaromatic polyamides and were harder and stiffer than the structurally related anthracene-based polymers that did not show chain folding due to steric repulsion in the required conformation.

KEYWORDS | polyamide, copolyamide, semiaromatic, semicrystalline, melt, blending, extrusion, kink, turn, transamidation

Résumé

La substitution de métaux par des matériaux à base de polymères techniques est considéré comme essentiel dans l'industrie automobile ou aérospatiale, par exemple, dans le but de réduire non seulement le poids mais aussi les coûts et les temps de fabrication. En ce sens, les polyamides semi-aromatiques sont particulièrement attractifs au vu de leurs propriétés mécaniques équilibrées et de leur facilité de mise en œuvre. Les noyaux aromatiques leur confèrent ainsi une grande résistance à la rupture et une bonne rigidité tandis que les chaînes aliphatiques, plus flexibles, amènent une plus grande ductilité et une meilleure mise en œuvre par rapport aux polyaramides. Néanmoins, le défi est de trouver un moyen d'améliorer encore plus leur allongement et leur résistance à la rupture, tout en évitant une réduction importante de leur seuil de plasticité ou de leur rigidité.

Dans cette thèse, deux approches complémentaires ont été utilisées pour relever ce défi. Suivant une approche pratique de l'ingénieur et adaptée à l'échelle industrielle, nous avons synthétisé des copolyamides aléatoires en extrudant à haute température un polyamide semi-aromatique avec différents polyamides aliphatiques. Le mélange de 30% en masse de PA66 ou de PA610 avec du PA6TI a ainsi conduit à une augmentation de l'allongement à la rupture par un facteur de cinq comparé au PA6TI seul, avec seulement une légère diminution du seuil de plasticité et sans modification majeure de la rigidité.

Inspirés par le rôle crucial qu'ont les chaînes de polymères dans des matériaux tels que la soie d'araignée, et suivant une approche plus axée sur la chimie, nous avons également synthétisé de nouveaux monomères rigides en forme de « U », afin de promouvoir le repliement régulier des chaînes de polyamides au sein de la phase cristalline. Contrairement aux polyamides contenant des coudes, qui sont généralement amorphes, nous avons observé que l'utilisation de tels monomères n'empêche en effet pas la cristallisation et que les polyamides à base d'acridine adoptent, à l'état solide, une conformation repliée qui est structurellement similaire aux serpentins présents dans les β-amyloïdes. Finalement, nous avons montré que le module d'élasticité de ces polymères est aussi comparable à celui d'autres polyamides semi-aromatiques et qu'ils sont plus résistants et rigides que leurs homologues à base d'anthracène, où un repliement de type serpentin est empêché par l'encombrement stérique.

MOTS CLÉS | polyamide, co-polyamide, semi-aromatique, semi-cristallin, fondu, mélange, extrusion, coude, repliement, transamidation

Table of Contents

List of Abbreviations

1D	one-dimensional
2D	two-dimensional
A	L-alanine
Å	angström
A/A_0	amplitude setpoint ratio (AFM)
AFM	atomic force microscopy
BFBF	benzofurobenzofuran
BTBT	benzothienobenzothiophene
°C	degree Celsius
c	concentration
$CaCl_2$	calcium chloride
calcd.	calculated
$CDCl_3$	deuterated chloroform
$CHCl_3$	chloroform
COSY	correlation spectroscopy (^1H–^1H NMR)
χ	degree of crystallinity
d	day
d	duplet (NMR)
δ	chemical shift (NMR)
Đ	dispersity (old: polydispersity)
DCM	dichloromethane
DFT	density functional theory
DIPEA	*N*,*N*-diisopropylethylamine
DMAC	*N*,*N*-dimethylacetamide
DMF	dimethylformamide
DMSO	dimethylsulfoxide
DSC	differential scanning calorimetry
ΔH_c	total enthalpy of crystallization
ΔH_m	total enthalpy of melting
ΔG	Gibbs free energy

ΔS_m	total entropy of melting
E	Young's modulus / elastic modulus
EDCI	1-ethyl-3(3-dimethylaminopropyl)carbodiimide
equiv.	equivalents
ESI	electrospray ionization (mass spectrometry)
EtOAc	ethylacetate
EtOH	ethanol
eV	electron volt
ϕ	mass fraction
FT/IR	Fourier transform infrared spectroscopy
g	gram
G	glycine
GF	glass fiber
GPC	gel permeation chromatography
h	hour
HCl	hydrogen chloride
HFIP	1,1,1,3,3,3-hexafluoropropane-2-ol
HMPA	hexamethylphosphoramide
HOBt	1-hydroxybenzotriazole
HRMS	high resolution mass spectrometry
HSQC	heteronuclear single quantum correlation spectroscopy (^{1}H–^{13}C NMR)
H_2SO_4	sulfuric acid
Hz	hertz
IR	infrared
J	coupling constant (NMR)
K	kelvin
K	potassium
K_2CO_3	potassium carbonate
$KMnO_4$	potassium permanganate
l	crystalline lamellar thickness (in SAXS)
L	lamellar long period (in SAXS)

L	liter
λ	wavelength
LiCl	lithium chloride
LiOH	lithium hydroxide
m	multiplet (NMR)
m	meter
M	molar
$[M]^+$	molecular peak (in MS)
mol	mole
mol%	mole percent
MALDI-TOF	matrix-assisted laser desorption/ionization-time of flight
MeCN	acetonitrile
MeOH	methanol
$MgSO_4$	magnesium sulfate
min	minute
M_n	number-average molecular weight
M_w	weight-average molecular weight
m/z	mass-to-charge ratio (in MS)
N	newton
ν	frequency
NaOH	sodium hydroxide
NEt_3	triethylamine
NH_4OH	ammonium hydroxide
NHS	*N*-hydroxysuccinimide
NMP	*N*-methyl-2-pyrrolidone
NMR	nuclear magnetic resonance
Pa	pascal
PA	polyamide
PEG	poly(ethylene glycol)
PMMA	poly(methyl methacrylate)
P_n	degree of polymerization

ppb	parts per billion (in NMR)
ppm	parts per million (in NMR)
q	quartet (NMR)
q	scattering vector modulus (X-ray)
R_f	retention factor
RH	relative humidity
σ	strength
σ_{max}	ultimate strength
σ_y	yield stress
s	second
s	singlet (NMR)
SAED	selected-area electron diffraction
SAXS	small angle X-Ray scattering
SEM	scanning electron microscopy
t	triplet (NMR)
t	time
θ	scattering angle
T_c	crystallization temperature
TEM	transmission electron microscopy
T_g	glass transition temperature
TGA	thermogravimetric analysis
THF	tetrahydrofuran
TLC	analytical thin-layer chromatography
T_m	melting temperature
TPP	triphenylphosphite
UV/vis	ultraviolet/visible
vol%	volume percent
WAXS	wide-angle X-Ray scattering
wt%	weight percent
XRD	X-ray diffraction

1

General Introduction

1 General Introduction

1.1 Semiaromatic Polyamide Composites for Replacement of Metals

Replacement of metals such as steel with polymer-based materials is nowadays considered key to reducing weight, cost, and cycle times in applications ranging from consumer electronics packaging to automotive and aeronautical components. This approach combines economic benefits and design flexibility with a significantly reduced environmental footprint.[1-5] In this regard, glass fiber-reinforced thermoplastics are among the most promising candidates, as they are less dense than steel by at least a factor of four and well suited to rapid automated processing such as thermoforming and injection molding (Figure 1*a*). However, the challenge remains to find economically viable ways to improve existing high-performance thermoplastics and thermoplastic composites in order to meet performance requirements in many of these applications, particularly at higher use temperatures (above 150–200 °C). This is because lightweight structural materials are increasingly required to show not only exceptional mechanical strength and stiffness but also outstanding toughness, properties that are generally considered to be mutually exclusive for most classes of materials (Figure 1*b*).[6] Indeed, the design of low density polymer-based materials that simultaneously exhibit excellent strength, stiffness, and toughness remains an unsolved problem in materials science.[7,8]

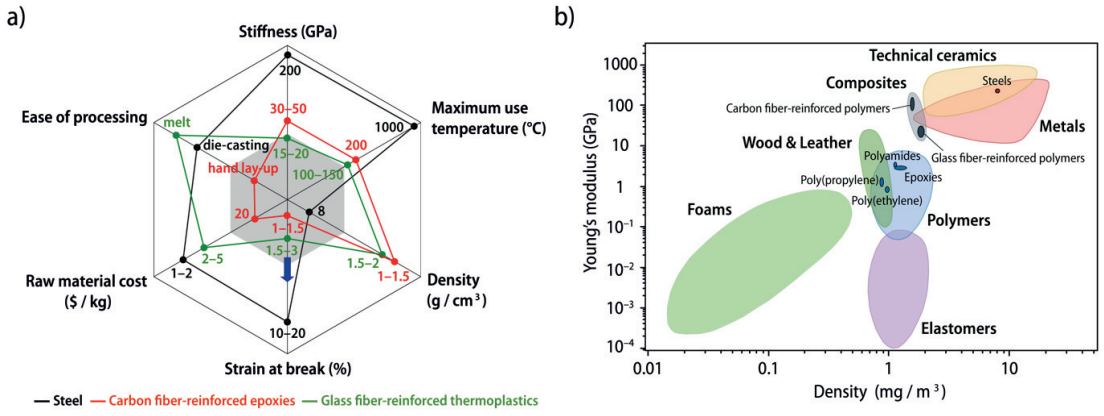

Figure 1. *a)* Glass fiber-reinforced thermoplastics could offer interesting alternatives to metals such as steel, providing an increase of the strain at break (blue arrow) without compromising at the same time the stiffness and maximum use temperature. *b)* Ashby plot of the Young's modulus (stiffness) as a function of density for various classes of materials. Such plots clearly show that lightweight materials cannot be at the same time strong, stiff and tough.

Aliphatic and semiaromatic polyamides are particularly attractive as high-performance thermoplastics, because they combine strong hydrogen-bonded networks, melt processability, and tuneable chain stiffness. In general, polyamides therefore show a wide range of thermomechanical properties. For instance, whereas lower melting temperatures and more ductile behavior are characteristic of aliphatic polyamides, semiaromatic polyamides generally show higher melting temperatures and stronger, stiffer behavior. The strength and stiffness of these materials may be improved further by the addition of inorganic reinforcements such as glass fibers. Glass fiber-polyamide composites are already used in automotive industry to replace metal parts such as oil pans or seat frames.[9] However, their ductility remains limited, and the consequent lack of toughness is currently a major obstacle to the wider industrial application of semiaromatic polyamides and semiaromatic polyamide composites. Hence, there is an urgent need to develop new approaches to the optimization of processing characteristics and properties in semiaromatic polyamide-based materials.

The present thesis demonstrates attempts to improve the ductility of semiaromatic polyamides by melt compounding them with small amounts of aliphatic polyamides to give random copolyamides. While successful, this approach depends on the availability of compatible polyamides on the market, and the remarkable gains in ductility are still accompanied by losses in strength and stiffness. Solving this conundrum is addressed in some biomaterials such as silks. For instance, spider dragline silk shows a remarkable combination of strength, ductility and toughness that cannot be reproduced with conventional polyamides. In a second part, this thesis therefore focuses on the synthesis of novel monomers that allow to prepare polyamides whose microstructure and morphology is inspired by that of natural structural polymers.

In the following sections, we will first provide an overview of the commonly applied synthesis strategies in polyamide research (Section 1.2). Then, we will focus on the different steps that are required to engineer high-performance polyamide composites, ranging from the choice of the polymer matrix to its ultimate mechanical reinforcement by the addition of inorganic fillers that will interact differently with the matrix, depending mostly on their nature and size (Section 1.3). Finally, a discussion of the structure of silks and their extraordinary mechanical properties will serve to show why the control of folding in polyamides may be a useful approach (Section 1.4).

1.2 The Amide Bond Formation in Polymer Science

This first section aims at exploring some of the main synthetic pathways available to synthesize polyamides, with a particular focus on bulk and solution polycondensations. The former method is mainly used in industry to produce on the kiloton scale most of the polyamides currently available on the market. Solution polycondensation encompasses a range of synthetic methods that are usually more suited to laboratory-scale syntheses. Many different procedures for the synthesis of polyamides can be found both in the patent literature and in scientific publications, but only the most relevant ones will be reviewed here.

1.2.1 Generalities on Polyamides and Nomenclature

Polyamides, sometimes referred to as "nylons" in the literature, can either be synthesized by ring-opening polymerization of cyclic amides (lactams), giving AB polyamides (Scheme 1*a*), or by polycondensation of two bifunctional monomers. In this case, suitable monomers could for example be amino acids to produce AB polyamides, or more commonly diamines and dicarboxylic acids, which will result in AABB polyamides (Scheme 1*b*).

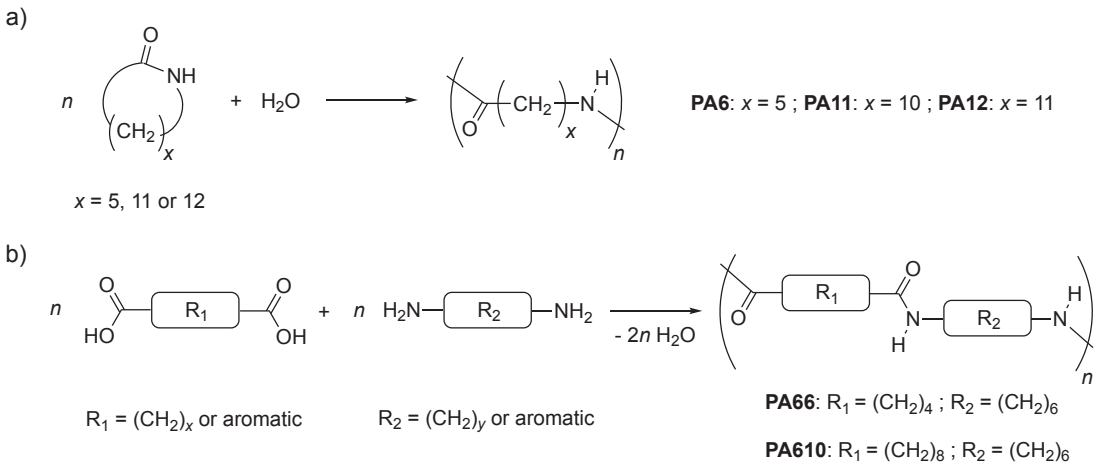

Scheme 1. General scheme of the amide-bond forming reactions for the synthesis of polyamides. *a)* Aliphatic AB-type polyamides are synthesized by the ring-opening polymerization of lactams in the presence of water or any other nucleophile. *b)* The polycondensation of two bifunctional monomers offers more versatility and leads to AABB aliphatic, semiaromatic or fully aromatic polyamides. The reaction pathway depicts the amide bond formed by the condensation of amine and carboxylic groups, accompanied with the release of water, but different reactive groups can be used. For both types of reactions, the structures of the most common aliphatic polyamides are given here to illustrate the usual nomenclature used in the polyamide field.

The lactam-based polymerization method strictly results in aliphatic polyamides, whereas the use of bifunctional monomers allows for more chemical diversity, with the possible introduction of aromatic moieties in the polymer backbone. The polycondensation of an aliphatic monomer with an aromatic monomer therefore yields a semiaromatic polyamide, and fully aromatic polyamides, or polyaramids, are obtained when both starting monomers are aromatic. By convention, AB polyamides are designated by the two-letter code "PA" followed by the number of carbon atoms that are present in the repeating unit. When the polyamide is obtained by the polycondensation of two aliphatic bifunctional monomers (AABB), the number of carbon atoms in the diamine repeating unit is given first, followed by the number of carbon atoms in the diacid repeating unit. The use of terephthalic or isophthalic acid monomers is usually denoted by the letters "T" or "I" respectively.

1.2.2 Bulk Synthesis of Industrial-Grade Polyamides

In any step-growth polymerization, the degree of polymerization and hence the molecular weight of the polymer are governed by the Carothers equations. In this context, the stoichiometric ratio of the reactants is of prime interest as it controls the theoretically achievable molecular weight of the polymer. In order to obtain the highest possible average molecular weight, this ratio has to be equal to one. This means that any stoichiometric excess rapidly limits the degree of polymerization.[10]

Therefore, AABB polymerizations are often performed starting from crystallizing a diammonium dicarboxylate salt ("nylon salt") from an aqueous solution of the dicarboxylic acid and diamine monomers, which results in a precise stoichiometric ratio of the reactive species (Scheme 2).[11] This salt is then transferred into a closed reactor, which was previously flushed with nitrogen, and heated to a temperature around 200 °C.[12,13] At this temperature, the polymerization proceeds fast, and the pressure in the vessel starts to increase due to water evaporation. The temperature is then increased above the melting temperature of the polyamide, and the pressure increases up to 18–20 bars. In order to displace the reaction equilibrium in favor of the amide formation, the water released during the process has to be evacuated from the reactor. The pressure is therefore slowly reduced using a steam of nitrogen, until it reaches the atmospheric pressure. During this last polycondensation step, the temperature is kept constant, and the viscosity of the reaction

mixture drastically increases, limiting chain diffusion and, consequently, slowing down the reaction. In order to achieve high conversions, the reaction temperature needs to be set substantially above the polyamide melting temperature but below its decomposition temperature. Polyamides which thermally decompose before melting, such as PA6T or polyaramids, can therefore not be synthesized *via* this method and are instead synthesized in solution by polycondensation of diamines and diacyl chlorides (Section 1.2.3).

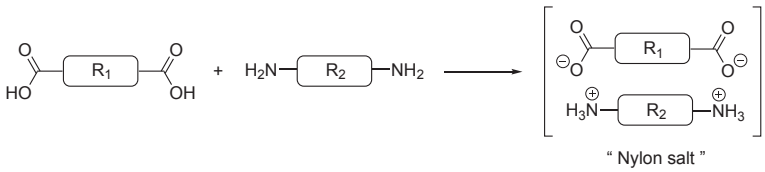

Scheme 2. The formation of a "nylon salt" is the first step of the polycondensation of two bifunctional monomers, allowing for a perfect control of the stoichiometry.

The polymerization of a lactam monomer is also performed in the bulk, albeit with a slightly modified procedure since the stoichiometric ratio between the amine and the carboxylic is automatically achieved in the case of an AB polymerization. The procedure is usually initiated by hydrolysis of the lactam molecules in the molten state, using a catalytic amount of water.[14] As soon as a certain number of end-groups have been generated in this way, the polyaddition starts and leads to the formation of an oligoamide (or prepolymer). Higher molecular weight polyamides are eventually obtained by polycendensation of these smaller units. Instead of activation with water, a catalytic amount of a strong base can also be used to produce the strongly nucleophilic lactamate anions so that polyamidea are obtained by a living anionic ring-opening polymerization.[15]

In any case, additives such as organic acids or monofunctional monomers are often used during the polymerization process that serve, respectively, as catalysts or end-capping agents to control the molecular weight of the final polyamide. Once the molten polyamide has been extracted from the reactor and cooled or spun to obtain either a resin or a fiber, its molecular weight can be further increased by solid-state post-condensation. In this process, the polyamide is heated in vacuum to a temperature typically 10–40 °C below its melting point, to ensure a sufficient mobility of the chain ends and avoid particle agglomeration.[16-18] If the temperature is sufficently high, the reactive end groups undergo condensation, and the water by-product is removed with a stream of inert gas.

1.2.3 Solution Polycondensation Reactions

As seen from the previous subsection, most industrial-grade aliphatic and semiaromatic polyamides are synthesized under solvent-free conditions in the bulk. However, when the polymer melting temperature is too high for this process to be used without inducing thermal degradation, as is the case for fully aromatic polyamides, solution-phase synthesis procedures have to be used.[19,20]

The low-temperature polycondensation of diacyl chlorides with diamines in solution was first developed by Dupont as one solution to produce the high-performance poly(*m*-phenylene isophthalamide) and poly(*p*-phenylene terephthalamide), commercialized under the tradenames Nomex™ and Kevlar™, respectively (Scheme 3).

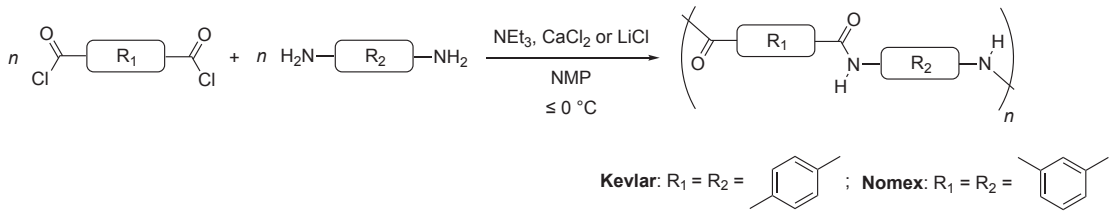

Scheme 3. The low-temperature solution polycondensation of diacyl chloride and diamine monomers allows for the synthesis of a variety of semiaromatic and fully aromatic polyamides. In particular, Kevlar and Nomex fibers can be synthesized in this way. The hydrogen chloride (HCl) produced by the amide bond formation is quenched by the tertiary amine (NEt_3).

Since then, this method has mainly been used for the synthesis of fully aromatic polyamides at the laboratory scale.[21-27] The reaction usually takes place over a few hours in polar aprotic solvents such as *N*,*N*-dimethylacetamide (DMAc) or *N*-methyl-2-pyrrolidone (NMP) in the presence of a stoichiometric amount of a tertiary amine, usually triethylamine (NEt_3), and a few weight percent of calcium chloride ($CaCl_2$) or lithium chloride (LiCl). The organic base has to have a pK_B value lower than the diamine in order to effectively neutralize the hydrogen chloride formed by condensation. The salt presumably forms a complex with the polyamide, supressing the possibility to form interchain hydrogen bonds between amide groups and hence improving the polymer solubility over the course of the reaction.[28]

The drawback of this method lies in the high sensitivity of the diacyl chloride end-groups towards hydrolysis so that the presence of water must absolutely be excluded from the reaction mixture

by using anhydrous reactants and solvents and by performing the reaction in an inert atmosphere. Acyl chlorides are also known to react with tertiary amines, forming ketenes[29] or an amide and an alkyl halide.[30] By performing the polycondensation at or below 0 °C, the rate of these chain-terminating side reactions can be drastically reduced as compared to the rate of the condensation reaction.[27]

Alternative routes avoiding the use of diacyl chloride monomers have therefore been explored in parallel. Yamazaki and Higashi were able to synthesize polyamides starting from dicarboxylic acid and diamine monomers within reasonable reaction times on the order of several hours. The reaction takes place in an inert atmosphere in NMP containing a metal salt (e.g., LiCl) and requires the addition of pyridine and triphenylphosphite (TPP) (Scheme 4). They postulated that the dicarboxylic acid moieties are activated through the formation of a pentavalent phosporous intermediate when heated at 80–120 °C, before aminolysis takes place.[31-36] In spite of attempts to replace TPP by a mixture of various triphenylphosphine derivatives and alkyl halides,[37] the original procedure developed by Yamazaki and Higashi remained the most popular one, because of better yields and higher polymer molecular weigths obtained.

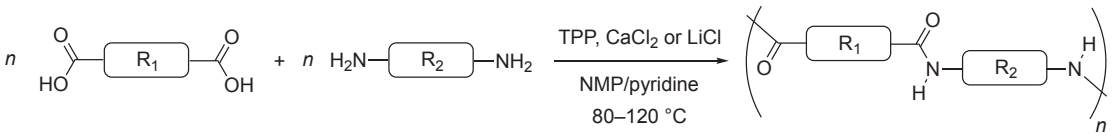

Scheme 4. Yamazaki-Higashi solution polycondensation of dicarboxylic acid and diamine monomers, used mainly for the synthesis of semiaromatic and fully aromatic polyamides.

Katsarava *et al.* popularized the active ester polycondensation route initiated by the work of Overberger and Sebenda[38] as well as Ogata *et al.*.[39] They activated several aliphatic and aromatic dicarboxylic acids by esterification reactions with pentachlorophenol[40] or *N*-hydroxysuccinimide[41] before performing a polycondensation with different aliphatic and aromatic diamines (Scheme 5). The reactions were carried out at temperatures between 30 and 120 °C, usually in hexamethylphosphoramide (HMPA). HMPA is a polar amide solvent that is known to have a great solubilizing power but is also classified as a potential carcinogen. Kricheldorf *et al.* therefore later replaced HMPA by the less toxic dimethylsulfoxide (DMSO) and studied the polycondensation at 60 °C of aliphatic diamines with the bis(4-chlorophenyl), bis(*N*-

hydroxysuccinimidyl) or bis(imidazolidyl) esters of sebacic acid.[42] Even though the latter approach led to slightly higher molecular weights, all three activated diesters were found to be efficient regarding to polycondensation reactions. Compared to the Yamazaki-Higashi route, this method has the advantage of requiring neither metal salt additives nor an organic base. The obtained polyamide can straightforwardly be recovered by precipitation into water, filtered off, and washed with more water and acetone, with no need of an additional purification by extraction under reflux.

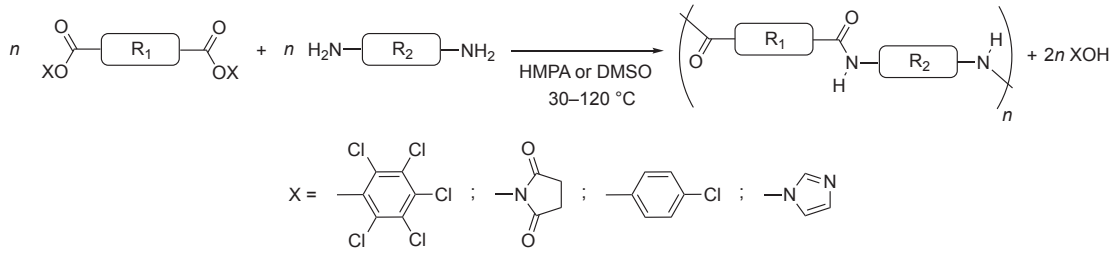

Scheme 5. The active ester solution polycondensation route popularized by Katsarava *et al*. which is particularly efficient for the synthesis of aliphatic and semiaromatic polyamides. The original method stated that the highest molecular weights were obtained with the use of the carcinogenic HMPA as the solvent, but Kricheldorf *et al*. later demonstrated that the reaction also works efficiently in DMSO.

It is worth noting that, for a polyamide synthesized by either one of the presented solution-phase method or in the bulk, the molecular weights obtained in the bulk will generally be higher. Indeed, the growth of the polymer chain in solution polycondensation is often limited because the polyamide ultimately precipitates from the solution. Moreover, the use of an organic solvent makes the solution-phase techniques presented above less suited to the production at the industrial scale. However, they provide convenient alternatives to the bulk processes and are particularly well suited for laboratory scale syntheses.

1.3 Engineering of High-Performance Polyamide Composites

In this section, we will review the essential steps in the design and engineering of high-performance polyamide composites for technical applications such as metal replacement. The process starts with the choice of a suitable polyamide matrix, based not only on its mechanical properties but also on its ease of processing. In making this choice, it is of primary importance to understand the role of hydrogen bonds between adjacent polyamide chains in the formation of

crystalline domains in the polymer matrix. The extent, structure, and stability of the crystalline phase are key to the thermomechanical properties of polyamides and their processability. We will also see that, owing to the relatively restricted number of commercially available polyamide matrices, the synthesis of semiaromatic copolyamides is of considerable interest, in so far as it may provide additional matrices with more balanced properties.

Even so, such melt-processable polyamides will always suffer from far lower stiffness than metals typically used in structural applications. This is why the final step towards a high-performance polymer-based material often involves reinforcement with a rigid filler. However, stiffness improvements obtained in this way are generally associated at the expense of substantial losses in ductility.

1.3.1 The Role of Hydrogen Bonds in the Crystal Structure of Polyamides

Most commercial polyamides are semicrystalline materials, containing a certain fraction of ordered crystalline domains embedded in a more disordered, amorphous phase. In such polymers, a periodic distribution of amide groups along the polyamide backbone favours the formation of crystalline structures stabilized by hydrogen bonds between NH and CO groups in neighboring chains. These well-ordered hydrogen-bonded chains most commonly form lamellar crystals, which are further organized into roughly spherical agglomerates, known as spherulites. In this subsection, we will show how the overall crystallinity of a polyamide depends not only on its chain configuration, but also on processing and cooling conditions.

The crystalline phases of typical aliphatic polyamides such as poly(hexamethylene adipamide) (PA66) and poly(ε-caprolactam) (PA6) are characterized by two-dimensional hydrogen-bonded sheets, that further stack due to Van der Waals interactions. The crystallization process therefore does not only involve the optimization of the conformational and packing energy, but also optimization of the interchain hydrogen bonds.[43] Moreover, kinetic factors and the temperature dependence of the different contributions to the overall free energy may give rise to a range of crystalline polymorphs, depending on the thermomechanical history.

The α and γ phases are the most commonly encountered phases in commercial aliphatic polyamides.[44] In α crystals, the chains adopt a fully extended zigzag conformation, while the amide

groups in γ crystals are rotated with respect to the plane of the methylene chain segments, resulting in a reduction in the chain repeat distance compared to that in the corresponding α crystal.[45] "Even" AB-type polyamides with long methylene chains (PA8, PA10, PA12) as well as "even-odd", "odd-even", and "odd-odd" AABB-type polyamides crystallize predominantly in the γ form.[46,47] On the other hand, "even-even" AABB-type polyamides such as PA66 and PA610 crystallize preferably in the triclinic α form, characterized by stacked hydrogen-bonded sheets of parallel extended chains in which adjacent chains show an axial shift by one methylene unit (Figure 2*a*).[48] The widely used PA6 is able to crystallize in both forms (Figure 2*b*), giving rise to different wide-angle X-ray scattering (WAXS) patterns.[49-53] The α form of PA6, in which the hydrogen-bonded sheets are made up of antiparallel chains, is either obtained by crystallization from a solvent or by slow cooling from the melt. On faster cooling, PA6 crystallizes in the γ form. External factors such as temperature, water content or applied strain can be used to reversibly transform γ crystallites into the α form.[54,55]

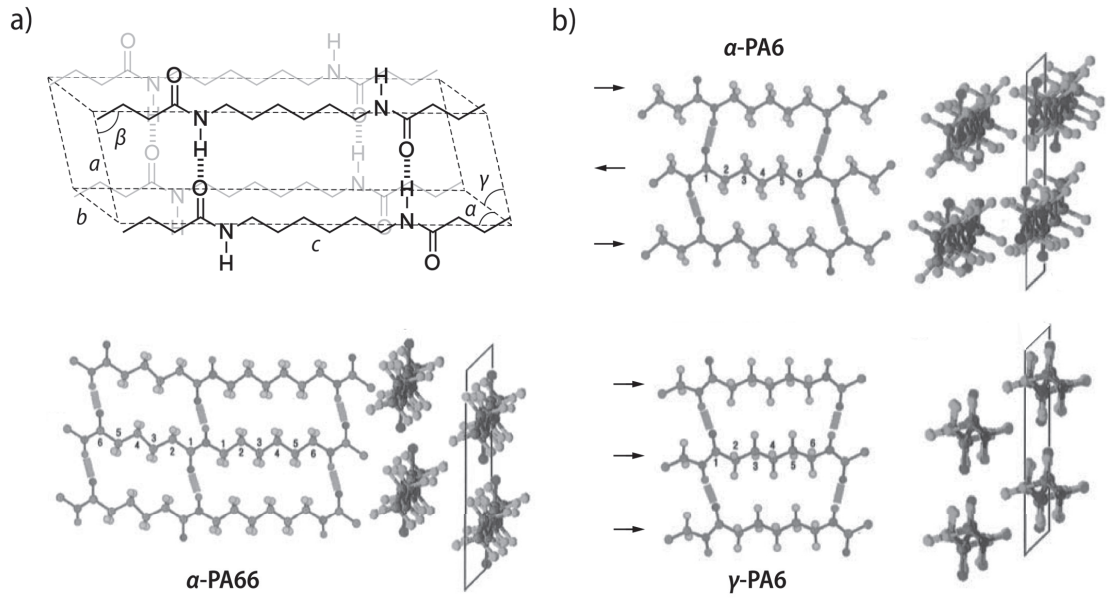

Figure 2. Common aliphatic polyamides usually crystallize either in the α or in the γ form. *a)* PA66 crystallizes in the triclinic α form, with lattice parameters *a* = 0.49 nm, *b* = 0.54 nm, *c* = 1.72 nm, α = 48.5°, β = 77.1° and γ = 63.5°. The chains adopt a planar zigzag conformation and form hydrogen-bonded sheets that are stacked in the *b*-direction. *b)* Depending on the crystallization conditions, PA6 may crystallize in either of the monoclinic α or γ forms. In the α form, adjacent chains in the hydrogen-bonded sheets are antiparallel (with respect to their N and C-termini). In the γ form, the chains are parallel and the hydrogen bonding direction is oblique to the plane of the zigzag conformation of the methylene groups. Figure adapted from [48] and [53].

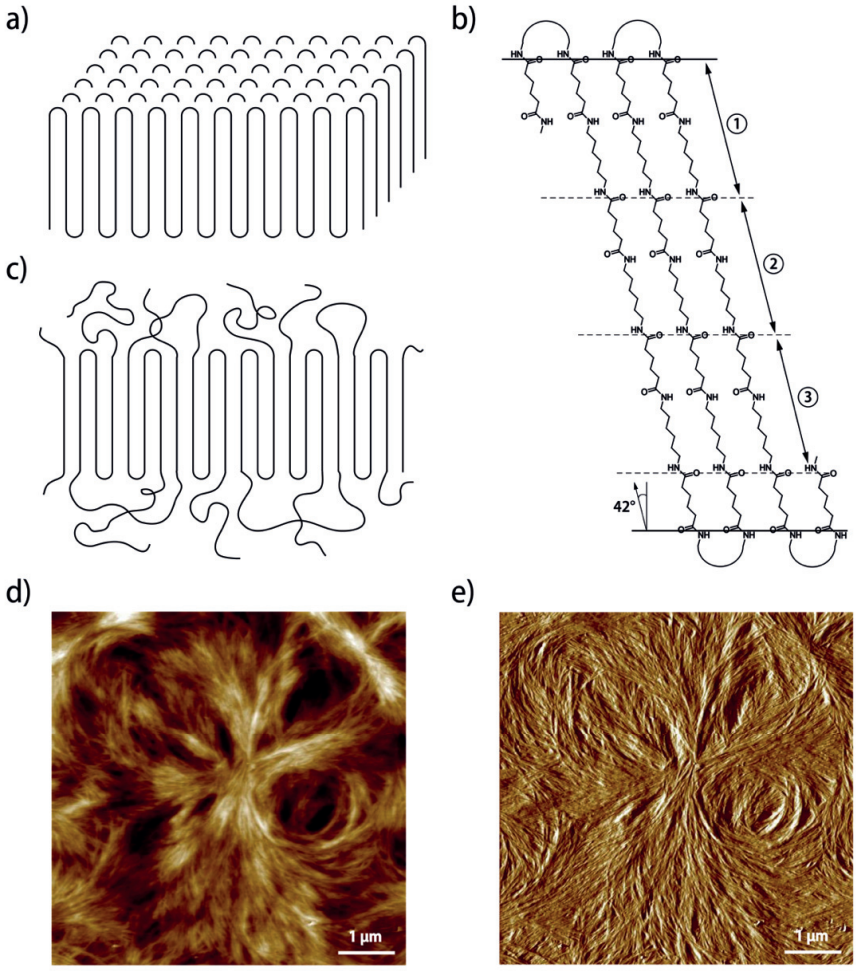

Figure 3. The folding of the polymer chains leads to the formation of crystalline lamellae which arrange themselves into spherulites with a size of a few microns. *a)* Typical lamellar structure of a polyethylene crystal upon folding of re-entrant chains as described by Keller. *b)* Dreyfuss and Keller demonstrated by SAXS and WAXS investigations that PA66 lamellae, obtained by recrystallization from solution, have a thickness of only a few nanometers, which corresponds to 3.5 repeat units. The more flexible diamine units better allow for re-entrant chain folding. *c)* Schematic representation of the disorder expected at the crystalline amorphous-interface of melt-crystallized semicrystalline polyamides. The loose amorphous chains at the interface serve to connect the crystalline lamellae which grow from different nucleation points in the sample to form spherical entities called spherulites. Such structures can be observed for example on the *d)* topographic, intermittent contact mode and *e)* error signal AFM images of cross sections of an injected-molded, semiaromatic copolyamide crystallized from the melt. Figures *a)–c)* adapted from [56] and [57].

Electron microscopy has shown that polyamide single crystals adopt a lamellar structure, with the chains aligned in the direction perpendicular to the lamellar surface, implying extensive re-entrant chain folding, as in polyethylene single crystals.[56] (Figure 3*a*) Dreyfuss and Keller, using a combination of wide-angle and small-angle X-ray measurements (WAXS and SAXS), observed a

lamellar thickness of about 5.5 nm in PA66 crystallized from solution, which corresponds to chain stems containing only three and a half monomer repeat units (Figure 3*b*).[57] They stated that only non-integer values of repeat units can be obtained in polyamides, due to the folding achieved through the more flexible diamine repeating units at both ends of the stems. When crystallized from the melt, however, polyamides typically exhibit spherulitic structures (Figures 3*d*, *e*). Spherulites are formed by the nucleation of crystalline lamellae at different points which grow as spherical, three-dimensional entities until neighboring spherulites impinge.[58,59] In these bulk phases, re-entrant chain folding is, different from polyolefins, *not* prevalent, and adjacent lamellae are connected through the loose amorphous chain segments at the crystalline-amorphous interphase (Figure 3*c*).

1.3.2 Thermal and Mechanical Properties of Aliphatic Polyamides and Polyaramids

The thermal properties of semicrystalline polymers are defined by a melting (T_m) and crystallization temperature (T_c), which correspond to the melting and crystallization of the crystallites respectively, and by a glass transition temperature (T_g), which marks the transition of the amorphous regions from the glassy to the rubbery state as the temperature is increased. Melt processing of fully amorphous polymers often requires much higher processing temperatures than T_g to enter the viscous flow regime, which is located at the end of the rubbery plateau.[60,61] However, most commercially available polyamides are semicrystalline and, because the T_g of a semicrystalline polymer is lower than its T_m, process temperatures just above T_m are usually sufficient to ensure a viscous response.[62]

From a thermodynamic point of view, the change in the Gibbs free energy (ΔG) during melting at constant pressure is equal to zero. This implies that the melting temperature is equal to the ratio of the enthalpy of melting (ΔH_m) and the entropy of melting (ΔS_m), according to equation *(1)*.

$$\Delta G = \Delta H_m - T\Delta S_m = 0 \iff T_m = \frac{\Delta H_m}{\Delta S_m} \qquad (1)$$

The entropy contribution ΔS_m increases with the number of chain conformations available in the melt and hence with chain flexibility. The enthalpic contribution ΔH_m increases with the strength of intermolecular forces in the crystal relative to the melt, which, in the case of aliphatic

polyamides, are strongly influenced by the optimization of hydrogen bonding. The amide groups in the chain backbone do not only give rise to hydrogen bonding, but also hinder rotation and hence restrict the number of chain conformations available in the melt. Therefore, the melting temperature of aliphatic polyamides decreases as the density of amide groups decreases, i.e., as the number of methylene units between amide groups increases (Figure 4*a*).[63-66] An additional "odd-even" dependence on the composition of the monomer units is also observed, with "odd" AB and "even-even" AABB polyamides exhibiting higher T_m than even AB and "even-odd" AABB polyamides of similar methylene/amide densities respectively. This may be attributed to hydrogen bonds that are only formed at the cost of energetically less favoured conformations. For example, the polymer chains in PA5 and PA7 are aligned parallel to one another while, in PA6, both parallel and antiparallel alignments can be achieved.

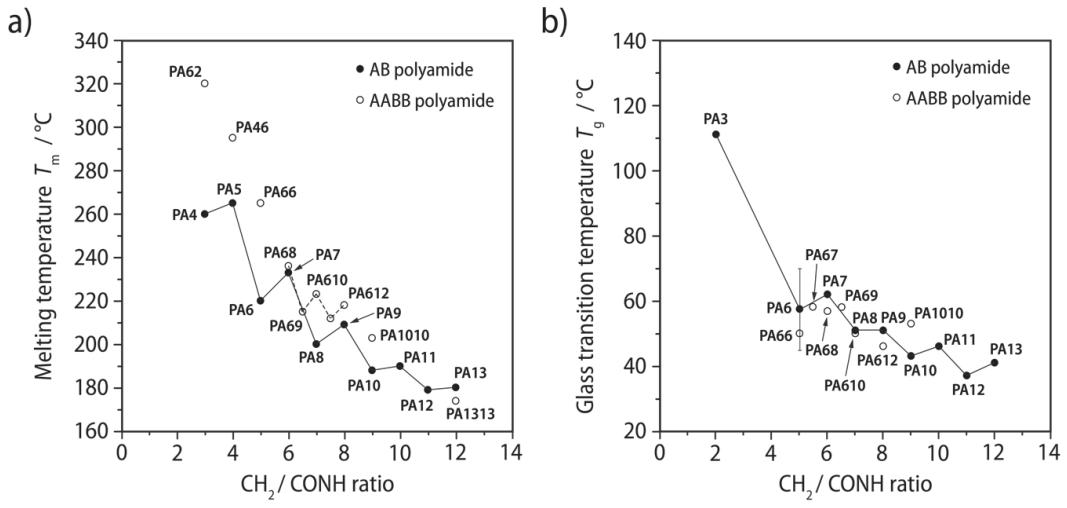

Figure 4. Influence of the methylene/amide ratio (CH_2/CONH) on the thermal properties of commercially available AB and AABB aliphatic polyamides. Both the *a)* melting temperatures (T_m) and *b)* glass transition temperatures (T_g) decrease as the density of hydrogen bonds decreases or, in other terms, when the number of methylene units between the amide bonds increases. An additional dependency of the odd-even composition of the monomer units can also be observed in the T_m and T_g of AB-type (solid lines) and AABB-type polyamides (dashed line). Figure obtained by compilation of the data from [65] and [66].

The inclusion of aromatic moieties in the polyamide backbone increases the backbone rigidity, and hence decreases ΔS_m. In addition to interchain hydrogen bonds, the π-π interactions between aromatic units in adjacent polymer chains contribute to increase ΔH_m. Both factors explain why the melting temperature increases upon the addition of aromatic cores, to the point where melting

occurs at higher temperatures than decomposition, as is the case for the fully aromatic Nomex and Kevlar. This is particularly remarkable because, in contrast to aliphatic polyamides that decompose above 350 °C, the 20 % higher C–C and C–N bond dissociation energies in these tightly packed polyaramids lead to decomposition temperatures of above 400 °C and 500 °C, respectively.[67] Fully aromatic polyamides therefore cannot be processed into final products from the melt. However, solution spinning can be employed instead to produce highly oriented fibers.

The number of methylene groups in the polymer backbone, the presence of rigid, aromatic moieties, the geometry of the chains in space, and the forces between them do not only control T_m in polyamides, but also affect the glass transition temperature, T_g. As revealed by both infrared (IR) spectroscopy[68-70] and solid-state nuclear magnetic resonance (NMR) spectroscopy,[71] interchain hydrogen bonds form both in the crystalline and the amorphous phases. Therefore, similar to T_m, a decrease in the hydrogen bond density, or, equivalently, an increase of the number of methylene units between the amide groups, leads to a decrease in T_g (Figure 4*b*).[66,72] Moreover, the inclusion of aromatic groups in the polyamide backbone increases the chain rigidity, and thus increases T_g.[73]

A pronounced reduction of the T_g of aliphatic polyamides is also observed upon water uptake,[74] which is suggested to take place primarily in the amorphous phase where the existence of free volume allows for the diffusion of small molecules.[75] Water is believed to act as a plasticizer that competes for and breaks the interchain hydrogen bonds, and thus increases the chain mobility. Water uptake results in a monotonic decrease of the T_g converging to a finite, limiting value.[76] For example, the wetting of PA66 matrix with 1 *wt*% water was shown to decrease its T_g value by more than 20 °C.[77] This effect is usually less important in (partially) aromatic polyamides, due to the slower rate of diffusion of water molecules in the tighter packed, higher T_g matrix.[78]

The overall degree of crystallinity (χ) plays a very important role for the mechanical properties of polyamides. In the case of polyaramids, χ is sensitive to the degree of fiber orientation during the final stage of the processing. For instance, the linear, *para*-oriented structure of the molecular chains in Kevlar provides it with a high χ of up to 95% in the case of Kevlar49 (a high modulus grade of Kevlar, used in cable and rope products).[79,80] The ultimate strength (σ_{max}) and extensibility of Kevlar are superior to those of steel, and its stiffness, given by the elastic modulus

or Young's modulus (*E*), also compares well with that of steel (Table 1).[81] The *meta*-oriented amide groups in Nomex result in more limited crystallinity, rendering it far more ductile than Kevlar and reducing its strength and stiffness by a factor of six.[82] The influence of χ on the mechanical properties of aliphatic polyamides has also been studied by Starkweather *et al.*.[83] These authors have shown that PA66 and PA610 become more brittle at higher degrees of crystallinity, but their elastic modulus and yield stress (σ_y) increase (Figure 5*a*, *b*). The same authors also observed an increase in the tensile strength of PA610 with χ, independently of the number average molecular weight of the polymer (Figure 5*c*).

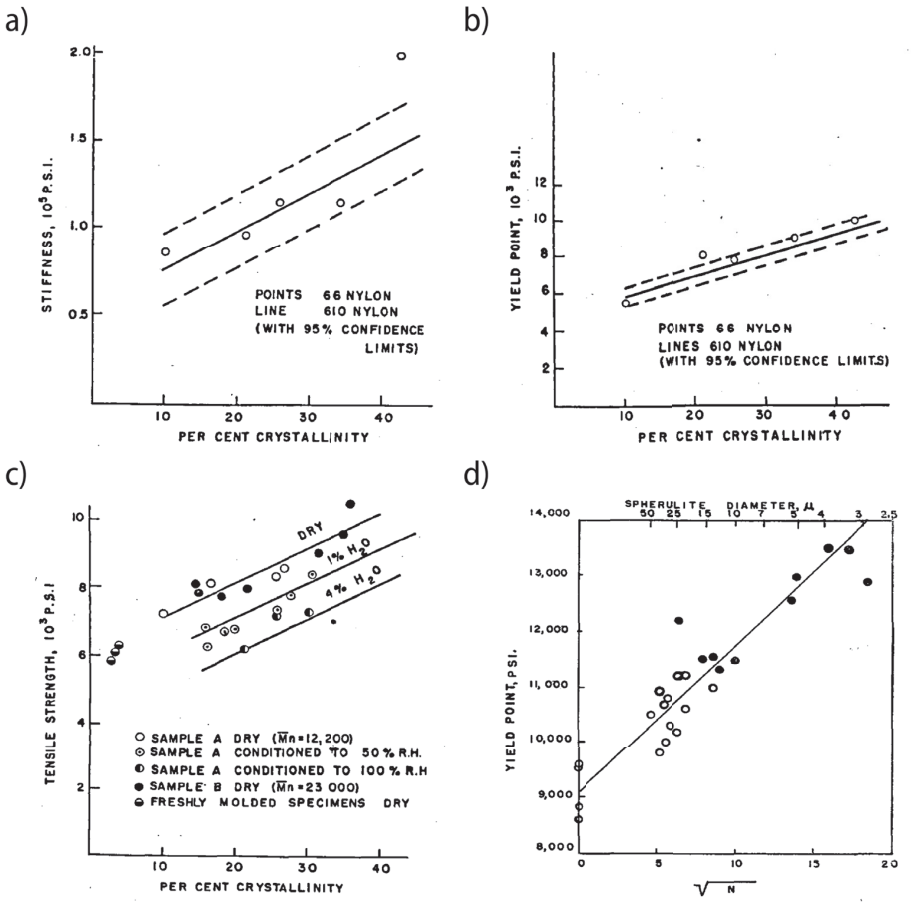

Figure 5. Influence of the degree of crystallinity (χ) and average spherulite size on the mechanical properties of PA66 and PA610. Both the *a)* stiffness (Young's modulus, *E*) and *b)* yield stress (σ_y) increase linearly with the degree of crystallinity for both polyamides. *c)* The tensile strength of PA610 was also found to follow the same trend, irrespective of the average molecular weight of the polyamide. *d)* The yield stress of PA66 films (open circles) or test bars (filled circles) produced by compression molding and injection molding, respectively, increases linearly with the square root of the number of spherulite boundaries per millimeter (*N*) or, in other terms, it decreases with the spherulite diameter. 1 p.s.i. (pound per square inch) corresponds approximately to 6.9 Pa. Graphs reproduced from [83] and [84].

Table 1. Typical values for the density, ultimate strength (σ_{max}), stiffness (Young's modulus, *E*), and strain at break of common aliphatic polyamides, polyaramids, and steel. The values obtained for aliphatic polyamides vary significantly according to the length of their aliphatic segments and their conditioning, because these polymers are very sensitive to the absorption of water. The properties of Kevlar may also vary significantly depending on processing conditions.

Material	Density / g·cm^{-3}	σ_{max} / MPa	*E* / GPa	Strain at break / %
Aliphatic PA	1.13–1.35	50–100	1–5	30–200
Nomex	1.38	500–700	11–22	15–30
Kevlar	1.4–1.5	2800–4000	70–150	2–4
Steel	7.8–8.0	1500	200	1

At the molecular level, the type of crystal lattice was found to have an influence on the mechanical properties of polyamides, as shown by Miri *et al.* for the tensile properties of PA6.[85] They measured higher yield stresses for PA6 containing mainly the crystalline α-structure than for any of its other crystalline forms. At a larger length scale, Starkweather and Brooks showed that the yield stress of PA66 increases with the spherulite diameter (Figure 5*d*), with smaller spherulites resulting in a lower strain at break and hence reduced ductility.[84]

The degree of crystallinity and the morphology of the crystalline phase thus strongly affect the mechanical properties of semicrystalline polymers. However, the mechanical properties also depend on the properties of the amorphous phase.

In the glassy state, below T_g, the mobility of the amorphous chains is severely reduced. In the rubbery state above T_g, however, the internal energy barriers to changes in conformation become negligible. It follows that, for temperatures far below T_g, semicrystalline polymers tend to be rigid (high *E* and σ_y), but above T_g, there is a marked drop in *E* and σ_y, generally accompanied by an increase in ductility and toughness. Thus, tensile stress-strain curves obtained by Shan *et al.* on dry PA6 specimens tested at constant strain rate were found to depend strongly on the drawing temperature (Figure 6).[86] Above 50 °C, i.e., around the T_g of PA6, the elastic modulus and the stress at break decreased, the strain at break increased, and the yield drop characteristic of low-temperature deformation disappeared.

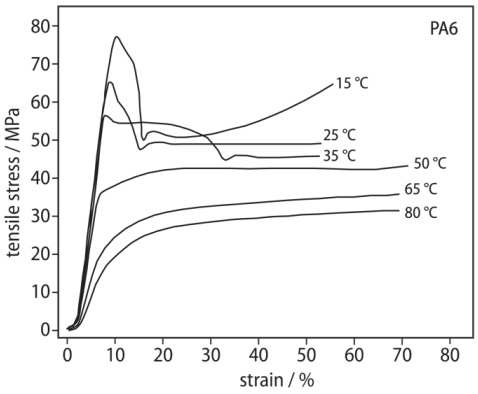

Figure 6. Influence of the drawing temperature on the mechanical properties of injection-molded PA6 specimens that had been dried in vacuum. *a)* Stress-strain curves of the specimens drawn at a constant strain rate of 10 mm/min and different temperatures. At drawing temperatures around and above the T_g of PA6 (≥ 45 °C), no yield drop is observed. Figure adapted from [86].

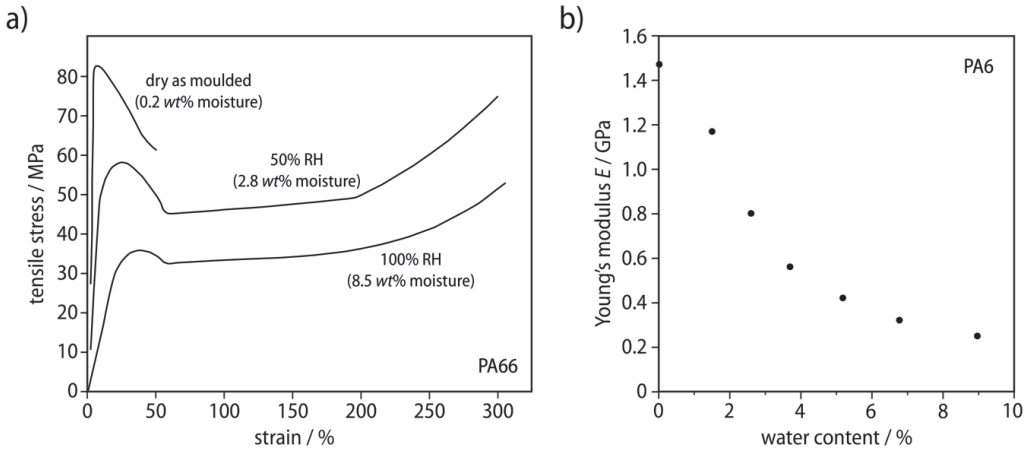

Figure 7. Effect of the water content on the mechanical properties of aliphatic polyamides. *a)* Tensile stress-strain curves for Zytel® 101 (PA66) at 298K. Increasing the moisture content by adjusting the relative humidity (RH) yields less strong and less stiff materials owing to plasticization. This results in a drastic improvement in ductility, which increases by a factor of six on absorption of 2.8 *wt*% water. *b)* Similarly, the stiffness of PA6, as expressed by the Young's modulus decreases exponentially with the water content in specimens with a crystallinity of about 40%. Figure adapted from [87] and [76].

As mentioned above, water can penetrate and plasticize the amorphous regions and thus strongly affect the T_g of the polyamide, especially in the case of aliphatic polyamides. At the same time, water absorption should also affect mechanical properties, because the mobility of the polymer chains is enhanced by the breaking of interchain hydrogen bonds. Hence, increasing the water content in Zytel® 101, a PA66 produced by DuPont, results in a decreased stiffness (lower E) and

strength (both the yield stress and the ultimate tensile strength).[87] At 25 °C, this is accompanied by a drastic increase in ductility, the strain at break increasing by a factor of six at only 2.8 *wt*% water content (Figure 7*a*). The same effects were reported by Miri *et al*. for PA6,[88] and Inoue and Hoshino observed a drop in the elastic modulus at 30 °C by a factor of five in fully saturated PA6 containing 9 *wt*% of water with respect to dry PA6 (Figure 7*b*).[89] Reimschuessel later fitted the data of Inoue and Hoshino with an exponential decay function, reflecting the drop of the elastic modulus to a finite value which did not change significantly upon further increase of the water concentration.[76]

To summarize, the thermal and mechanical properties of polyamides are strongly interrelated and can be at least partly understood in terms of the structure of the polymer chain and its ability to form crystalline domains *via* an extended hydrogen bond network. Polyaramids are high-performance materials with high chain stiffness, but they cannot be processed via rapid, cost-effective melt processing techniques. On the other hand, varying the length of the aliphatic segments makes it possible to tune the melting temperature of aliphatic polyamides in the approximate range 180–280 °C, making them melt-processable, and hence cheaper to produce, with high throughput. These polymers have a higher strain at break than strongly π-π stacked and hydrogen-bonded solution spun polyaramid fibers, but far lower strengths and stiffnesses. They are also more susceptible to water absorption than fully aromatic polyamides and, hence, to plasticization, which further diminishes their elastic modulus and yield stress. A good balance between mechanical and thermal properties and moisture resistance can be obtained using carefully designed semiaromatic polyamides, providing an extended range of operating temperatures, without sacrificing melt processability.

1.3.3 Random Copolyamides and Transamidation Reactions at High Temperatures

The bulk polycondensation of three or more bifunctional monomers leads to the formation of random copolyamides (Scheme 6*a*). Thus, semiaromatic polyamides with a wide range of thermo-mechanical characteristics may be prepared by combining rigid terephthalic acid (T) and isophthalic acid (I) monomers with aliphatic diamines such as hexamethylene diamine (6).[90] Pure PA6T shows a high degree of crystallinity, a glass transition temperature, T_g, of about 140 °C, and a yield stress of up to 480 MPa. However, its melting point, T_m, of around 370 °C is too high for

conventional melt processing to be possible without excessive thermal degradation.[90,91] Pure PA6I also has a T_g of 125 °C but is fully amorphous.[92] Hence, the incorporation of isophthaloyl units in PA6T backbone reduces T_m while leaving T_g essentially unchanged.[90,91,93] Random copolymerization of PA6T with about 30 *mol*% of PA6I therefore leads to a high-performance, semicrystalline polyamide (T_m = 315 °C, T_g = 130 °C), referred to as PA6TI (Scheme 6*b*), that is far better suited to injection molding and thermoforming than PA6T.[91]

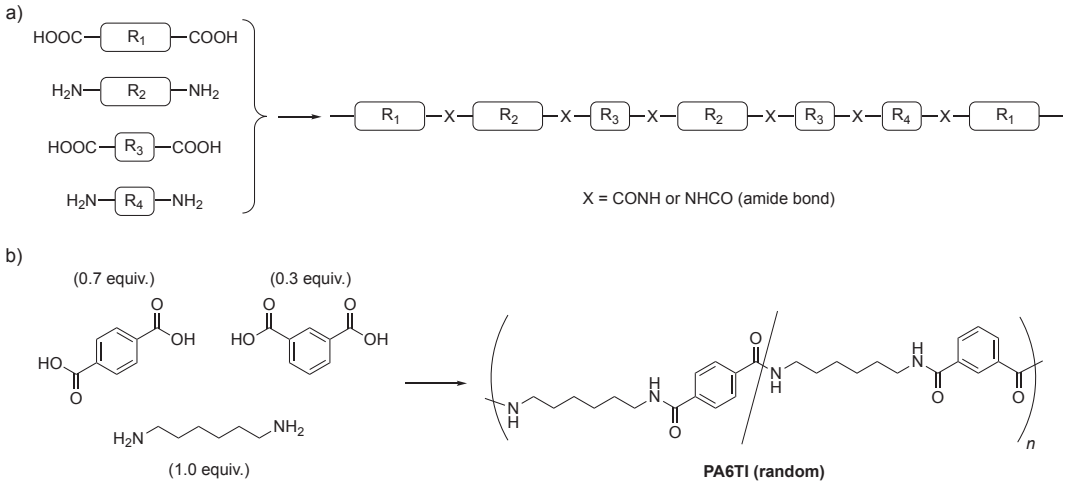

Scheme 6. *a)* Formation of a random copolyamide by bulk synthesis using at least three different bifunctional monomers. All monomers must be added at the same time to avoid the formation of specific blocks. *b)* Synthesis of PA6TI random copolyamide starting from terephthalic acid, isophthalic acid, and hexamethylene diamine. The inclusion of 30 *mol*% of the kinked isopththalic acid reduces the melting point of PA6TI with respect to the PA6T homopolymer, rendering it melt-processable.

An alternative way to obtain copolymers is to use exchange reactions, or transamidation reactions, which take place in polyamide melts during high-temperature processing, potentially leading to copolymerization in blends of two or more different polyamides.[94-97] Transamidation is a general term that covers "inner-inner" amide exchanges (amidolysis) but also "inner-outer" exchanges with the reactive terminal groups NH_2 and COOH (aminolysis and acidolysis) that are already present as polymer end groups or generated *in-situ* by thermal or hydrolytic cleavage (Scheme 7). While "inner-inner" exchange reactions are common in polyester and polycarbonate blends,[98,99] Miller reported that amidolysis reactions are not observed in polyamide melt blends at temperatures below 280 °C.[100] The initial miscibility of the blend components plays an important role for these reactions to take place.[101,102] For example, limited miscibility in

PA66/PA612 blends has been suggested to hinder transamidation reactions in the absence of a catalyst.[103] It was also shown that PA6/PA12 and PA6/PA1212 blends exhibit phase separation despite the fact that hydrogen bonds may form between the chains, unless some chemically modified rubber compatibilizers are used.[104-106]

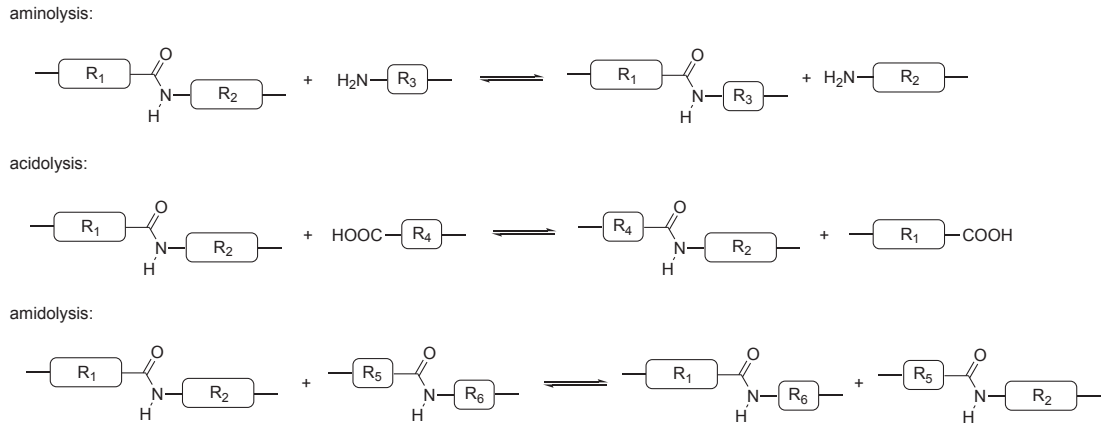

Scheme 7. Schematic illustration of the different types of transamidation reactions that can take place in polyamide melts, leading to randomization of the polyamide backbones. Aminolysis and acidolysis involve the amine and acid end groups, respectively, and are therefore dependent on their respective concentrations, while amidolysis reactions only take place at elevated temperatures.

The bulk properties of such blended materials are expected to depend on the nature and proportions of the original polyamides, with exciting possibilities for synergy, given the wide range of commercially available candidates. Even so, previous investigations have been limited to binary blends composed of a semicrystalline aliphatic polyamide and either another semicrystalline aliphatic polyamide or an amorphous semiaromatic polyamide.[94-98,103,107] In this latter case, the extent of transamidation and, hence, the degree of randomness estimated from nuclear magnetic resonance experiments have always been found to be low (< 25%).[94,95] Puglisi and Samperi determined the degree of randomness in equimolar blends of semicrystalline PA66 and PA610 by comparison of the measured peak intensities from matrix-assisted laser desorption/ionization-time of flight (MALDI-TOF) mass spectra with those of mass spectra determined from numerical models.[96] They later used the same procedure on equimolar blends of PA6 with either PA610 or PA46.[103] Although a quantitative analysis solely based on relative mass peak intensities should be treated with caution, the transamidation reactions were in all

cases found to be efficient, with degrees of randomness of up to 60–100%, depending on the compounding time and blending temperature.

To the best of our knowledge, however, there has so far been no detailed investigation of aliphatic/semiaromatic polyamide blends in which both components were semicrystalline.

1.3.4 Matrix Reinforcement by the Addition of Rigid Fillers

Despite the possibilities for tuning the thermomechanical properties of polyamides described in the last sections, their mechanical properties and, in particular, their stiffness remain greatly inferior to those of steel. In order to be good candidates for metal replacement, the incorporation of rigid reinforcing fillers serves to provide polymer composites with a strength and stiffness that are significantly improved compared to those of the pure polymer matrix. In addition to their direct effect on the mechanical properties, most reinforcing fillers also provide nucleation sites that increase the rate of crystallization of the polymer matrix upon cooling from the melt.[108,109] A commonly used method for the production of moldable composites is usually to blend the polyamide with microscopic or nanoscopic fillers such as reinforcing microfibers or nanoparticles in an extruder at a temperature above the T_m of the polyamide matrix (Figure 8).[110]

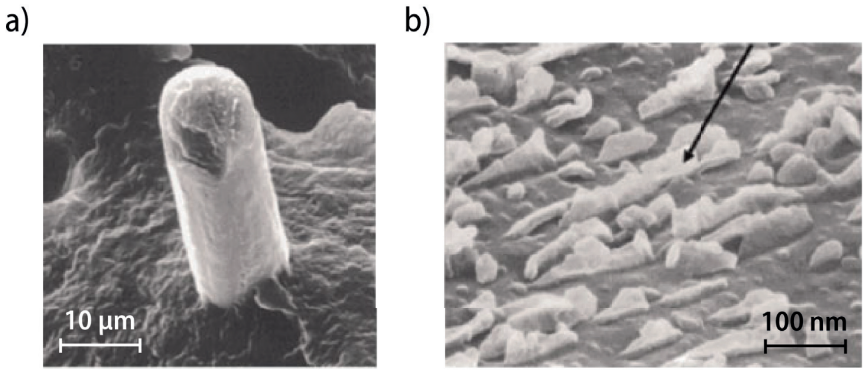

Figure 8. SEM images of PA6 with *a)* glass fibers and *b)* 1.85 *wt*% of exfoliated montmorillonite clay nanoparticles. These images illustrate the difference in size between these two types of reinforcement, the scales between the two pictures differing by a factor of one hundred. Images reproduced from [110].

By far the most common way to improve the thermomechanical properties of polyamides remains addition of silica-based (SiO_2) microfibers, commonly named glass fibers (GF). This results in materials with significantly increased stiffness and heat deflection temperature, a property

commonly used in industry to qualify the ability of a thermoplastic material to withstand high service temperatures.[111] Three main factors have been found to affect the mechanical properties of glass fiber-reinforced polyamide composites, namely *i)* the concentration and the geometry of the fibers, *ii)* the orientation of the fibers in the matrix, and *iii)* the interfacial adhesion between the glass fibers and the polymer matrix.

For a given glass fiber content, higher strength and stiffness are generally obtained using long glass fibers, which typically refers to fibers with an aspect ratio (defined as the ratio of fiber length to diameter) of 100–1000 in the final product, rather than shorter ones (aspect ratio of 20–30).[112] However, both the concentration and the length of the fibers that may be incorporated in the thermoplastic material are limited by the requirement of an adequate viscosity during the processing steps to allow for a good flow of the melt.[113]

The embrittlement, i.e., the decrease of ductility observed upon addition of the fibers also limits the extent of strength and stiffness improvement.[114] In their study of glass fiber-reinforced PA66, Curtis *et. al*. observed an increase in both the elastic modulus and the stress at break on increasing the fiber volume fraction, which was always accompanied by a decrease of the strain at break, regardless of the fiber length.[113] However, for a given fiber volume fraction, the "long-fiber" composites (average fiber lengths of 0.5 mm) always exhibited higher strength and stiffness than the "short-fiber" composites (0.27 mm). Similar results were obtained by Thomason, who also showed that the average diameter of the fibers may also influence the tensile strength of the composites.[115] Thus, at constant fiber content, increasing the fiber diameter results in a decrease in tensile strength, which is more pronounced for shorter glass fibers (a loss of about 1.7% per micron).

The fiber orientation in the composite results in high degrees of anisotropy and inhomogeneity in the material properties and is influenced by multiple factors such as the overall shape of the molded part and its thickness, the position of the injection gate(s), the flow rate of the melt, and also the fiber length distribution.[116,117] For a simple square plate geometry, it is generally assumed that a layered structure is formed after injection, consisting of a skin, a shell and a core.[118-120] In the shell, close to the walls of the mold, the flowing composite is subject to a high shear stress, which tends to orientate the fibers parallel to the mold flow direction (MFD) (Figure 9*a*). These

shear stresses tend to vanish in the core, however, and the fibers often retain an orientation perpendicular to the MFD acquired as a result of divergent flow in the injection gate. In the very thin skin layer (with a thickness of a few hundred micrometers), the orientation distribution is more random due to the rapid solidification of the melt upon contact with the colder walls of the mold. Bernasconi *et al.* have shown that, in standard dogbone-shaped tensile test specimens made by blending 30 *wt*% glass fibers with PA6, most of the fibers tend to align with the specimen axis and the MFD, minimizing the width of the core layer (Figure 9*b*).[121]

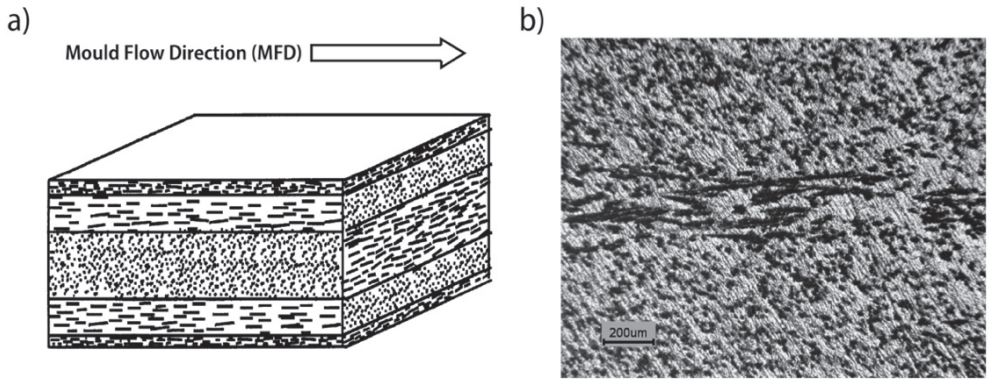

Figure 9. *a)* Schematic representation of fiber orientation in a square plate of 6 mm thickness relative to the mould flow direction (MFD) in the three different layers of the specimen: perpendicular to MFD in the core, parallel to MFD in the shell and random in the skin. *b)* Optical micrograph of a polished section cut perpendicular to the MFD in a PA6 dogbone specimen reinforced with 30 *wt*% glass fibers. The core thickness is only 0.2–0.3 mm for a total specimen width of 3.2 mm, and most of the fibers are aligned in flow direction. Images reproduced from [119] and [121].

To illustrate the importance of the fiber orientation for the mechanical properties of the composite, the authors cut specimens at different orientations θ with respect to the longitudinal axis of a square mould. The tensile tests showed a decrease up to 60% of the ultimate tensile stress, elastic modulus, and strain at break when increasing θ from 0° (standard conditions) to 90°. In any case, the fiber orientation in real parts can be very different from the standardized specimen due to complex shapes and/or irregular flow involved, which makes the transfer of results from standard tests to real components not straightforward. Therefore, injection-molding simulations are often performed to predict the fiber orientations and distributions, and the results are then transferred to modelling software that uses finite element analysis for mechanical property prediction.[122,123]

The fiber-matrix interface also plays an important role in the composite mechanical properties. Strong interactions between these two components reduce and delay the creation of voids at the interface and, ultimately, the failure of the material during deformation. Stronger adhesion is obtained by using a coupling agent capable of forming strong covalent or ionic bonds between the two materials. Silane molecules with different reactive functionalities can be hydrolyzed and condensed with the naturally occurring silanol groups on the glass surface to form functionalized glass fibers. [124] In polyamides, amine-modified glass fibers are typically used, the NH_2 groups being able to react with either carboxylic end groups or amide bonds along the polymer backbone.[125,126]

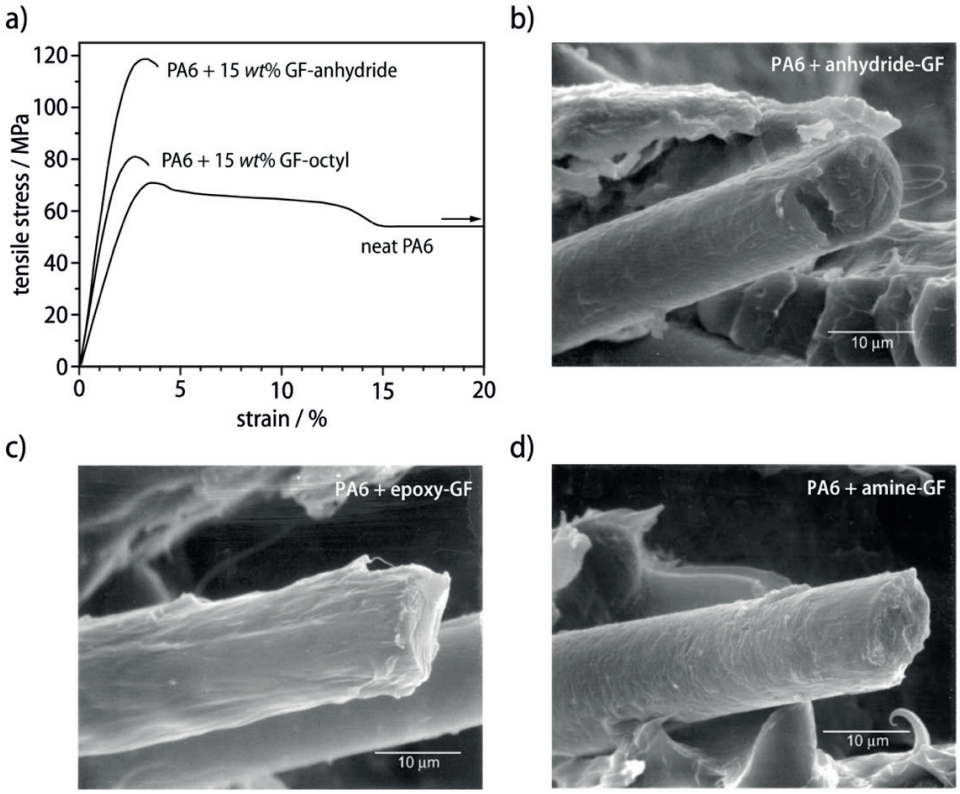

Figure 10. *a)* Stress-strain curves of neat and 15 *wt*% glass-fiber reinforced PA6. The composites using the reactive anhydride, epoxy, and amine sizing (only anhydride is displayed here) gave better mechanical properties compared to the unreactive alkyl sizing. This can be explained by good adhesion of the polyamide to the fibers, as observed on the SEM images of the fractured surfaces of the composites containing the glass fibers modified with reactive *b)* anhydride, *c)* epoxy, and *d)* amine functions. Figure adapted from [127].

For example, Laura et al. have studied the effect of the coupling agent on the mechanical properties of PA6 reinforced with 15 wt% glass fibers.[127] By using glass fibers modified with

anhydride, epoxy, or amine functions, they improved the stiffness, strength and ductility of the material by at least 10 % compared with composites processed with the same amount of unreactive octyl-functionalized glass fibers (Figure 10*a*). At the fracture surface, the fibers with reactive coupling agents were coated with a sheath of matrix material as observed by SEM micrographs (Figure 10*b*–*d*), and the failure occurred in the polymer matrix rather than at the matrix-fiber interface, as had been observed for the unreactive octyl-functionalized glass fibers.

The nanoscale mechanical reinforcement of polyamides using phyllosilicate clay nanoparticles has also gained considerable attention over the last decades. Phyllosilicate clays have a layered structure made up of stacked silicate sheets with a thickness as low as 1 nm and very high aspect ratios (between 100 and 1,000).[128] Most related investigations in the literature are based on aluminosilicate montmorillonite clay.

In order to obtain the maximum reinforcing effect from montmorillonite, a homogeneous nanoscale dispersion of the individual exfoliated silicate sheets in the polyamide matrix is generally sought.[129] However, exfoliation is difficult to achieve because the negatively charged sheets in the native clay are strongly bound together by electrostatic forces arising from the presence of intercalated counter cations, principally sodium and calcium.[128] Exfoliation therefore requires the use of dispersing or intercalating agents, which are principally amphiphilic quaternary ammonium cations that undergo ion exchange with the counter ions.[130,131] In the absence of dispersing agents, the interfacial interactions between the polymer matrix and the clay are generally weak.[132] This issue can be solved by choosing dispersing agents that are able to physically interact with the polymer of interest. For example, grafted amine-functionalized silanes can form a covalent bond with the polyamide and the clay, hence increasing the interaction and dispersion of the clay in the matrix.[129]

Polyamide nanocomposites thus offer interesting possibilities. However, thermal degradation of the quaternary ammonium molecules that are often used to exfoliate the clay nanosheets is often a problem in high performance thermoplastics. For instance, Xie *et. al.* have shown that montmorillonite modified with alkyl quaternary ammonium surfactants degrades at temperatures of 155–180 °C, which is lower than the melting temperature of most commercially available aliphatic polyamides.[133] Xiao *et. al*. studied the effect of modified montmorillonite on the

onset of degradation of polycarbonate and showed the degradation temperature to be reduced by 65 °C compared with the unmodified polymer.[134] Therefore, even if polyamide nanocomposites show significant mechanical property enhancement with respect to pure polyamides, the applicability of this technology to high melting point polyamides is limited by the thermal degradation of the organically modified clay.

1.4 Silk Materials as a Source of Inspiration for the Design of Novel Monomers

In order to broaden the options available for the engineering of semiaromatic polyamides, synthetic pathways towards novel monomers may take inspiration from biomaterials. Structural proteins such as silk materials can be regarded as the biological analogue of synthetic polyamides and have long been a major source of inspiration for the design of novel polymer materials. Some structural aspects of silk materials, such as their reliance on amide (peptide) hydrogen bond networks and their overall degree of crystallinity, may at first sight look very similar to those observed in synthetic polyamides. However, their respective microstructures are actually quite different, thanks to the ability of silk materials to fold into defined conformations and self-assemble into well-ordered secondary and tertiary structures.

These are responsible for the often extraordinary properties or unusual property combinations observed for silk materials.[135-137] In particular, spider *major ampullate* silk ("dragline silk") has attracted attention in this respect, owing to its remarkable combination of excellent strength, stiffness, and toughness, properties that are notoriously difficult to optimize simultaneously in synthetic materials.[138,139]

1.4.1 The Importance of Chain Folding for the Mechanical Properties of Silk Materials

Silk materials are composed of alternating alanine-rich hard segments and glycine-rich soft segments. The hard segments are typically amino acid sequences with about six repeating units and are either composed exclusively of L-alanine repeating units, or of alternating glycine (G) and L-alanine (A) repeating units. The former hard segments give rise to relatively well-ordered parallel pleated β-sheet secondary structures that further aggregate into well-defined, helically twisted nanofibrils comprising about six stacked β-sheets. These nanofibrils typically exhibit a length on the order of 50 nm and a width of 5 nm (Figure 11*a*), and they have been shown to

provide a highly efficient means of reinforcement, with tensile strengths of more than 1 GPa.[140,141] The less well-ordered GAGAGA-based hard segments are separated by sequences that serve to template β-turns and thus promote chain folding into several short, single, antiparallel pleated β-sheet structures, which are further lined up into a "beads-on-a-string"-like morphology (Figure 11*a*).[142-144] These two types of "crystalline" (but still quite disordered) domains are embedded into an "amorphous" matrix of the soft segments, which in turn still has a relatively high degree of residual order in the form of sequences with α-helical or 3_{10}-helical secondary structures.

Hence, chain folding in silk materials creates an intricate balance of order and disorder on several length scales that ultimately serves to distribute the stresses onto different components under different states of load and is thus responsible for the unusual combination of high stiffness, strength, ductility, and toughness. The nanofibrils most likely form a "crystalline" percolation network that takes up load at small strains and thus provides high stiffness. The break-down of this network at larger strains then allows for an efficient stress transfer to the matrix, where the folded "beads-on-a-string" and different helical segments become progressively unfolded. The concomitant breaking of hydrogen bonds does not only allow for energy dissipation and local stress relaxation,[145,146] but also for a successive recrystallization of the unfolded segments into β-sheet structures with a hydrogen-bonding direction perpendicular to the strain direction.

The overall process results in a stress-strain behavior that does not exhibit a yield point, but shows a continuous extension and strain hardening and hence results in a remarkable combination of elasticity and extensibility, ultimate strength, and toughness (Figure 11*b*).[147,148] The sophisticated role of chain folding also permits to tailor and optimize silk materials over a wide range of mechanical properties (Figure 11*c*, Table 2).[149,150] Besides *major ampullate* silk, which shows excellent strength and toughness, other types of silk display interesting properties such as the highly extensible *flagelliform* silk, with an extensibility up to 500% or the aggregate silk, which exhibits a glue-like behavior.

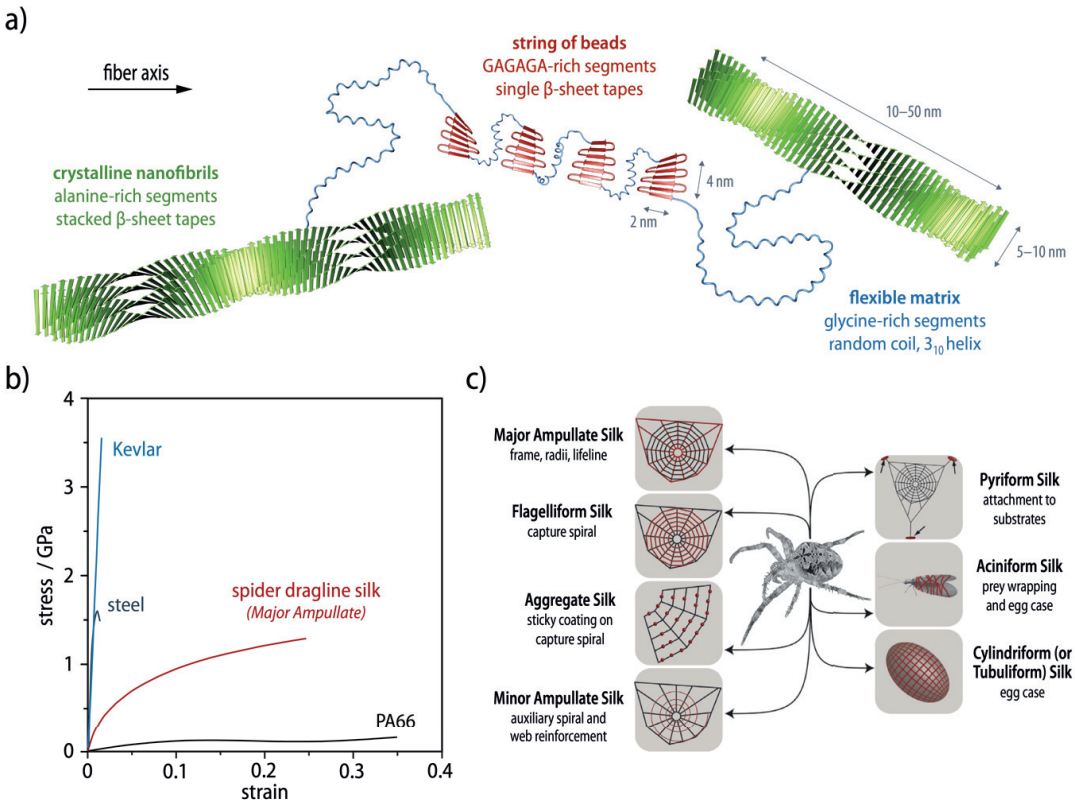

Figure 11. *a)* Schematic representation of the different nanoscopic features observed in spider dragline silk. Only one segment between the crystalline nanofibrils is displayed for clarity. Image reproduced from [144]. *b)* Schematic stress-strain curves of spider dragline silk versus different polyamides and steel. *c)* Overview of the different types of silk produced by orb-weaving spiders. Each type of silk (highlighted in red) has a different purpose, with mechanical properties tailored for this specific purpose (Table 2). Image reproduced from [149].

Table 2. The mechanical properties of silk fibers are dependent on the type of silk and also vary between different species. Hereafter are presented the mechanical properties (engineering values) of five different types of silk from *Argiope argentata*, as given by Blackledge and Hayashi.[150]

Silk	σ_{max} / MPa	*E* / GPa	Strain at break / %	Toughness / J·cm^{-3}
major ampullate	1220 ± 60	8.0 ± 0.8	23 ± 1	136 ± 7
tubuliform	360 ± 70	11.6 ± 2.1	34 ± 2	95 ± 10
minor ampullate	670 ± 110	10.6 ± 1.2	40 ± 1	137 ± 22
aciniform	640 ± 80	10.4 ± 1.4	51 ± 4	230 ± 31
flagelliform	100 ± 10	0.001 ± 0.0001	465 ± 3	75 ± 6

1.4.2 Turn Motifs in Silk Materials and Fibrillar Proteins

Since chain folding is crucial for the properties of structural proteins such as silk materials, amino acid sequences that give rise to "turns" are one of their key features. These turn sequences provide templates or nucleation sites for the folding of micro-domains. Two types of turn motifs can be distinguished in structure proteins, β-hairpin structures and β-serpentine structures.

The β-hairpin motif consists of a short segment made up of 2–5 amino acids often comprising L-proline units that connects adjacent β-strands within an antiparallel β-sheet (Figure 12*a, top*).[151-153] Isolated β-hairpins may be found in some protein domains, but they are more typically found in a series of β-strands that collectively form a single β-sheet tape, stabilized by interstrand, intrachain hydrogen bonding (Figure 12*a, bottom*), aided in some cases by ionic bonds between the amino acid residues.

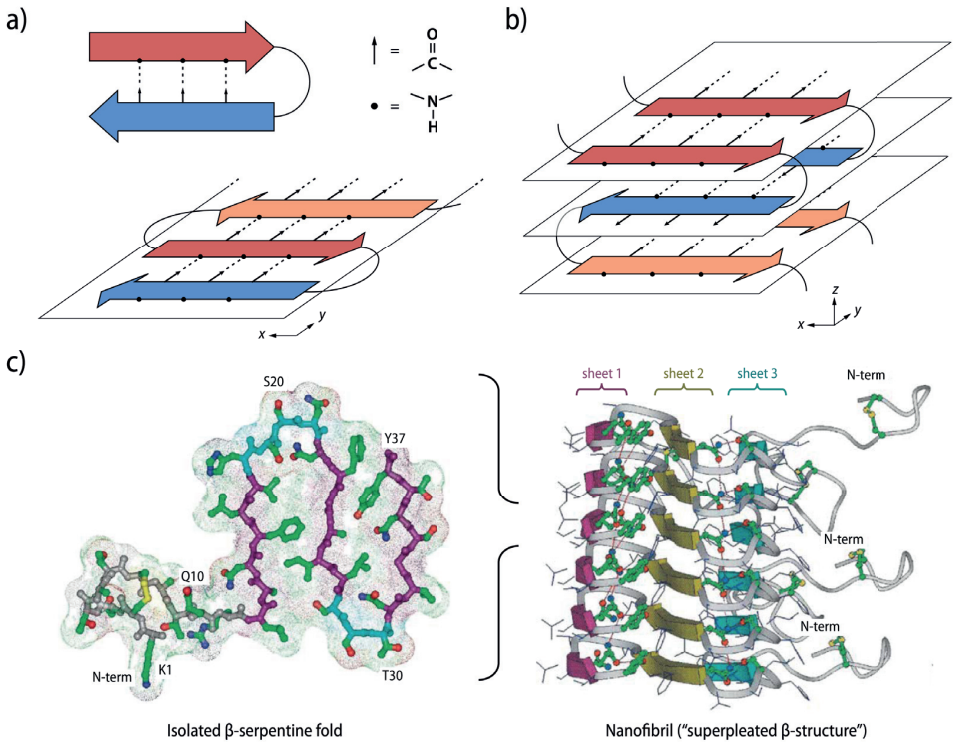

Figure 12. Schematic representations of turn motifs in natural proteins. *a)* The β-hairpin motif consists of antiparallel peptide strands connected by a short turn or loop of 2–5 amino acids, stabilized by interstrand, intrachain hydrogen bonding (dotted lines), resulting in single, antiparallel, pleated β-sheet tapes. *b)* By contrast, β-serpentine folds consist of β-strands in an antiparallel orientation held together by hydrophobic interactions between amino acid residues. β-serpentine folds then aggregate by interchain hydrogen bonding, resulting in nanofibrils, also termed "superpleated β-structures",[154,155] comprising a defined number of stacked, parallel pleated β-sheets. *c)* Structural model for human amylin, forming "superpleated β-structures". The figure of the amylin model was adapted from [155].

By contrast, β-serpentine folds are typically formed from 3–4 amino acids, often comprises two consecutive L-serine units, and connects β-strands in an antiparallel orientation; however, these β-strands are not connected by interstrand, intrachain hydrogen bonding but by hydrophobic interactions between the amino acid residues.[154,155] Interchain hydrogen bonding between independent β-serpentine structures promotes an aggregation such that a nanofibril with a defined number (corresponding to the number of connected β-strands in the β-serpentine fold) of stacked, parallel β-sheets is formed (Figure 12*b*). Such nanofibrils have also been termed "superpleated β-structures"[154,155] and are prevalent in fibrillar proteins, including the crystalline nanofibrils in silk materials and fibrillar aggregates in amyloidogenic proteins, such as those of the amyloid protein Aβ (associated with Alzheimer's disease), the prion forms of the yeast proteins Sup35p and Ure2p (associated with Creutzfeldt-Jakob disease), or human amylin (whose fibrillogenesis is linked to amyloid formation in type II diabetes) (Figure 12*c*).[156-158]

1.4.3 Synthetic β–Hairpin Mimics

A few linear peptides and peptide-polymer conjugates were shown to fold in aqueous solutions[159] and even form multiple stacks of β-sheets,[160] owing to the shielding of their hydrophobic surfaces from the polar solvent. However, a more consistent approach to the preparation of synthetic β-hairpin motifs is to graft peptide strands to a rigid molecular scaffold that templates a fixed dihedral angle of 180° at a defined distance. In what follows, we will refer to such scaffolds as "U-turn" units. In order to be a good template for the formation of folds similar to β-hairpins, the U-turn unit should define a distance of 4–5 Å between the two strands.

Photoresponsive 3,3'-disubstituted azobenzenes[161] and fused heterocyclic systems such as 2,8-disubtituted dibenzofurans[162] or 3,6-disubtituted carbazoles[163] have been postulated to give rise to β-hairpin-like structures, although the interstrand distance is more on the order of 5–9 Å in all of these cases. The dibenzofurans and carbazoles-based U-turns were shown to self-assemble into fiber-like nanostructures with a length of up to a few microns (Figure 13). The observed structures could in both cases be attributed to the formation of antiparallel β-sheets between the oligopeptide chains by interdigitation, and nanoribbons were assumed to form by further stacking into double β-sheets.

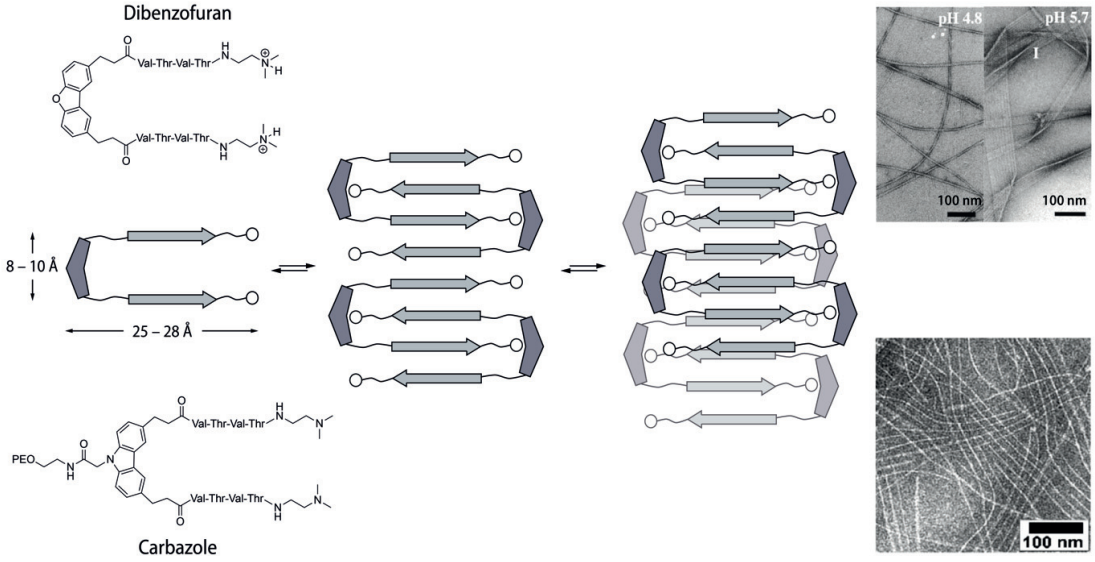

Figure 13. Oligopeptide-modified dibenzofuran and carbazole molecules form interdigitated β-sheet arrangements, which self-assemble into nanoscopic fibrillar aggregates as shown by TEM images. Figure adapted from [162] and [163].

Inspired by the structure of silk fibers, Sogah and coworkers synthesized a 4,6-dicarboxy-substituted phenoxathiin core to which they grafted silk-mimicking segments such as GAGA.[164-167] These rigid, β-hairpin domains were interconnected by soft segments based on poly(ethylene glycol) (PEG), producing hard-soft block copolymers. Solid-state infrared (IR) spectroscopy and powder X-ray diffraction both revealed that these copolymers tend to self-assemble into antiparallel or mixed parallel-antiparallel β-sheets, in addition to a substantial amount of random conformations (Figure 14). Indeed, the intrastrand distance of 4.5–5.0 Å templated by the phenoxathiin core should allow for the efficient formation of β-sheets *via* intrachain hydrogen bonding. However, the characterization of the resulting aggregates remained sketchy and the postulated structures of the resulting aggregates questionable because it did not match the spectroscopic findings. Using similar oligopeptide-connected phenoxathiin derivatives, Wagner and Feigel demonstrated by 2D-NMR experiments the inherent issue correlated to such molecular designs, i.e, the formation of macrocycles.[168]

The examples presented above show that folding of oligopeptides can be achieved using rigid scaffolds that mimic the β-hairpin motifs. However, the effect of such templates on the materials mechanical properties has never been systematically investigated to date, and these templates have, to the best of our knowledge, never been used for the preparation of bulk thermoplastic materials such as polyamides.

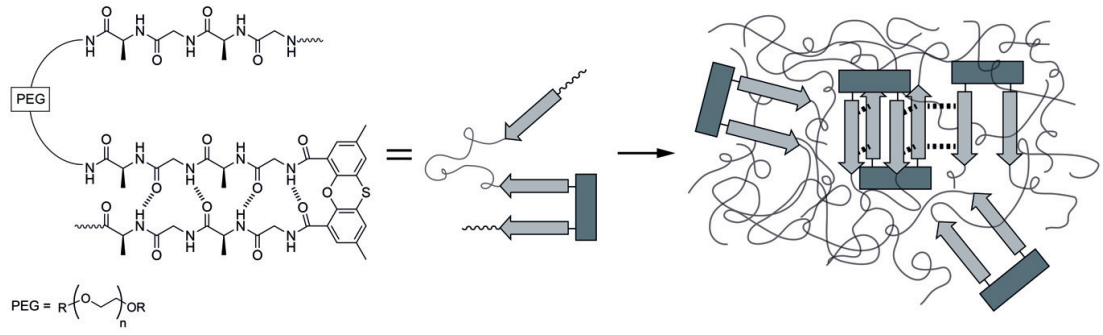

Figure 14. Hard-soft block copolymers comprising phenoxathiin-based β-hairpins. These units are postulated to self-assemble into antiparallel *β*-sheets, mixed parallel-antiparallel *β*-sheets or adopt random conformations. Figure adapted from [167].

1.5 Scope and Outline of this Thesis

From the results presented above, it becomes evident that semiaromatic polyamides are attractive as engineering polymers owing to their balanced mechanical properties and processability. They combine high strength and stiffness due to the rigid aromatic repeating units, with greater ductility than for fully aromatic polyamides thanks to the incorporation of flexible aliphatic segments. The presence of the aliphatic segments also makes them far easier to process than polyaramids, which are unsuitable for melt extrusion or injection molding. The strain at break of semiaromatic polyamides and their composites nevertheless remains limited, with adverse consequences for their toughness. This important technological issue must be addressed if polyamide-based structural materials are to continue to replace metals in engineering applications.

In the present thesis, we therefore aim to develop new pathways to semiaromatic polyamide-based materials that maintain the high strength and stiffness of existing commercial materials, but show significantly improved ductility and toughness. Two different approaches are taken. In a first engineering-driven approach, we intend to combine commercially available materials with complementary thermomechanical properties. To this end, we employ high-temperature melt blending of a semicrystalline, semiaromatic polyamide (PA6TI) with different amounts of the more ductile semicrystalline aliphatic PA66, PA610 and PA12 (Chapter 2). We then investigate the morphology and mechanical properties of the blends and their short glass fiber-reinforced composites (Chapter 3). In a second, more chemistry-driven approach, we intend to synthesize

novel dicarboxylic acid monomers to template polymer chain folding in the resulting polyamides, by analogy with certain structural features observed in silk materials (Chapters 4 and 5).

Within this framework, we will try to address the following research questions:

- Can we establish a simple and efficient procedure suitable for industrial scale-up that allows us to fine-tune the chemical structures, and hence the thermomechanical properties of semiaromatic polyamides? For this purpose, we will employ high temperature melt processing to combine different monomers with "compatible" chemical structures, hydrogen bonding patterns, and crystalline structures, with the goal to obtain homogeneous materials exhibiting well-defined distributions of substitutional defects among their constituent phases.
- Does the detailed control of order and disorder in semicrystalline polymers at various length scales have a significant influence on their mechanical response? We will attempt to correlate the measured thermomechanical properties of the melt-blended materials with our investigations on their microstructures and nanostructures. Here, we would like to gain better understanding of how to optimize the ductility and toughness in bulk mouldings of semiaromatic polyamides and their glass fiber-reinforced composites, without suffering from drastic concomitant reductions in strength and stiffness.
- Can we enforce the folding of polyamide chains, promoting their aggregation into well-defined tertiary structures such as the β-hairpins or β-serpentines motifs observed in structural proteins? To this end, we will synthesize semiaromatic polyamides starting from different rigid monomers to introduce kinks or turns, and verify whether re-entrant chain folding is achieved at the crystalline lamellar interfaces.
- Does this folding result in altered mechanical properties thanks to stress transfer to the surrounding matrix on unfolding? We will attempt to establish structure-property relationships to show the influence of re-entrant chain folding at the crystalline lamellar interfaces on the thermomechanical properties of the polyamides.

The results achieved during the present thesis will be presented in the style of a cumulative dissertation, with each chapter corresponding to a paper that has been or will be published in peer-reviewed scientific journals.

2

High Temperature Copolyamides by Efficient Transamidation of Polyamide Blends

All the results presented in this chapter have been published in:

"High Temperature Copolyamides by Efficient Transamidation of Crystalline-Crystalline Polyamide Blends", Cretenoud, J.; Galland, S.; Plummer, C. J. G.; Michaud, V.; Bayer, A.; Lamberts, N.; Hoffmann, B.; Frauenrath, H. *J. Appl. Polym. Sci.*, **2017**, *134*, 44349.

J. C. characterized the polyamide blends by GPC, MALDI-TOF, DSC and TGA, while WAXS and AFM measurements were performed together by S. G. and C. J. G. P. This work was supervised by V. M. and H. F. (EPFL) and A. B., N. L. and B. H. (EMS-Chemie, Domat-EMS, Switzerland).

2 High Temperature Copolyamides by Efficient Transamidation of Polyamide Blends

2.1 Introduction

A straightforward route to tailoring the properties of thermoplastics is to combine existing synergistically interacting polymers through melt blending and/or copolymerization.[169] Copolymerization generally leads to homogeneous materials with stable thermo-mechanical performance. By contrast, a frequent concern with melt-blended polymers is their limited miscibility, so that control of interfacial properties may be crucial to optimizing their morphology and bulk properties.[170] One way to achieve this is to use copolymer compatibilizers, in which case it is clearly advantageous in terms of the number of production steps if at least some degree of copolymerization takes place *in situ* during the melt blending process.[171-173]

Semiaromatic polyamides are particularly attractive as high-performance thermoplastics, because they combine strong intermolecular hydrogen-bonding with tunable chain stiffness. For example, the random copolymerization of the more rigid PA6T with 30 *mol*% of the kinked PA6I leads to high-performance, semicrystalline polyamides (T_m = 315 °C, T_g = 125 °C), referred to as PA6TI in what follows, that are far better suited to injection molding and thermoforming than pure PA6T.[91] However, the ductility of such materials still remains limited, with PA6TI failing at less than 10% tensile strain under standard test conditions as compared with more than 60% strain for typical aliphatic polyamides. The consequent lack of toughness is currently a major obstacle to the wider industrial application of semiaromatic polyamides and semiaromatic polyamide composites. There is hence an urgent need to develop new approaches to the optimization of processing characteristics and properties in semiaromatic polyamide-based materials.

It is well known that transamidation reactions take place in polyamide melts during high-temperature processing, potentially leading to copolymerization in blends of two or more different polyamides.[94-97] This therefore raises the possibility of facile *in-situ* preparation of modular polyamide-based materials, which may be either homogeneous or show well-defined phase-separated morphologies with high interfacial strengths. The bulk properties of such

materials are expected to depend on the nature and proportions of the original polyamides, with exciting possibilities for synergy, given the wide range of commercially available candidates.

In the present chapter, we show that rapid and extensive transamidation in blends composed of a semicrystalline semiaromatic polyamide with a semicrystalline aliphatic polyamide can result in homogeneous random copolymers. To this end, we melt-blended PA6TI with different proportions of PA66, PA610 and PA12 (Scheme 8).

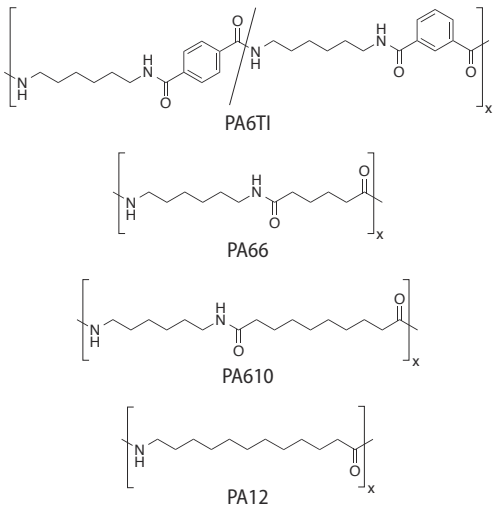

Scheme 8. Chemical structures of the semiaromatic polyamide poly(hexamethylene terephthalamide-*co*-isophthalamide) (PA6TI) and the three aliphatic polyamides poly(hexamethylene adipamide) (PA66), poly(hexamethylene sebacoamide) (PA610), and poly(laurolactam) (PA12) used in this work.

In the case of the even-even polyamides PA66 and PA610, MALDI-TOF spectrometry confirmed the formation of random copolymers with PA6TI during melt compounding, resulting in homogeneous materials with single melting temperatures as well as glass transitions, contrary to blends processed from solution. A high degree of crystalline order was observed in these blends, as evidenced by differential scanning calorimetry (DSC) and wide-angle X-ray scattering (WAXS). By contrast, blends of PA6TI with the more hydrophobic and less hydrogen-bonded polyamide PA12 showed phase separation and a less efficient transamidation process. We propose that semicrystalline polyamides with compatible crystal structures, a high degree of hydrogen bonding and similar hydrogen-bonding show good initial compatibility and, therefore, undergo extensive transamidation. This opens the way to the systematic design and preparation of novel high performance thermoplastic polyamides by simple melt compounding.

2.2 Copolymer Formation by Transamidation during Melt Compounding

Specimens of the semiaromatic polyamide PA6TI were blended with varying proportions of the aliphatic polyamides PA66, PA610, or PA12 by melt compounding for 20 min at 330°C. TGA measurements on the individual polyamides proved that they were thermally stable under these conditions (Figure 15, Table 3).

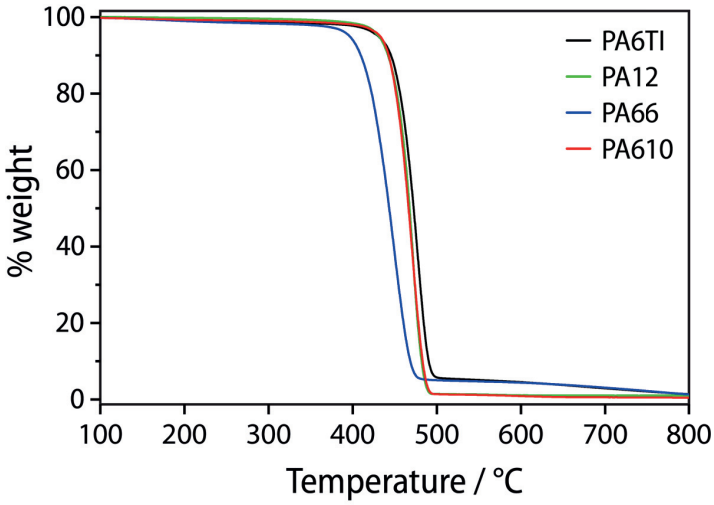

Figure 15. TGA scans of PA6TI, PA12, PA66 and PA610 performed in a nitrogen atmosphere at a heating rate of 10 °C/min. All polyamides are stable up to at least 400 °C, well beyond the extrusion temperature (330°C).

Table 3. Decomposition temperatures T_{95} and T_{90} of PA6TI, PA12, PA66 and PA610 determined by thermogravimetric analysis at 95 *wt*% and 90 *wt*% residual mass, respectively. Mass loss Δm_{330} in isothermal thermogravimetric analysis at 330°C for 20 min.

Polyamide	T_{95} / °C	T_{90} / °C	Δm_{330} / *wt*%
PA6TI	432	446	0.9
PA12	433	443	1.1
PA66	398	410	2.4
PA610	434	443	1.4

MALDI-TOF mass spectrometry provided clear evidence for extensive transamidation as a result of melt compounding. Previous investigations into transamidation have suggested that interchange reactions in copolyamides are driven principally by the concentration of carboxyl end

groups in the native polyamides through acidolysis reactions,[96,98,103] although it was not possible to verify this from the present measurements. Transamidation is therefore used here as a general term encompassing all possible interchange reactions in polyamides, i.e. acidolysis, aminolysis or amidolysis.

All observed peaks in the mass spectra from reference blends, obtained by mixing the as-received components in solution at room temperature, could be assigned to either linear or cyclic sequences of the individual polyamide components. In stark contrast, the mass spectra of all melt-compounded blends showed additional peaks (Figure 16). These peaks could be assigned to oligomers containing various combinations of the aromatic and aliphatic diacid repeat units present in the original blend components.

For instance, in the case of PA6TI blended with 50 *wt*% of PA610, the individual contributions to the spectra were well resolved, and oligomers containing a given total number of repeat units (with, e.g., 5 diamine and 5 diacid repeating units) were now characterized by a series of peaks corresponding to all of the different possible ratios of the aliphatic and aromatic diacid repeat units. The envelope of each such series of peaks was bell-shaped; the highest intensity peaks were those corresponding to the oligomers with roughly equal proportions of the aliphatic and aromatic carboxylic acids (e.g., 5 diamine and 2+3 or 3+2 terepthalic acid and sebacoic acid repeating units, respectively), while the peaks associated with the pure compounds showed significantly reduced intensities. Since the whole group of oligomers have the same end groups, molecular weights, and chemical functionalities, their ionization and detection probabilities should be approximately equal.

The observed distribution of mass peaks is hence consistent with extensive transamidation and randomization of the polymer sequence in the copolymers PA6TI-PA610 resulting from melt compounding. Complete series of additional peaks were also observed in PA6TI-PA66, indicating a similarly extensive randomization of the polymer sequence, although the coincidence of mass peaks of different oligomers made more detailed analysis difficult. Nevertheless, our results unambiguously prove that random copolymers have been formed by transamidation during the melt compounding of the systems PA6TI-PA66 and PA6TI-PA610.

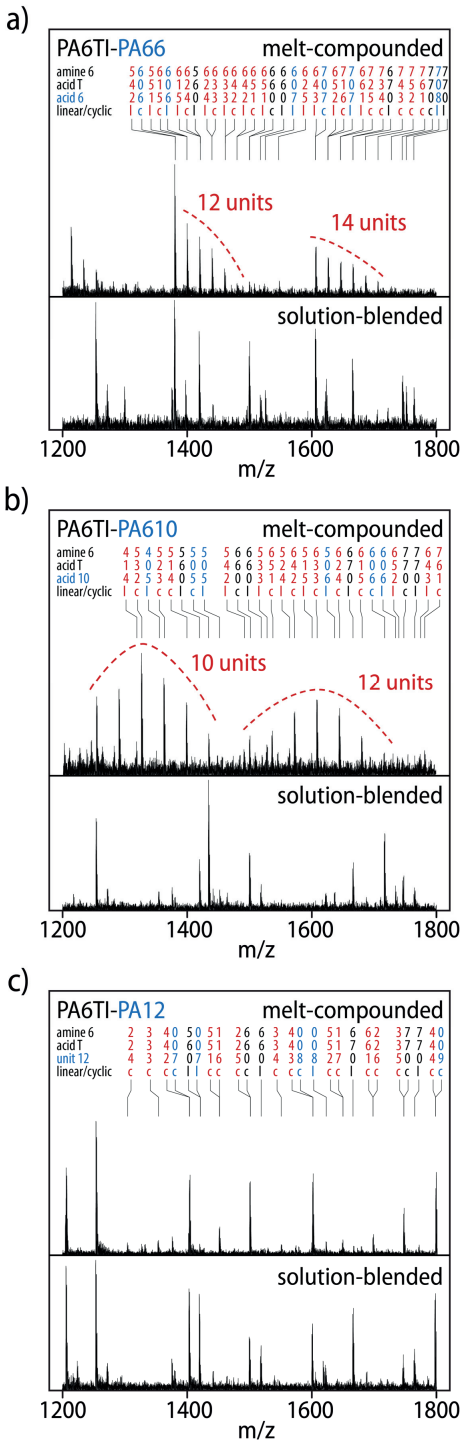

Figure 16. MALDI-TOF spectra of semiaromatic PA6TI melt compounded with 50 *wt*% of aliphatic *a)* PA66, *b)* PA610 or *c)* PA12, together with the corresponding reference spectra of the polymers solution-blended at room temperature. Peaks are assigned to the pure PA6TI (black), the pure aliphatic segments (blue), and copolymer segments consisting of a mixture of the two components (red).

Table 4. Number average and weight average molar masses (M_n and M_w), as well as dispersities ($Đ$) determined by GPC for the pure polyamides PA6TI, PA66, PA610, and PA12, as well as for melt-compounded and solution-blended samples of the semicrystalline semiaromatic PA6TI and semicrystalline aliphatic PA66, PA610 or PA12 at different compositions. The compounding time (t) was set to 20 minutes at 330 °C, and the reference specimens (t = 0) were obtained by solution-mixing of the two polyamides at room temperature.

Polyamide	*wt*%	t / min	M_n / g/mol	M_w / g/mol	$Đ$
PA66	100	0	21'400	40'900	1.91
PA610	100	0	16'200	28'800	1.96
PA12	100	0	19'600	33'500	1.71
PA6TI	100	0	11'700	23'500	2.01
PA66-PA6TI	50-50	0	15'300	31'800	2.08
PA66-PA6TI	50-50	20	18'800	46'500	2.47
PA66-PA6TI	80-20	0	12'300	26'400	2.15
PA66-PA6TI	80-20	20	13'200	35'100	2.66
PA610-PA6TI	50-50	0	15'500	31'100	2.01
PA610-PA6TI	50-50	20	13'400	32'500	2.43
PA610-PA6TI	80-20	0	12'100	25'800	2.13
PA610-PA6TI	80-20	20	11'100	31'400	2.85
PA12-PA6TI	50-50	0	13'300	27'600	2.08
PA12-PA6TI	50-50	20	13'400	29'900	2.23
PA12-PA6TI	80-20	0	11'900	24'600	2.07
PA12-PA6TI	80-20	20	14'600	32'800	2.25

2.3 Thermal Behavior of the Aromatic Copolyamides

The glass transition temperatures, T_g, melting temperatures, T_m, and melting enthalpies, ΔH_m, of the melt compounded copolymers were determined from the second of two differential scanning calorimetry (DSC) heating scans (Figure 17). The results clearly suggested that homogeneous materials were formed from all three polyamide combinations at all compositions, except for compositions rich in PA12, which were clearly phase-separated, as will be discussed in more detail at the end of this section. Two well-separated melting peaks were also observed in a narrow range of PA610 contents around 60 *wt*%, but the lack of any discontinuity in T_g, the high degree

of randomness and the absence of direct evidence for long-range phase separation, pointed to the co-existence of two crystalline phases with similar compositions in this case. All the copolymers nevertheless showed reduced microscale order, as evidenced by their significantly broader melting peaks compared with the pure components, indicating a correspondingly wide range of lamellar thicknesses and/or compositional fluctuations within the crystalline phase.

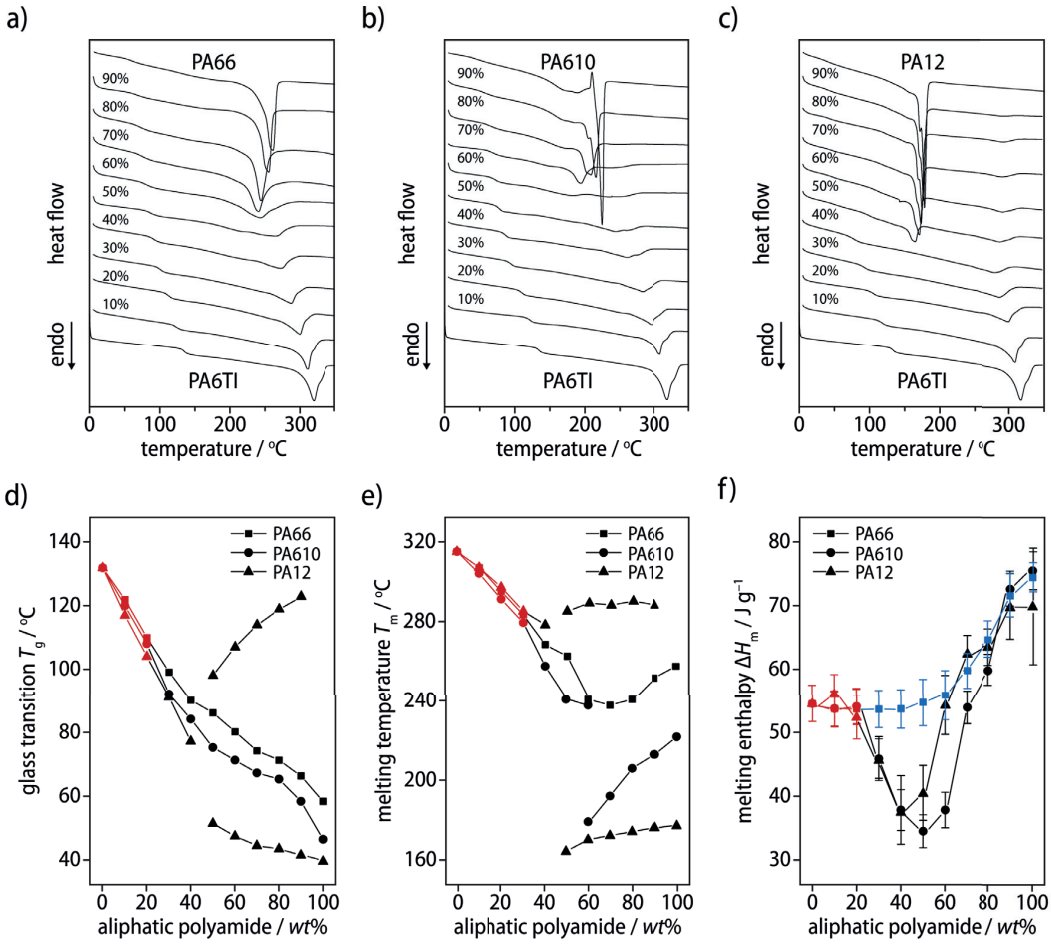

Figure 17. Second DSC heating scans from PA6TI melt compounded with different amounts of *a)* PA66, *b)* PA610 or *c)* PA12. *d)* Glass transition temperatures (T_g), *e)* melting temperatures (T_m), and *f)* melting enthalpies (ΔH_m) of PA6TI melt compounded with aliphatic PA66, PA610 or PA12, as a function of the content of the aliphatic component. In materials containing up to 20 *wt*% of the aliphatic component, ΔH_m, T_g and T_m were insensitive to the nature of the aliphatic component, and ΔH_m remained roughly constant in this composition range (red). In the case of PA66, ΔH_m did not show a minimum at intermediate compositions (blue).

Most importantly, all three series of blends showed both a single glass transition and a single melting peak at up to 40 *wt*% aliphatic content, showing the average composition of the

amorphous and crystalline domains, respectively, to be uniform in any given blend. This is in stark contrast to the thermal properties of solution-blended samples in all three series that showed two melting temperatures coinciding with the melting temperatures of the pure polymers, irrespective of the nature of the aliphatic component and the composition (Figure 18).

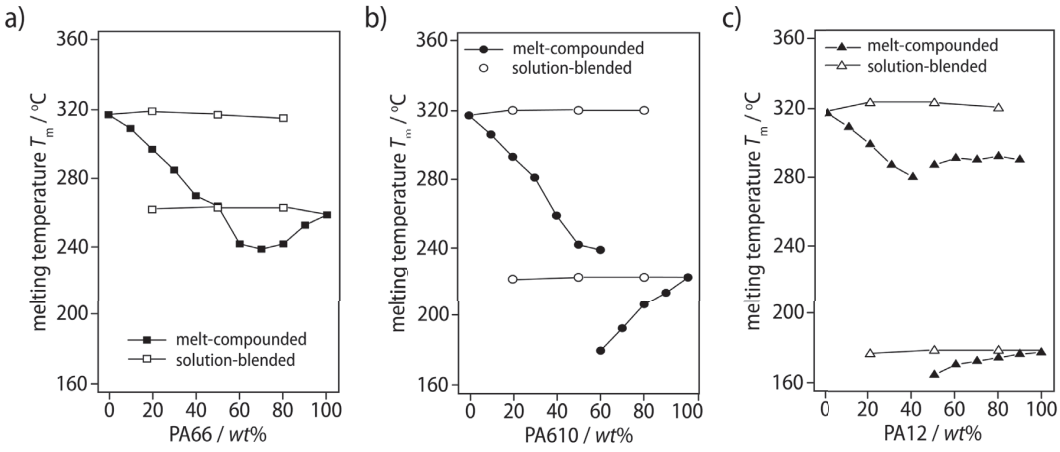

Figure 18. Comparison of the melting temperatures determined from the second of two DSC heating scans of solution-blended (open symbols) or melt-compounded (solid symbols) samples at different ratios of PA6TI and *a)* PA66, *b)* PA610 or *c)* PA12.

Moreover, the melting temperatures, T_m, of the different copolymers were similar at any given aliphatic polyamide content up to 30 *wt*%, in spite of the very different T_m of the pure aliphatic homopolymers of 178, 223 and 259 °C for PA12, PA610 and PA66, respectively. At the same time, the melting enthalpies, ΔH_m, remained roughly independent of the overall composition, and similar for all three types of blend at aliphatic contents of up to 20 *wt*% (Figure 17*f*). All of these findings indicate that, within this range of compositions, the degree of crystallinity, and the structure and stability of the crystalline domains were dominated by the semiaromatic PA6T, and were insensitive to the nature and concentration of the aliphatic component.

Another salient observation was that the copolymers of PA6TI with PA610 or PA66 remained essentially homogenous at even higher contents of the aliphatic component. The melting temperature, T_m, passed through a minimum of 240 °C at 70 *wt*% PA66; and at 60 *wt*% PA610, both the upper and lower T_m reached minima with respect to higher PA6TI and PA610 contents, respectively. The melting enthalpies of copolymers with PA610 also showed a minimum at

50 *wt*% PA610, as is widely observed in random copolymers that show a single crystalline phase, because the co-monomers are unable to achieve optimum packing and optimize their specific interactions in a non-periodic environment.[174] By contrast, the melting enthalpies of copolymers with PA66 increased monotonically with increasing PA66 content. This may be accounted for by isomorphous exchange of the adipoyl and terephthaloyl or isophthaloyl units in the crystalline phase in this case, which implies a limited enthalpy penalty.[175]

Comparison of the melting temperatures with literature data for the random copolyamides PA6T-*co*-PA66 and PA6T-*co*-PA10 prepared by co-polycondensation (Figure 19),[176-178] shows that the inclusion of isophthaloyl units in the PA6TI copolymers investigated here resulted in an overall decrease in T_m by about 40 °C at high aromatic contents, but was little affected by the presence of the isophthaloyl units at low aromatic contents. However, in spite of this systematic shift in T_m, the relative changes in T_m with composition were similar to those seen in the PA6T-based copolymers. This similarity strongly supports our assertion that the melt compounded PA6TI copolyamides reported here undergo extensive transamidation and sequence randomization, as concluded from MALDI-TOF mass spectrometry.

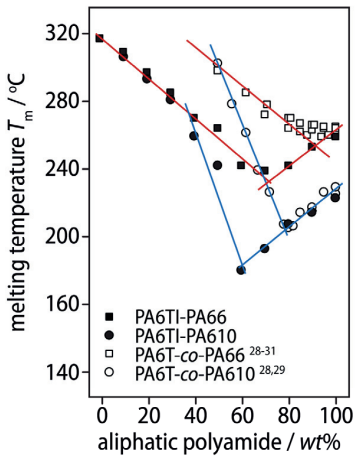

Figure 19. Melting temperatures T_m of the copolymers prepared in this work by melt compounding of PA6TI with PA66 or PA610, compared to literature data for random copolymers PA6T-*co*-PA66 and PA6T-*co*-PA610 obtained by co-polycondensation.[176-178]

In marked contrast to the other two series of copolymers, the PA6TI blends with PA12 containing ≥50 *wt*% of PA12 showed two glass transitions and two melting temperatures. Moreover, as the

PA12 content increased, the upper and lower glass transition temperatures approached those of pure PA6TI and PA12, respectively, indicating phase separation into PA6TI and PA12-rich domains with a high degree of phase purity. Hence, although there was evidence from MALDI-TOF mass spectrometry for some degree of transamidation in this system, the composition of the resulting copolymers presumably also depended on the extent of phase separation at high PA12 contents.

2.4 Morphology of the Blends and Copolymers

Intermittent contact mode AFM amplitude images of the free surfaces of sections from the various compounds generally showed well-defined two-dimensional spherulitic textures with spherulite diameters of the order of a few microns. It was not possible to determine absolute lamellar dimensions unambiguously from the AFM images, but the internal textures of the spherulites obtained from PA6TI and all its copolymers with PA66 or PA610 varied little with composition under the chosen crystallization conditions (Figure 20), consistent with a homogenous chemical microstructure. In each case the spherulites showed fibrillar morphologies similar to those characteristic of pure PA66 spherulites (Figure 20*a*–*e*),[179] although the lamellae appeared somewhat broader at high PA6TI contents.

In stark contrast, the spherulitic texture of melt compounded blends PA6TI-PA12 at high PA12 contents was strongly influenced by phase separation, as inferred from the DSC data. AFM images of these materials (Figure 20*f*) showed circular domains with diameters on the order of a few micrometers. The envelopes of these domains were marked by discontinuities in the lamellar trajectories, and hence effectively broke up the spherulitic morphology. Comparison of the lamellar textures with those of the respective pure polyamides confirmed the dispersed domains to correspond to PA6TI-rich inclusions in a continuous PA12 matrix, which was characterized by a more plate-like lamellar morphology (Figure 20*g*). Similar circular features with diameters of 1–5 μm were also observed in optical differential interference contrast images of molten films, as well as microtomed sections from the solid extrudates (Figure 21).

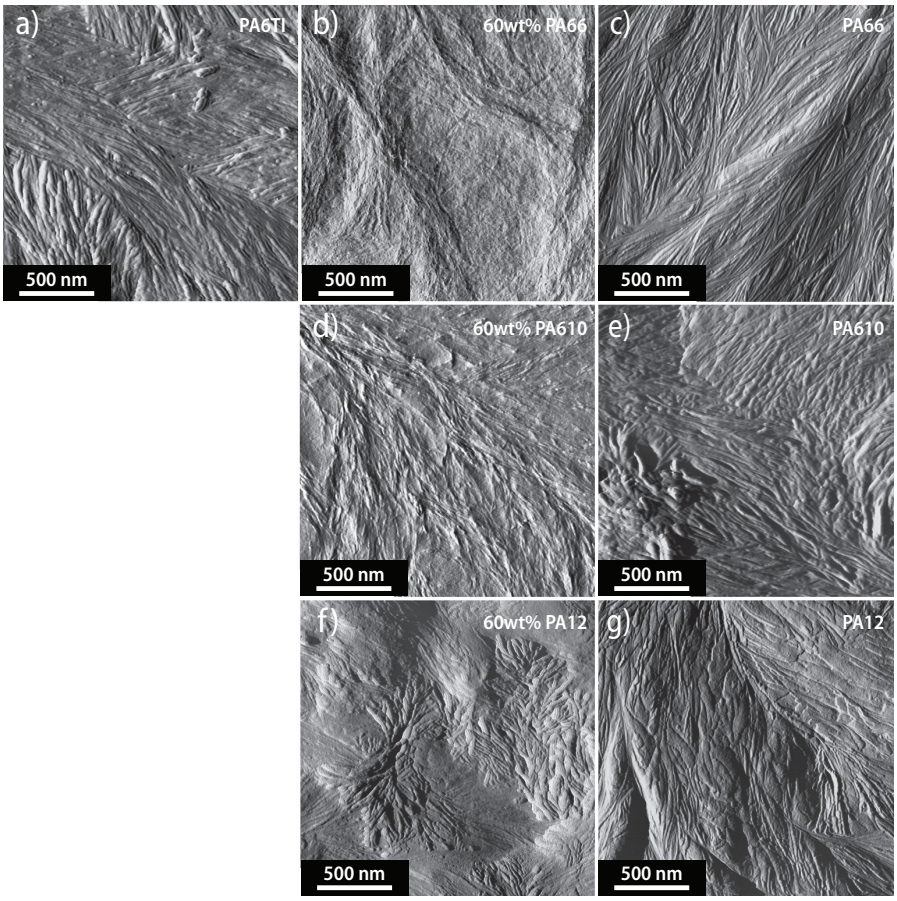

Figure 20. AFM amplitude images in intermittent contact mode ($A/A_0 \approx 0.8$ unless mentioned otherwise), obtained with intermediate gain settings in order to eliminate coarse variations in topography, of free surfaces of microtomed thin sections from the melt compounded specimens recrystallized on a glass substrate by cooling in air from $T > T_m$ at about 40 °C/min: *a)* PA6TI; *b)* PA6TI/60 *wt*% PA66 ($A/A_0 \approx 0.4$); *c)* PA66; *d)* PA6TI/60 *wt*% PA610 ($A/A_0 \approx 0.4$); *e)* PA610; *f)* detail of a PA6TI-rich inclusion in PA6TI/60 *wt*% PA12; *g)* PA12.

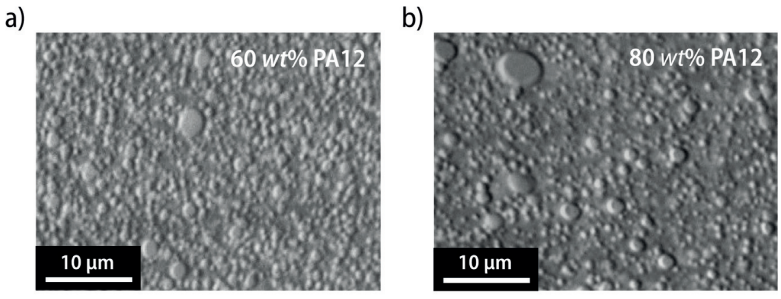

Figure 21. Nomarski differential interference contrast images of 5 µm thick microtomed sections from PA6TI-PA12 blends with high PA12 contents indicated the presence of phase-separated domains with a domain size of the order of 1–5 µm.

The morphological data were hence globally consistent with the DSC results and proved that PA6TI-PA66 and PA6TI-PA610 were homogenous materials, whereas the blends PA6TI-PA12 were phase-segregated into aliphatic and semi-aromatic domains, particularly at high PA12 contents. Similar results were obtained using a purely amine-terminated PA12 (Figure 22).

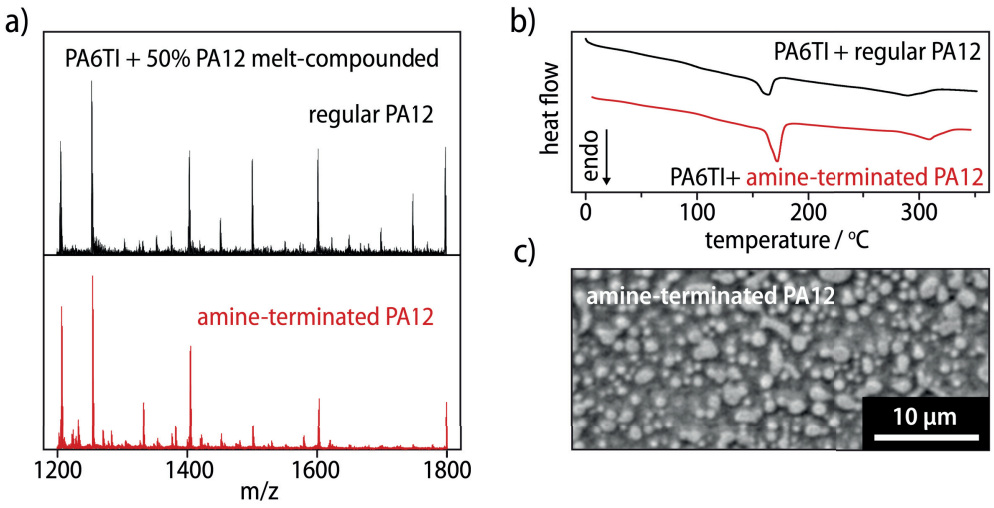

Figure 22. Comparison of PA6TI melt-compounded for 20 min at 330 °C with 50 *wt*% of either regular PA12 (carboxylic acid terminated) or amine-terminated PA12. *a)* MALDI-TOF mass spectrometry show little evidence for transamidation in both cases. *b)* Differential scanning calorimetry scans still exhibit two melting temperatures and glass transitions. *c)* Optical micrographs show a phase-segregated morphology with very similar feature sizes (see Figure 22 for comparison). Therefore, the different end groups of the two PA12 grades do not appear to have an impact on transamidation.

2.5 Crystal Structure from Wide-angle X-Ray Scattering

WAXS patterns from the homopolymers and all the different blends or copolymers showed diffraction patterns that were very close to that of PA6TI at aliphatic polyamide contents of up to 40 *wt*% (Figure 23), which explains the similar melting behavior observed for the various copolymers in this composition range (Figure 17*e*). The WAXS patterns for the PA66 and PA610-rich copolymers were characteristic of the triclinic α structure of the respective aliphatic polyamides, which consists of stacked planar sheets of parallel hydrogen-bonded chains aligned with the (010) planes in the standard representation of the unit cell.[180] The main WAXS peaks nevertheless converged as the PA6TI content was increased from 0 to 40 *wt*%, indicating significant modifications to the lattice parameters.

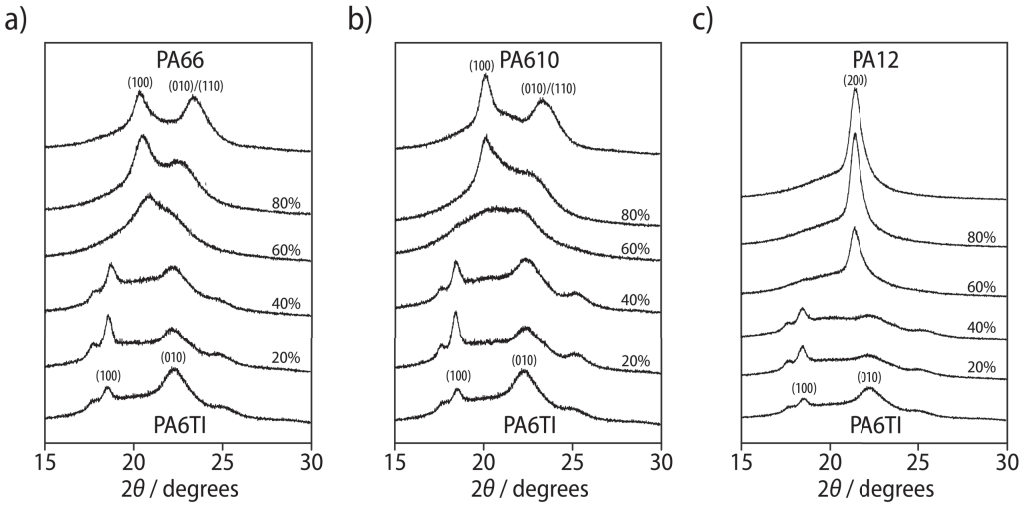

Figure 23. WAXS diffractograms of semiaromatic PA6TI melt compounded with *a)* PA66, *b)* PA610 or *c)* PA12 at different weight fractions of the aliphatic component.

On the basis of literature results for other even even semiaromatic polyamides with similar repeat units,[181] the disposition of the NH and CO groups in PA6TI is also expected to favor the α structure. Indeed, as alluded to previously, it has been suggested that isomorphous substitution of the adipoyl units by terephthaloyl units may be possible in the α structure of PA66.[175] Hence the peak at $2\theta = 22.4°$ in the diffractions patterns observed at high PA6TI contents was again assumed to originate from sheets of parallel hydrogen-bonded chains, with the hydrogen bonds forming a similar arrangement to those in PA66, but with substantially modified interchain distances owing to the more sterically demanding aromatic units in PA6TI.

In the case of the PA12 blends, the diffraction patterns at ≥60 *wt*% of PA12 were close to that of pure PA12 (Figure 23*c*), showing a single strong reflection corresponding to a *d*-spacing of about 4.2 Å, regardless of the PA6TI content in this range. This is the signature of the pseudo-hexagonal γ phase of PA12, in which the NH groups are tilted out of the plane containing the methylene carbons, and packing of the methylene groups is optimized, reflecting a greater contribution of these latter to interchain interactions than in PA66 and PA610.[50,182] One may hence argue that the extensive transamidation observed during high-temperature melt compounding of PA6TI with the "even-even" polyamides PA66 and PA610 reflects the compatibility of their optimum hydrogen-bonding configurations. On the other hand, both the limited transamidation and the

phase separation inferred from calorimetry (Figure 17) and microscopy (Figure 21) in the compounds containing the more hydrophobic “odd” polyamide PA12 may be attributed to the lower density of hydrogen-bonding sites and its different hydrogen-bonding pattern in its preferred crystalline state.

2.6 Conclusion

Our study has proven the formation of random copolymers through extensive and rapid transamidation by simple melt compounding at 330 °C of a semicrystalline semiaromatic and a semicrystalline aliphatic polyamide, with no evidence of thermal degradation. The structural compatibility of the semicrystalline PA6TI with the aliphatic PA66 or PA610 allowed the formation of homogeneous copolymers with extensive randomization. By contrast, less efficient transamidation and phase segregation were observed in the blends rich in PA12, which we found not be the result of either polymer degradation under the extrusion conditions nor related to the end groups of the employed PA12 grade.

The melting behavior of all the PA6TI-rich copolymers was remarkably similar at a given aliphatic content, regardless of the chemical structure of the aliphatic polyamide. Moreover, a high melting enthalpy persisted at up to 20 *wt*% aliphatic content. These observations suggested the structure of the crystalline domains to be dominated by the semiaromatic component and the degree of crystallinity to remain high in this composition range. However, while isomorphous replacement of 6T by 66 units in the crystal structure resulted in a monotonic variation in the melting enthalpy across the whole composition range in PA6TI/PA66, the loss of hydrogen bonding in the case of PA6TI/PA610 led to a strong minimum in the melting enthalpy at intermediate compositions.

Promising candidates for matrix material in thermoplastic composites may thus be identified among the polyamide copolymers developed in this work. The copolymers with low aliphatic contents (e.g. 20 *wt*%) showed good thermal stability ($T_m \approx 300$ °C and $T_g > 100$ °C). Moreover, given their high degree of crystallinity, one expects good mechanical stiffness and strength in these materials, while the presence of mobile aliphatic segments should provide for additional ductility. The mechanical behavior and the detailed nanoscale distribution of semicrystalline

order/disorder distribution in these copolymers is the subject of ongoing investigations, together with the preparation of short glass fiber reinforced composites using melt compounding for the *in-situ* generation of polyamide copolymer matrices.

3

High Performance Polyamides with Exceptional Ductility

The results presented in this chapter are part of a manuscript in preparation:

"Engineering Order and Disorder at the Nanoscale: High Performance Polyamides with Exceptional Ductility", Galland, S., Cretenoud, J.; Candau, N.; Gasparotto, P.; Ceriotti, M.; Balog, S.; Michaud, V.; Plummer, C. J. G.; Frauenrath, H. *To be submitted.*

C. J. G. P. measured SAED and DSC, together with J. C., while all the mechanical tests were performed by S. G. Computations were performed under the supervision of M. C. and C. J. G. P. by P. G. The SAXS measurements were performed by S. B. at Adolph Merkle Institute in Fribourg, Switzerland. This work was supervised by V. M. and H. F.

3 High Performance Polyamides with Exceptional Ductility

3.1 Introduction

In the previous chapter, we have shown that chemically homogeneous, semicrystalline random copolyamides with no apparent chemical phase separation may be obtained during the melt compounding of the semiaromatic PA6TI with the aliphatic PA66 or PA610, thanks to the efficient transamidation reactions that take place under these conditions. By contrast, transamidation was found to be less efficient when using PA12 as the aliphatic component and, indeed, macroscopic phase separation was observed in blends rich in PA12. The thermal properties of the different blends and comparison of their WAXS patterns provided first indications of the crystallinity of the different materials. For a PA66 or PA610 content of up to 40 *wt*%, the WAXS patterns were very close to that of PA6TI, consistent with the similar melting temperatures observed for the various copolymers in this composition range. Indeed, a monotonic variation in the melting enthalpy (ΔH_m) was observed in PA6TI/PA66 over the whole composition range, which suggested isomorphous replacement of 6T by 66 units may be possible in the crystalline phase.

Here, we present our investigations to further elucidate the microstructure of the obtained materials. In order to gain a better understanding of both the PA6TI crystal structure and the distribution of the comonomers among the different phases, we complemented our WAXS results with selected-area electron diffraction (SAED). Small angle X-ray scattering (SAXS) provided quantitiative information on the lamellar morphology in the polyamide homopolymers and copolyamide blends. Isomorphous replacement of 6T units by 66 units in the crystalline domains was confirmed by a combination of T_g studies and numerical simulations and, because of the reduced thickness of the crystalline lamellae, isomorphous replacement of 6T units by 610 units was also shown to occur.

Blending and injection molding of the different polyamide systems into specimens for tensile testing was then performed with a particular focus on: *(i)* verifying whether the inclusion of small amounts of aliphatic polyamide in the stronger and stiffer PA6TI matrix led to an enhancement in ductility, as is often observed in solid polymers; and *(ii)* investigating whether the nanoscopic features observed in the different blends influenced their overall macroscopic mechanical

properties. Finally, with a view to potential transfer of knowledge to technological applications, composites using the same blend compositions with addition of up to 50 *wt*% of glass fibers were also prepared and tested under the same conditions.

3.2 Lamellar Morphology

The wide-angle X-ray scattering (WAXS) patterns from the injection moldings of PA6TI presented in the previous chapter were formally indexed assuming a triclinic unit cell containing a single poly(hexamethylene terephthalamide) (PA6T) chemical repeat unit with lattice parameters a = 5.02 Å, b = 5.4 Å, c = 16.40 Å, α = 50.5 °, β = 79 °, γ = 94 °, derived from selected-area electron diffraction (SAED) of oriented thin PA6TI films (Figure 24).

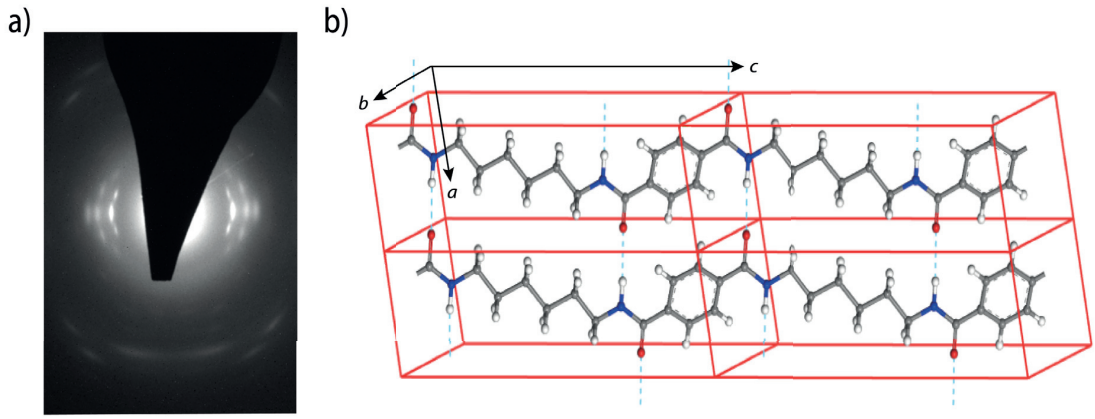

Figure 24. *a)* Selected-area electron diffraction (SAED) fiber pattern from an oriented thin film of PA6TI friction deposited onto a freshly cleaved crystal of KBr at about T_m – 10 K and picked up on a carbon covered TEM grid after dissolution of the KBr. *b)* Crystal structure proposed for PA6T.

In common with other semiaromatic even-even polyamides, PA6TI was inferred to crystallize in an α-type structure under the present conditions, comprising stacked sheets of hydrogen-bonded chains with the carbon-carbon single bonds in an all-*trans* conformation. The benzene rings were tilted with respect to the plane of the amide groups to allow optimization of the hydrogen bond distances and π-π stacking. Remarkably, as recalled in the introduction, this structure persisted with only minor changes in lattice parameters in the random compounds PA6TI-PA66 and PA6TI-PA610 for an aliphatic polyamide content as high as 40 *wt*% (Figure 23). WAXS patterns from

moldings of the even-even aliphatic polyamides PA66 and PA610 were also dominated by an α-type structure, but with lattice parameters close to those reported in the literature for these polymers,[180] and hence substantially different from those determined for PA6TI. Moreover, there were marked shifts in the positions of the (100) and (010)/(110) reflections as the PA6TI content was increased in the compounds rich in aliphatic polyamide, indicating the aromatic linkages to strongly perturb the crystal structures of PA66 and PA610.

Consistent with the dominance of the PA6TI crystal structure, the nanoscopic morphology of the random copolymers PA6TI-PA616 and PA6TI-PA610 showed little change at low aliphatic contents. Indeed, the 1D correlation functions for the small angle X-ray scattering (SAXS) peak at q = 0.2–1.3 nm^{-1} (Figure 25) showed the thickness of the crystalline lamellae, l, to remain constant at about 2 nm for all the copolymers, regardless of their composition (Figure 25*e*). As reported previously for both polyamide homopolymers and copolyamides crystallized at high supercoolings,[178,183] this is only about 1.5 times the observed (001) spacings of 12.8 and 12.06 Å in PA66 and PA6TI, respectively, which implies chain sequences deposited at the lamellar growth front during crystallization to contain an average of only four amide groups. Because chain folding involving the hexamethylene units is expected to be more favorable energetically than folding of the conformationally rigid aromatic units,[57] the lamellae in the PA6TI-rich compounds must hence consist mainly of terephthalamide-hexamethylene-terephthalamide (T6T) sequences.

Whereas compounding of PA6TI with PA12 led to a marked reduction in the apparent degree of crystallinity (SAXS), χ, a salient feature of the SAXS results was that the degree of crystallinity in the copolymers PA6TI-PA610 and PA6TI-PA66 remained approximately constant at χ = 23–25 *vol*% for an aliphatic content of up to 20 and 40 *wt*%, respectively, consistent with previous observations of the evolution of the enthalpy of fusion, and even increased in PA6TI-PA66 at higher PA66 contents (Figures 17*f*, 25*f*). This observation strongly suggested isomorphous co-crystallization of the adipoyl and terephthaloyl units to take place, a phenomenon that has been invoked in the past to account for the dependence of the melting point, T_m, on composition in copolymers of PA66 and PA6T.[175,184]

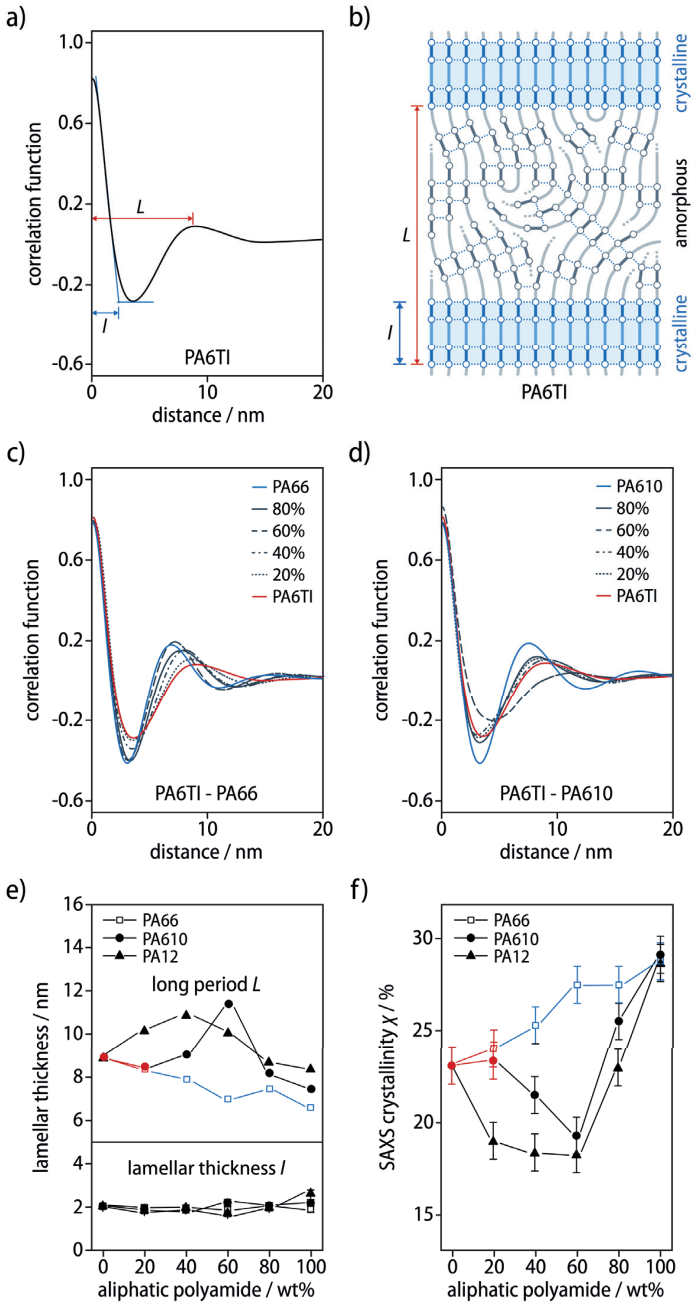

Figure 25. *a)* 1D correlation function obtained from the SAXS pattern of PA6TI by Fourier transformation as a representative example for the determination of *b)* the crystalline lamellar thickness *l* and the long period *L* in the semicrystalline polyamides. *c), d)* 1D correlation functions of the SAXS patterns of the systems of PA6TI-PA66, and PA6TI-PA610 at various compositions. *e)* The crystalline lamellar thickness remained constant at $l \approx 2$ nm for all compositions, while *L* remained between 8 and 9 nm in PA6TI-PA66 and PA6TI-PA610 at aliphatic contents at and below 20 wt% (highlighted in red) and even slightly decreases at high aliphatic contents. *f)* The corresponding estimates for the degree of crystallinity, χ, as a function of aliphatic polyamide content, showing that χ remained constant for PA6TI-PA610 at an aliphatic content of ≤20 *wt*% and did not decrease at all for PA6TI-PA66, which is indicative of isomorphous substitution of terephthaloyl units by adipoyl units in the dominant crystalline phase.

3.3 Nanoscale Segregation of the Comonomers

The extent of isomorphous co-crystallization, i.e., the composition of the crystalline phase, should find a reflection in the composition of the amorphous phase, which may, in turn, be estimated from the materials' glass transition temperature, T_g.

In amorphous specimens of the copolymers prepared by quenching from the melt, T_g showed a monotonic decrease with increasing aliphatic content that could be approximately fitted using the Brekner-Schneider-Cantow expression for miscible binary blends of two components A and B according to equation *(2)*.[185]

$$T_g(\phi) = T_{g,A} + \left(T_{g,B} - T_{g,A}\right)\left((1 + k_1)\phi - (k_1 + k_2)\phi^2 + k_2\phi^3\right) \qquad (2)$$

where ϕ is the mass fraction of component B, and k_1 and k_2 are empirical constants.

After crystallization by cooling from 330 °C at 10 K/min, conditions that closely reproduced the thermal conditions applied during the injection molding, T_g increased in PA6TI and in the aliphatic homopolymers, presumably owing to confinement effects.[186] (Expulsion of I units into the amorphous phase during crystallization of PA6TI was assumed to have a negligible influence on T_g given the comparable T_g of PA6TI (130 °C) and PA6I (125 °C).[187])

More importantly, the T_g measured before and after crystallization remained very similar in PA6TI-PA66 at low PA66 contents (Figure 26*a*), suggesting limited preferential segregation of the adipoyl units into the amorphous phase. This implies that the adipoyl content of the crystalline phase had to be close to the overall adipoyl content. On the other hand, at a PA66 content above 40 $wt\%$, T_g increased markedly subsequent to crystallization, implying the aromatic I and T units to be concentrated in the amorphous phase. Similar trends were observed in PA6TI-PA610 (Figure 26*b*), whereas the results for PA6TI-PA12 indicated strong segregation of the laurolactam units into the amorphous phase at low PA12 content, T_g decreasing markedly after crystallization (Figure 26*c*).

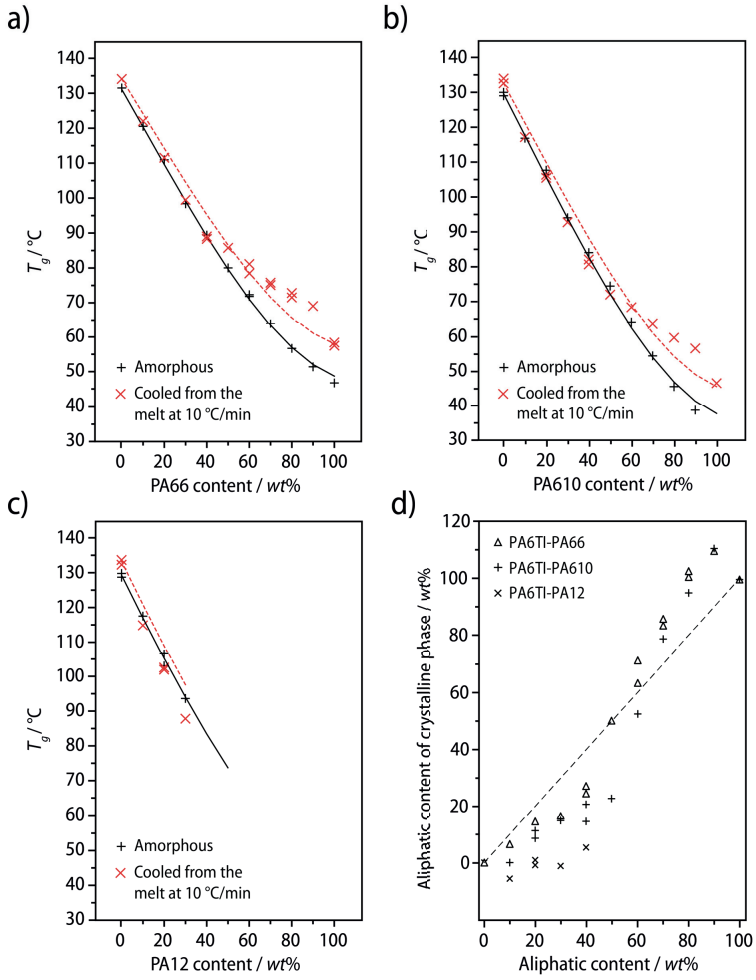

Figure 26. T_g measured from DSC heating scans at 10 K/min on initially fully amorphous specimens of PA6TI melt-compounded with different mass fractions of: *a)* PA66; *b)* PA610; *c)* PA12, before and after crystallization by cooling from 330 °C at 10 K/min. The solid curves are fits to the data obtained by adjusting k_1 and k_2 in equation *(2)*, and the hatched curves were obtained using the same values of k_1 and k_2, but with $T_{g,A}$ and $T_{g,B}$ shifted to match the experimental T_g values obtained for PA6TI and the respective aliphatic homopolymers after crystallization. Deviations between the hatched curves and T_g measured at intermediate compositions after crystallization were interpreted to reflect differences between the composition of the amorphous phase and the overall composition. *d)* Aliphatic content of the crystalline phase estimated from the T_g data in *a–c)* as well as the SAXS data in Figure 25*f*.

Assuming the dependence of T_g on the local aliphatic comonomer content in the semicrystalline specimens to be given by the hatched curves in Figure 26, obtained by interpolation with the Brekner-Schneider-Cantow expression using the same fitting parameters k_1 and k_2 as for the fully amorphous specimens, the measured T_g may be used to estimate the composition of the amorphous phase in the semicrystalline specimens. When combined with the degree of crystallinity χ as determined by SAXS (Figure 25*f*), this permitted quantification of the weight

fraction of aliphatic comonomer units in the crystalline phase, if one assumes a uniform composition in the amorphous phase. The results showed that, while PA12 units were completely excluded from the crystalline phase in the blends of PA6TI containing up to 40 *wt*% PA12, the concentration of PA66 and PA610 units in the crystalline phases of PA6TI-PA66 and PA6TI-PA610 at 0–40 *wt*% aliphatic contents, respectively, was about half their overall concentration (Figure 26*d*), implying isomorphous co-crystallization to take place not only in PA6TI-PA66 but also in PA6TI-PA610 in this concentration range.

Numerical simulations provided a further independent indication of the compatibility of the various comonomers with the crystalline phase of PA6T. To this end, we generated 6 × 6 × 3 supercells of the PA6T α phase structure based on the diffraction data (Figure 24*b*), replaced the central terephthaloyl unit with an isophthaloyl, adipoyl, or sebacoyl unit, and relaxed the structure in order to identify low energy configurations (Figure 27).

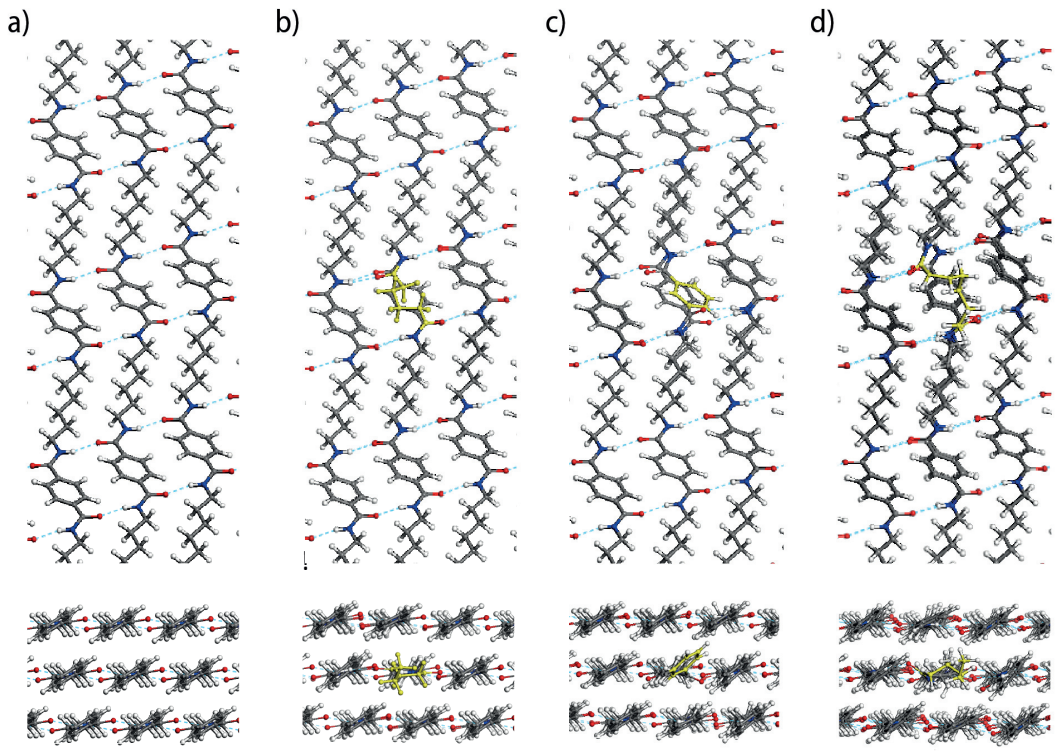

Figure 27. (010) and (001) projections of the optimized crystalline structures for *a)* 6 × 6 × 3 supercells of the PA6T α phase and *b–d)* the same supercells containing a single adipoyl, isopthaloyl, and sebacoyl defect unit, respectively, replacing the central terephthaloyl unit (highlighted in yellow).

In each case, the displacement field induced by introducing the defect was small and localized relative to the PA6T bulk structure, with atomic displacements of less than 1 Å and limited to chains immediately adjacent to the defect, so that the long-range packing of the pure PA6T crystal was unaffected. Moreover, while the adipoyl (6) unit could maintain the hydrogen bonding pattern of PA6T by adopting a compact conformation matching the length of a terephthaloyl unit, both the reversed carbonyl orientation and conformational rigidity in the case of the isophthaloyl (I) unit and the length mismatch in the case of the sebacoyl (10) unit resulted in a loss of two hydrogen bonds. The minimum observed energy change ε upon incorporation of a defect unit was –16, +156 and +155 kJ/mol for the adipoyl, isophthaloyl, and sebacoyl units, respectively. This confirmed incorporation of PA66 into bulk PA6T crystals to be energetically favorable, and incorporation of PA6I to be highly unfavorable. However, the large values of ε obtained for the sebacoyl units were clearly inconsistent with the results in Figure 26*d*, which indicated PA610 units to be readily incorporated into the crystalline lamellae present in PA6TI-PA610 after cooling from the melt.

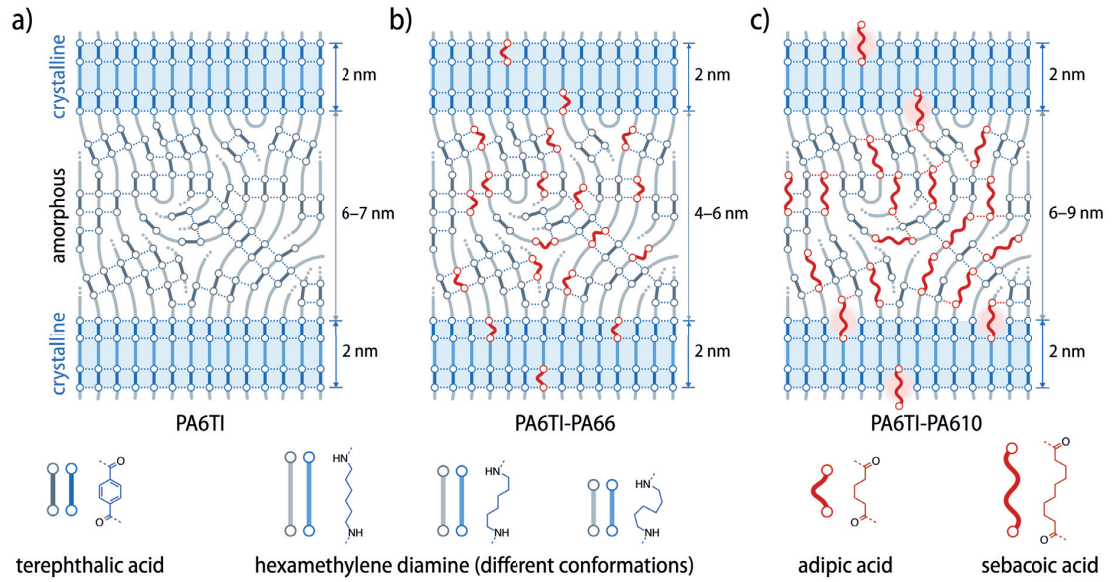

Figure 28. Schematic representation of how aliphatic groups might be included into the lamellar crystalline domains of *a)* PA6T. *b)* In the case of PA66, isomorphous substitution of the terephthaloyl units by adipoyl units is possible even inside a crystalline domain of PA6T if the units adopt a non-extended conformation. *c)* Although the inclusion of the longer sebacoyl units associated with PA610 in the crystalline domains is energetically less favorable, these units may still be accommodated at the lamellar surface, extending into the amorphous phase.

The energy cost of incorporating PA610 units into PA6T crystals may be further facilitated by the reduced constraints on comonomers at the lamellar surfaces at the crystalline-amorphous infterface. In fact, for lamellar thicknesses of only 2 nm observed in the present case, all diacid units that are part of the crystalline lamellae must be adjacent to the lamellar surfaces, so that any sebacoyl units present are able to extend into the amorphous phase, albeit at the cost of two intralamellar hydrogen bonds (Figure 28). Inclusion of the PA66 and PA610 monomers in the crystalline phase therefore implies a smoother gradient in the concentration of aliphatic units at the lamellar-amorphous interface than for lamellae containing exclusively T6T units.

3.4 Mechanical Properties of the Blends

It follows from the previous section that it should be possible to maintain the extent and morphology of the PA6TI crystalline domains, while systematically modifying their defect structure, the properties of the amorphous layers, and the effective breadth of the crystalline-amorphous interface. Consistent with this, the PA6TI-PA66 and PA6TI-PA610 copolymers showed only small decreases in stiffness and strength upon the addition of up to 30–40 *wt*% of PA66 or PA610, but the ductility was drastically improved with respect to PA6TI (Figure 29*a*, *b*).

More specifically, the Young's modulus, *E*, remained close to 3.6 GPa in copolymers containing as much as 30 wt% PA66 or PA610, which was comparable with the values obtained for PA6TI and PA66 and represents a 40% increase in stiffness over pure PA610 (Figure 29*d*). The yield stress, σ_y, showed only a moderate decrease from 140 MPa to about 110 MPa, i.e. 30% and 80% higher than the yield stresses of pure PA66 or PA610, respectively (Figure 29*e*). At the same time, however, in both materials systems, the strain at break underwent an unprecedented five-fold increase from 10% to around 50%. It should be noted that this value even exceeded the strain at break of pure PA66 (Figure 29*f*). Moreover, given the very different mechanical properties of the pure PA66 and PA610, it is equally remarkable that the copolymers with PA6TI at corresponding compositions of up to 30 *wt*% of the aliphatic component showed almost identical stiffness, strength, and ductility, and only diverged at higher aliphatic contents. This confirms the dominant role of the crystalline structure of the pure PA6TI and the persistently high crystallinity, χ, for the materials properties of the copolyamides at low to intermediate aliphatic contents.

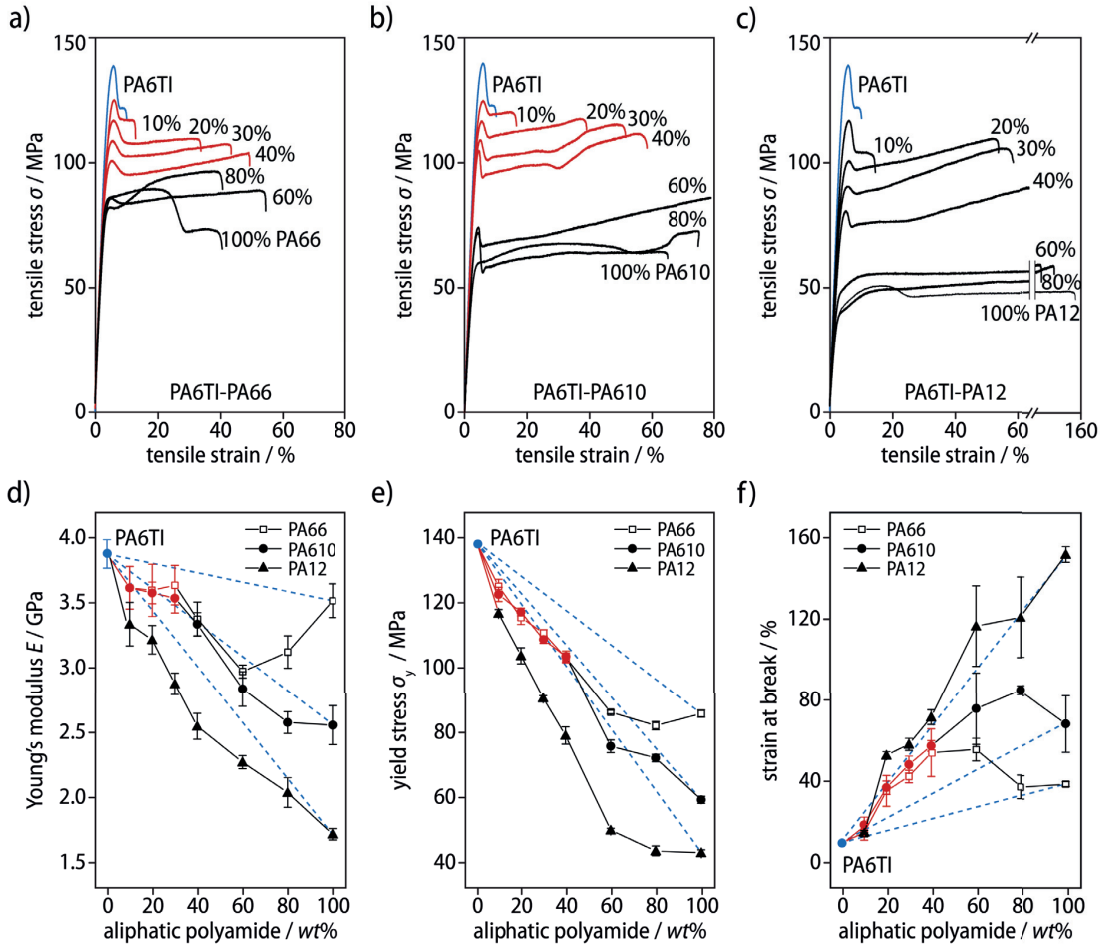

Figure 29. *a–c)* Stress-strain curves of melt-compounded samples of PA6TI-PA66, PA6TI-PA610, and PA6TI-PA12. Plots of *d)* Young's modulus, *E*, *e)* yield stress, σ_y, and *f)* strain at break as a function of aliphatic polyamide content show (highlighted in red) that for PA6TI-PA66 and PA6TI-PA610 with less than 40 *wt*% of the aliphatic component, the stiffness (*E*) plateaus after an initial small decrease, the strength (σ_y) only moderately decreases, and the ductility drastically increases beyond the behavior expected according to the rule of mixtures (blue lines).

In marked contrast, the addition of PA12 to PA6TI resulted in a response more typical of semicrystalline random copolymers, that is, a large increase in ductility, but a steep decrease in both strength and stiffness. This can probably be attributed to the incompatibility of both the hydrogen bonding patterns and the crystal structures of the two components, which resulted in a drastic decrease in crystallinity, χ, even at low PA12 content (Figure 25*f*).

The Young's modulus of a multiphase material is a morphology-dependent average of the elastic properties of its individual components, which are generally considered to be structure-insensitive, i.e. weakly dependant on the presence of local defects.[188] The weak variation in the

room temperature Young's modulus on copolymerization of PA6TI with up to 30–40 *wt*% PA66 or PA610 therefore follows immediately from the approximately constant morphology and phase behavior. By contrast, the yield stress and tensile strength of ordered materials are generally considered to be structure-sensitive, in that they are strongly dependent on the presence of defects, such as dislocations. The increased density of aliphatic surface defects in the PA6T crystalline lamellae, together with the increase in mobility in the unconstrained regions of the amorphous phase implied by the concomitant decrease in the glass transition temperature, T_g, may therefore play a crucial role in the high strain behavior. The compact conformations of the aliphatic defects may, furthermore, give rise to additional stress relaxation mechanisms within the crystalline phase by smoothing local deformation gradients, favoring cooperative microdeformation modes and consequently promoting local ductility.

3.5 Mechanical Properties of Glass Fiber Reinforced Composites

We then explored the potential of our approach to the nanoscale engineering of the crystalline-amorphous interface as a strategy to address the stiffness-strength-toughness conundrum to be applied to glass fiber reinforced composites using PA6TI-PA610 with an aliphatic content of 20 or 40 *wt*% as the matrix. Composites with 30, 40, and 50 *wt*% of glass fibers all exhibited a significant increase in ductility upon the addition of 20 *wt*% aliphatic polyamide in the matrix, while the stiffness and strength remained at a level comparable to those of the corresponding semi-aromatic PA6TI composites (Figure 30). In composites with 50 *wt*% glass fibers, the addition of 20 *wt*% PA610 resulted in an increase in strain at break from 2.5 to 3.3 %, which represents a 30% improvement in ductility, while the stiffness and strength remained unchanged within experimental error, at 17.1 GPa and 214 MPa, respectively. It is also remarkable that the ductility of this material is comparable to the ductility of a composite with the same glass fiber content and a pure PA610 matrix (3.1 %), although the latter material has only a stiffness of 12.8 GPa and a strength of 136 MPa. Similarly, composites with 50 *wt*% glass fiber and 40 *wt*% PA610 exhibited a marginally reduced stiffness (15.7 GPa), a strength (193 MPa) that remained 40% higher than that of a pure PA610 composite, but a significantly improved ductility (4.3 %) that was 70 % and 40 % higher than those of the corresponding pure PA6TI and PA610 composites, respectively.

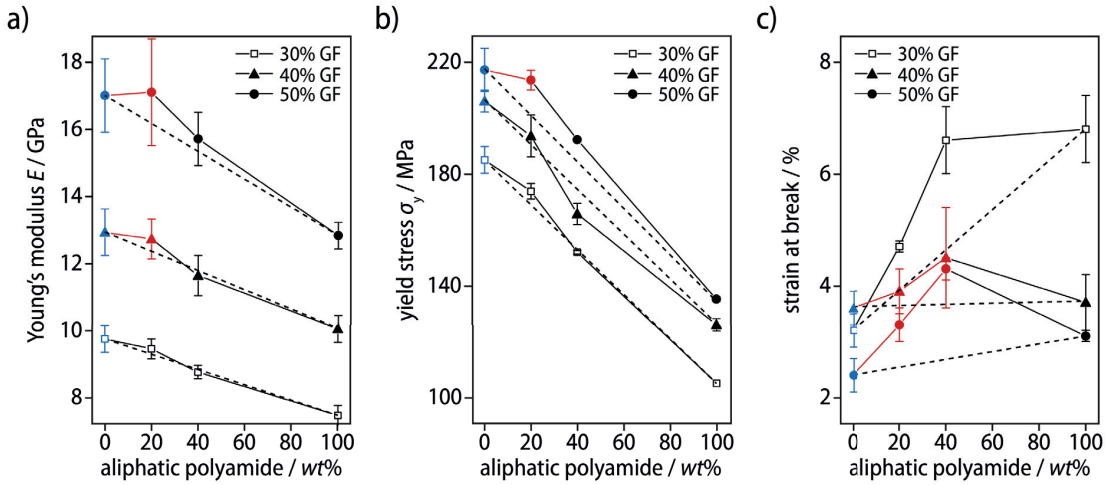

Figure 30. Plots of *a)* Young's modulus, E, *b)* yield stress, σ_y, and *c)* strain at break as a function of aliphatic polyamide contents in the copolymer PA6TI-610, at different glass fiber (GF) contents. While strength and stiffness remained high at high glass fiber contents, the ductility showed an up to two-fold increase at 20–40 *wt*% of the aliphatic polymer.

In the presence of short fiber reinforcements and at low strains, the contributions to stiffness are shared between the matrix and the stiff fibers, so that the small drop in stiffness observed on the neat polymer matrix becomes insignificant for the fiber-reinforced composites. Also, the behavior of the composites at large strains is dominated by the ductile behavior of the matrix and its ability to accomodate large shear deformations, hence, relaxing the stresses accumulated around the stiff and brittle fibers. Although further investigations are needed to elucidate the influence of possible changes in fracture and crack propagation mechanisms in these materials, we may already conclude that the improvement in matrix ductility achieved by the nanoscale engineering approach discussed above also translates into improvements in ductility in macroscale composite materials.

3.6 Conclusion

Melt compounding of the high performance semiaromatic semicrystalline copolyamide PA6TI with PA66 or PA610 provides a straightforward tool for the preparation of homogeneous, semicrystalline random copolyamides comprising aromatic and aliphatic units. Random copolymerization of semicrystalline polymers typically leads to eutectic behavior, i.e. a strong depression in melting point with respect to those of the corresponding homopolymers, and a

substantial (or even total) loss in crystallinity, which often results in poor mechanical strength and stiffness. In the present case, however, the aliphatic units were shown to co-crystallize with the PA6T units to form partly disordered, PA6T α-phase lamellae at aliphatic contents of up to 40 *wt*%, so that the degree of crystallinity and its influence on mobility in the amorphous phase remained substantially unchanged. This was shown to provide a remarkably simple way to tailor the balance between the microscopic order and disorder and hence the ductility and toughness of these materials, while maintaining levels of stiffness at room temperature comparable with those of PA6TI.

4

Semiaromatic Polyamides with Benzofurobenzofuran Repeating Units

All the results presented in this chapter have been published in:

"Synthesis and Characterization of Semiaromatic Polyamides Comprising Benzofurobenzofuran Repeating Units", Cretenoud, J.; Özen, B.; Schmaltz, T.; Görl, D.; Fabrizio, A.; Corminboeuf, C.; Fadaei Tirani, F.; Scopelliti, R.; Frauenrath, H. *Polym. Chem.*, **2017**, *8*, 2197.

All monomers and polyamides were synthesized and characterized by J. C., with the help of B. Ö. for WAXS measurements and D. G. for the interpretation of UV-Vis measurements. The crystal structures were measured and refined by F. F. T. and R. S. and the DFT computations were performed under the supervision of C. C. by A. F. OFET devices were prepared and characterized by T. S. This work was supervised by H. F.

4 Semiaromatic Polyamides with Benzofurobenzofuran Repeating Units

4.1 Introduction

Semiaromatic polyamides are attractive engineering polymers as they combine the strength and stiffness brought by the rigid aromatic repeating units with a higher ductility due to the incorporation of flexible aliphatic repeating units.[90,189-191] For the same reason, they are also significantly better processable than aromatic polyamides such as Kevlar or Nomex that cannot be processed by melt extrusion or injection molding.[192,193] The use of kinked aromatic repeating units decreases the crystallinity of the polyamide, which, in turn, results in further facilitated and enhanced processability.[194,195] Moreover, kinked and extended π-conjugated building blocks into the polyamide backbone may be employed to introduce optical or electronic properties without negatively impacting the processing of the material.

Extended π-conjugated systems based on fused heterocycles, such as the benzothieno[3,2-*b*]benzothiophene (BTBT) derivatives and polymer semiconductors incorporating structurally related repeating units, have shown excellent charge transport properties in thin film transistor devices.[196-202] However, no semiaromatic polyamides comprising repeating units based on such building blocks have previously been reported, and their compatibility with laboratory-scale procedures for the synthesis of semiaromatic polyamides has hitherto been unknown.

We therefore chose the corresponding benzofurobenzofuran (BFBF) derivatives as a model system, as they are structurally related and may still exhibit interesting optoelectronic properties,[203,204] but are synthetically better accessible via their dihydro-derivatives. The latter can be straightforwardly synthesized in an acid-catalyzed condensation reaction of glyoxal derivatives with a variety of *p*-substituted phenols.[205,206] Since these reactions are fast and can easily be scaled up to the multi-gram scale, BFBF units are interesting candidates as aromatic building blocks in semiaromatic polyamides. However, the regioselectivity of the condensation reaction was reported to not favor the formation of the 2,7-disubstituted dihydrobenzofuro[3,2-*b*]benzofurans (C_2-symmetric) but instead the 2,9-disubstituted dihydrobenzofuro[2,3-*b*]benzofurans (C_s-symmetric) (Scheme 9).[207]

The preparation of polyamides incorporating BFBF-units requires the synthesis of the corresponding dicarboxylic acid derivatives. According to previously described procedures, the fully aromatic benzofurobenzofuran dicarboxylic acid can, for instance, be synthesized in two steps starting from *p*-cresol.[208-211] Banashemi *et al*. reported the synthesis of the *cis*-5a,10b-dihydro-2,9-dimethylbenzofuro[2,3-*b*]benzofuran from glyoxal and *p*-cresol, followed by an oxidation reaction with potassium permanganate. They concluded from ambiguous analytical data that this reaction simultaneous oxidized the methyl groups to carboxylic acid moieties and dehydrogenated the dihydro precursor to yield the completely aromatic BFBF core.

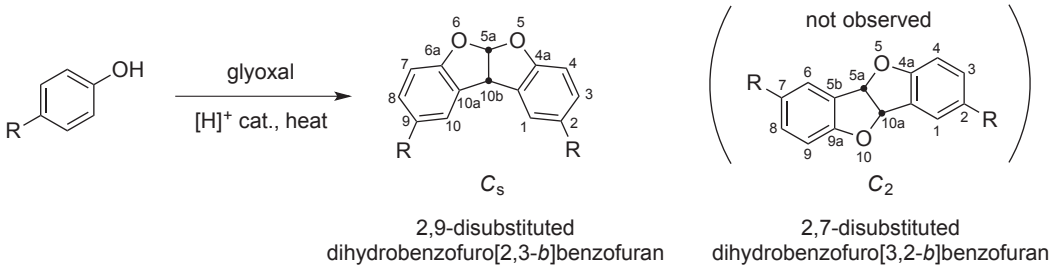

Scheme 9. The acid-catalyzed reaction condensation of glyoxal derivatives with two equivalents of *p*-substituted phenols yields the C_s-symmetric 2,9-disubstituted dihydrobenzofuro[2,3-*b*]benzofuran and not the C_2-symmetric 2,7-disubstituted dihydrobenzofuro[3,2-b]benzofuran.[207]

Here, we demonstrate that the reported synthesis does not result in complete aromatization to the desired benzofurobenzofuran molecule but that a water adduct is obtained instead. We show that the targeted C_{2v}-symmetric benzofurobenzofuran dicarboxylic acid can successfully be prepared in three additional steps starting from this hydrated intermediate. Moreover, we demonstrate that benzofurobenzofuran derivatives are compatible with typical Yamazaki-Higashi activation conditions for the polycondensation with aliphatic diamines. We have thus prepared three corresponding semiaromatic polyamides by polycondensation of benzofurobenzofuran dicarboxylic acid with different aliphatic diamines, and we report their thermal as well as optoelectronic properties.

4.2 Synthesis and Characterization of BFBF Monomer and Model Compounds

As part of our investigations on the incorporation of extended π-conjugated systems with optical or electronic properties into semiaromatic polyamides, we chose the benzofurobenzofuran (BFBF) as a model compound because of its synthetic accessability and structural similarity to organic semiconductor materials based on the benzothienobenzothiophene core that have been found to show excellent charge transport properties.[196-202] The goal was to investigate whether the BFBF core is compatible with typical activation conditions for the polycondensation of aromatic dicarboxylic acids with diamines to yield the corresponding polyamides. Therefore, we first synthesized the benzofurobenzofuran dicarboxylic acid as a monomer. According to previously published procedures, the condensation reaction of glyoxal derivatives with two equivalents of *p*-substituted phenols under reflux in acidic media results in the formation of the corresponding dihydrobenzofurobenzofurans.[205,206] Consistent with the literature, we thus obtained the C_s-symmetric dihydrobenzofuro-benzofuran **1** when we reacted *p*-cresol with glyoxal sodium bisulfite. Nuclear magnetic resonance spectroscopy unambiguously proved that this reaction regioselectively furnished the 2,9-disubstituted dihydrobenzofuro[2,3-*b*]benzofuran **1** with a central ketal moiety, and not the 2,7-disubstituted dihydrobenzofuro[3,2-*b*]benzofurans.[207]

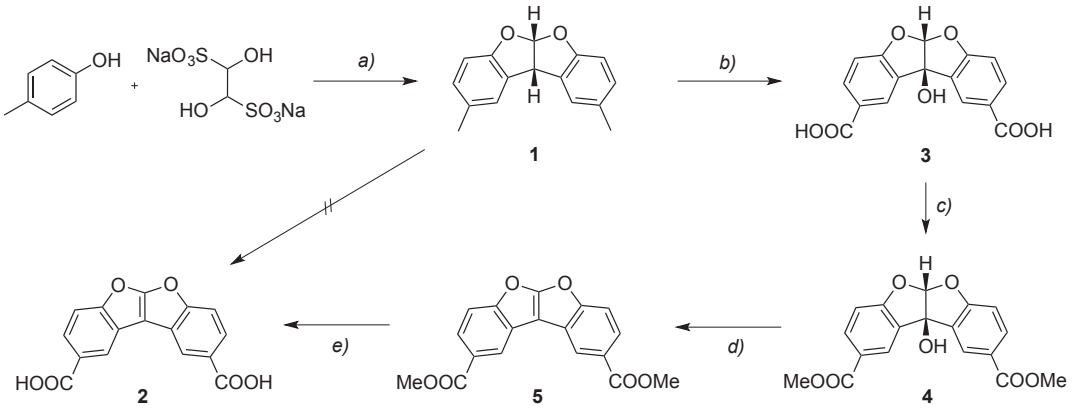

Scheme 10. Dimethyl dihydrobenzofurobenzofuran **1** was obtained by the acid-catalyzed reaction of *p*-cresol and glyoxal sodium bisulfite. Contrary to previous reports,[208,211] the oxidation of **1** with potassium permanganate did not yield the aromatic, C_{2v}-symmetric benzofurobenzofuran dicarboxylic acid **2** but its water adduct **3** that could not be straightforwardly dehydrated. Instead, we synthesized **2** by esterification of **3**, dehydration with phosphoryl chloride, and ester cleavage. *Reagents and conditions: a)* H_2SO_4 (conc.), AcOH/H_2O, reflux, 3 h, 35%; *b)* $KMnO_4$, pyridine/H_2O, reflux, 5 h, 86%; *c)* HCl/MeOH, reflux, 16 h, 90%; *d)* $POCl_3$, pyridine, 0°C to room temperature, 2 h, 83%; *e)* LiOH, THF/H_2O, reflux, 3 h, 89%.

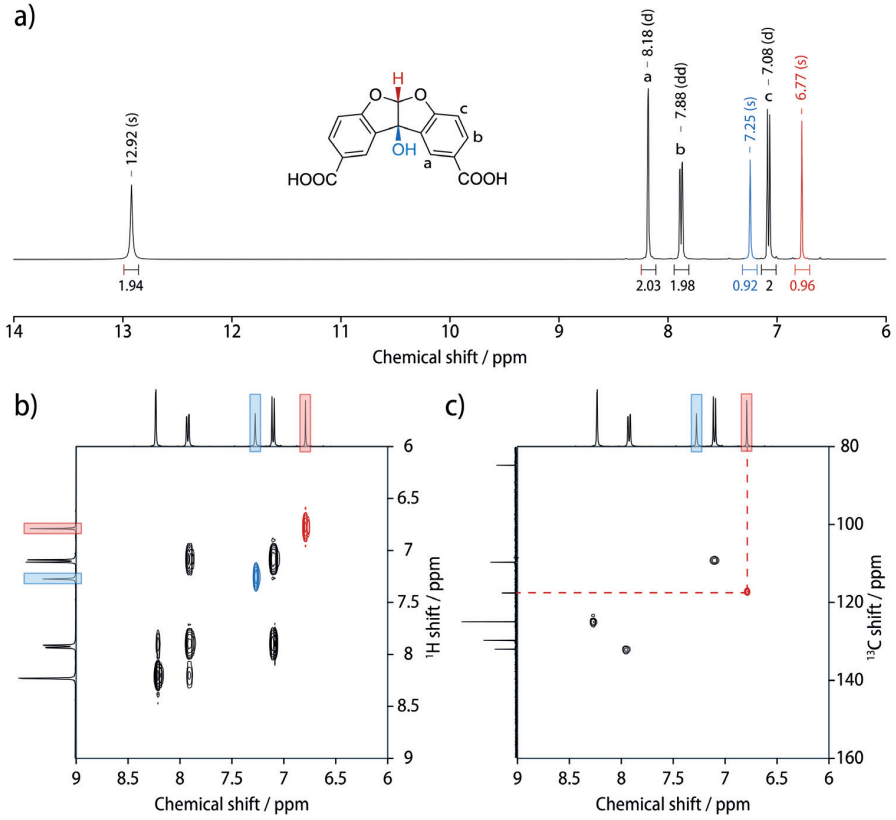

Figure 31. *a)* ^{1}H NMR spectra, *b)* ^{1}H-^{1}H COSY NMR spectra, and *c)* ^{1}H-^{13}C HSQC NMR spectra of **3**. The ^{1}H NMR spectrum showed five distinct peaks in the region 6.7–8.2 ppm and the signal for the carboxylic acid protons at 12.9 ppm, integrating to 1:2:1:2:2:2. The two singlets at 6.77 ppm (red) and 7.25 ppm (blue) did not show off-diagonal peaks in the COSY NMR spectrum. The proton at 7.25 ppm was not correlated to a carbon atom according to the HSQC spectrum.

Previous reports suggested that the oxidation of **1** with potassium permanganate would straightforwardly furnish the C_{2v}-symmetric aromatic benzofurobenzofuran dicarboxylic acid **2** (Scheme 10).[208,211] However, we found that the product of this reaction was the non-planar, non-aromatic, hydrated dicarboxylic acid **3** instead. This result was not due to a different outcome of the reaction in our hands, but due to an incorrect interpretation of the analytical data in the literature. For instance, the ^{1}H NMR spectrum of the product was identical to the one reported previously, with five distinct peaks (three singlets and two duplets) in the region 6.7–8.2 ppm and a peak at 12.9 ppm for the carboxylic acid protons (Figure 31*a*).[208] Hence, neither the number of peaks nor their multiplicities or their integration of 1:2:1:2:2:2 for a total of 10 protons were in agreement with the reported structure of **2** but consistent with the structure of its water adduct **3**, which is also proven by a combination of ^{1}H-^{1}H COSY (Figure 31*b*) and ^{1}H-^{13}C HSQC (Figure 31*c*)

2D-NMR experiments. The COSY experiments revealed that, while the peaks at 8.18, 7.88 and 7.08 ppm corresponded to the aromatic protons, the singlets at 7.25 and 6.77 ppm were not correlated to any other protons. Moreover, HSQC NMR spectroscopy indicated that the proton at 6.77 ppm coupled with the carbon atom at 118 ppm, whereas the proton signal at 7.25 ppm was not correlated with any carbon in the molecule at all. Furthermore, the molecular ion peak in MALDI-TOF mass spectrometry (Appendix) was consistent with the mass of the water adduct **3**, of which the structure was ultimately proven by single-crystal X-ray structure analysis (see below).

All attempts to dehydrate compound **3** directly, in order to obtain the completely aromatic benzofurobenzofuran dicarboxylic acid **2** were unsuccessful. Performing the reaction in neat $SOCl_2$ required heating at reflux for the reaction to start, but product degradation occurred within less than 30 min. Upon addition of sulfuric acid (H_2SO_4) to **3**, either as a catalyst or as the reaction solvent, an immediate decomposition of the starting material was observed. Heating **3** in phosphoric acid (H_3PO_4) appeared to result in an opening of the heterocycles according to proton and carbon NMR. Since the dehydration of **3** was impossible to achieve, one might have considered the dehydrogenation of **1** before oxidation, following a bromination-dehydrohalogenation route that had already been used for similar molecules.[212-214] However, this approach had already been shown to not work in the specific case of compound **1**.[215]

On the other hand, dehydrations of alcohols at low temperatures have often been reported to work efficiently using chlorinating agents such as phosphoryl chloride ($POCl_3$) or thionyl chloride ($SOCl_2$) when the compounds are soluble in chlorinated solvents or pyridine.[216] Therefore, we subjected **3** to heating to reflux in MeOH/HCl overnight in order to obtain the corresponding dimethyl ester **4**, which exhibited a significantly improved solubility in organic solvents. This diester was subsequently dehydrated using an excess of $POCl_3$ in pyridine at 0°C to yield the completely aromatic dimethyl benzofurobenzofuran dicarboxylate **5**. Saponification of **5** using an excess of lithium hydroxide (LiOH) in THF/water mixture upon heating to reflux overnight eventually furnished the desired aromatic benzofurobenzofuran dicarboxylic acid **2**. Hence, three additional steps were necessary to dehydrate the dicarboxylic acid **3**, which nevertheless could be synthezised in a good yield of 66% over all three steps. The comparison of the proton NMR spectra of dicarboxylic acids **3** and **2** showed the disappearance of the two singlets of the CH and

hydroxyl groups (Figure 32*a*). The remaining three aromatic peaks, associated to the three different couples of aromatic protons, were additionally shifted downfield by respectively 0.62, 0.12 and 0.81 ppm (Figures 32*a*, *b*). This observation was consistent with the aromatization of the molecule upon dehydration. Negative-mode high-resolution MALDI-TOF mass spectrometry was found to match the desired dicarboxylic acid **2** (Appendix).

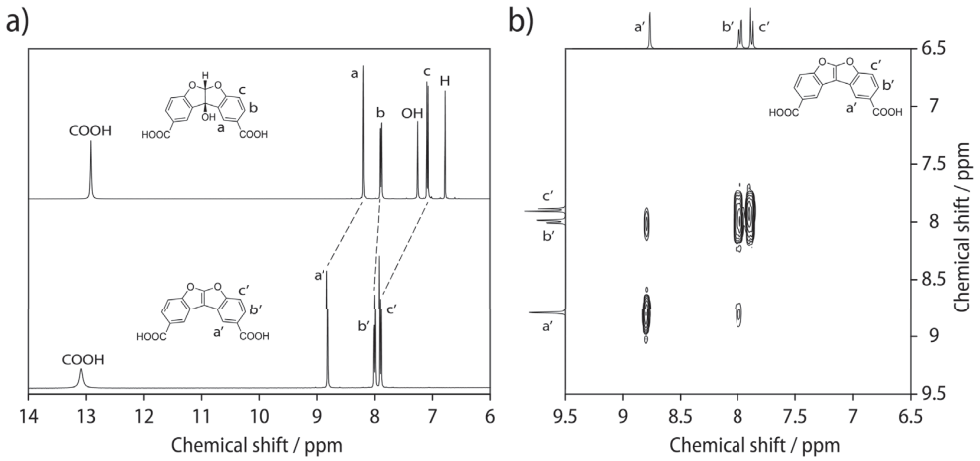

Figure 32. *a)* Comparison of the proton NMR spectra of dicarboxylic acids **3** (top) and **2** (bottom), both recorded in DMSO-d^6. The two singlets associated to the water adduct disappeared and the three couple of aromatic protons were shifted downfield, consistent with the aromatization of the molecule. *b)* The ^{1}H-^{1}H COSY NMR spectrum of **2** helped to unambiguously assign the b' and c' protons.

Single-crystal X-ray structure analyses performed on different model compounds brought the ultimate proof that the oxidation of **1** with potassium permanganate did not yield the aromatic, planar C_{2v}-symmetric benzofurobenzofuran dicarboxylic acid **2** but its water adduct **3**. To this end, the hydrated benzofurobenzofuran dicarboxylic acid **3** was converted into the corresponding dipropyl dicarboxamide **6** using ethyl dimethylaminopropyl carbodiimide (EDCI) and hydroxybenzotriazole (HOBt) as the coupling reagents (Scheme 11, *top*). Recrystallization of **6** from hot ethanol allowed us to obtain single crystals suitable for X-ray structure analysis. Moreover, we prepared the diamide **7** as well as the diester **8** of the benzofurobenzofuran dicarboxylic acid **2** by an EDCI/HOBt-promoted coupling with propylamine and a nucleophilic substitution reaction with 1-bromopropane, respectively (Scheme 11, *bottom*). While various attempts towards the recrystallization of **7** remained unsuccessful, single crystals of the diester **8** were obtained upon slow evaporation of a solution in EtOAc at room temperature.

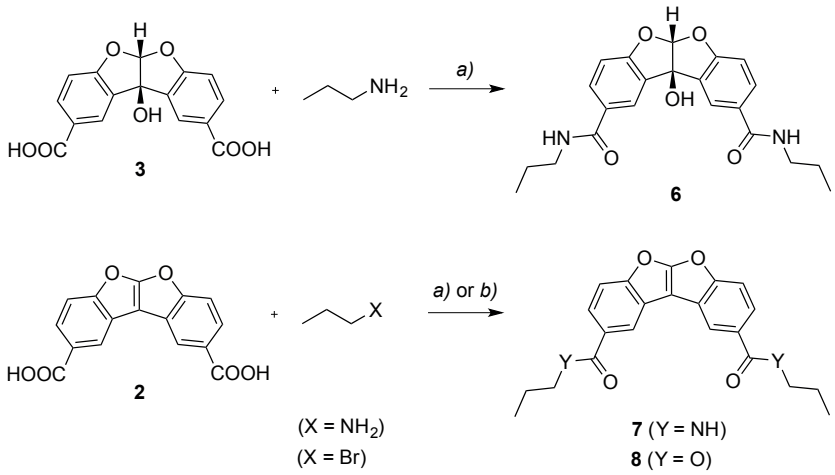

Scheme 11. Synthesis of the benzofurobenzofuran dicarboxamide (**6**, **7**) and diester (**8**) derivatives. Reagents and conditions: *a)* EDCI, HOBt, DIPEA, DMF, room temperature, 16h, 42–87% *b)* K_2CO_3, DMF, 70°C, 16h, 33%.

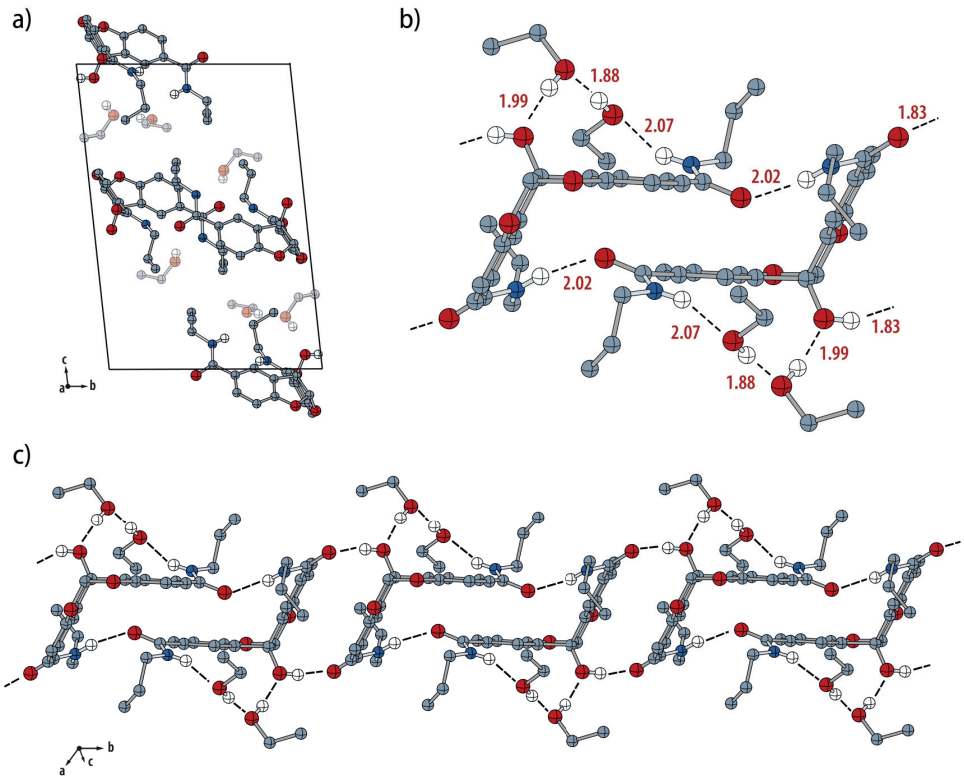

Figure 33. Ball-and-stick representations of the single-crystal X-ray structure of dicarboxamide **6** (CCDC 1528255). *a)* Representation of the unit cell of **6**; the included ethanol molecules are rendered semi-transparent for clarity. *b)* Hydrogen bond distances (in Ångstroms). *c)* Illustration of the one-dimensional hydrogen bonding network along the crystallographic *b*-axis; all hydrogen atoms except those that participate in hydrogen bonding have been omitted for clarity.

The hydrated dicarboxamide derivative **6** crystallized in the form of colorless, needle-like crystals in the triclinic unit cell P-1 with the lattice parameters a = 10.1910(3) Å, b = 13.7072(3) Å, c = 19.0724(5) Å, α = 90.789(2) °, β =103.313(3) °, and γ =109.953(2) ° (Figure 33*a*). The unit cell consists of four molecules of **6** and six ethanol molecules. The molecule exhibits a non-planar structure with an angle of 116.7 ° between the planes of the furan rings, similar to related heterocyclic compounds reported previously.[217,218] Each dicarboxamide molecule participates in six intermolecular hydrogen bonds (Figure 33*b*) involving the amide groups, the central hydroxyl function, and two of the three independent ethanol molecules, which in turn generates a one-dimensional hydrogen bonding network along the crystallographic *b*-axis (Figure 33*c*).

Similar to **6**, the diester **8** gave rise to colorless, needle-like crystals and crystallized in the triclinic space group P-1 with the lattice parameters a = 8.7557(4) Å, b = 10.3822(4) Å, c = 11.1677(5) Å, α = 63.052(4) °, β = 82.840(4) °, and γ = 86.270(4) ° (Figure 34*a*). In the crystal structure, the benzofurobenzofuran core of **8** contrary to **6** exhibits an almost perfect planar structure, as shown by the torsion angles C(18)-C(11)-C(12)-O(3) = –179.6° and C(9)-C(11)-C(12)-O(4) = 179.2°. The benzofurobenzofuran **8** is arranged into layers within which all molecules have the same orientation, and a 180° rotated orientation between alternating layers. These layers form pairs that can be described by a parallel-displaced π-stacked arrangement within the centrosymmetric dimers A–B (Figure 34*b*) with an overlap equating to one of the benzofuran moieties. The interaction between these layer pairs is characterized by the centrosymmetric dimers B–C that have a much smaller overlap. Intermolecular C···O and C···C short contacts of 3.35 Å and 3.33 Å (Figure 34*c*) as well as interlayer distances of 3.3 Å were observed, which is significantly smaller than the interlayer distance found in benzothieno[2,3-*b*]benzothiophene (3.58 Å),[219] in line with closer packings previously reported for herringbone arrangements of certain furans as compared to the corresponding thiophenes.[220]

More importantly, however, the absence of the typical packing motifs observed for the C_{2h}-symmetric benzothieno[3,2-*b*]benzothiophene derivatives (herringbone packing, parallel-displaced π-stacks) and the preference for a pair-wise π-stacking with a 180° rotated orientation show that the supramolecular arrangement of the C_{2v}-symmetric benzofuro[2,3-*b*]benzofuran derivatives was dominated by their permanent molecular dipole.

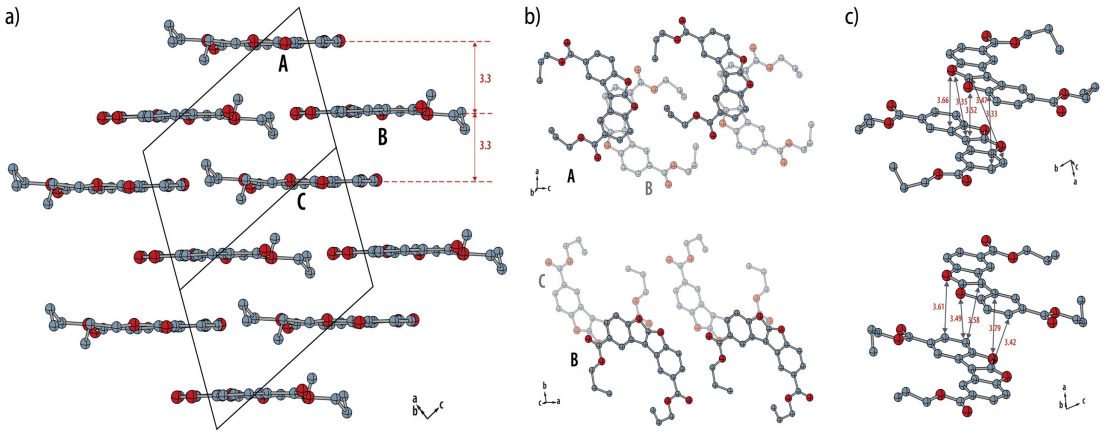

Figure 34. Ball-and-stick representations of the single-crystal X-ray structure of **8** (CCDC 1528254) *a)* Representation of the unit cell of **8** including the interlayer distances. *b)* Top view of the two types of centrosymmetric dimers and *c)* an illustration of short contacts and distances (in Ångstroms); all hydrogen atoms omitted for clarity.

4.3 Synthesis and Characterization of Polyamides Comprising BFBF Units

The benzofurobenzofuran dicarboxylic acid **2** was incorporated into the semiaromatic polyamides **PA6B**, **PA9B** and **PA12B** by solution-phase polycondensation with 1,6-hexanediamine, 1,9-nonanediamine, and 1,12-dodecanediamine, respectively, using Yamazaki-Higashi conditions (Scheme 12).[31-36] The obtained polyamides were found to be insoluble in most common organic solvents, but partially soluble in hot dimethylsulfoxide (DMSO) and well soluble in 1,1,1,3,3,3-hexafluoropropane-2-ol (HFIP, 40 mg/mL).

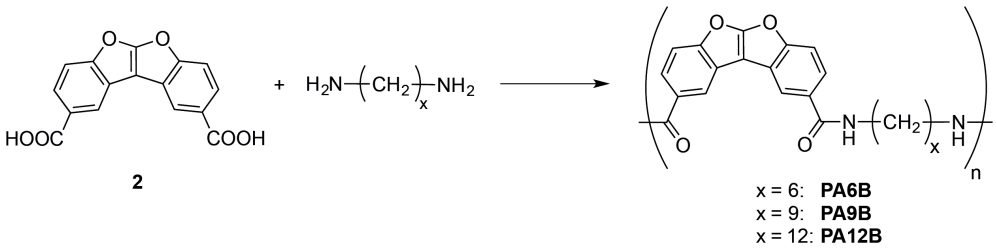

Scheme 12. Synthesis of the benzofurobenzofuran-based semi-aromatic polyamides **PA6B**, **PA9B** and **PA12B** using Yamazaki-Higashi conditions: TPP, LiCl, pyridine/NMP (1:4), 110°C, 4h, 72–88%.

Both ^{1}H NMR and solid-state infrared spectroscopy indicated the successful conversion into polyamides. Indeed, the peak positions and integration in the ^{1}H NMR spectra matched the structure of the expected polyamides, and the amide protons could be clearly observed at 5.90–

5.92 ppm (Figure 35*a*). Moreover, small additional signals were visible in the aromatic region of **PA6B** that we assigned to the aromatic protons of the BFBF carboxylic acid end groups. Since no amine end groups could be detected, the integration of the aromatic end group signals relative to those of the repeating units translate into a molecular weight of M_n = 10'900 (degree of polymerization P_n = 29), in reasonable agreement with the molecular weight of M_n = 7'100 ($Đ$ = 1.28) determined by gel permeation chromatography (GPC) in HFIP. GPC measurements revealed similar molecular weights and dispersities of M_n = 7'100 ($Đ$ = 1.35) and M_n = 7'000 ($Đ$ = 1.34) for **PA9B** and **PA12B**, which is an indication for the good reproducibility of the chosen polycondensation protocol.

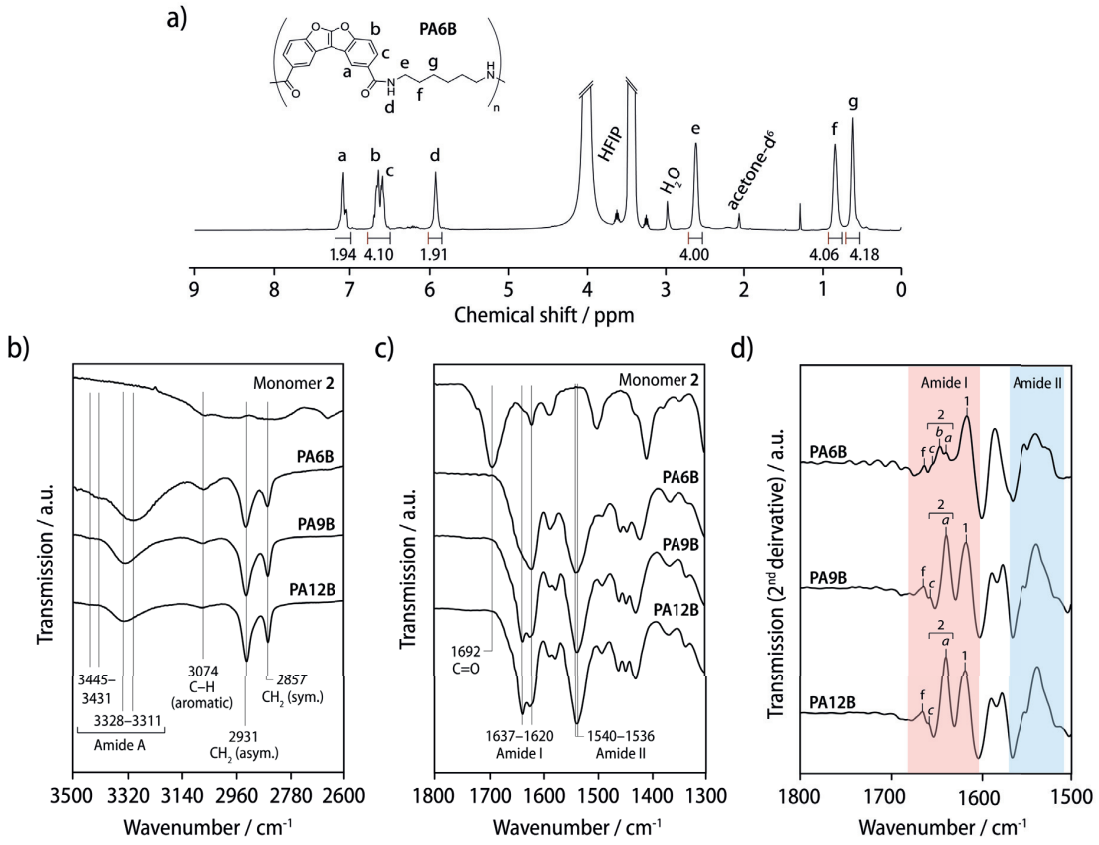

Figure 35. *a)* ^{1}H-NMR spectrum of the semiaromatic **PA6B** recorded in HFIP/acetone-d^6. The amide protons of the repeating unit are visible at 5.92 ppm. *b), c)* Comparison of the solid-state IR spectra of the benzofurobenzofuran dicarboxylic acid monomer **2** and the semiaromatic polyamides **PA6B**, **PA9B** and **PA12B**; the C=O and O–H bands of the carboxylic acid function of **2** disappeared upon polycondensation, and the appearance of the amide II, I, and A bands as well as the symmetric and asymmetric CH_2 stretching vibrations of the aliphatic units indicated that the polycondensations were successful. *d)* Second derivative analysis of the IR spectra of the amide I and amide II regions of the polyamides **PA6B**, **PA9B** and **PA12B**.

Table 5. Amide A (N–H stretching) and amide I (C=O stretching) bands of the polyamides **PA6B**, **PA9B**, and **PA12B**. The width at half-height ($W_{1/2}$) is given in parentheses for the hydrogen-bonded portion of the amide A band. The amide I band was found to be composed of a main band ν_1 and additional bands ν_2 of hydrogen-bonded C=O groups, as well as the band ν_{free} of the free C=O groups.

Polyamide	*Amide A*		*Amide I*		
	$\nu_{H\text{-}bonded}$ ($W_{1/2}$)/cm^{-1}	ν_{free}/cm^{-1}	ν_1/cm^{-1}	ν_2 /cm^{-1}	ν_{free}/cm^{-1}
PA6B	3311 (153)	3431	1617	1640, 1647, 1656	1664
PA9B	3326 (104)	3445	1617	1639, 1657	1664
PA12B	3328 (104)	3443	1618	1639, 1658	1664

IR spectroscopy confirmed that the broad absorption at 2700–3500 cm^{-1} and the band at 1692 cm^{-1} that correspond to the O–H and C=O stretching vibrations of the carboxylic acid group of **2** completely disappeared upon polycondensation. Instead, five new peaks were observed at 3311–3328, 2931, 2857, 1620–1637, and 1536–1540 cm^{-1} that can be attributed to the amide A, asymmetric CH_2 stretching, symmetric CH_2 stretching, amide I, and amide II bands of the semiaromatic polyamides (Figure 35*b*, *c*). In all cases, the peak positions of the main amide A band and its shoulder could be assigned to the N–H stretching vibrations of hydrogen-bonded and free amide groups, respectively.

The peak positions as well as the large widths at half-height ($W_{1/2}$ > 100 cm^{-1}) were in good agreement with what had previously been reported for amorphous polyamides (Table 5),[70] while a more red-shifted band and a smaller $W_{1/2}$ would typically be observed in the case of semi-crystalline polyamides.[221] Consistently, the amide I absorptions were broad and composed of a series of bands, as became evident from a second derivative analysis (Figure 35*d*). For all three polyamides, the main contributions at 1617–1618 cm^{-1} could be assigned to C=O groups in a resonant array of hydrogen bonds. While **PA6B** showed a series of bands that can be assigned to more disordered hydrogen-bonded and free C=O groups, these bands were fewer and more distinct for **PA9B** and **PA12B**. This can be explained by the increasing hydrophobicity of the polyamide matrix with increasing length of the aliphatic unit, which reinforces defined hydrogen-bond geometries even in the amorphous phase.

Wide-angle X-ray scattering measurements (WAXS) showed only an amorphous halo for **PA6B**, but additionally a broad, weak diffraction centered at $2\theta = 18.73°$ and 19.10°, for **PA9B** and **PA12B**, respectively (Figure 36*a*). As the corresponding spacing of 4.6–4.7 Å should roughly correspond to the intermolecular distance of hydrogen-bonded BFBF pairs, one may assume that the latter tend to form clusters by dipolar interactions in the more hydrophobic polymers **PA9B** and **PA12B**.

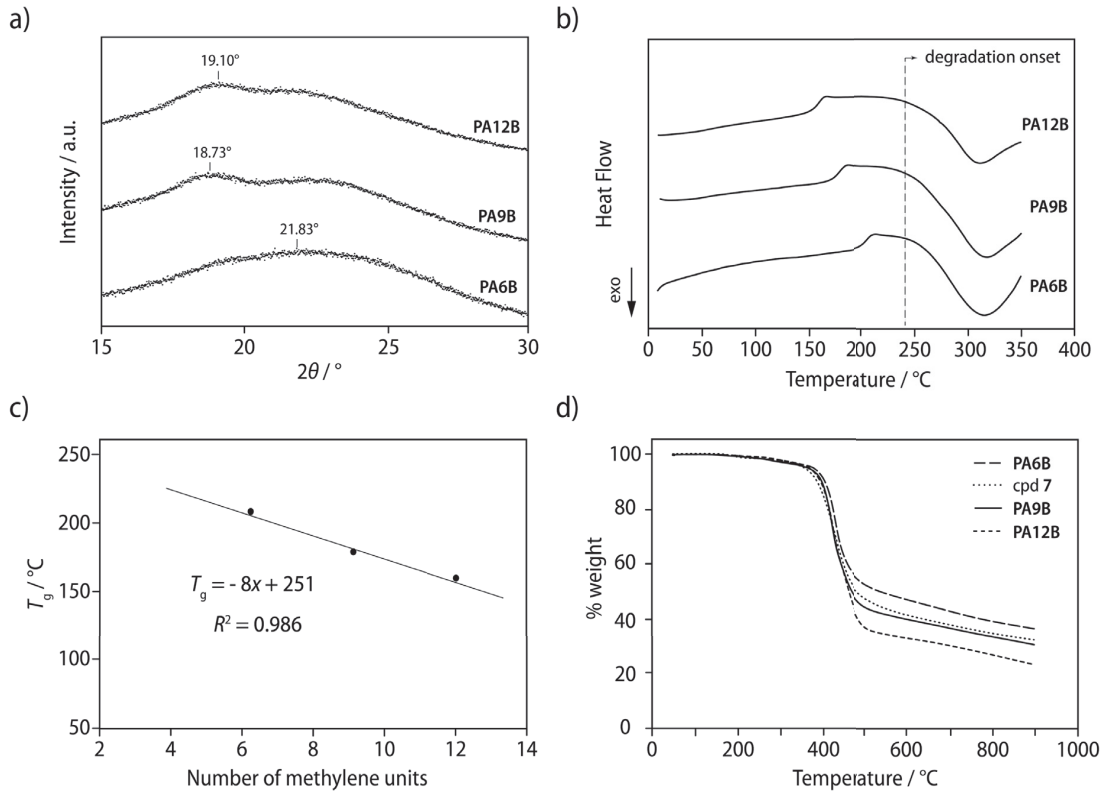

Figure 36. *a)* Wide-angle X-ray scattering (WAXS) of the polyamides **PA6B**, **PA9B** and **PA12B**. **PA6B** shows an amorphous halo centered at $2\theta = 21.83$ °, as well as a broad diffraction peak at $2\theta = 18.73$ ° and 19.10 ° for **PA9B** and **PA12B**, respectively. *b)* Second heating scans in differential scanning calorimetry (DSC) of **PA6B**, **PA9B** and **PA12B** indicated a decrease of the glass transition temperature (T_g) with increasing length of the aliphatic unit; no melting peaks were obersved as the materials underwent exothermic degradation above 240–250°C. *c)* The linear correlation between T_g and the number of methylene units x in the aliphatic unit was consistent with group contribution theory.[222] *d*) Thermogravimetric analysis (TGA) scans of **PA6B** (long dashes), **PA9B** (solid line), **PA12B** (short dashes) and model compound **7** (dotted line) in nitrogen; the exothermic degradation observed in DSC corresponded to only a minor weight loss (<2.5 *wt*%) in TGA.

Consistent with IR spectroscopy and WAXS results, no melting transitions were observed for either of the three polyamides in differential scanning calorimetry (DSC), as they were found to

degrade at temperatures of 240–250°C (Figure 36*b*). The polyamides exhibited glass transition temperatures (T_g) of 205°C for **PA6B**, 176°C for **PA9B**, and 157°C for **PA12B** (Table 6). Consistent with estimates from group contribution theory[222] considering the presence of the rigid, fused BFBF units, these are significantly higher than the T_g ≤ 130°C of typical semiaromatic polyamides[223] based on terephthalic and/or isophthalic acid and decreased proportional to the length of the aliphatic unit (Figure 36*c*). Thermogravimetric analysis of all three polyamides (Figure 36*d*) showed that the observed exothermic degradation in the DSC was associated with only a minor mass loss (<2.5 *wt*%). This observation combined with the fact that the overall behavior of all three polyamides and the dicarboxamide model compound **7** were identical up to 400°C suggest that the initial degradation should be related to reactions of the heterocyclic core.

Table 6. Glass transition temperatures T_g, as well as decomposition temperatures T_d (from the intersection of the tangents of the exothermic decomposition peak with the baseline in DSC), and T_{95} (from 5 *wt*% mass loss in TGA) of the semiaromatic polyamides **PA6B**, **PA9B** and **PA12B**.

Polyamide	*DSC*		*TGA*
	T_g / °C	T_d / °C	T_{95} / °C
PA6B	205	251	370
PA9B	176	244	359
PA12B	157	256	361

Fused benzothiophenes have been shown to exhibit excellent semiconducting properties,[196-202] while organic semiconductors based on related benzofurans have more recently been reported, as well.[203,204] Therefore, the structural similarity of the benzofurobenzofuran core to benzothienobenzothiophene (BTBT) called for an investigation of the optical and electronic properties of films of the benzofurobenzofuran-based polyamides. Computations on the benzofurobenzofuran dimethylcarboxamide **9** (used as a proxy for **PA6B**, **PA9B**, **PA12B** and the model compound **7**) revealed a non-trivial excited state behavior arising from energetically close-lying excited states. The first five transition energies as well as their oscillator strengths were determined based on consistent excited state computations with TD-DFT (PBE0 functional using Tamm-Doncoff approximation) and ADC(2). The two brightest transitions matched well the two optical bands experimentally observed in the UV/vis absorption spectra of **PA6B** and **7** (Figure

37*a*, solid lines). Thus, the highest wavelength absorption at 269 nm was assigned to the HOMO–LUMO transition, while the most intense optical band at 237 nm matched the HOMO–(LUMO+2) transition. Thin films obtained from dropcasting the materials onto quartz substrates exhibited similar absorptions albeit with a small solid-state red shift to 276 and 244 nm (Figure 37*a*, dashed lines). According to the computations, the transition had a π–π* character with a strong shift of electron density from the central enediol-type double bond into the neighboring benzene units, indicating the break-up of conjugation in the dominant excited states (Figure 37*b*). Moreover, the large HOMO-LUMO gap of 5.08 eV and the fact that both the very low-lying HOMO (–6.36 eV) and the high-lying LUMO (–1.28 eV) are energetically mismatched with the utilized gold source/drain electrodes (work function ≈ 5eV),[224] appears to render the C_{2v}-symmetric BFBF-based materials not suitable for use in organic electronic devices. In agreement with this assessment, field-effect transistors fabricated from thin films of either the polyamide **PA6B** or the model compound **7** showed no charge transport across the thin films, neither in bottom-gate bottom-contact nor in bottom-gate top-contact configurations.

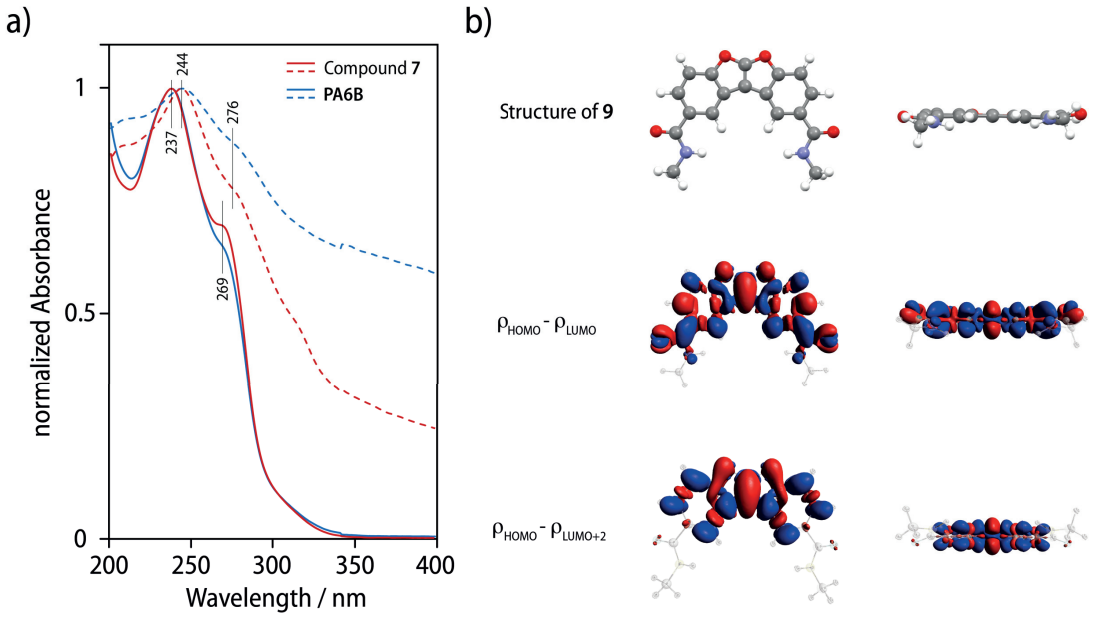

Figure 37. *a)* Normalized UV/vis absorption spectra of solutions (solid lines) and thin films (dashed lines) of **PA6B** and the model compound **7** measured at 25°C. *b)* Density differences at the ADC(2)/def2-SVP level for the corresponding dimethyl carboxamide **9** in its first and fifth singlet excited-state PBE/def2-SVP optimized geometry. Isodensities = – 0.0005 (red) and +0.0005 (blue).

4.4 Conclusion

In conclusion, we have developed the synthesis of a benzofurobenzofuran (BFBF) dicarboxylic acid building block for its inclusion in semiaromatic polyamides, aiming at proving the synthetic applicability of Yamazaki-Higashi conditions for solution polycondensation and investigating the thermal and optoelectronic properties of the resulting polyamides. The fused benzofuran-based cores were primarily chosen because of the straightforward synthetic accessibility of C_{2v}-symmetric BFBF monomers and their molecular resemblance to benzothienobenzothiophenes, which had previously been shown to be efficient semiconductors that exhibit high carrier mobilities.

We first established a synthetic route that furnished the desired benzofurobenzofuran dicarboxylic acid monomer over five steps in a total yield of 20% on the multi-gram scale, starting from commercial precursors. Due to the previously unreported formation of a water adduct upon oxidation of the methyl side chains to carboxylic acid residues, additional synthetic steps were required to dehydrate the molecule and furnish the planar, aromatic benzofurobenzofuran dicarboxylic acid. The structure of the latter was unambigously established by 1D and 2D NMR spectroscopy, mass spectrometry, and X-ray structure analysis. The semiaromatic polyamides **PA6B**, **PA9B** and **PA12B** were then obtained by the solution-phase polycondensation of the BFBF dicarboxylic acid with 1,6-hexanediamine, 1,9-nonanediamine and 1,12-dodecanediamine respectively, using Yamazaki-Higashi conditions. Our investigations by IR spectroscopy, WAXS, and DSC revealed that all three polyamides were amorphous, with some variations in their overall degree of order that we attributed to the increasing hydrophobicity of the polyamide matrix within the series. The rigidity of the fused benzofuran core resulted in glass transition temperatures well above those usually reported for common semiaromatic polyamides based on isophthalic or terephthalic acid but were well in line with group contribution theory.[222] All materials decomposed above the glass transition, supposedly due to a degradation of the heterocyclic BTBT core at temperatures above 240–250°C.

UV/vis spectroscopy and computations revealed a large HOMO-LUMO gap, a strong mismatch of the HOMO and LUMO levels with the work function of the gold electrodes, as well as a significant shift of electron density from the central enediol-type double bond of the BFBF moiety into the

neighboring benzene units upon excitation, resulting in the break-up of conjugation in the dominant excited states. All of these factors serve to explain why the BFBF-based materials failed to function in organic electronic devices. However, since previous research had demonstrated that amide hydrogen bonding did not constitute a general impediment to charge transport in organic semiconductors,[225-231] the fact that polyamides comprising extended π-conjugated systems from fused heterocycles can be straightforwardly prepared using Yamazaki-Higashi polycondensation conditions may stimulate further research on the way towards polyamide-based semiconductors from better suited chromophores in the future.

5

Semiaromatic Polyamides with U-turn Repeating Units

The results presented in this chapter are part of a manuscript in preparation:

"Synthesis and Characterization of Semiaromatic Polyamides with U-Turn Repeating Units", Cretenoud, J.; Plummer, C. J. G.; Özen, B.; Baudat, E.; Fadaei Tirani, F.; Scopelliti, R.; Frauenrath, H. *To be submitted.*

All monomers and polyamides were synthesized and characterized by J. C, with the help of E. B. for some of the NMR measurements and C. J. G. P. for the interpretation and simulation of WAXS patterns. The crystal structures were measured and refined by F. F. T. and R. S. Nanoindentation measurements were perfomed by B. Ö. This work was supervised by H. F.

5 Semiaromatic Polyamides Comprising U-turn Repeating Units

5.1 Introduction

Semicrystalline aliphatic and semiaromatic polyamides are attractive engineering materials, because they combine excellent melt processability with mechanical properties that can be tailored as a function of their degree of crystallinity and the morphology of the crystalline phase.[90,174,189,190] Structural proteins such as silk materials can be regarded as the biological analogues of synthetic polyamides because their degree of crystallinity and the crucial role of interchain hydrogen bonded networks between amide groups are very similar. However, their respective microstructures are in fact quite different, as are the resulting properties. While the hydrogen-bonded chains in synthetic polyamides most commonly form lamellar crystals,[56,57] silk proteins fold into defined conformations and self-assemble into well-defined secondary and tertiary structures on the nanoscopic length scale.[140-144] The key feature in the molecular structure responsible for chain folding are amino acid sequences that give rise to turn motifs such as β-hairpin structures[151-153] and β-serpentine folds.[154-158] Rigid molecular scaffolds based on azobenzenes[161] 2,8-disubstituted dibenzofurans,[162] 3,6-disubtituted carbazoles,[163] or 4,6-disubstituted phenoxathiins[164-167] have been investigated as synthetic turn mimics because they template a fixed dihedral angle of 180° at a distance of about 4.8 Ångstroms. However, the effect of such templates on the folding and mechanical properties of bulk thermoplastics such as polyamides has never been systematically studied to date.

Here, we show that polymer chain folding in synthetic polyamides can indeed be templated by incorporating specifically designed rigid frameworks based aromatic turn mimics, which we will refer to as “U-turns” in what follows. Due to the commercial availability of suitable precursors, we used dicarboxylic acid monomers based on 4,5-disubstituted acridine and 1,8-disubstituted anthracene derivatives and prepared the corresponding polyamides by solution polycondensation reactions. A combination of X-ray analysis as well as IR and optical spectroscopy of the polymers and model compounds revealed that the acridine-based polyamides indeed assumed folded conformations in the crystalline state that were reminiscent of β-serpentine folds and further organize into lamellar crystals with extensive re-entrant chain

folding, stabilized by intermolecular hydrogen bonding. Nanoindentation measurements revealed that the obtained polyamides exhibited a hardness of up to 320 MPa and an elastic modulus of up to 3.6 GPa, similar to non-folding semiaromatic polyamides.

5.2 Synthesis of U-turn Monomers and Model Compounds

The selective two-fold introduction of bromomethyl substituents at the 4,5-positions of acridine was achieved analogously to published procedures.[232] The bromomethylation of acridine was carried out in warm concentrated sulfuric acid (96% H_2SO_4) with a two-fold excess of bromomethyl methyl ether (Scheme 13).

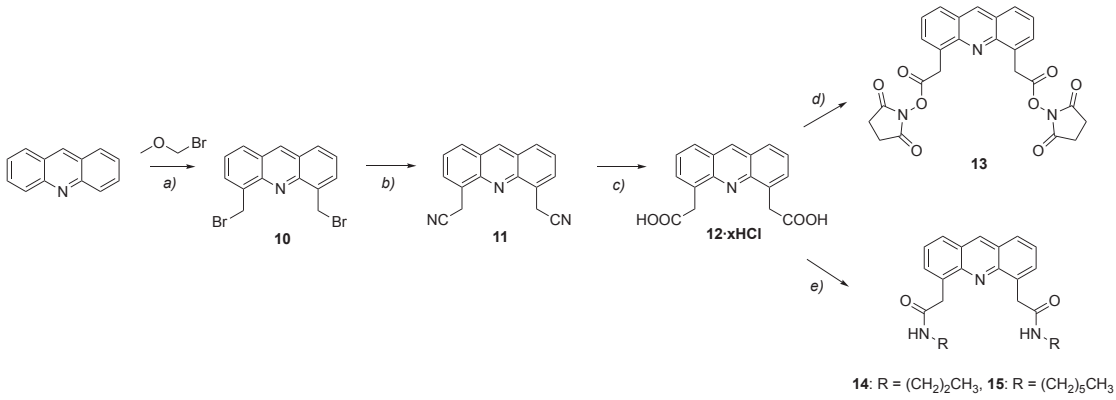

Scheme 13. Synthesis of acridine-based active ester monomers for polycondensations and diamide model compounds. *Reagents and conditions: a)* H_2SO_4 (conc.), 50 °C, 16 h, 50%; *b)* NaCN, DMF, r.t., 2 h, 95%; *c)* HCl (conc.), reflux, 16 h, 74%. *d)* NHS (2 equiv.), EDCI, DIPEA, DMF, r.t., 2.5 h, 46%; *e)* 1-propylamine or 1-hexylamine (2 equiv.), EDCI, HOBt, DIPEA, DMF, r.t., 16 h, 47–53%.

The subsequent two-fold cyanation of di(bromomethyl) acridine **10** with sodium cyanide was then performed at room temperature in DMF. Care was taken to not raise the temperature above 40–50 °C during the course of the reaction because the di(cyanomethyl) acridine **11** was found to degrade at higher temperatures. Because of the high reactivity of the acridine core towards reducing reagents, we opted for an acidic hydrolysis of the nitrile groups to obtain the di(carboxymethyl) acridine hydrochloride **12**. We initially intended to perform the polycondensation of this dicarboxylic acid directly with aliphatic diamines using Yamazaki-Higashi conditions. However, this would have required an activation of the carboxylic function by triphenylphosphite and pyridine. To avoid competing reactions between the acridine core and the

pyridine activator, we therefore decided to perform the polycondensation using the corresponding active esters. The esterification of **12** with *N*-hydroxysuccinimide yielded the acridine active ester monomer **13**. This four-step synthesis was subsequently scaled up to the multi-gram scale with a 16% overall yield, which was mostly limited by the moderate 50% yield of the initial selective 4,5-dibromomethylation.

Moreover, peptide coupling of the di(carboxymethyl) acridine hydrochloride **12** with either 1-propylamine or 1-hexylamine using EDCI/HOBt as coupling promoters furnished the acridine di(propyl amide) **14** and the di(hexylamide) **15**, respectively, which are to serve as model compounds to study the packing of the hydrogen-bonded U-turn frameworks (vide infra).

The synthesis of an anthracene-based monomer started by the two-fold ether coupling of commercially available 1,8-dihydroxyanthraquinone to ethyl bromoacetate yielding the anthraquinone diester **16**, followed by saponification to obtain the anthraquinone dicarboxylic acid **17**, analogous to established procedures (Scheme 14).[233-235] Reduction of the anthraquinone using zinc powder in a refluxing aqueous NH_4OH solution then furnished the corresponding anthracene dicarboxylic acid **18**. Avoiding a large an excess of zinc in this last step turned out to be critical, as it resulted in over-reduction of the anthracene core. The anthracene dicarboxylic acid **18** was subsequently synthesized on a multi-gram scale from commercially available precursors with a 31% total yield over the three steps of the synthesis, limited mainly by the purification of compound **16** by recrystallization.

Also in the case of the anthracene-derivatives, we performed a EDCI/HOBt-promoted peptide coupling of **18** and 1-propylamine to prepare the di(propylamide) **19** as a model compound for packing analysis.

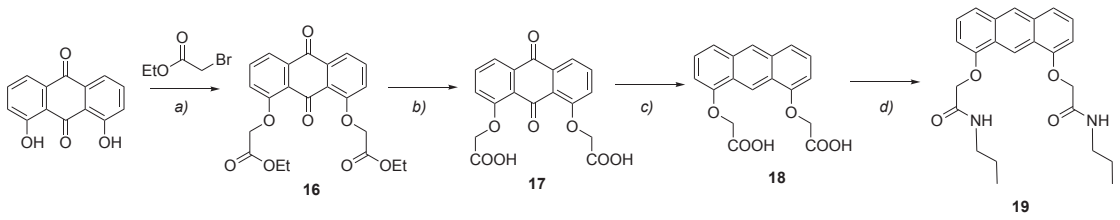

Scheme 14. Synthesis of anthracene-based active ester monomers for polycondensations and diamide model compounds. *Reagents and conditions: a)* K_2CO_3, acetone, reflux, 16 h, 46%; *b)* LiOH, THF:water 4:1, reflux, 16 h, 93%; *c)* Zn powder, aq. NH_4OH (25%), reflux, 16 h, 73%; *d)* 1-propylamine (2 equiv.), EDCI, HOBt, DIPEA, DMF, r.t., 16 h, 97%.

5.3 Crystal Structure Analysis

Single crystals of the acridine di(propylamide) **14** were obtained by the slow diffusion of diethyl ether into a DCM solution of the compound, while needle-like single crystals of acridine di(hexylamide) **15** were obtained by slow cooling of a hot saturated MeOH solution, and columnar single crystals of anthracene di(propylamide) **19** were prepared by the slow evaporation of a saturated DCM/MeOH (9:1) solution at room temperature.

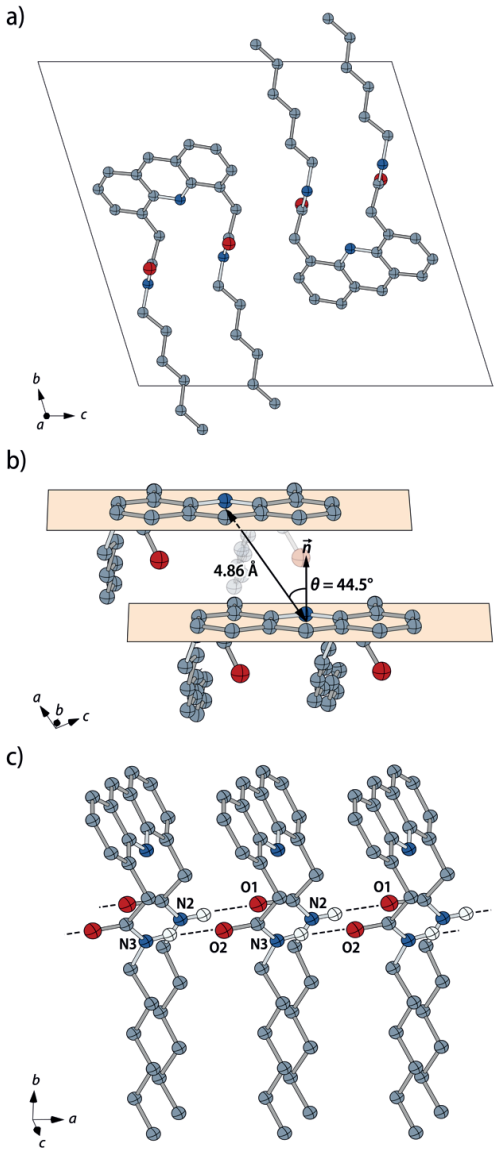

Figure 38. Ball-and-stick representations of the single-crystal X-ray structure of acridine di(hexylamide) **15**. *a)* Projection along the *a*-axis. *b)* The acridines show parallel-displaced π–π stacking and *c)* form infinite stacks along the a-axis held together by two infinite arrays of intermolecular N–H · · · O=C hydrogen bonds. All hydrogen atoms except those that participate in hydrogen bonding have been omitted for clarity.

Under these conditions, both **14** and **15** crystallized in the triclinic space group $P\bar{1}$ with overall very similar molecular packing, with the differences in lattice parameters mainly stemming from the differences in the alkyl chain lengths. Since **14** resulted in less satisfactory structure determinations, we will focus our discussion to model compound **15**. The unit cell exhibited lattice parameters a = 4.8589(3) Å, b = 16.4620(11) Å, c = 17.1521(14) Å, α = 107.110(7)°, β = 93.194(5)°, and γ = 92.383(5)° (Figure 38*a*). The planar acridine moieties formed parallel-displaced π–π stacks along the *a*-axis with an interplanar distance of 3.456(1) Å, a centroid-to-centroid distance of 4.86 Å, and an inclination of the centroid-to-centroid vector by θ = 44.5 ° with respect to the plane normal (Figure 38*b*). The unit cell was traversed by two such stacks related by a center of inversion, and the stacks were held together by two infinite arrays of intermolecular N–H · · · O=C hydrogen bonds (Figure 38*c*, Table 7). The hexyl chains were packed in all-trans conformation.

Table 7. Hydrogen bonds observed in single crystals of acridine model compound **15**.

D–H···A	*d*(H···A) / Å	*d*(D···A) / Å	∠ (DHA)
N(2)–H(2N)···O(1)	1.997	2.830(2)	178.0°
N(3)–H(3N)···O(2)	1.929	2.795(2)	167.5°

By contrast, the anthracene di(propylamide) **19** crystallized in the monoclinic space group $P1(2_1/c)1$ with lattice parameters a = 16.7948(3) Å, b = 15.6952(2) Å, c = 9.59134(16) Å and γ = 102.3875(16)°. The unit cell contained four molecules of **19** and four DCM molecules (Figure 39*a*) and provides an illustration of the subtle interplay of weak interactions involved in structure formation in these compounds. Parallel-displaced π–π stacked pairs of anthracene generated by a center of inversion formed staggered dimers with a interplanar distance of 3.404(1) Å that were then packed into a typical sandwich herringbone pattern[236] in the (101) plane generated by a *c*-glide (Figure 39*c*, *d*). The molecular conformation was stabilized by two *intramolecular* N–H · · · O=C hydrogen bonds, such that both carbonyl groups were twisted outwards. The edge-to-face pairs in the herringbone arrangement were further connected by a pair of bifurcated intermolecular N–H · · · O=C hydrogen bonds (Figure 39*b*, Table 8). The incorporation of DCM further stabilized the structure via C–Cl · · · O=C halogen bonds. The presence of the DCM must

hence be assumed to play an important role in the molecular packing, which may render the observed structure less representative for the packing in the corresponding polyamides.

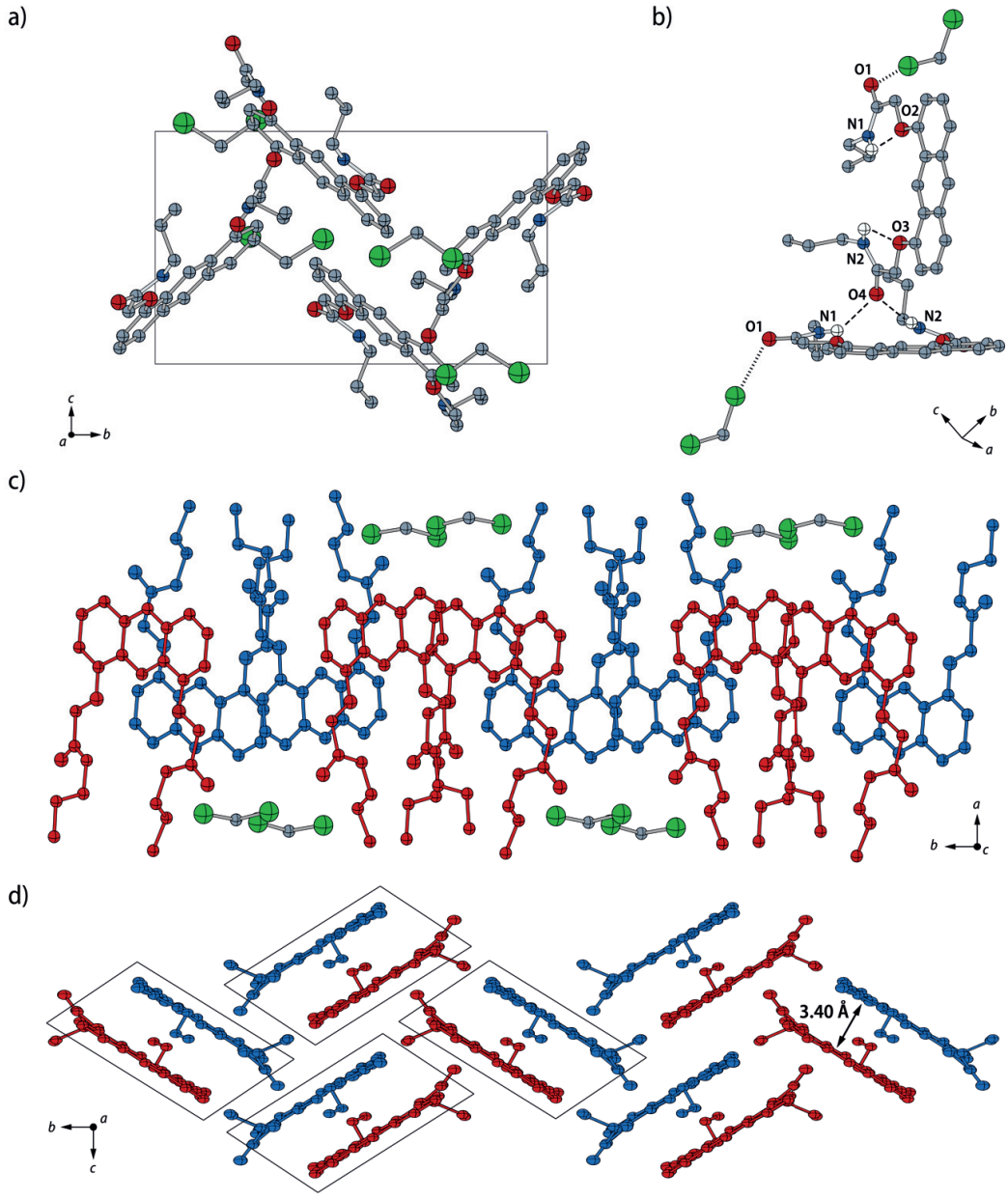

Figure 39. Ball-and-stick representations of the single-crystal X-ray structure of the anthracene di(propylamide) **19**. *a)* Projection along the *a*-axis of the unit cell of **19** including the co-crystallized DCM molecules. *b)* Intramolecular and bifurcated intermolecular hydrogen bonds observed in the edge-to-face pairs packed of **19**. All hydrogen atoms except those that participate in hydrogen bonding have been omitted for clarity. *c)* Side-view and *d)* top-view of the molecules lying in different *bc* planes (red and blue) that form a sandwich herringbone pattern (DCM molecules have been omitted in *d)* for clarity).

Table 8. Hydrogen bonds observed in single crystals of anthracene model compound **19**.

D–H···A	*d*(H···A) / Å	*d*(D···A) / Å	∠ (DHA)
N(1)–H(1)···O(2)	2.250	2.648(2)	110.0°
N(2)–H(2)···O(3)	2.282	2.673(2)	108.1°
N(2)–H(2)···O(4)	2.137	2.858(2)	142.2°
N(1)–H(1)···O(4)	2.351	2.961(2)	131.3°

Solution-phase and solid-state IR spectra (Figure 40*a*, *b*) of the model compounds **15** and **19** were performed with the aim to correlate the observed structures to the packing in the solid polyamides. In the case of the acridine **15**, a single amide A (N–H stretching) band at 3278 cm^{-1} and a single amide I (C=O stretching) vibration at 1635 cm^{-1} in the solid state indicated a uniform type of hydrogen bonded amides. The positions of these bands were consistent with the presence of infinite arrays of intermolecular N–H · · · O=C observed in the crystal structure of **15**. In addition to the free N–H stretching vibration at 3430 cm^{-1}, the amide A region of **15** in CD_2Cl_2 solution showed a broad peak at 3310 cm^{-1} regardless of concentration, which may imply the formation of weak intramolecular hydrogen bonds (Figure 40*a*). Similar features were also observed for acridine di(propylamide) **14**. By contrast, the solid-state IR spectra of the anthracene di(propylamide) **19** showed two amide A bands (3399, 3298 cm^{-1}) and at least three amide I absorptions (1683, 1665, 1649 cm^{-1}) (Figure 40*b*), consistent with the presence intramolecular and the bifurcated intermolecular N–H · · · O=C hydrogen bonding motifs as implied by the crystal structure of **19**. In CD_2Cl_2 solutions of **19**, a single amide A peak was observed at 3435 cm^{-1}, consistent with complete disruption of hydrogen bonds in solution.

Concentration-dependent NMR measurements on **15** and **19** in CD_2Cl_2. showed little variation in the chemical shift of the NH group signal in a concentration range of 1–50 mmol/L (Figure 40*c*). The dimerization of monofunctional amides usually only starts at higher concentrations (>50–100 mmol/L),[237] at which **15** and **19** were no longer fully soluble. The formation of intermolecular hydrogen bonds in solution can therefore be indeed excluded. It is known from the peptide and oligoamide literature that the variation of the chemical displacement with temperature in solvents that do not compete for hydrogen bonding provides a good indication of the presence of intramolecular hydrogen bonds,[237-239] if values significantly larger than $-\delta(\mathrm{NH})/\Delta T$ = 2.5 ppb/K

(reported for the reference compound *N*-methylacetamide that cannot form intramolecular hydrogen bonds) are observed. Temperature-dependent NMR spectroscopy of dilute solutions of **15** and **19** in CD_2Cl_2 (c = 1 mmol/L) in the temperature range 218–298 K resulted in values of 1.9 ppb/K for **19** and 4.2 ppb/K for **15** (Figure 40*d*). Hence, only the latter shows the formation of intramolecular hydrogen bonds, which is in agreement with our interpretation of the solution-phase IR spectra. At least two different types of intramolecular hydrogen bonds may be envisaged for **15**, either with participation of the acridine nitrogen atom or between the two amide groups (Figure 40*e*). DFT computations on compound **14** revealed that the latter configuration was energetically favored by 37 kJ/mol relative to a non-hydrogen bonded state (Figure 40*f*), while no convergence was obtained for the N–H · · · N hydrogen-bonded structure.

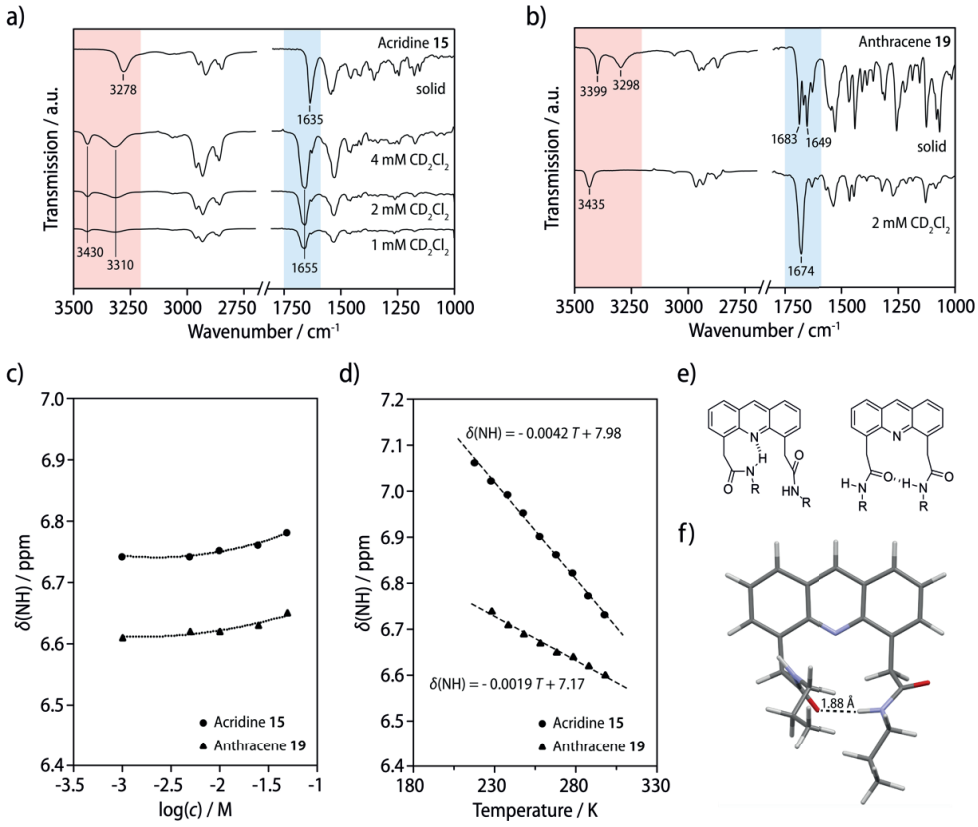

Figure 40. Solid-state and solution IR spectra of *a)* the acridine di(hexylamide) **15** and *b)* the anthracene di(propylamide) **19** reveal that acridine diamides form an intramolecular hydrogen bond in solution while anthracene diamides do not. The amide A and I regions are highlighted in red and blue respectively. Chemical shifts of the amide ^{1}H NMR signals of **15** and **19** as a function of *c)* the concentration (room temperature, CD_2Cl_2) and *d)* the temperature (CD_2Cl_2, c = 1 mmol/L). *e)* Different types of intramolecular hydrogen bond for **15** in solution. *f)* Energetically favored hydrogen-bonded conformation in DCM according to DFT calculation on acridine **14** (wB97X-D/Def2-SVP).

This intramolecular hydrogen bond is hence significantly weaker, and the small H · · · O=C angle of 125 ° indicates a more dipolar character than what is typical for the almost linear N–H · · · O=C hydrogen bonds in a β-sheet. Therefore, although the templated intrastrand distance of about 4.8 Å appeared to be large enough to accommodate *intramolecular* hydrogen bonds,[164-167] the strands need to be tilted with respect to the aromatic core to achieve a linear intramolecular N–H · · · O=C. This results in a shorter *effective* intrastrand distance of about 4.5 Å, and hence explains why the strong and almost linear *intermolecular* hydrogen bonds are preferred in the solid state (Figure 38*c*). The fact that the anthracene derivative **19** neither gives rise to weak intramolecular hydrogen bonds in solution nor shows a similar, strong intermolecular hydrogen bonding in the solid state can probably be attributed to the steric hindrance induced by the central anthracene C–H group.

5.4 Synthesis and Characterization of Polyamides Compring U-turn Units

We prepared the polyamides **PA6Acr**, **PA8Acr**, **PA10Acr**, and **PA12Acr** by solution-phase polycondensation of the active ester monomer **13** with 1,6-hexanediamine, 1,8-octanediamine, 1,10-decanediamine and 1,12-dodecanediamine, respectively (Scheme 15).[40-42]

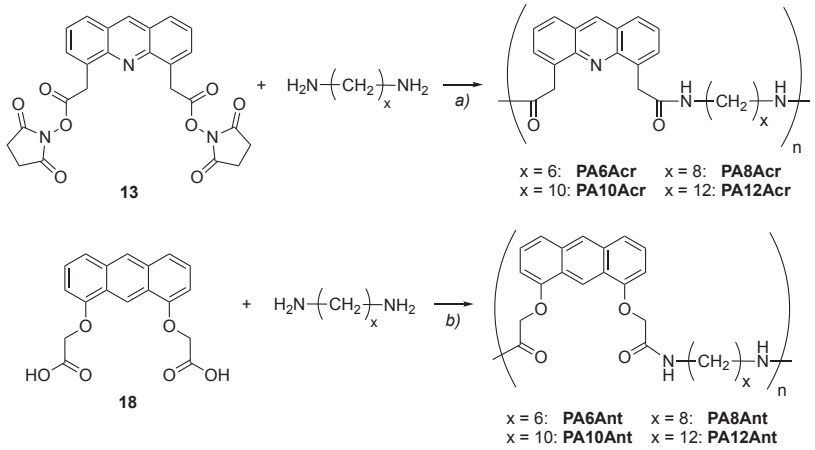

Scheme 15. Synthesis of the polyamides **PA*x*Acr** and **PA*x*Ant** (*x* = 6, 8, 10, 12). *Reagents and conditions: a)* DMSO, 120 °C, 2 h, 75–85%. *b)* TPP, LiCl, pyridine/NMP (1:4), 120 °C, 4 h, 60–75%.

The *N*-hydroxysuccinimide side product was readily soluble in water, which greatly simplified work-up. The advantage of this approach over Yamazaki-Higashi polycondensations using the

free carboxylic acid is that it does not require an activating agent that may suffer from competition by the acridine. As this was not an issue with the anthracene-based monomers, we synthesized the polyamides **PA6Ant**, **PA8Ant**, **PA10Ant**, and **PA12Ant** by direct polycondensation of the anthracene dicarboxylic acid **18** with the same aliphatic diamines using Yamazaki-Higashi conditions (Scheme 15).[31-36]

The successful conversion was proven by ^{1}H NMR spectroscopy (Appendix) as well as solid-state IR spectroscopy (Figure 41). In the series **PA*x*Acr**, the absorptions associated with the monomer **13** at 1807 (ν(C=O) of ester), 1778 (ν_s(C=O) of NHS), 1729 (ν_{as}(C=O) of NHS), 1361 (ν_s(C-N-C)), 1196 (ν_{as}(C-N-C)) and 1063 cm^{-1} (ν(N-C-O) of NHS)[240,241] were no longer present after polycondensation (Figure 41*a*). Likewise, the IR absorptions of the anthracene dicarboxylic acid **18** at 3300–2600 cm^{-1} (ν(O–H) of carboxylic acid) and the sharp band at 1729 cm^{-1} (ν_s(C=O) of carboxylic acid) were absent after polycondensation (Figure 41*b*).

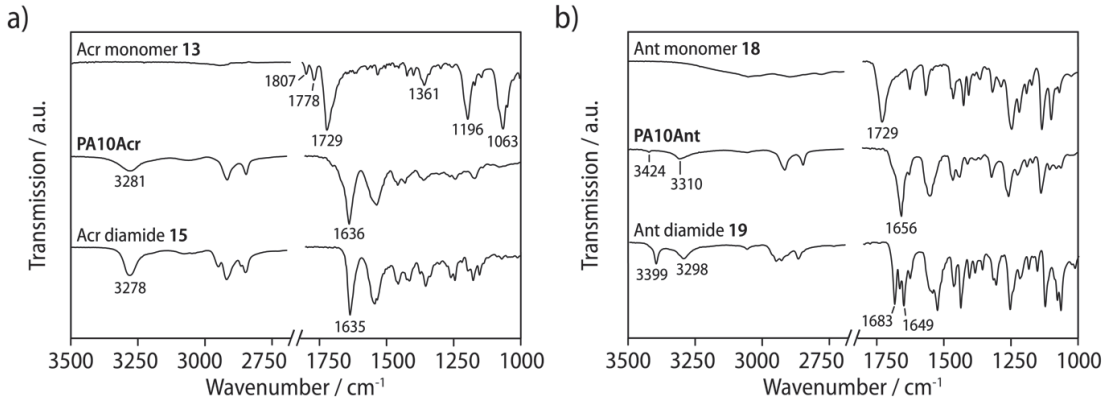

Figure 41. IR spectra of the U-turn polyamides *a)* **PA10Acr** and *b)* **PA10Ant**, chosen as representative examples for the **PA*x*Acr** and **PA*x*Ant** series respectively, along with their corresponding starting monomers (top) and diamide model compounds (bottom).

Gel permeation chromatography (GPC) gave number average molecular weights (M_n) in the range 9,000–12,000 for both series (Table 9), which is close to typical values for commercially available semiaromatic polyamides. The observed dispersities of $Đ$ = 1.30–1.84 can be attributed to the removal of small macrocycles and short oligomers during workup, which also explains the yields of 80–90% and 65–75% for **PA*x*Acr** and **PA*x*Ant** after purification. Mainly macrocyclic species with m/z ≤ 3,500–4,000 were detected in MALDI-TOF reflection mode. All polyamides were

insoluble in most common organic solvents but partially soluble in hot dimethyl sulfoxide (DMSO) and well soluble in 1,1,1,3,3,3-hexafluoropropane-2-ol (HFIP).

Table 9. Number average and weight average molar masses (M_n and M_w), and dispersities ($Đ$) determined by GPC for the polyamides **PA*x*Acr** and **PA*x*Ant** (x = 6, 8, 10, 12).

Polyamide	M_n / g/mol	M_w / g/mol	$Đ$
PA6Acr	10,100	13,200	1.30
PA8Acr	9,400	12,000	1.27
PA10Acr	9,400	12,800	1.35
PA12Acr	10,100	14,800	1.46
PA6Ant	12,400	20,300	1.64
PA8Ant	11,700	21,500	1.84
PA10Ant	11,900	20,400	1.72
PA12Ant	9,800	15,000	1.53

The solid-state IR spectra of the acridine-based polyamides **PA*x*Acr** revealed the characteristic polyamide amide A and amide I absorptions at 3281 and 1636 cm^{-1}, respectively, which also clearly proved the presence of infinite, resonance-enhanced arrays of N–H · · · O=C hydrogen bonds. It is worth noting that these are very similar in position and shape compared to the ones associated with the acridine model compound **15**, indicating a similar packing and hydrogen bonding pattern in the solid state (Figure 41*a*), which is relevant for relating the crystal structure of the latter to the bulk structure of the corresponding polyamides (vide infra). By contrast, the amide A and amide I bands of the anthracene-based polyamides **PA*x*Ant** in the solid state were detected at 3310 and 1656 cm^{-1}, respectively (Figure 41*b*). These bands were different from the model compound **19**, and moreover suggest weaker and less defined hydrogen bonding in these latter polyamides, as does the additional weak amide A absorption at 3424 cm^{-1} that can be assigned to non-aggregated amide groups.

UV-vis and fluorescence spectroscopy were used to further investigate the packing of the polyamides in the solid state and in solution in comparison with that of the respective model compounds. As the low solubility of the polyamides in common organic solvents made it necessary to use HFIP (pKa = 9.3) for the solution measurements on the polyamides, the acridine-based

polyamides became partially protonated. This is reflected by a broad shoulder centered at about 410 nm in the absorbance spectrum of **PA6Acr**, resulting from a shift in the first electronic transition (π-π^*, ^1L_a) from 356 to 445 nm (Figure 42*a*).[242-245]

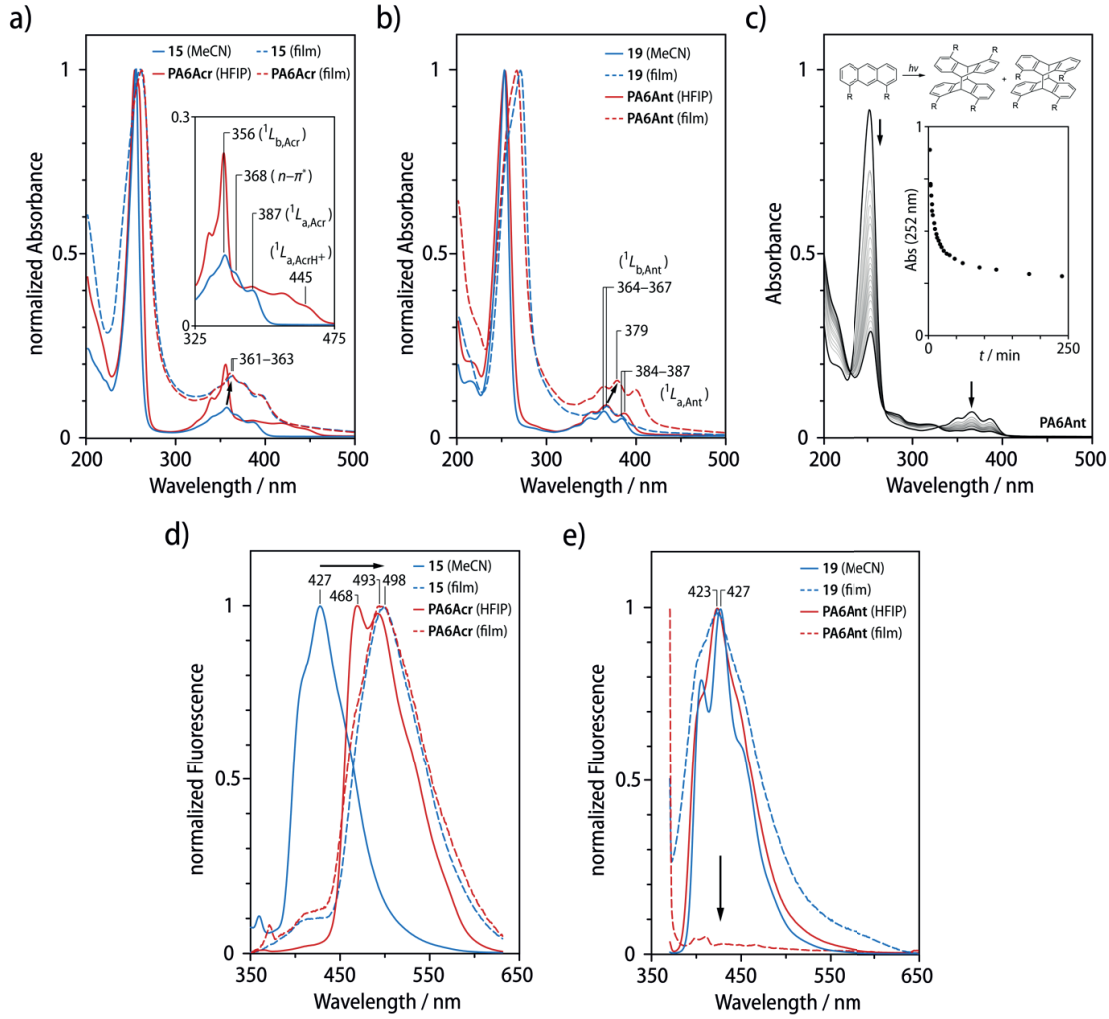

Figure 42. *a)* Normalized absorption spectra of *a)* **PA6Acr** and *b)* **PA6Ant** with respect to their model compounds **6** and **10** in solution (solid lines) and films spin-coated onto quartz substrate (dotted lines). The insert in *a)* shows a zoom of the visible region of the solution spectra with all the characteristic electronic transitions of the acridine moiety (Acr). *c)* Photodimerization experienced by **PA6Ant** at room temperature in an HFIP solution (20 μM) upon excitation at 380 nm. The insert shows the decay of the main absorption peak over time ($t_{1/2}$ = 16 min). Emission spectra for *d)* **PA6Acr** and *e)* **PA6Ant** with respect to their model compounds **15** and **19** in solution (solid lines) and films (dashed lines) made from dispersions in PMMA matrix, recorded at an excitation wavelength of 350 and 365 nm respectively.

Thin films prepared from the acridine model compound **15** and **PA6Acr** both retained the electronic structure of the non-protonated, small molecule in solution, with a weak solid-state

red-shift in each case (5–7 nm). The electronic states of the anthracene-based compounds were found to be similar to those of their nitrogen-containing analogues, with the obvious absence of any *n*-π^* transition (Figure 42*b*). However, whereas the **PA6Ant** film displayed a solid-state red shift (12–15 nm), the model compound **19** did not. As expected from literature,[246-249] the anthracene core was photosensitive towards a [4+4] dimerization that occurred within minutes, even at low excitation energies (Figure 42*c*). The intensity maximum in the fluorescence emission spectra of films of **15** and **PA6Acr** was red-shifted in both cases by about 70 nm as compared to the non-protonated model compound, which we attributed to the formation of excimers (Figure 42*d*). On the other hand, **PA6Ant** and anthracene compound **19** were found to show similar fluorescence in solution, but the polyamide exhibited a strong fluorescence quenching when dispersed in a PMMA film (Figure 42*e*). A possible explanation for this is the photodimerization of the anthracene moieties.

In combination with IR spectroscopy, optical spectroscopy hence provided additional evidence that the acridine-based polyamides **PA*x*Acr** exhibited a packing very similar to the acridine model compound **15**. One must hence conclude that the majority of the polymer chains in the polyamides **PA*x*Acr** assume a folded structure in the solid state that is structurally related to the β-serpentine folds in amyloids, stabilized by infinite arrays of intermolecular hydrogen bonds and π-π interactions between the acridine cores in the crystalline state. This is not the case in the anthracene-based polyamides **PA*x*Ant** that only give rise to weak hydrogen bonds in the solid state.

5.5 Microstructure of the Polyamides

Wide-angle X-ray scattering (WAXS) patterns of as-synthesized powders of the polyamides **PA*x*Acr** and **PA*x*Ant** showed well-defined Bragg peaks in all cases, superposed on an amorphous background (Figure 43*a*, *b*). The latter was estimated to account for 70–80% of the total scattered intensity, implying degrees of crystallinity of 20–30%. The overall shape of the WAXS patterns within each series varied little with *x*, qualitatively suggesting a similar packing. In the case of the acridine-based polyamides **PA*x*Acr**, the lowest angle peaks were identified as second order reflections associated with a *d*-spacing in the range approximately 23–31 Å, depending on *x*. The

increments in *d*-spacing on incrementing *x* by 2 were roughly consistent with the orthorhombic polyethylene unit cell *c* repeat distance of 2.55 Å, i.e. two CH_2 units in an extended conformation (Figure 43*c*).

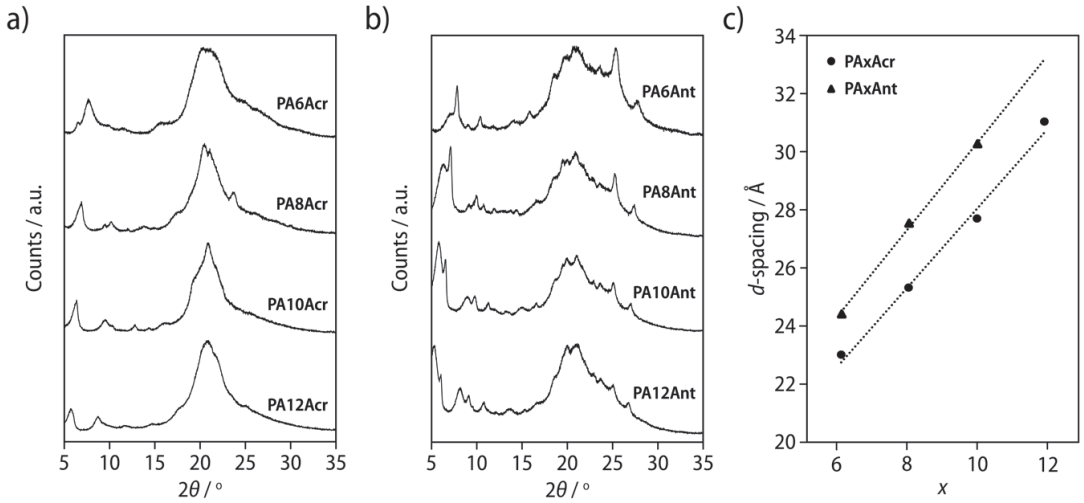

Figure 43. *a)* WAXS powder patterns for **PA*x*Acr**; *b)* WAXS powder patterns for **PA*x*Ant**. *c)* Implied lamellar repeat distance in **PA*x*Acr** and **PA*x*Ant** as a function of *x*.

Based on the conformation and the packing of the model compound **15** and consistent with the solid-state IR results, we constructed a model triclinic unit cell for **PA8Acr** as a representative example of the series, in which stacks of the molecules in an almost planar β-serpentine conformation constitute lamellae stabilized by intermolecular hydrogen bonds (Figure 44*a*, *b*). Further stacking of the lamellae accounted for the low-angle Bragg peaks, which were hence identified with the lamellar repeat distance. After energy minimization and unit cell optimization using the generic Dreiding forcefield, the intermolecular hydrogen bond distances, *d*(H···A) were found to be approximately 1.90 Å, and the alkyl chains showed pseudo-hexagonal packing similar to that in model compound **15**. This packing could be represented by a monoclinic $M_{||}$ sub-cell with a_s = 4.66 Å, b_s = 4.57 Å, c_s = 4.57 Å and γ = 109 °, which are close to the sub-cell dimensions reported for certain fatty acids.[250]

A WAXS powder pattern was calculated from the energy-minimized model assuming uniform crystal dimensions of 200 Å in order to simulate the broadening of the experimental Bragg peaks (Figure 44*c*). Similar features were seen in the amorphous background-subtracted experimental

WAXS pattern obtained for **PA8Acr** (a fit to the background was obtained by adjusting the width and amplitude of two broad Gaussian peaks centered at 2θ = 20.8 and 23.5 °, corresponding to *d*-spacings of 4.27 and 3.78 Å respectively). Although the diffraction data were insufficiently well resolved to permit further refinement, the experimental peaks at 2θ = 20–21 ° were inferred from the model structure to be associated with the lateral spacing of the alkyl chains, while the peaks at 2θ = 23–25 ° were associated with the intermolecular spacing perpendicular to the *c* axis.

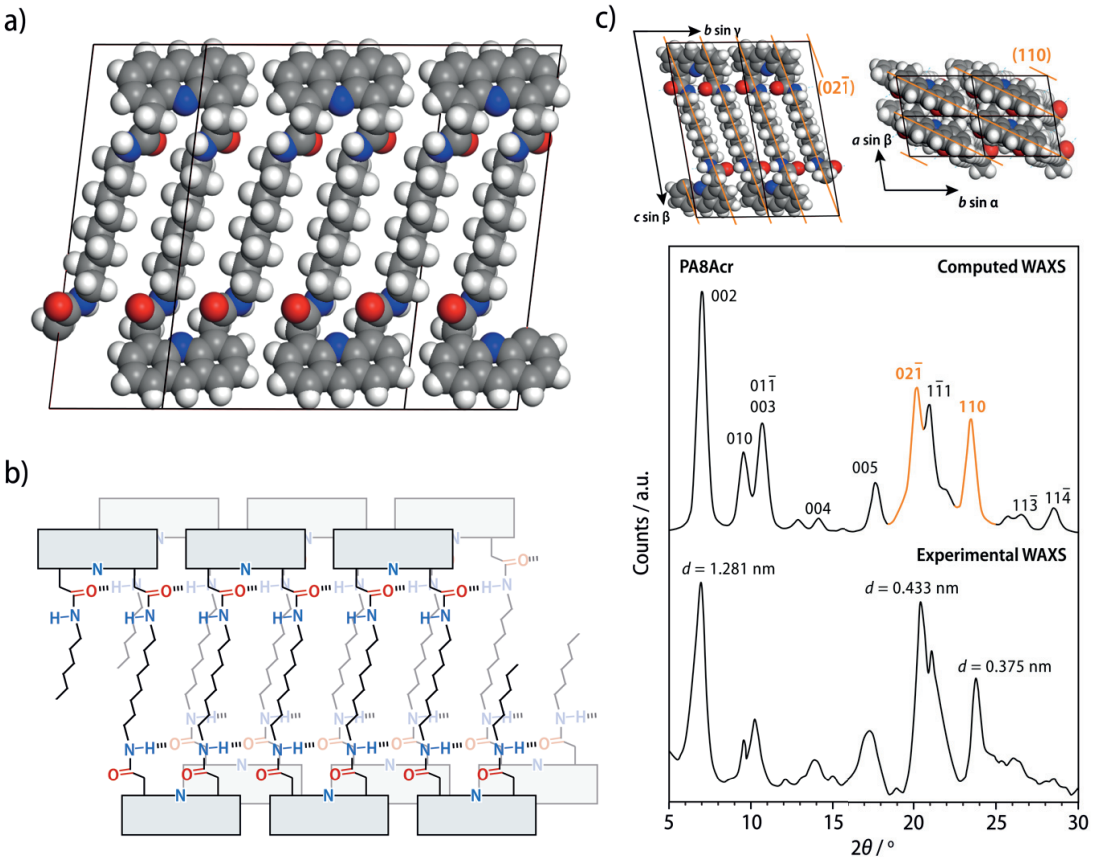

Figure 44. *a)* Model triclinic $P\bar{1}$ unit cell for **PA8Acr** with intermolecular hydrogen bonding, viewed perpendicular to (110) (a = 4.58 Å, b = 9.48 Å, c = 26.02 Å, α = 80.50 °, β = 90.85 °, γ = 101.00 °). *b)* Schematic representation of the intermolecular hydrogen bonds in between consecutive 2D serpentine structures. *c)* Comparison of the background-subtracted experimental diffraction pattern for **PA8Acr** and computed WAXS powder diffraction pattern for **PA8Acr** based on the model structure. The peaks corresponding to the lateral spacing of the alkyl chains and the intermolecular spacing perpendicular to the c-axis are highlighted in orange and depicted above the WAXS patterns.

Hence, our WAXS results clearly demonstrate that the acridine-based polyamides **PA8Acr**, different from typical semiaromatic polyamides with a high content of kinked repeating units such as PA6I, are not amorphous but semicrystalline. Moreover, the good fit between the measured and

computed WAXS powder diffraction patterns of **PA8Acr** proves that this is possible because the acridine-based repeating units template the formation of β-serpentine folds in the crystalline state. Our results thus furthermore imply that, very different from typical semicrystalline aliphatic or semiaromatic polyamides, the acridine-based polyamides **PA8Acr** exhibit crystalline lamellae with extensive re-entrant chain folding stabilized by intermolecular hydrogen bonds.

By contrast, the poor resolution of the WAXS data and significant disparities between the solid-state IR data for the model compound **19** and **PAxAnt** and also between those for **PAxAnt** and **PAxAcr** (Figure 41), made *a priori* assumptions about the crystalline conformations of **PAxAnt** hard to justify. Moreover, the multiplicity of the low angle WAXS peaks suggested more than one crystalline phase to have been present in the as-synthesized **PAxAnt**.

5.6 Thermomechanical Properties of the Polyamides

Differential scanning calorimetry (DSC) heating scans (Figure 45*a*) from the **PA*x*Ant** series showed clear melting peaks, whose maximum was taken to define the melting temperature, T_m, and a corresponding crystallization peak (T_c) upon cooling from temperatures immediately above T_m in each case. A glass transition temperature (T_g) was also visible in the heating scans for the lowest *x*. Both T_m and T_g decreased with increasing *x*, while T_c passed through a minimum at $x = 10$ (Figure 45*b*). Moreover, for the lowest *x*, the crystallization enthalpies (ΔH_c) determined from the cooling scans were significantly lower than the enthalpies corresponding to the main melting peaks (ΔH_m), and a cold crystallization peak was observed during the second heating step. A mass loss of 1–2% was already apparent from thermal gravimetric analysis (TGA) of **PA*x*Ant** in the temperature range 260–300 °C at the same heating rate in nitrogen (Figure 45*c*), which accelerated sharply above 300 °C. The DSC data in and beyond this temperature range must hence be assumed to be strongly influenced by thermal degradation. The DSC data of the **PA*x*Acr** series showed similar trends, but the melting and crystallization peaks were less well defined (Figure 45*d*, *e*). As for the **PA*x*Ant** series, a mass loss of 1–2% was already observed on the thermal gravimetric analysis (TGA) of **PA*x*Acr** above 250–260 °C, which again accelerated sharply above 300 °C (Figure 45*f*).

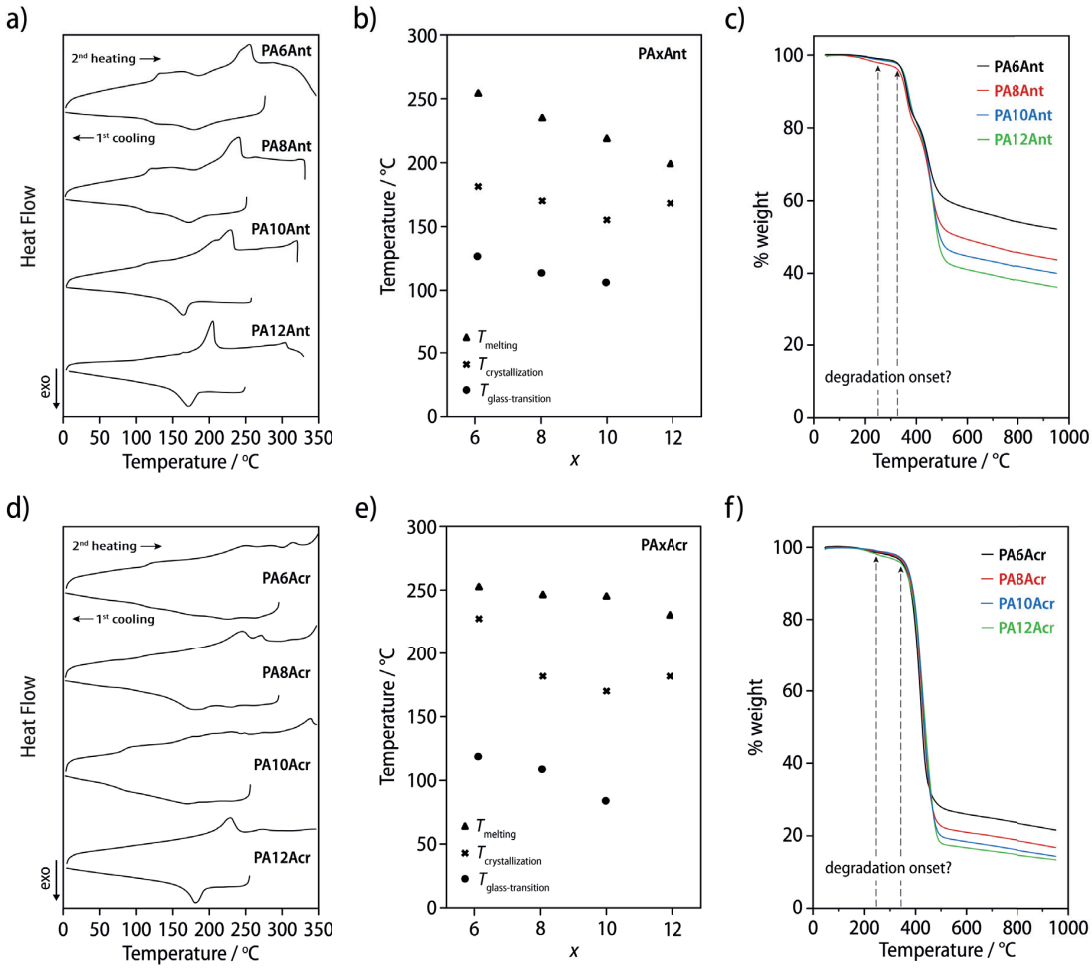

Figure 45. *a)* First cooling and second heating scans from **PA*x*Ant** measured by DSC in nitrogen. *b)* T_g, T_m and T_c in **PA*x*Ant** as a function of *x*. *c)* TGA scans of **PA*x*Ant** in nitrogen. *d)* First cooling and second heating scans from **PA*x*Acr** measured by DSC in nitrogen. *e)* T_g, T_m and T_c in **PA*x*Acr** as a function of *x*. *f)* TGA scans of **PA*x*Acr** in nitrogen. The scanning rate was set at 10 K/min for each measurement.

Nanoindentation measurements (Figure 46*a*) performed on films of the polyamides **PA*x*Acr** and **PA*x*Ant** (*x* = 8, 10, 12) prepared in a hot press just below the melting temperature showed that all polyamides (except for **PA12Ant**) exhibited a hardness in-between those of the aliphatic PA610 and the semiaromatic PA6TI, which decreased with an increasing length of the aliphatic segments (Figure 46*b*). Interestingly, the hardness measured for the acridine-based polyamides **PA*x*Acr** reached up to 320 MPa and was consistently 15–50 % higher than for the corresponding anthracene-based polyamides **PA*x*Ant**. Since hardness correlates with the microstructure and crystalline morphology, this can probably be attributed to the tight arrangement of the polymer chains due to chain folding and stronger intermolecular hydrogen bonds in **PA*x*Acr** versus

PA*x*Ant. Moreover, all polyamides **PA*x*Acr** and **PA*x*Ant** (except for **PA12Ant**) exhibited instrumented elastic moduli that were 50–75 % higher than that of PA610 and reached up to 3.6 GPa in the case of both **PA10Acr** and **PA10Ant** (Figure 46*c*), reaching the instrumented elastic modulus of PA6TI.

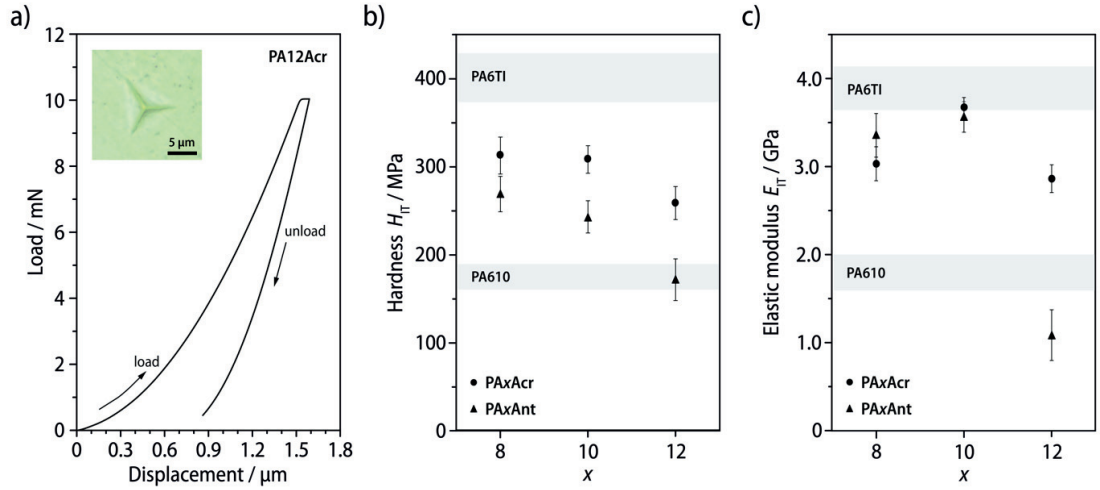

Figure 46. Nanoindentation measurements performed on hot-pressed films of **PA*x*Acr** and **PA*x*Ant** (x = 8, 10, 12). *a)* Typical loading-unloading curve obtained for each nanoindent (shown in the insert). *b)* Instrumented hardness (H_{IT}) and *c)* instrumented elastic modulus (E_{IT}) of both polyamide series as a function of x. The instrumented hardness and elastic modulus of commercial aliphatic PA610 and semiaromatic PA6TI are given as references.

5.7 Conclusion

In summary, we successfully synthesized novel U-turn monomers based on acridine and anthracene cores to template chain folding in semiaromatic polyamides. We used a detailed comparison of the IR, UV-vis, and fluorescence spectra, as well as WAXS data of the acridine-based polyamides **PA*x*Acr** to the spectra and the single-crystal X-ray structure of the corresponding model compound **15** to conclude that the majority of the polymer chains in the polyamides **PA*x*Acr** assumed a folded structure in the solid state that was structurally related to the β-serpentine folds in amyloids. Contrary to other semiaromatic polyamides with kinked repeating units that are amorphous, the use of U-turn monomers apparently does not impede crystallization. The polyamides **PA*x*Acr** exhibited a lamellar crystalline morphology with extensive re-entrant chain folding, which is usually not observed in semiaromatic polyamides. This structure was stabilized by infinite arrays of intermolecular hydrogen bonds and π-π

interactions between the acridine cores in the crystalline state. The acridine-based polyamides were found to exhibit a modulus comparable to other semiaromatic polyamides as were harder and stiffer than the very similar anthracene-based polymers **PA*x*Ant** that do not show chain folding due to steric repulsion in the required conformation. While the extensive re-entrant chain folding observed in the polyamides **PA*x*Acr** probably renders them brittle materials in macroscopic tensile testing, further efforts should be devoted to the melt-blending of such U-turn polyamides with aliphatic polyamides at temperatures below their degradation temperature, with the aim to produce copolyamides with a tailored degree of re-entrant chain folding.

6

Conclusions and Outlook

6 Conclusions and Outlook

In the present thesis, we followed two complementary approaches to improve the strain at break and toughness of semiaromatic polyamides and their composites, without inducing adverse consequences for their strength and stiffness. In an engineering-driven approach suitable for industrial scale-up, we prepared semiaromatic copolyamides and glass fiber-reinforced composites by high temperature extrusion of commercially available semicrystalline polyamides.

- We found that the semiaromatic PA6TI produced homogeneous random copolyamides upon high-temperature melt blending with the more ductile aliphatic polyamides PA66 and PA610, owing to rapid and efficient transamidation occurring under those conditions. By contrast, the use of the more hydrophobic PA12 resulted in phase segregation, particularly at high contents of the aliphatic component.
- The incorporation of up to 30 *wt*% of PA66 or PA610 in PA6TI resulted in an unprecedented five-fold increase of the strain at break compared to that of pure PA6TI, from 10 to 50%, inducing almost no change in stiffness (3.6 GPa) and only a minor loss in strength (from 140 to 110 MPa). The same trend was observed in their composites reinforced with up to 50 *wt*% glass fibers.
- We were able to attribute this beneficial effect on the mechanical properties to the microstructure of the materials, where the lamellar crystalline domains continue to be predominantly formed by PA6TI even at substantial aliphatic contents. However, the replacement of terephthalic acid by adipic or sebacoic acid units at the crystalline-amorphous interface resulted in surface defects that, combined with the increase in mobility in the unconstrained regions of the amorphous phase, overall explained the improved ductile behavior and maintained stiffness.

In a chemistry-driven approach inspired by the crucial role of polymer chain folding in silk materials, we designed and synthesized three rigid aromatic monomers to potentially induce re-entrant chain folding in bulk semiaromatic polyamides and study the effect of folding on their mechanical properties. Using aliphatic diamines of various lengths, we successfully synthesized several semiaromatic polyamide by solution polycondensation.

- The kinked 2,9-disubstitued benzofurobenzofuran core strictly furnished amorphous polyamides, while the use of the 4,5-disubstituted acridine and the 1,8-disubstitued anthracene derivatives, which were designed to result in "U-turn" folds, resulted in semicrystalline polymers.
- We demonstrated that the acridine-based polyamides assumed folded conformations in the crystalline state that were reminiscent of β-serpentine folds and were further organized into lamellar crystals with extensive re-entrant chain folding, stabilized by intermolecular hydrogen bonding and π-π interactions.
- These acridine-based polyamides exhibited a modulus comparable to other semiaromatic polyamides and were harder and stiffer than the similar anthracene-based polymers that did not show chain folding due to steric repulsion in the required conformation.

However, several interesting aspects still need to be addressed in future work:

- It would be important to complement the characterization of the mechanical properties of the materials by nanoindentation with an investigation of the macroscopic properties by tensile testing. This will, first of all, require the scale-up of the synthesis of the anthracene and acridine-based monomers and corresponding semiaromatic polyamides. The polyamides with longer diamines, such as decyl or dodecyl amine, would be preferred in this regard, in order to produce materials with an as low as possible melting temperature, so that thermal degradation during melt processing can be avoided.
- The high-temperature melt blending and injection molding of these "U-turn" polyamides with commercially available aliphatic polyamides having "compatible" chemical structures, hydrogen bonding patterns, and crystalline structures, such as PA1212 or PA1010, should result in random copolyamides. Mechanical testing of these copolyamides would be a test for our hypothesis that the formation of crystalline domains with a tailored degree of re-entrant chain folding may result in materials with maintained strength and stiffness but enhanced ductility and toughness.

7

Experimental Part

7 Experimental Part

7.1 Instrumentation and Methods

Materials. All materials and solvents for reactions were purchased from commercial suppliers and used without further purification. Chromatography solvents were purchased as reagent grade and distilled once prior to use. The progress of reactions was monitored by thin-layer chromatography (TLC) on Merck TLC plates (Silica gel 60 F_{254}) using eluents of various polarities. UV light (254 nm) was used for detection of compounds on the TLC plates.

Melt Compounding of Polyamide Blends. All the commercial polyamides used in this work were provided by EMS Chemie AG and stored in vacuum for at least 48 h before processing. Poly(hexamethylene adipamide) (PA66, M_n = 21'000 g/mol, M_w = 41'000 g/mol), poly(hexamethylene sebacoamide) (PA610, M_n = 16'000 g/mol, M_w = 32'000 g/mol), and poly(laurolactam) (PA12, M_n = 19'000 g/mol, M_w = 34'000 g/mol) were melt-compounded with poly(hexamethylene terephthalamide-co-isophthalamide) (PA6TI, M_n = 12'000 g/mol, M_w = 24'000 g/mol) in a co-rotating twin-screw micro-compounder (DSM Micro 5). The barrel temperature was set to 330 °C, and the polymers were compounded for about 20 min at a screw speed of 100 rpm. For the preparation of glass fiber reinforced composites, chopped staple glass fibers with a length of 4.5 mm and a diameter of 10 μm (Vetrotex 995, Saint Gobain) were fed into the micro-compounder at the same time as the polymer pellets. The barrel temperature was set to 330 °C in each case, and the polymers were compounded for about 20 min at a screw speed of 100 rpm. The molten material was transferred directly from the compounder to a reservoir pre-heated to 340 °C and injected (DSM Micro-Injection-Molding Machine, 5.5 ml shot volume) at 6 bars into a mold held at 180 °C to form dog-bone shaped tensile test bars with a 20 × 4 × 2 mm^3 gauge section. In order to ensure a similar thermal history, all the test-bars were annealed for 1 h at 180 °C under vacuum and stored at room temperature in vacuum before further testing and analysis.

Mass Spectrometry. High-resolution mass spectrometry was carried out using either a Waters Q-ToF Ultima for ESI or a Waters QTOF Xevo G2-S for APCI/APPI. The MALDI-TOF mass spectra of the polyamides were acquired in reflectron mode, using an Axima-CFR Plus (Shimadzu Biotech)

mass spectrometer, equipped with a nitrogen laser (λ = 337 nm, pulse width = 3 ns), operated in positive ion mode. The accelerating voltage was 20 kV, and the laser irradiance was maintained close to the instrument threshold. The specimens used for the MALDI analyses were prepared by mixing an appropriate volume of a solution of the polyamide (c = 3 mg/mL in HFIP) with a matrix solution of α-cyano-4-hydroxycinnamic acid (c = 10 mg/mL in THF) at volume ratios of 1:1 and 1:10 *v/v*. An aliquot of 1 µL of each analyte/matrix mixture was then placed onto the MALDI sample holder and allowed to dry slowly in air. For the melt-compounded copolyamides, the mass spectra were then compared to a reference sample obtained by solution-mixing 1 mL of a solution of the aliphatic polyamide in HFIP (c = 3 mg/mL) with 1 mL solution of PA6TI in HFIP (c = 3 mg/mL). The subsequent steps of the procedure were identical to what is descibed above for the polyamides.

Gel Permeation Chromatography (GPC). The number and weight average molecular weights, M_n and M_w, as well as the dispersity indices, $Đ$, of the polyamides and polyamide blends were determined using a 1260 Infinity GPC/SEC system (Agilent) with a refractive index detector and a column length of 650 mm (PSS PFG). 1,1,1,3,3,3-hexafluoropropane-2-ol (HFIP) was used as the eluent at a flow rate of 1 mL/min and temperature of 35 °C. Eight poly(methyl methacrylate) (PMMA) standards with molar masses between 2'000 and 100'000 g/mol and $Đ \leq 1.1$ were used for calibration. The polyamides, polyamide blends, and PMMA standards were all dissolved in neat HFIP (c = 3 mg/mL).

Differential Scanning Calorimetry (DSC). DSC measurements (TA Instruments Q100) were performed in nitrogen (50 mL/min) using specimens of about 5 mg and a scanning rate of 10 °C/min. T_g was defined as the half-height of the heat capacity step associated with the glass transition during heating scans (2nd heating); T_m was taken to be the temperature corresponding to the maximum in the melting endotherm (2nd heating); and T_c was taken to be the minimum in the crystallization exotherm observed during cooling. Estimating the total melting enthalpy, ΔH_m, required integration over a wide range of temperatures owing to the broadness of the endotherms observed in the polyamides and polyamide blends (2nd heating). Because the choice of baseline was ambiguous, an experimental error for ΔH_m was estimated from integrations carried out with a range of possible baselines. In cases where two distinct melting endotherms were observed,

both were included in the determination of ΔH_m. Fully amorphous reference specimens were prepared from dry films wrapped in aluminum foil that were molten on a hot plate, and then rapidly cooled by pressing them between blocks of aluminum pre-cooled in liquid nitrogen.

Preparation of Films Specimens by Solution Blending for DSC. Stock solutions (c = 20 mg/mL) of each polyamide were prepared by letting the polyamide dissolve overnight in HFIP. An aliquot of the stock solution of the aliphatic polyamide was then mixed with an aliquot of the stok solution of PA6TI, and the mixed solution was stirred for 20 min. Then, 1 mL of the mixed solution was evaporated in a small vial in air. The resulting films were finally dried overnight at 135°C in high vacuum.

Thermogravimetric Analysis (TGA). TGA measurements were conducted on a Perkin Elmer TGA 4000. Samples (5–10 mg) were dried in high vacuum at 80°C for 24 h, annealed in the TGA chamber at 110°C for 2 min and then heated from 30°C to 950°C at a scanning rate of 10°C/min in a flow of nitrogen (20 mL/min).

Atomic Force Microscopy (AFM). Thin slices of the melt compounded polymer blends with a thickness of 200–300 nm were prepared by ultramicrotomy with a diamond knife (Diatome). The sections were deposited on a flat glass substrate, melted at 350 °C and cooled in air to 180 °C. The resulting surface microstructure was observed by intermittent contact mode AFM (Bruker Nanoscope IIIa) with a MikroMasch NSC14 silicon probe (RMS free amplitude, A_0 = 2 V; set-point amplitude, A = 0.6 to 1.2 V).

Wide-Angle X-ray Scattering. Wide-angle X-ray scattering (WAXS) measurements were carried out with a PANalytical X'Pert Pro MPD diffractometer (CuKα, λ=1.54 Å) in Bragg-Brentano geometry. The X-ray tube was operated at 45 kV and 40 mA. Scanning was carried out from 15° to 30° (polyamide blends, BFBF-based polyamides) or from 5° to 30° (U-turn-based polyamides) 2θ angles using a fixed divergence slit of 0.25°, a step size of 0.0167° and a time per step of 120.015 s.

Selected-Area Electron Diffraction (SAED). SAED was carried out using an FEI Talos transmission electron micrsocope (TEM) equipped with a field emission gun and operated at 200 keV. In order to obtain fiber diffraction patterns, oriented thin films were friction deposited onto freshly cleaved crystals of KBr at about 10 K below the melting point and picked up on a carbon covered

TEM grid after dissolution of the KBr. Additional (hk0) patterns were obtained by recrystallizing thin sections obtained by ultramicrotomy (Leica EM UC7/Diatome 35 ° diamond knife) of the extrudates on carbon-covered TEM grids in nitrogen.

Small Angle X-ray Scattering (SAXS). SAXS was performed on 0.5 to 1 mm thick specimens mounted on a Kapton™ backing film, using a Rigaku S-MAX3000 pinhole camera with a CuKα X-ray source (Rigaku Innovative Technologies, Auburn Hills, USA). The specimens were maintained in vacuum at room temperature during the measurements. The scattering data are given as a function of the scattering vector modulus $q = 4\pi/\lambda \sin(\theta/2)$, where θ is the scattering angle and λ is the X-ray wavelength. The 1D correlation functions were obtained from the Fourier transform of the corresponding 1D SAXS intensity profiles $I(q)$. A short and long correlation distance were determined as described by Strobl and Schneider, providing estimates for the mean lamellar thickness, l, and lamellar long-period, L, respectively, assuming $l < L - l$.

Numerical Simulations. Crystalline supercells with and without defect units were generated using the Materials Studio graphics user interface based on the observed unit cell parameters for PA6TI and relaxed using classical force field-based energy minimization with the general purpose Dreiding force field[251] and the method of steepest descents with charge equilibration. Trial crystal structures for the acridine-based polyamides **PAxAcr** were generated *ad hoc* using the BIOVIA Materials Studio graphics user interface. Their geometry was then optimized with respect to all structural degrees of freedom subject to periodic boundary conditions, using classical force field-based energy minimization with the generic Dreiding force field[251] and the method of steepest descents with charge equilibration. Wide-angle X-ray diffraction patterns were simulated using the BIOVIA Reflex software package.

Tensile Testing. The tensile test bars were tested using a universal testing machine (Walter+Bai UTM) at a nominal strain rate of 10 % min^{-1}. The strain was measured using a clip-on extensometer with a gauge length of 20 mm, and the Young's modulus was calculated as the slope of the nominal stress-strain curve in the linear elastic regime (i.e. for strains ranging from 0% to 1%). A minimum of 5 specimens were tested for each material.

1D and 2D NMR Spectroscopy. ^{1}H and ^{13}C NMR spectroscopy was carried out at 298 K using a Bruker Avance III 400 spectrometer at frequencies of 400 MHz and 100 MHz respectively. The

spectra were calibrated to the residual solvent peaks of DMSO-d^6 (2.50 ppm ^{1}H NMR; 39.52 ppm ^{13}C NMR), CD_2Cl_2 (5.32 ppm ^{1}H NMR; 53.84 ppm ^{13}C NMR) or $CDCl_3$ (7.26 ppm ^{1}H NMR; 77.16 ppm ^{13}C NMR). ^{1}H-^{1}H correlation spectroscopy (COSY) and ^{1}H-^{13}C heteronuclear single-quantum correlation spectroscopy (HSQC) were recorded using the same instrument. Concentration-dependent ^{1}H NMR spectroscopy of model compounds **14** and **15** (1–50 mM in CD_2Cl_2) was carried out at 298 K on the same instrument. Temperature-dependent ^{1}H-NMR spectroscopy of model compounds **15** and **19** (1 mM in CD_2Cl_2, 298–218 K) was carried out using a Bruker Avance NEO 400 spectrometer equipped with a liquid Nitrogen cooling system at a frequency of 400 MHz. The ^{1}H NMR spectra of the polyamides were recorded at 298 K either in non-deuterated 1,1,1,3,3,3-hexafluoropropan-2-ol with acetone-d^6 as the internal standard (2.05 ppm in ^{1}H NMR) or in $CDCl_3$ containing 10 vol% of 1,1,1,3,3,3-hexafluoropropan-2-ol-d^2 (HFIP-d^2) and calibrated with the residual solvent peaks of $CDCl_3$ (7.26 ppm ^{1}H NMR).

Infrared Spectroscopy. Solid-state infrared (IR) spectra were recorded with a JASCO FT/IR 6300 spectrometer equipped with an ATR crystal. Solution-phase IR spectra were recorded on the same instrument using a cell mounted with two KBr windows. Second derivatives were calculated using Savitzky-Golay algorithm (second order polynomial, 21 points).

Optical Spectroscopy. Solution-phase UV-vis spectra in acetonitrile (MeCN) or 1,1,1,3,3,3-hexafluoropropane-2-ol (HFIP) using Hellma quartz cuvettes (1 cm path length) were recorded with a Jasco V-670 spectrometer. An excitation wavelength of 380 nm was chosen for photobleaching experiments on the polyamides, and absorption spectra of HFIP solutions (20 μM) were recorded at different times over 3–4 h. Thin films were investigated using the same instrument. Thin films of BFBF-based small molecules and polyamides were processed by drop-casting 1–2 mL of a stock solutions (0.1 mg/mL in HFIP) onto a quartz substrates. Thin films of acridine or anthracene-based model compounds and polyamides were prepared by spin-coating 100 μL of a stock solution (5 mg/mL in HFIP) onto a quartz substrate (5000 rpm, 1 min). Solution-phase fluorescence emission spectra of the acridine and anthracene derivatives were recorded on a Jasco FP-6500 spectrofluorometer in MeCN or HFIP using Hellma quartz cuvettes (1×1 cm^2) with excitation wavelengths of 350 and 365 nm respectively. For solid-state fluorescence spectra, films of comprising solid particles of the compounds dispersed in a PMMA matrix were prepared

by from dispersions that had been obtained from placing 5 mg of the specimen in 5.2 g of a 17% *w*/*v* solution of PMMA in toluene under strong magnetic stirring. These dispersions were cast onto transparent polyester substrates (Byko-Charts, BYK Gardner, USA) using a doctor blade. The films were left to dry in air for 90–120 min and were further dried in high vacuum for 2 d after detachment from the substrate. The emission spectra of such films with a thickness of about 600 μm were recorded with a Horiba Jobin Yvon FluoroMax-3.

X-ray Structure Analysis. Single-crystal X-ray diffraction of compounds **6** and **8** was performed at low temperature [140(2) K] and [100(2) K], respectively, using Cu *K*α radiation on a RigakuSuperNova dual system equipped with an Atlas CCD detector. The datasets were reduced and corrected for absorption with CrysAlisPro.[252] The solution and refinement for the structures were performed by SHELXT[253] and SHELXL-2016 (release 6),[254] respectively. The crystal structures were refined using full-matrix least-squares based on F^2 with all non-hydrogen atoms anisotropically refined. The hydrogen atoms were found in the difference map and their positions were refined in the case of **8**. In the crystal structure of **6**, the hydrogen atoms attached to the carbon atoms were placed in calculated positions by means of the "riding" model. The structure of **6** includes three ethanol solvent molecules in the asymmetric unit which one is disordered over two positions. The atoms of each orientation were identified in the difference Fourier map. The major and minor parts were refined anisotropically, but distance and similarity restraints (DFIX and SIMU) had to be applied for a convergent least-square refinement, yielding site occupancy ratios of 0.736(5) / 0.264(5). The Bragg intensities of compounds **15** and **19** were measured at low temperature [100(2) K] using Cu *K*α radiation with a Rigaku SuperNova dual system equipped with an Atlas CCD detector. The data sets were reduced and corrected for absorption with CrysAlisPro. [252] Solution and refinement of the crystal structures were performed using SHELXS,[255] SHELXT[253] and SHELXL-2017[254] (release 1). The structures were refined using full-matrix least-squares based on F^2 with all non-hydrogen atoms defined anisotropically. The hydrogen atoms in compounds **15** and **19** were located from the difference map and their positions refined freely.

Computations. The DFT computations on the proxy molecule **9** were performed using the Turbomole 7.1 package.[256] Ground state geometries were optimized at the PBE[257] level using the

def2-SVP[258,259] basis set. Excitation energies were computed both at the ADC(2)[260,261] and at the TD-PBE0[262] level within the Tamm-Dancoff approximation. In the ADC(2) computations, the resolution of identity and the frozen core approximation were employed. The density differences were visualized with the Avogadro[263] software package. The structure of acridine **14** has been optimized with the ωB97X-D[264] density functional, combined with the def2-SVP basis set.[265] The structural relaxation has been performed with implicit solvation (SMD model,[266] solvent: dichloromethane). Harmonic thermochemical corrections were computed by a Hessian computation on the fully relaxed structure.

Thin Film Transistors. Thin film transistors were fabricated in top- as well as bottom-contact configuration. In all cases, silicon wafers with a 100 nm thermal SiO_2 layer served as substrates. The silicon was used as common gate electrode, and the SiO_2 as the dielectric. Bottom source/drain electrodes were lithographically patterned, top contacts were patterned via shadow masks. In all cases, gold was used as the electrode material. The BFBF polyamide and the model compounds **7** and **8** were spin-coated or drop-cast onto the substrates from HFIP (**8**, **PA6B**) or toluene (**7**) solution. The devices were electronically characterized in the inert atmosphere of a glovebox with a Keithley 4200 parameter analyzer.

7.2 Synthtesis Procedures and Analytical Data for Compounds

***cis*-5a,10b-dihydro-2,9-dimethylbenzofuro[2,3-*b*]benzofuran 1.** The synthesis of compound **1** was adapted from literature.[208] A three-neck round-bottom flask was fitted with a reflux condenser and a dropping funnel. Glyoxal sodium bisulfite (28.4 g, 0.100 mol) and *p*-cresol (21.6 g, 20.9 mL, 0.200 mol) were suspended in a mixture of H_2O (320 mL) and acetic acid (150 mL). The mixture was then heated at 85°C and concentrated sulfuric acid (96%, 140 mL) was then slowly added dropwise to the obtained solution over 3 h under strong stirring. After cooling to room temperature, the obtained green precipitate was filtered off and washed with water and EtOH until the product turned white. Drying the product in vacuum afforded pure **1** (8.42 g, 35% yield).

^{1}H NMR (400 MHz, DMSO-*d*^{6}): δ = 7.35 (d, *J* = 1.9 Hz, 2H), 6.99–6.91 (m, 3H), 6.76 (d, *J* = 8.1 Hz, 2H), 5.07 (d, *J* = 6.7 Hz, 1H), 2.24 (s, 6H) ppm. ^{13}C NMR (101 MHz, DMSO-*d*^{6}): δ = 155.14, 130.64, 128.90, 127.65, 124.85, 112.55, 109.05, 49.33, 20.38 ppm. HRMS (ESI): calcd for $C_{16}H_{15}O_2$ ([M+H]$^+$): 239.1072; found: 239.1079.

Benzofuro[2,3-*b*]benzofuran-2,9-dicarboxylic acid 2. The benzofurobenzofuran diester **5** (0.68 g, 2.1 mmol) was suspended in a THF/water solution (100 mL, 4:1) before addition of LiOH (0.41 g, 17 mmol, 8 equiv.). The mixture was then heated to reflux for 3 h. After cooling the solution to room temperature, the THF was removed under reduced pressure, and the residue was diluted with more water (80 mL). The aqueous solution was acidified to pH 1 with HCl (6 M), and the resulting yellow precipitate was filtered and washed with water as well as Et_2O until the complete disappearance of the yellow color. After drying in vacuo, the dicarboxylic acid **2** was obtained as a white powder and used without further purification (0.55 g, 89% yield).

^{1}H NMR (400 MHz, DMSO-*d*^{6}): δ = 13.05 (s, 2H), 8.80 (s, 2H), 7.99 (d, *J* = 8.6 Hz, 2H), 7.88 (d, *J* = 8.7 Hz, 2H) ppm. ^{13}C NMR (101 MHz, DMSO-*d*^{6}): δ = 167.19, 166.39, 157.31, 127.54, 125.17, 122.68, 122.13, 112.58, 96.83 ppm. HRMS (MALDI): calcd for $C_{16}H_7O_6$ ([M_2-H]$^-$): 591.0564; found: 591.0556.

***cis*-5a-hydro-10b-hydroxybenzofuro[2,3-*b*]benzofuran-2,9-dicarboxylic acid 3.** Compound **1** (8.40 g, 35.3 mmol) was suspended in a pyridine/water mixture (340 mL, 10:7) in a three-neck round-bottom flask equipped with a reflux condenser. The suspension was heated to 90°C, and then $KMnO_4$ (66.8 g, 0.424 mol, 12 equiv.) was added carefully and portionwise over 30 min. The temperature was then raised to 120°C, and reflux was continued for 5 h. After cooling, the formed MnO_2 was filtered off, and the filtrate was acidified to pH 1–2 with concentrated HCl (37%, 400 ml). The precipitated crude product was filtered off, washed with water, and recrystallized from EtOH/H_2O (300 mL, 1:1) to afford pure **3** (8.75 g, 86% yield) as white crystals.

^{1}H NMR (400 MHz, DMSO-*d*^{6}): δ = 12.92 (s, 2H), 8.18 (d, *J* = 1.9 Hz, 2H), 7.88 (dd, *J* = 8.5, 1.9 Hz, 2H), 7.25 (s, 1H), 7.08 (d, *J* = 8.4 Hz, 2H), 6.77 (s, 1H) ppm. ^{13}C NMR (101 MHz, DMSO-*d*^{6}): δ = 166.47, 161.61, 132.32, 130.13, 125.47 (2 C), 118.29, 110.58, 86.36 ppm. HRMS (MALDI): calcd for $C_{32}H_{19}O_{14}$ ([M_2-H]$^-$): 627.0775; found: 627.0803.

Dimethyl *cis*-5a-hydro-10b-hydroxybenzofuro[2,3-*b*]benzofuran-2,9-dicarboxylate 4. The dicarboxylic acid **3** (2.25 g, 7.16 mmol) was dissolved in HCl/MeOH (80 mL, 1.25 M) and heated to reflux overnight. Evaporation of the solvent yielded a crude material that was purified by column chromatography (silica gel, DCM/MeOH 9:1) to obtain pure diester **4** as a white powder (2.21 g, 90% yield).

^{1}H NMR (400 MHz, DMSO-*d*^{6}): δ = 8.23 (d, *J* = 1.9 Hz, 2H), 7.90 (dd, *J* = 8.5, 1.9 Hz, 2H), 7.28 (s, 1H), 7.11 (d, *J* = 8.5 Hz, 2H), 6.80 (s, 1H), 3.84 (s, 6H) ppm. ^{13}C NMR (101 MHz, DMSO-*d*^{6}): *δ* = 165.44, 161.86, 132.33, 130.25, 125.43, 124.36, 118.33, 110.87, 86.36, 52.12 ppm. HRMS (APPI): calcd for $C_{18}H_{14}O_7Na$ ([M+Na]$^+$): 365.0638; found: 365.0632. R_f: 0.90 (DCM/MeOH 9:1).

Dimethyl benzofuro[2,3-*b*]benzofuran-2,9-dicarboxylate 5. A flame-dried 100 mL Schlenk flask was purged with argon and charged with diester **4** (1.27 g, 3.62 mmol) as well as anhydrous pyridine (20 mL). The resulting solution was cooled to 0°C using an ice bath, and then $POCl_3$ (1.4 mL, 4 equiv.) was added dropwise under continued stirring. The ice bath was removed and stirring continued at room temperature for 2 h to afford a precipitate. The reaction mixture was transferred into a separatory funnel and diluted with cold water (100 mL). The aqueous phase was extracted using DCM (3 × 25 mL). The combined organic phases were dried with $MgSO_4$, and the solvent was evaporated under reduced pressure. After drying in vacuum, the crude benzofurobenzofuran diester **5** was recrystallized from hot toluene to yield small white needles (1.00 g, 83% yield).

^{1}H NMR (400 MHz, DMSO-*d*^{6}): *δ* = 8.83 (d, *J* = 1.8 Hz, 2H), 7.99 (dd, *J* = 8.7, 1.9 Hz, 2H), 7.90 (d, *J* = 8.7 Hz, 2H), 3.93 (s, 6H) ppm. ^{13}C NMR (101 MHz, DMSO-*d*^{6}): δ = 166.49, 166.12, 157.42, 126.36, 125.05, 122.74, 122.11, 112.80, 96.81, 52.28 ppm. HRMS (ESI): calcd for $C_{36}H_{25}O_{12}$ ([M_2+H]$^+$): 649.1342; found: 649.1341.

***N*,*N*′-dipropyl *cis*-5a-hydro-10b-hydroxybenzofuro[2,3-*b*]benzofuran-2,9-dicarboxamide 6.** Dicarboxylic acid **3** (0.51 g, 1.72 mmol) was suspended in 10 mL DMF before 1-ethyl-3-(3-dimethylaminopropyl)carbodiimide (EDCI) (0.73 g, 3.79 mmol, 2.2 equiv.) and 1-hydroxybenzotriazole hydrate (HOBt) (0.58 g, 3.79 mmol, 2.2 equiv.) were added. The mixture was stirred at room temperature for 30 min until a clear solution was obtained. Eventually, propylamine (0.23 g, 3.79 mmol, 2.2 equiv.) and N,N-diisopropylethylamine (DIPEA) (0.93 g, 7.22

mmol, 4.2 equiv.) were added, and the solution was stirred at room temperature overnight. The clear solution was then poured into 150 mL water and the resulting white precipitate was filtered off, washed with water, and dried in vacuum. Transparent, needle-like single crystals of dicarboxamide **6** (272 mg, 42% yield) suitable for X-ray analysis were obtained by recrystallization from a hot EtOH solution and slow evaporation of the solvent.

^{1}H NMR (400 MHz, DMSO-d^6): δ = 8.42 (t, J = 5.8 Hz, 2H), 8.16 (d, 2H, J = 1.8 Hz), 7.79 (dd, J = 8.5, 1.9 Hz, 2H), 7.09 (s, 1H), 7.02 (d, J = 8.5 Hz, 2H), 6.68 (s, 1H), 3.21 (dp, J = 19.5, 6.3 Hz, 4H), 1.52 (h, J = 7.3 Hz, 4H), 0.88 (t, J = 7.4 Hz, 6H) ppm. ^{13}C NMR (101 MHz, DMSO-d^6): δ = 165.18, 160.21, 129.77, 129.64, 129.37, 123.68, 118.18, 109.88, 86.91, 41.01, 22.44, 11.48 ppm. HRMS (ESI): calcd for $C_{22}H_{25}N_2O_5$ ([M+H]$^+$): 396.1764; found: 396.1768. R_f: 0.35 (DCM/MeOH 19:1).

***N,N'*-dipropyl benzofuro[2,3-*b*]benzofuran-2,9-dicarboxamide 7.** Dicarboxylic acid **2** (0.99 g, 3.34 mmol) was suspended in 28 mL DMF before EDCI (1.41 g, 7.35 mmol, 2.2 equiv.) and HOBt (1.13 g, 7.35 mmol, 2.2 equiv.) were added. The mixture was stirred at room temperature for 20 min until a clear solution was obtained. Eventually, propylamine (0.43 g, 7.35 mmol, 2.2 equiv.) and DIPEA (1.81 g, 14.0 mmol, 4.2 equiv.) were added, and the solution was stirred at room temperature overnight. The clear solution was then poured into 350 mL water and the resulting precipitate was filtered off, washed with water, and dried in vacuum. The crude product was purified by column chromatography (silica gel, DCM/MeOH 19:1) to obtain pure dicarboxamide **7** as a white powder (1.10 g, 87% yield).

^{1}H NMR (400 MHz, DMSO-d^6): δ = 8.59 (t, J = 5.7 Hz, 2H), 8.54 (s, 2H), 7.94 – 7.83 (m, 4H), 3.24 (q, J = 7.4, 5.6 Hz, 4H), 1.59 (h, J = 7.3 Hz, 4H), 0.94 (t, J = 7.4 Hz, 6H) ppm. ^{1}H NMR (400 MHz, $CDCl_3$): δ = 8.23 (d, J = 1.6 Hz, 2H), 7.74 (dd, J = 8.6, 1.7 Hz, 2H), 7.61 (d, J = 8.6 Hz, 2H), 6.29 (s, 2H), 3.51 (q, J = 6.7 Hz, 4H), 1.72 (h, J = 7.4 Hz, 4H), 1.05 (t, J = 7.4 Hz, 6H). ^{13}C NMR (101 MHz, DMSO-d^6): δ = 166.30, 165.76, 156.31, 131.54, 122.99, 122.33, 118.97, 112.34, 96.78, 41.17, 22.45, 11.52 ppm. HRMS (ESI): calcd for $C_{22}H_{23}N_2O_4$ ([M+H]$^+$): 379.1658; found: 379.1656. R_f: 0.38 (DCM/MeOH 19:1).

Dipropyl benzofuro[2,3-*b*]benzofuran-2,9-dicarboxylate 8. Dicarboxylic acid **2** (0.12 g, 0.40 mmol) and potassium carbonate (K_2CO_3) (0.22 g, 1.6 mmol, 4 equiv.) were suspended in anhydrous DMF (10 mL) in a flame-dried 50 mL two-neck round-bottom flask equipped with a

reflux condenser, and purged with argon. Then, 1-bromopropane (0.11 mL, 1.2 mmol, 3 equiv.) was added dropwise, and the mixture was heated to reflux under vigorous stirring for 16 h. Most of the DMF was then removed under reduced pressure at 60°C, and the obtained residue was taken up in water (20 mL). The aqueous phase was extracted with EtOAc (3 × 20 mL), the combined organic phases were washed once more with water (20 mL), and then dried with $MgSO_4$. Upon slow evaporation of the solvent, colorless crystals of **8** suitable for X-ray analysis were obtained (0.05 g, 33% yield).

^{1}H NMR (400 MHz, $CDCl_3$): δ = 8.58 – 8.51 (m, 2H), 8.08 (dd, J = 8.8, 1.8 Hz, 2H), 7.64 (d, J = 8.7 Hz, 2H), 4.37 (t, J = 6.7 Hz, 4H), 1.88 (h, J = 7.2 Hz, 4H), 1.10 (t, J = 7.4 Hz, 6H). ^{13}C NMR (101 MHz, $CDCl_3$): δ = 167.25, 166.64, 158.13, 127.26, 125.29, 123.31, 121.67, 112.46, 97.56, 77.48, 77.16, 76.84, 67.05, 22.34, 10.77. HRMS (ESI): calcd for $C_{22}H_{20}O_6$ ($[M+H]^+$): 381.1338; found: 381.1337.

General Procedure for the Synthesis of BFBF-Containing Semiaromatic Polyamides. A flame-dried 25 mL Schlenk tube was purged with argon and charged with the aliphatic diamine (0.50–1.0 mmol), dicarboxylic acid **2** (1.00 eq.), a mixture of anhydrous *N*-methylpyrrolidone (NMP) and anhydrous pyridine (4:1, 2–4 mL), triphenylphosphite (TPP) (2.01 equiv.), as well as anhydrous lithium chloride (LiCl) (4 *wt*%). The suspension was heated to 110°C under vigorous stirring, when it eventually turned into a clear solution. After 4 h, the solution was cooled to 50–60°C, and poured into MeOH (50 mL). The obtained white precipitate was filtered off, washed several times with hot MeOH, and dried in vacuum to yield the desired polyamide as white powder.

Poly(hexamethylene benzofurobenzofurandicarboxamide) PA6B. Following the general procedure for the synthesis of semiaromatic polyamides, starting from 1,6-hexanediamine (105 mg, 0.900 mmol) and dicarboxylic acid **2** (0.900 mmol), we obtained the polyamide **PA6B** in a yield of 300 mg (88%) after precipitation.

^{1}H NMR (400 MHz, acetone-d^6): δ = 7.18–7.01 (m, 2H), 6.74–6.53 (m, 4H), 5.99–5.85 (m, 2H), 2.70–2.48 (br, 4H), 0.93–0.73 (br, 4H), 0.70–0.50 (br, 4H). GPC (HFIP): M_n = 7’100 ($Đ$ = 1.28).

Poly(nonamethylene benzofurobenzofurandicarboxamide) PA9B. Following the general procedure for the synthesis of semiaromatic polyamides, starting from 1,9-nonanediamine (104 mg, 0.660 mmol) and dicarboxylic acid **2** (195 mg, 0.660 mmol), we obtained the polyamide **PA9B** in a yield of 200 mg (72%) after precipitation.

^{1}H NMR (400 MHz, acetone-d^6): δ = 7.26–7.03 (m, 2H), 6.68 (s, 4H), 5.90 (s, 2H), 2.60 (s, 4H), 0.82 (s, 4H), 0.54 (s, 12H). GPC (HFIP): M_n = 7'100 ($Đ$ = 1.35).

Poly(dodecamethylene benzofurobenzofurandicarboxamide) PA12B. Following the general procedure for the synthesis of semiaromatic polyamides, starting from 1,12-dodecanediamine (101 mg, 0.500 mmol) and dicarboxylic acid **2** (150 mg, 0.500 mmol), we obtained the polyamide **PA12B** in a yield of 200 mg (87%) after precipitation.

^{1}H NMR (400 MHz, acetone-d^6): δ = 7.13 (s, 2H), 6.69 (s, 4H), 5.90 (s, 2H), 2.58 (s, 4H), 0.79 (s, 4H), 0.48 (d, J = 24.2 Hz, 16H). GPC (HFIP): M_n = 7'000 ($Đ$ = 1.34).

4,5-Bis(bromomethyl)acridine 10. The synthesis of compound **10** was carried out according to literature procedure[232] and the crude product (50% yield) was purified by column chromatography (dry loading, DCM/pentane 1:3, R_f: 0.50) to give pure 4,5-bis(bromomethyl)acridine **10** as a yellow solid.

2,2'-(Acridine-4,5-diyl)diacetonitrile 11. 4,5-Bis(bromomethyl)acridine **10** (4.03 g, 0.011 mol) was suspended in DMF (200 mL), and NaCN (1.09 g, 0.022 mol, 2.01 equiv.) added in portions over 10 min. The mixture was stirred at room temperature for 2 h, during which it turned into a clear solution. The volume of DMF was reduced to about 30 mL under reduced pressure and at controlled temperature (<50 °C) to avoid degradation of the product. The resulting slurry was then diluted with water (250 mL), and the precipitate was filtered off and washed with additional water. After drying in vacuum, 2,2'-(acridine-4,5-diyl)diacetonitrile **11** was obtained as a beige powder and used without further purification (2.70 g, 95% yield).

^{1}H NMR (400 MHz, $CDCl_3$): δ = 8.85 (s, 1H), 8.05 (d, J = 8.5 Hz, 2H), 7.94 (d, J = 6.8 Hz, 2H), 7.63–7.54 (m, 2H), 4.52 (s, 4H) ppm. ^{13}C NMR (101 MHz, $CDCl_3$): δ = 145.82, 137.11, 130.12, 129.44, 128.85, 126.74, 126.00, 118.62, 20.91 ppm. HRMS (ESI): calcd for $C_{17}H_{12}N_3$ ($[M+H]^+$): 258.1031; found: 258.1035. R_f: 0.36 (DCM).

2,2'-(Acridine-4,5-diyl)diacetic acid hydrochloride 12. 2,2'-(acridine-4,5-diyl)diacetonitrile **11** (6.24 g, 24.3 mmol) was saponified by refluxing (100 °C) a solution in concentrated HCl (35%, 400 mL) overnight. After cooling the solution in an ice bath, it was diluted with cold water (700 mL), and NaOH pellets were carefully added to increase the pH to 13–14. The basic solution was

then transferred to an extraction funnel and washed with DCM (2 × 300 mL). Acidification of the aqueous phase with concentrated HCl caused the product to precipitate as an orange-brown powder that was filtered off and washed several times with water to remove acid residues. The resulting 2,2'-(acridine-4,5-diyl)diacetic acid hydrochloride **12** (5.95 g, 74% yield) was used for ester or amide coupling reactions without further purification.

^{1}H NMR (400 MHz, DMSO-d^6): δ = 12.19 (s, 2H), 9.11 (s, 1H), 8.10 (d, J = 8.5 Hz, 2H), 7.77 (d, J = 6.8 Hz, 2H), 7.58 (t, J = 7.6 Hz, 2H), 4.28 (s, 4H) ppm. ^{13}C NMR (101 MHz, DMSO-d^6): δ = 173.05, 146.22, 136.60, 134.10, 130.76, 127.38, 125.98, 125.65, 36.70 ppm. HRMS (APCI): calcd for $C_{17}H_{14}NO_4$ ([M+H]$^+$): 296.0917; found: 296.0938.

Bis(*N*-succinimide)-2,2'-(acridine-4,5-diyl)diacetate 13. The crude 2,2'-(acridine-4,5-diyl)diacetic acid hydrochloride **12** (3.38 g, 10.19 mmol) was suspended in anhydrous DMF in an argon atmosphere. *N*-hydroxysuccinimide (NHS) (2.81 g, 24.45 mmol, 2.4 equiv.), 1-ethyl-3-(3-*N*,*N*-dimethylaminopropyl)carbodiimide (EDCI) (7.81 g, 40.76 mmol, 4 equiv.) and *N*,*N*-diisopropylethylamine (DIPEA) (8.9 mL, 50.95 mmol, 5 equiv.) were added successively to the suspension which subsequently turned into a clear solution. The solution was stirred for 2.5 h, during which the reaction went to completion as confirmed by TLC. The volume of the solution was reduced under reduced pressure (55 °C) to about 20 mL, and water (300 mL) was added to the resulting slurry. The precipitate was filtered off, washed with water, and dried in vacuum. The crude product (4.5 g) was purified by column chromatography (silica gel, DCM/MeOH 98:2) to give pure bis(*N*-succinimide)-2,2'-(acridine-4,5-diyl)diacetate **13** as a bright yellow powder (2.30 g, 46% yield).

^{1}H NMR (400 MHz, $CDCl_3$): δ = 8.77 (s, 1H), 7.97 (d, J = 8.4 Hz, 2H), 7.80 (d, J = 6.6 Hz, 2H), 7.52 (dd, J = 8.4, 6.9 Hz, 2H), 4.80 (s, 4H), 2.77 (s, 8H) ppm. ^{13}C NMR (101 MHz, $CDCl_3$): δ = 169.34, 168.03, 146.70, 136.65, 131.95, 131.29, 128.39, 126.77, 125.79, 34.71, 25.73 ppm. HRMS (ESI): calcd for $C_{25}H_{20}N_3O_8$ ([M+H]$^+$): 490.1250; found: 490.1256. R_f: 0.44 (DCM/MeOH 98:2).

***N*,*N*'-Dipropyl 2,2'-(acridine-4,5-diyl)diacetamide 14.** 2,2'-(acridine-4,5-diyl)diacetic acid hydrochloride **12** (0.94 g, 2.83 mmol) was suspended in 10 mL DMF, and 1-ethyl-3-(3-dimethylaminopropyl)carbodiimide (EDCI) (1.19 g, 6.23 mmol, 2.2 equiv.) and 1-

hydroxybenzotriazole hydrate (HOBt) (0.95 g, 6.23 mmol, 2.2 equiv.) were added. The mixture was stirred at room temperature for 15–20 min. *N*,*N*-diisopropylethylamine (DIPEA) (2.1 mL, 11.9 mmol, 4.2 equiv.) and 1-propylamine (0.51 mL, 6.23 mmol, 2.2 equiv.) were then successively added, and the resulting solution was stirred at room temperature overnight. It was then poured into 150 mL water and the resulting precipitate was filtered, washed with water, and dried under vacuum. The crude product was purified by column chromatography (silica gel, DCM/MeOH 15:1, 53% yield) and subsequently recrystallized by slow diffusion of Et_2O vapors into a DCM solution containing the product to obtain single crystals of *N*,*N*'-dipropyl 2,2'-(acridine-4,5-diyl)diacetamide **14** suitable for X-ray analysis.

^{1}H NMR (400 MHz, DMSO-*d*^{6}): δ 9.08 (s, 1H), 8.07 (d, *J* = 8.4 Hz, 2H), 8.03 (t, *J* = 5.2 Hz, 2H), 7.75 (d, *J* = 6.7 Hz, 2H), 7.62–7.53 (m, 2H), 4.15 (s, 4H), 3.03 (q, *J* = 6.6 Hz, 4H), 1.38 (h, *J* = 7.2 Hz, 4H), 0.73 (t, *J* = 7.4 Hz, 6H) ppm. ^{13}C NMR (101 MHz, DMSO-*d*^{6}): *δ* = 170.70, 146.24, 136.64, 135.09, 130.57, 127.14, 126.00, 125.70, 40.54, 39.07, 22.35, 11.26 ppm. T_m (DSC): 234 °C R_f: 0.34 (DCM/MeOH 15:1). HRMS (ESI): calcd for $C_{23}H_{28}N_3O_2$ ([M+H]$^+$): 378.2181; found: 378.2175.

***N*,*N*'-Dihexyl 2,2'-(acridine-4,5-diyl)diacetamide 15.** 2,2'-(acridine-4,5-diyl)diacetic acid hydrochloride **12** (1.00 g, 3.01 mmol) was suspended in 10 mL DMF, and 1-ethyl-3-(3-dimethylaminopropyl)carbodiimide (EDCI) (1.27 g, 6.63 mmol, 2.2 equiv.) and 1-hydroxybenzotriazole hydrate (HOBt) (1.02 g, 6.63 mmol, 2.2 equiv.) were added. The mixture was stirred at room temperature for 15–20 min. *N*,*N*-diisopropylethylamine (DIPEA) (2.2 mL, 12.7 mmol, 4.2 equiv.) and 1-hexylamine (0.87 mL, 6.63 mmol, 2.2 equiv.) were then successively added, and the resulting solution was stirred at room temperature overnight. It was then poured into 150 mL water and the resulting precipitate was filtered, washed with water, and dried under vacuum. The crude product was purified by column chromatography (silica gel, DCM/MeOH 14:1, 47% yield), and subsequently recrystallized from hot MeOH to yield *N*,*N*'-dihexyl 2,2'-(acridine-4,5-diyl)diacetamide **15** as thin yellowish needle-like crystals suitable for X-ray analysis.

^{1}H NMR (400 MHz, DMSO-*d*^{6}): *δ* = 9.08 (s, 1H), 8.07 (d, *J* = 8.4 Hz, 2H), 7.99 (t, *J* = 5.2 Hz, 2H), 7.75 (d, *J* = 6.7 Hz, 2H), 7.57 (t, *J* = 7.6 Hz, 2H), 4.12 (s, 4H), 3.05 (q, *J* = 6.4 Hz, 4H), 1.39–1.28 (m, 4H), 1.04 (s, 12H), 0.71 (t, *J* = 6.1 Hz, 6H) ppm. ^{13}C NMR (101 MHz, DMSO-*d*^{6}): *δ* = 170.68, 146.24,

136.61, 135.06, 130.69, 127.16, 126.04, 125.69, 39.31, 38.72, 30.92, 29.04, 25.96, 21.92, 13.76 ppm. HRMS (ESI): calcd for $C_{29}H_{40}N_3O_2$ ([M+H]$^+$): 462.3120; found: 462.3125. T_m (DSC): 201 °C. R_f: 0.47 (DCM/MeOH 14:1).

Diethyl 2,2'-((9,10-dioxo-9,10-dihydroanthracene-1,8-diyl)bis(oxy))diacetate 16. 1,8-dihydroxyanthraquinone (13.98 g, 58.2 mmol) was suspended in acetone (500 mL). Ethylbromoacetate (16.1 mL, 0.145 mol, 2.5 equiv.) and K_2CO_3 (32.2 g, 0.23 mol, 4 equiv.) were added under strong stirring. The resulting mixture was refluxed overnight (63 °C) and the progress of the reaction was monitored by TLC. After cooling to room temperature, the purple precipitate was removed by filtration. The acetone and unreacted ethylbromoacetate were then removed under reduced pressure, and the crude product was purified by recrystallization from hot EtOH to give diethyl 2,2'-((9,10-dioxo-9,10-dihydroanthracene-1,8-diyl)bis(oxy))diacetate **16** as a bright yellow solid (11.0 g, 46% yield).

^{1}H NMR (400 MHz, CD_2Cl_2): δ = 7.87 (d, J = 7.7 Hz, 2H), 7.64 (t, J = 8.0 Hz, 2H), 7.22 (d, J = 8.3 Hz, 2H), 4.83 (s, 4H), 4.27 (q, J = 7.1 Hz, 4H), 1.29 (t, J = 7.1 Hz, 6H) ppm. ^{13}C NMR (151 MHz, CD_2Cl_2) δ = 183.70, 182.19, 168.71, 157.91, 135.28, 134.17, 125.20, 120.59, 120.53, 67.13, 61.91, 14.33 ppm. HRMS (ESI): calcd for $C_{22}H_{20}O_8Na$ ([M+Na]$^+$): 435.1056; found: 435.1059. R_f: 0.37 (petroleum ether/EtOAc 1:1).

2,2'-((9,10-Dioxo-9,10-dihydroanthracene-1,8-diylbis(oxy))diacetic acid 17. Diethyl 2,2'-((9,10-dioxo-9,10-dihydroanthracene-1,8-diyl)bis(oxy))diacetate **7** was saponified according to a literature procedure.[235] The obtained 2,2'-((9,10-Dioxo-9,10-dihydroanthracene-1,8-diylbis-(oxy))diacetic acid **17** (93% yield) was used without further purification.

2,2'-(Anthracene-1,8-diylbis(oxy))diacetic acid 18. 2,2'-((9,10-Dioxo-9,10-dihydroanthracene-1,8-diylbis(oxy))diacetic acid **17** (8.75 g, 24.56 mmol) was suspended in aqueous NH_4OH (25%, 500 mL). Zinc powder (8.03 g, 0.122 mol, 5 equiv.) was added, and the mixture was stirred under reflux (68 °C) for 3 h. The reaction mixture was then cooled, additional zinc powder (6.42 g, 4 equiv.) in aqueous NH_4OH (25%, 50 mL) was added, and reflux was continued overnight. The solution was then cooled in an ice bath before acidification to pH 1 with concentrated aqueous HCl (37%), which resulted in a beige precipitate that was too fine to be filtered. The aqueous phase

was therefore extracted with EtOAc (3 × 350 mL), and the combined organic phases were washed once with water (400 mL) and once with brine (400 mL), and dried with $MgSO_4$. The solvent was then evaporated under reduced pressure. After drying in vacuum, pure 2,2'-(anthracene-1,8-diylbis(oxy))diacetic acid **18** was obtained as a light brown powder (5.76 g, 73% yield).

^{1}H NMR (400 MHz, DMSO-d^6): δ = 13.13 (s, 2H), 9.22 (s, 1H), 8.48 (s, 1H), 7.65 (d, J = 8.6 Hz, 2H), 7.41 (t, J = 8.0 Hz, 2H), 6.81 (d, J = 7.5 Hz, 2H), 5.00 (s, 4H) ppm. ^{13}C NMR (101 MHz, DMSO-d^6): δ = 170.07, 153.54, 132.44, 125.91, 125.24, 123.63, 120.47, 115.19, 103.20, 64.80 ppm. HRMS (ESI): calcd for $C_{18}H_{13}O_6$ ([M-H]$^-$): 325.0712; found: 325.0715.

***N,N'*-Dipropyl 2,2'-(anthracene-1,8-diylbis(oxy))diacetamide 19.** Diethyl 2,2'-((9,10-dioxo-9,10-dihydroanthracene-1,8-diyl)bis(oxy))diacetate **18** (2.01 g, 6.16 mmol) was suspended in 20 mL DMF, and 1-ethyl-3-(3-dimethylaminopropyl)carbodiimide (EDCI) (2.60 g, 13.6 mmol, 2.2 equiv.) and 1-hydroxybenzotriazole hydrate (HOBt) (2.07 g, 13.6 mmol, 2.2 equiv.) were added. The mixture was stirred at room temperature for 15–20 min. *N*,*N*-diisopropylethylamine (DIPEA) (4.5 mL, 25.9 mmol, 4.2 equiv.) and 1-propylamine (1.10 mL, 13.6 mmol, 2.2 equiv.) were then successively added, and the resulting solution was stirred at room temperature overnight. It was then poured into 200 mL water and the resulting precipitate was filtered, washed with water, and dried under vacuum. The crude product was purified by column chromatography (silica gel, DCM/MeOH 19:1, 56% yield), followed by recrystallization by slow evaporation (16 h) a solution of *N*,*N*'-dipropyl 2,2'-(anthracene-1,8-diylbis(oxy))diacetamide **19** in DCM/MeOH (10:1, 0.2 M) at room temperature. The resulting transparent needle-like crystals were suitable for X-ray analysis. ^{1}H NMR (400 MHz, DMSO-d^6): δ = 9.28 (s, 1H), 8.49 (s, 1H), 8.24 (t, J = 5.4 Hz, 2H), 7.66 (d, J = 8.5 Hz, 2H), 7.42 (t, J = 8.0 Hz, 2H), 6.82 (d, J = 7.5 Hz, 2H), 4.78 (s, 4H), 3.15 (q, J = 6.6 Hz, 4H), 1.49 (h, J = 7.2 Hz, 4H), 0.86 (t, J = 7.4 Hz, 6H) ppm. ^{13}C NMR (101 MHz, DMSO-d^6): δ = 167.33, 153.75, 132.41, 125.90, 125.19, 123.59, 120.62, 115.73, 103.61, 67.55, 40.16, 22.35, 11.30 ppm. HRMS (ESI): calcd for $C_{24}H_{29}N_2O_4$ ([M+H]$^+$): 409.2127; found: 409.2129. R_f: 0.46 (DCM/MeOH 19:1).

General Procedure A for the Preparation of the Acridine-Based Polyamides. A flame-dried 10 mL Schlenk tube was purged with argon and charged with the corresponding aliphatic diamine (0.7–0.8 mmol, 1.00 equiv.), bis(*N*-succinimide)-2,2'-(acridine-4,5-diyl)diacetate **13** (1.00 equiv.), and

anhydrous DMSO (3.1–3.4 mL). The suspension was heated to 120 °C under vigorous stirring, at which point it briefly converted to a clear solution. After 2 h, the reaction mixture was cooled to 50–60 °C and poured into cold water (40 mL). The resulting yellow precipitate was filtered off, washed with water and acetone, and dried in vacuum to yield the corresponding polyamide **PA*x*Acr** (*x* = 6, 8, 10, 12).

PA6Acr. The polyamide **PA6Acr** was prepared following general procedure A from bis(*N*-succinimide)-2,2'-(acridine-4,5-diyl)diacetate **13** (412 mg, 0.84 mmol) and 1,6-diaminohexane (98 mg, 0.84 mmol). The polyamide **PA6Acr** was obtained as a yellow powder in a yield of 73%.

^{1}H NMR (400 MHz, $CDCl_3$:HFIP-d^2 9:1): δ = 9.74–8.54 (m, 1H), 8.46–7.31 (m, 6H), 4.33–3.83 (m, 4H), 3.22–2.50 (m, 4H), 1.72–0.34 (m, 8H).

PA8Acr. The polyamide **PA8Acr** was prepared following general procedure A from bis(*N*-succinimide)-2,2'-(acridine-4,5-diyl)diacetate **13** (384 mg, 0.78 mmol) and 1,8-diaminooctane (113 mg, 0.78 mmol). The polyamide **PA8Acr** was obtained as a yellow powder in a yield of 80%.

^{1}H NMR (400 MHz, $CDCl_3$:HFIP-d^2 9:1): δ = 8.79 (s, 1H), 8.33–7.37 (m, 6H), 4.46–3.98 (m, 4H), 3.32–2.96 (m, 4H), 1.62–0.38 (m, 12H).

PA10Acr. The polyamide **PA610Acr** was prepared following general procedure A from bis(*N*-succinimide)-2,2'-(acridine-4,5-diyl)diacetate **13** (340 mg, 0.70 mmol) and 1,10-diaminodecane (120 mg, 0.70 mmol). The polyamide **PA10Acr** was obtained as a yellow powder in a yield of 87%.

^{1}H NMR (400 MHz, $CDCl_3$:HFIP-d^2 9:1): δ = 8.81 (s, 1H), 8.44–7.33 (m, 6H), 4.37–3.99 (m, 4H), 3.30–2.98 (m, 4H), 1.70–0.56 (m, 16H).

PA12Acr. The polyamide **PA12Acr** was prepared following general procedure A from bis(*N*-succinimide)-2,2'-(acridine-4,5-diyl)diacetate **13** (342 mg, 0.70 mmol) and 1,12-diaminododecane (140 mg, 0.70 mmol). The polyamide **PA12Acr** was obtained as a yellow powder in a yield of 86%.

^{1}H NMR (400 MHz, $CDCl_3$:HFIP-d^2 9:1): δ = 8.84 (s, 1H), 8.30–7.42 (m, 6H), 4.35–4.04 (m, 4H), 3.23–2.91 (m, 4H), 1.64–0.59 (m, 20H).

General Procedure B for the Preparation of Anthracene-Based Polyamides. A flame-dried 50 mL Schlenk tube was purged with argon and charged with the corresponding aliphatic diamine (2–3 mmol, 1.00 equiv.), 2,2'-(anthracene-1,8-diylbis(oxy))diacetic acid **18** (1.00 equiv.), anhydrous *N*-methylpyrrolidone (NMP) (6.4–9.7 mL), anhydrous pyridine (1.6–2.4 mL), triphenylphosphite (TPP) (1.0–1.6 mL, 2.01 equiv.), and anhydrous lithium chloride (LiCl) (0.41–0.62 g). The suspension was heated to 120 °C under vigorous stirring, at which point it briefly turned into a clear solution. After 4 h, the reaction mixture was cooled to 50–60 °C and poured into MeOH (100 mL). The resulting brown precipitate was filtered, washed with hot MeOH, refluxed in MeOH for 24 h, filtered again, and dried in vacuum to yield the corresponding polyamide **PA*x*Ant** (*x* = 6, 8, 10, 12).

PA6Ant. The polyamide **PA6Ant** was prepared following general procedure B from 2,2'-(anthracene-1,8-diylbis(oxy))diacetic acid **18** (786 mg, 2.41 mmol) and 1,6-diaminohexane (280 mg, 2.41 mmol). The polyamide **PA6Ant** was obtained as a brown powder in a yield of 61%.

^{1}H NMR (400 MHz, $CDCl_3$:HFIP-d^2 9:1): δ = 9.21–9.01 (m, 1H), 8.42–8.24 (m, 1H), 7.74–7.52 (m, 2H), 7.46–7.27 (m, 2H), 6.73–6.55 (m, 2H), 4.84–4.59 (m, 4H), 3.38–2.95 (m, 4H), 1.65–0.99 (m, 8H).

PA8Ant. The polyamide **PA8Ant** was prepared following general procedure B from 2,2'-(anthracene-1,8-diylbis(oxy))diacetic acid **18** (666 mg, 2.04 mmol) and 1,8-diaminooctane (294 mg, 2.04 mmol). The polyamide **PA8Ant** was obtained as a brown powder in a yield of 62%.

^{1}H NMR (400 MHz, $CDCl_3$:HFIP-d^2 9:1): δ = 9.24–9.01 (m, 1H), 8.47–8.30 (m, 1H), 7.78–7.57 (m, 2H), 7.49–7.29 (m, 2H), 6.78–6.59 (m, 2H), 4.85–4.66 (m, 4H), 3.42–2.96 (m, 4H), 1.68–0.99 (m, 12H).

PA10Ant. The polyamide **PA10Ant** was prepared following general procedure B from 2,2'-(anthracene-1,8-diylbis(oxy))diacetic acid **18** (980 mg, 3.02 mmol) and 1,10-diaminodecane (520 mg, 3.02 mmol). The polyamide **PA10Ant** was obtained as a brown powder in a yield of 65%.

^{1}H NMR (400 MHz, $CDCl_3$:HFIP-d^2 9:1): δ = 9.12 (s, 1H), 8.49–8.31 (m, 1H), 7.79–7.59 (m, 2H), 7.49–7.31 (m, 2H), 6.79–6.62 (m, 2H), 4.78 (s, 4H), 3.43–2.97 (m, 4H), 1.69–0.97 (m, 16H).

PA12Ant. The polyamide **PA12Ant** was prepared following general procedure B from 2,2'-(anthracene-1,8-diylbis(oxy))diacetic acid **18** (632 mg, 1.94 mmol) and 1,12-diaminododecane (388 mg, 1.94 mmol). The polyamide **PA12Ant** was obtained as a brown powder in a yield of 75%.

^{1}H NMR (400 MHz, $CDCl_3$:HFIP-d^2 9:1): δ = 9.11 (s, 1H), 8.50–8.30 (m, 1H), 7.80–7.61 (m, 2H), 7.46–7.31 (m, 2H), 6.78–6.61 (m, 2H), 4.97–4.64 (m, 4H), 3.43–2.98 (m, 4H), 1.72–0.94 (m, 20H).

8

References

8 References

(1) Chawla, K. K. *Composite Materials, Science and Engineering*, 3rd ed.; Springer: New York, 2012.

(2) Jeon, S. H.; Kim, H. M.; Park, T.-H.; Choi, B.-H.; Choi, W. C. Development of Polycarbonate/Acrylonitrile-Butadiene-Styrene Copolymer Based Composites with Functional Fillers for Car Audio Chassis. *Mater. Des.* **2011**, *32* (3), 1306–1314.

(3) Brady, M.; Brady, P. Technology Developments in Automotive Composites. *Reinf. Plast.* **2010**, *54* (6), 25–29.

(4) Moriarty, P.; Honnery, D. The Prospects for Global Green Car Mobility. *J. Cleaner Prod.* **2008**, *16* (16), 1717–1726.

(5) Folkes, M. J. *Short Fibre Reinforced Thermoplastics*; Research Studies Press/Wiley: Chichester/New York, 1982.

(6) Ashby, M. F. Material Property Charts. In *Materials Selection in Mechanical Design*; Oxford, 2005; pp 43–78.

(7) Ritchie, R. O. The Conflicts Between Strength and Toughness. *Nat. Mater.* **2011**, *10* (11), 817–822.

(8) Launey, M. E.; Ritchie, R. O. On the Fracture Toughness of Advanced Materials. *Adv. Mater.* **2009**, *21* (20), 2103–2110.

(9) Stewart, R. Automotive Composites Offer Lighter Solutions. *Reinf. Plast.* **2010**, *54* (2), 22–28.

(10) Cowie, J. M. G.; Arrighi, V. Step-Growth Polymerizations. In *Polymers Chemistry and Physics of Modern Materials*; Boca Raton, 2007; pp 29–56.

(11) Ravve, A. Step-Growth Polymerizations and Step-Growth Polymers. In *Principles of Polymer Chemistry*; 2000; pp 327–448.

(12) Chanda, M.; Roy, S. K. *Plastics Technology Handbook*, 4 ed.; CRC Press: Boca Raton, FL, USA, 2007.

(13) Gaymans, R. J. Polyamides. In *Synthetic Methods in Step-Growth Polymers*; Rogers, M. E., Long, T. E., Eds.; John Wiley & Sons, Inc.: Hoboken, NJ, USA, 2003; pp 135–195.

(14) Seavey, K. C.; Liu, Y. A. Reaction Kinetics. In *Step-Growth Polymerization Process Modeling and Product Design*; John Wiley & Sons, Inc.: Hoboken, NJ, USA, 2008; pp 135–197.

(15) Carlotti, S.; Peruch, F. Cyclic Monomers: Epoxides, Lactide, Lactones, Lactams, Cyclic Silicon-Containing Monomers, Cyclic Carbonates and Others. In *Anionic Polymerization*; Hadjichristidis, N., Hirao, A., Eds.; Tokyo, Japan, 2015; pp 191–306.

(16) Srinivasan, R.; Almonacil, C.; Narayan, S.; Desai, P.; Abhiraman, A. S. Mechanism, Kinetics and Potential Morphological Consequences of Solid-State Polymerization. *Macromolecules* **1998**, *31* (20), 6813–6821.

(17) Almonacil, C.; Desai, P.; Abhiraman, A. S. Morphological Consequences of Interchange Reactions During Solid State Polymerization in Oriented Polymers. *Macromolecules* **2001**, *34* (12), 4186–4199.

(18) Kim, Y. J.; Yohana, K. E.; Lee, H.-S.; Kim, J. Solid-State Polymerization of Semiaromatic

Copolyamides of Nylon-4,T and Nylon-4,6: Composition Ratio Effect and Thermal Properties. *Ind. Eng. Chem. Res.* **2012**, *51* (49), 15801–15810.

(19) Lin, J.; Sherrington, D. C. Recent Developments in the Synthesis, Thermostability and Liquid Crystal Properties of Aromatic Polyamides. In *Polymer Synthesis*; Advances in Polymer Science; Springer, Berlin, Heidelberg: Berlin/Heidelberg, 1994; Vol. 111, pp 177–219.

(20) Mallakpour, S.; Dinari, M. High Performance Polymers in Ionic Liquids: a Review on Prospects for Green Polymer Chemistry. Part I: Polyamides. *Iran. Polym. J.* **2010**, *19* (12), 983–1004.

(21) Morgan, P. W. Synthesis and Properties of Aromatic and Extended Chain Polyamides. *Macromolecules* **1977**, *10* (6), 1381–1390.

(22) Takayanagi, M.; Ogata, T.; Morikawa, M.; Kai, T. Polymer Composites of Rigid and Flexible Molecules: System of Wholly Aromatic and Aliphatic Polyamides. *J. Macromol. Sci. B* **1980**, *17* (4), 591–615.

(23) Fukushima, Y. Preparation and Characterization of a New Polyamide Containing Ethidium Bromide. *Polym. Bull.* **2001**, *45* (6), 465–470.

(24) Hatke, W.; Schmidt, H.-W.; Heitz, W. Substituted Rod-Like Aromatic Polyamides: Synthesis and Structure-Property Relations. *J. Polym. Sci. A* **1991**, *29* (10), 1387–1398.

(25) Jeong, H.-J.; Kakimoto, M.-A.; Imai, Y. Synthesis and Characterization of Novel Aromatic Polyamides From 3,4-Bis(4-Aminophenyl)-2,5-Diphenylpyrrole and Aromatic Diacid Chlorides. *J. Polym. Sci. A* **1991**, *29* (5), 767–772.

(26) Zuo, J.; Li, S.; Bouzidi, L.; Narine, S. S. Thermoplastic Polyester Amides Derived From Oleic Acid. *Polymer* **2011**, *52* (20), 4503–4516.

(27) de Ruijter, C.; Jager, W. F.; Groenewold, J.; Picken, S. J. Synthesis and Characterization of Rod−Coil Poly(Amide-*block*-Aramid) Alternating Block Copolymers. *Macromolecules* **2006**, *39* (11), 3824–3829.

(28) Jia, Q.-X.; Xiong, Z.-J.; Shi, C.-M.; Zhang, L.-Q.; Wang, X.-N. Preparation and Properties of Polyamide 6 Fibers Prepared by the Gel Spinning Method. *J. Appl. Polym. Sci.* **2012**, *124* (6), 5165–5171.

(29) Hanford, W. E.; Sauer, J. C. Preparation of Ketenes and Ketene Dimers. In *Organic Reactions*; John Wiley & Sons, Inc.: New York, USA, 1946; Vol. 3, pp 108–140.

(30) Hess, O. Ueber Einige Benzoylderivate Aromatischer Amine. *Ber. Dtsch. Chem. Ges.* **1885**, *18* (1), 685–688.

(31) Yamazaki, N.; Higashi, F. Studies on Reactions of the N-Phosphonium Salts of Pyridines. VII. *Tetrahedron* **1974**, *30* (11), 1323–1326.

(32) Yamazaki, N.; Higashi, F. Studies on Reactions of N-Phosphonium Salts of Pyridines. VIII. Preparation of Polyamides by Means of Diphenyl Phosphite in Pyridine. *J. Polym. Sci. B Polym. Lett. Ed.* **1974**, *12* (4), 185–191.

(33) Yamazaki, N.; Higashi, F.; Kawabata, J. Studies on Reactions of the N-Phosphonium Salts of Pyridines. XI. Preparation of Polypeptides and Polyamides by Means of Triaryl Phosphites in Pyridine. *J. Polym. Sci. Polym. Chem. Ed.* **1974**, *12* (9), 2149–2154.

(34) Yamazaki, N.; Matsumoto, M.; Higashi, F. Studies on Reactions of the N-Phosphonium Salts

of Pyridines. XIV. Wholly Aromatic Polyamides by the Direct Polycondensation Reaction by Using Phosphites in the Presence of Metal Salts. *J. Polym. Sci. Polym. Chem. Ed.* **1975**, *13* (6), 1373–1380.

(35) Higashi, F.; Taguchi, Y.; Kokubo, N.; Ohta, H. Effect of Initiation Conditions on the Direct Polycondensation Reaction Unsing Tripheylphosphite and Pyridine. *J. Polym. Sci. Polym. Chem. Ed.* **1981**, *19* (11), 2745–2750.

(36) Higashi, F.; Mochizuki, A. Direct Polycondensation Reaction with Triphenyl Phosphite Initiated by Tertiary Amine Hydrochlorides. *J. Polym. Sci. Polym. Chem. Ed.* **1983**, *21* (11), 3337–3340.

(37) Ogata, N.; Sanui, K.; Tan, S. Synthesis of Aliphatic Polyamides by Direct Polycondensation with Triphenylphosphine. *Polym. J.* **1984**, *16* (7), 569–574.

(38) Overberger, C. G.; Šebenda, J. Synthesis of Polyamides From Rigid and Sterically Hindered Dicarboxylic Acids and Diamines Under Mild Conditions. *J. Polym. Sci. A* **1969**, *7* (10), 2875–2887.

(39) Ogata, N.; Sanui, K.; Kanasugi, K.; Ohira, N. Active Polycondensation of Aromatic Hydroxyl Diesters with Diamines. *Polym. J.* **1975**, *7* (5), 544–549.

(40) Katsarava, R. D.; Kunchuliya, D. P.; Avalishvili, L. M.; Andronikashvili, G. G.; Zaalishvili, M. M. The Use of Activated Bis-Pentachlorophenyl Esters of Dicarboxylic Acids in Synthesis of Polyamides. *Polym. Sci. (USSR) (Engl. Transl.)* **1979**, *21* (12), 2978–2984.

(41) Katsarava, R. D.; Kharadze, D. P.; Avalishvili, L. M.; Zaalishvili, M. M. Synthesis of Polyamides Using Activated Bis-N-Oxysuccinimide Esters of Dicarboxylic Acids. *Polym. Sci. (USSR) (Engl. Transl.)* **1984**, *26* (7), 1668–1678.

(42) Kricheldorf, H. R.; Bornhorst, K.; Schellenberg, J.; Schwarz, G. Aliphatic Poly(Ether Amide)s by Polycondensation of Activated Sebacic Acid Derivatives. *J. Macromol. Sci. A* **2007**, *44* (2), 119–124.

(43) Murthy, N. S. Hydrogen Bonding, Mobility, and Structural Transitions in Aliphatic Polyamides. *J. Polym. Sci. B* **2006**, *44* (13), 1763–1782.

(44) Gianchandani, J.; Spruiell, J. E.; Clark, E. S. Polymorphism and Orientation Development in Melt Spinning, Drawing, and Annealing of Nylon-6 Filaments. *J. Appl. Polym. Sci.* **1982**, *27* (9), 3527–3551.

(45) Miyasaka, K.; Makishima, K. Transition of Nylon 6 γ-Phase Crystals by Stretching in the Chain Direction. *J. Polym. Sci. A-1 Polym. Chem.* **1967**, *5* (12), 3017–3027.

(46) Kinoshita, Y. An Investigation of the Structures of Polyamide Series. *Macromol. Chem. Phys.* **1959**, *33* (1), 1–20.

(47) Jones, N. A.; Atkins, E. D. T.; Hill, M. J.; Cooper, S. J.; Franco, L. Chain-Folded Lamellar Crystals of Aliphatic Polyamides. Comparisons Between Nylons 4 4, 6 4, 8 4, 10 4, and 12 4. *Macromolecules* **1996**, *29* (18), 6011–6018.

(48) Bunn, C. W.; Garner, E. V.; Sir Lawrence Bragg, F. R. S. The Crystal Structures of Two Polyamides ("Nylons"). *Proc. R. Soc. Lond. A* **1947**, *189* (1016), 39–68.

(49) Holmes, D. R.; Bunn, C. W.; Smith, D. J. The Crystal Structure of Polycaproamide: Nylon 6. *J. Polym. Sci. A* **1955**, *17* (84), 159–177.

(50) Arimoto, H.; Ishibashi, M.; Hirai, M.; Chatani, Y. Crystal Structure of the γ-Form of Nylon 6.

J. Polym. Sci. A **1965**, *3* (1), 317–326.

(51) Vogelsong, D. C. Crystal Structure Studies on the Polymorphic Forms of Nylons 6 and 8 and Other Even Nylons. *J. Polym. Sci. A* **1963**, *1* (3), 1055–1068.

(52) Bradbury, E. M.; Brown, L.; Elliott, A.; Parry, D. A. D. The Structure of the Gamma Form of Polycaproamide (Nylon 6). *Polymer* **1965**, *6* (9), 465–482.

(53) Dasgupta, S.; Hammond, W. B.; Goddard, W. A. Crystal Structures and Properties of Nylon Polymers From Theory. *J. Am. Chem. Soc.* **1996**, *118* (49), 12291–12301.

(54) Miyasaka, K.; Ishikawa, K. Effects of Temperature and Water on the $\gamma \rightarrow \alpha$ Crystalline Transition of Nylon 6 Caused by Stretching in the Chain Direction. *J. Polym. Sci. B* **1968**, *6* (7), 1317–1329.

(55) Hiramatsu, N.; Hirakawa, S. Melting and Transformation Behavior of γ Form Nylon 6 Under High Pressure. *Polym. J.* **1982**, *14* (3), 165–171.

(56) Keller, A. Polymer Crystals. *Rep. Prog. Phys.* **1968**, *31* (2), 623–704.

(57) Dreyfuss, P.; Keller, A. Chain Folding in Polyamides: a Study on Nylons 66, 610, and 612 as Crystallized From Solution. *J. Macromol. Sci. B* **2011**, *4* (4), 811–835.

(58) Bassett, D. C. *Principles of Polymer Morphology*; Cambridge University Press: Cambridge, UK, 1981; pp 16–36.

(59) Young, R. J. *Introduction to Polymers*; Chapman and Hall: London, UK, 1981; pp 149–210.

(60) Han, C. D. Morphology Evolution in Immiscible Polymer Blends During Compounding. In *Rheology and Processing of Polymeric Materials*; Oxford, UK, 2007; pp 132–180.

(61) Gaymans, R. J.; Van der Ham, A. G. J. Nylon 4,I: an Amorphous Polyamide. *Polymer* **1984**, *25* (12), 1755–1758.

(62) Ebewele, R. O. Thermal Transitions in Polymers. In *Polymer Science And Technology*; CRC Press: Boca Raton, FL, USA, 2008.

(63) Xenopoulos, A.; Wunderlich, B. Thermodynamic Properties of Liquid and Semicrystalline Linear Aliphatic Polyamides. *J. Polym. Sci. B* **1990**, *28* (12), 2271–2290.

(64) Yang, H. H. Polyamide Fibers. In *Handbook of Fiber Chemistry*; Lewin, M., Ed.; Boca Raton, FL, USA, 2010; pp 31–137.

(65) Alger, M. *Polymer Science Dictionary*, 3rd ed.; Springer Netherlands: Dordrecht, 2017.

(66) Miller, R. L. Crystallographic Data for Various Polymers. In *Polymer Handbook*; Brandrup, J., Immergut, E. H., Eds.; New York, 1989.

(67) Gabara, V.; Hartzler, J. D.; Lee, K. S.; Yang, H. H. Aramid Fibers. In *Handbook of Fiber Chemistry*; Lewin, M., Ed.; CRC Press: Boca Raton, FL, USA, 2010; pp 975–1029.

(68) Garcia, D.; Starkweather, H. W. Hydrogen Bonding in Nylon 66 and Model Compounds. *J. Polym. Sci. B* **1985**, *23* (3), 537–555.

(69) Schroeder, L. R.; Cooper, S. L. Hydrogen Bonding in Polyamides. *J. Appl. Phys.* **1976**, *47* (10), 4310–4317.

(70) Skrovanek, D. J.; Howe, S. E.; Painter, P. C.; Coleman, M. M. Hydrogen Bonding in Polymers: Infrared Temperature Studies of an Amorphous Polyamide. *Macromolecules* **1985**, *18* (9), 1676–1683.

(71) Miura, H.; Hirschinger, J.; English, A. D. Segmental Dynamics in the Amorphous Phase of

Nylon 66: Solid State Deuterium NMR. *Macromolecules* **1990**, *23* (8), 2169–2182.

(72) Buchanan, D. R.; Walters, J. P. Glass-Transition Temperatures of Polyamide Textile Fibers. *Textile Research Journal* **1977**, *47* (6), 398–406.

(73) Elias, H.-G.; Vohwinkel, F. *New Commercial Polymers 2*; Gordon and Breach, Science Publishers, Inc.: New York, 1986; pp 290–309.

(74) Williams, J. C. L.; Watson, S. J.; Boydell, P. Properties. In *Nylon Plastics Handbook*; Kohan, M. I., Ed.; Munich, 1995; pp 291–360.

(75) Murthy, N. S.; Stamm, M.; Sibilia, J. P.; Krimm, S. Structural Changes Accompanying Hydration in Nylon 6. *Macromolecules* **1989**, *22* (3), 1261–1267.

(76) Reimschuessel, H. K. Relationships on the Effect of Water on Glass Transition Temperature and Young's Modulus of Nylon 6. *J. Polym. Sci. A* **1978**, *16* (6), 1229–1236.

(77) Lim, L.-T.; Britt, I. J.; Tung, M. A. Sorption and Transport of Water Vapor in Nylon 6,6 Film. *J. Appl. Polym. Sci.* **1999**, *71* (2), 197–206.

(78) Kemmish, D. J. *Practical Guide to High Performance Engineering Plastics*; Smithers Rapra: Shawbury, 2011; pp 47–56.

(79) Panar, M.; Avakian, P.; Blume, R. C.; Gardner, K. H.; Gierke, T. D.; Yang, H. H. Morphology of Poly(*p*-Phenylene Terephthalamide) Fibers. *J. Polym. Sci. B* **1983**, *21* (10), 1955–1969.

(80) Hindeleh, A. M.; Halim, N. A.; Ziq, K. A. Solid-State Morphology and Mechanical Properties of Kevlar 29 Fiber. *J. Macromol. Sci. B* **1984**, *23* (3), 289–309.

(81) Akato, K.; Bhat, G. High Performance Fibers From Aramid Polymers. In *Structure and Properties of High-Performance Fibers*; Duxford, UK, 2017; pp 245–266.

(82) Yang, H. H. Nomex Aramid Fiber. In *Handbook of Fiber Science and Technology Volume 3*; Lewin, M., Preston, J., Eds.; New York, 1993; pp 77–178.

(83) Starkweather, H. W.; Moore, G. E.; Hansen, J. E.; Roder, T. M.; Brooks, R. E. Effect of Crystallinity on the Properties of Nylons. *J. Polym. Sci. A* **1956**, *21* (98), 189–204.

(84) Starkweather, H. W.; Brooks, R. E. Effect of Spherulites on the Mechanical Properties of Nylon 66. *J. Appl. Polym. Sci.* **1959**, *1* (2), 236–239.

(85) Miri, V.; Persyn, O.; Lefebvre, J. M.; Séguéla, R. Effect of Water Absorption on the Plastic Deformation Behavior of Nylon 6. *Eur. Polym. J.* **2009**, *45* (3), 757–762.

(86) Shan, G.-F.; Yang, W.; Yang, M.-B.; Xie, B.-H.; Feng, J.-M.; Fu, Q. Effect of Temperature and Strain Rate on the Tensile Deformation of Polyamide 6. *Polymer* **2007**, *48* (10), 2958–2968.

(87) DuPont. Minlon® and Zytel® Design Guide - Module II. *dupont.com*.

(88) Miri, V.; Persyn, O.; Lefebvre, J. M.; Séguéla, R. Effect of Water Absorption on the Plastic Deformation Behavior of Nylon 6. *Eur. Polym. J.* **2009**, *45* (3), 757–762.

(89) Inoue, K.; Hoshino, S. Swelling of Nylon 6 Film Due to Water Sorption. *Journal of Polymer Science: Polymer Physics Edition* **1976**, *14* (8), 1513–1526.

(90) Marchildon, K. Polyamides - Still Strong After Seventy Years. *Macromol. React. Eng.* **2011**, *5* (1), 22–54.

(91) Chapman, R. D.; Holmer, D. A.; Pickett, O. A.; Lea, K. R.; Saunders, J. H. Relationships Between Chemical Structure and Properties of Fibers From Certain Partially Aromatic

Polyamides. *Textile Research Journal* **1981**, *51* (9), 564–573.

(92) Brisson, J.; Côté, P. Factors Affecting the Miscibility of Nylon-6I/Nylon-6,6. *Macromolecules* **1996**, *29* (5), 1839–1841.

(93) Gorton, B. S. Adhesive Properties of Polyisophthalamides. *J. Appl. Polym. Sci.* **1965**, *9* (11), 3753–3758.

(94) Eersels, K. L. L.; Groeninckx, G. Influence of Interchange Reactions on the Crystallization and Melting Behaviour of Polyamide Blends as Affected by the Processing Conditions. *Polymer* **1996**, *37* (6), 983–989.

(95) Berti, C.; Celli, A.; Marchese, P.; Sullalti, S.; Vannini, M.; Lorenzetti, C. Transamidations in Melt-Mixed MXD6 and PA6I-6T Polyamides: 1. Determination of the Degree of Randomness and Block Length by 1H-NMR Analysis. *Eur. Polym. J.* **2012**, *48* (11), 1923–1931.

(96) Puglisi, C.; Samperi, F.; Di Giorgi, S.; Montaudo, G. Exchange Reactions Occuring Through Active Chain Ends. MALDI-TOF Characterization of Copolymers From Nylon 6,6 and Nylon 6,10. *Macromolecules* **2003**, *36* (4), 1098–1107.

(97) Eersels, K. L. L.; Groeninckx, G.; Koch, M. H. J.; Reynaers, H. Influence of Transreaction Processes on the Morphology of Semicrystalline Aliphatic/ Aromatic Polyamide Blends. *Polymer* **1998**, *39* (17), 3893–3900.

(98) Kotliar, A. M. Interchange Reactions Involving Condensation Polymers. *J. Polym. Sci. Macromol. Rev.* **1981**, *16* (1), 367–395.

(99) Xanthos, M.; Warth, H. Effects of Transreactions on the Compatibility and Miscibility of Blends of Condensation Polymers. In *Transreactions in Condensation Polymers*; Fakirov, S., Ed.; Weinhein, 1999; pp 411–428.

(100) Miller, I. K. Amide-Exchange Reactions in Mixtures of N-Alkyl Amides and in Polyamide Melt Blends. *J. Polym. Sci. A* **1976**, *14* (6), 1403–1417.

(101) Ellis, T. S. Critical Miscibility Limits in Blends of Aliphatic Polyamides Containing an Aromatic Polyamide. *Polymer* **1990**, *31*, 1058–1064.

(102) Ellis, T. S. Miscibility and Immiscibility of Polyamide Blends. *Macromolecules* **1989**, *22* (2), 742–754.

(103) Samperi, F.; Montaudo, M. S.; Puglisi, C.; Di Giorgi, S.; Montaudo, G. Structural Characterization of Copolyamides Synthesized via the Facile Blending of Polyamides. *Macromolecules* **2004**, *37* (17), 6449–6459.

(104) Kyotani, M. Solution Crystallization of Blends of Nylon 6 and Nylon 12. *J. Macromol. Sci. B* **1982**, *21* (2), 219–230.

(105) Ong, E. S.; Kim, Y.; Williams, H. L. Dynamic Mechanical Properties of Some Nylons and Their Blends. *J. Appl. Polym. Sci.* **1986**, *31* (2), 367–383.

(106) Xie, T.; Yang, G. Effects of Maleated Styrene–(Ethylene-*co*-Butene)–Styrene on Compatibilization and Properties of Nylon-12,12/Nylon-6 Blends. *J. Appl. Polym. Sci.* **2004**, *93* (3), 1446–1453.

(107) Lake, W. B.; Kalakkunnath, S.; Kalika, D. S. Crystallization, Melting, and Rheology of Reactive Polyamide Blends. *J. Appl. Polym. Sci.* **2004**, *94* (3), 1245–1252.

(108) Fornes, T. D.; Paul, D. R. Crystallization Behavior of Nylon 6 Nanocomposites. *Polymer*

2003, *44* (14), 3945–3961.

(109) Miri, V.; Elkoun, S.; Peurton, F.; Vanmansart, C.; Lefebvre, J. M.; Krawczak, P.; Séguéla, R. Crystallization Kinetics and Crystal Structure of Nylon6-Clay Nanocomposites: Combined Effects of Thermomechanical History, Clay Content, and Cooling Conditions. *Macromolecules* **2008**, *41* (23), 9234–9244.

(110) Okada, A.; Usuki, A. Twenty Years of Polymer-Clay Nanocomposites. *Macromol. Mater. Eng.* **2006**, *291* (12), 1449–1476.

(111) Frihi, D.; Layachi, A.; Gherib, S.; Stoclet, G.; Masenelli-Varlot, K.; Satha, H.; Séguéla, R. Crystallization of Glass-Fiber-Reinforced Polyamide 66 Composites: Influence of Glass-Fiber Content and Cooling Rate. *Comp. Sci. Technol.* **2016**, *130* (C), 70–77.

(112) Karger-Kocsis, J.; Friedrich, K. Fracture Behavior of Injection-Molded Short and Long Glass Fiber—Polyamide 6.6 Composites. *Comp. Sci. Technol.* **1988**, *32* (4), 293–325.

(113) Curtis, P. T.; Bader, M. G.; Bailey, J. E. The Stiffness and Strength of a Polyamide Thermoplastic Reinforced with Glass and Carbon Fibres. *J. Mater. Sci.* **1978**, *13* (2), 377–390.

(114) Bowyer, W. H.; Bader, M. G. On the Re-Inforcement of Thermoplastics by Imperfectly Aligned Discontinuous Fibres. *J. Mater. Sci.* **1972**, *7* (11), 1315–1321.

(115) Thomason, J. L. The Influence of Fibre Length, Diameter and Concentration on the Strength and Strain to Failure of Glass Fibre-Reinforced Polyamide 6,6. *Compos. Part A Appl. Sci. Manuf.* **2008**, *39* (10), 1618–1624.

(116) Shaharuddin, S. I. S.; Salit, M. S.; Zainudin, E. S. A Review of the Effect of Moulding Parameters on the Performance of Polymeric Composite Injection Moulding. *Turkish J. Eng. Env. Sci.* **2006**, *30*, 23–34.

(117) Mortazavian, S.; Fatemi, A. Fatigue of Short Fiber Thermoplastic Composites: a Review of Recent Experimental Results and Analysis. *Int. J. Fatigue* **2017**, *102*, 171–183.

(118) Akay, M.; Barkley, D. Fibre Orientation and Mechanical Behaviour in Reinforced Thermoplastic Injection Mouldings. *J. Mater. Sci.* **1991**, *26* (10), 2731–2742.

(119) Horst, J. J.; Spoormaker, J. L. Fatigue Fracture Mechanisms and Fractography of Short-Glassfibre-Reinforced Polyamide 6. *J. Mater. Sci.* **1997**, *32* (14), 3641–3651.

(120) Skourlis, T. P.; Pochiraju, K.; Chassapis, C.; Manoochehri, S. Structure-Modulus Relationships for Injection-Molded Long Fiber-Reinforced Polyphthalamides. *Composites Part B* **1998**, *29* (3), 309–319.

(121) Bernasconi, A.; Davoli, P.; Basile, A.; Filippi, A. Effect of Fibre Orientation on the Fatigue Behaviour of a Short Glass Fibre Reinforced Polyamide-6. *Int. J. Fatigue* **2007**, *29* (2), 199–208.

(122) Guster, C.; Pinter, G.; Mösenbacher, A.; Eichlseder, W. Evaluation of a Simulation Process for Fatigue Life Calculation of Short Fibre Reinforced Plastic Components. *Procedia Eng.* **2011**, *10*, 2104–2109.

(123) Sonsino, C. M.; Moosbrugger, E. Fatigue Design of Highly Loaded Short-Glass-Fibre Reinforced Polyamide Parts in Engine Compartments. *Int. J. Fatigue* **2008**, *30* (7), 1279–1288.

(124) Pluddemann, E. P. *Silane Coupling Agents*, 2nd ed.; Plenum Press: New York, 1991.

(125) Jenneskens, L. W.; Venema, A.; Van Veenendaal, N.; Huysmans, W. G. B. Evidence for Interphasial Amide Formation Between Surface-Bound Poly(3-Aminopropyltrisiloxane) and Polyamide-6 in Glass Bead Reinforced Polyamide-6 Model Composites. *J. Polym. Sci. A* **1992**, *30* (1), 133–136.

(126) Jenneskens, L. W.; Schuurs, H. E. C.; Simons, D. J.; Willems, L. Molecular Mechanisms of Adhesion Promotion by Silane Coupling Agents in Glass Bead-Reinforced Polyamide-6 Model Composites. *Composites* **1994**, *25* (7), 504–511.

(127) Laura, D. M.; Keskkula, H.; Barlow, J. W.; Paul, D. R. Effect of Glass Fiber Surface Chemistry on the Mechanical Properties of Glass Fiber Reinforced, Rubber-Toughened Nylon 6. *Polymer* **2002**, *43* (17), 4673–4687.

(128) Cotterell, B.; Chia, J. Y. H.; Hbaieb, K. Fracture Mechanisms and Fracture Toughness in Semicrystalline Polymer Nanocomposites. *Eng. Fract. Mech.* **2007**, *74* (7), 1054–1078.

(129) Alvi, M. U.; Zulfiqar, S.; Yavuz, C. T.; Kweon, H.-S.; Sarwar, M. I. Influence of Aminosilane Coupling Agent on Aromatic Polyamide/Intercalated Clay Nanocomposites. *Ind. Eng. Chem. Res.* **2013**, *52* (21), 6908–6915.

(130) Tjong, S. C. Structural and Mechanical Properties of Polymer Nanocomposites. *Mater. Sci. Eng. R Rep.* **2006**, *53* (3-4), 73–197.

(131) Fornes, T. D.; Yoon, P. J.; Hunter, D. L.; Keskkula, H.; Paul, D. R. Effect of Organoclay Structure on Nylon 6 Nanocomposite Morphology and Properties. *Polymer* **2002**, *43* (22), 5915–5933.

(132) Besco, S.; Lorenzetti, A.; Roso, M.; Modesti, M. PA66/PA12/Clay Based Nanocomposites: Morphology and Physical Properties. *Polym. Adv. Technol.* **2010**, *22* (12), 1563–1571.

(133) Xie, W.; Gao, Z.; Pan, W.-P.; Hunter, D.; Singh, A.; Vaia, R. Thermal Degradation Chemistry of Alkyl Quaternary Ammonium Montmorillonite. *Chem. Mater.* **2001**, *13* (9), 2979–2990.

(134) Xiao, J.; Wang, S.; Lu, P.; Hu, Y. Effect of Organically Modified Montmorillonite on Thermal Degradation Mechanism of Polycarbonate Nanocomposites. *Procedia Eng.* **2013**, *62*, 791–796.

(135) Heim, M.; Römer, L.; Scheibel, T. Hierarchical Structures Made of Proteins. the Complex Architecture of Spider Webs and Their Constituent Silk Proteins. *Chem. Soc. Rev.* **2010**, *39* (1), 156–164.

(136) Johnson, J. C.; Korley, L. T. J. Enhanced Mechanical Pathways Through Nature's Building Blocks: Amino Acids. *Soft Matter* **2012**, *8* (45), 11431–12.

(137) Lintz, E. S.; Scheibel, T. R. Dragline, Egg Stalk and Byssus: a Comparison of Outstanding Protein Fibers and Their Potential for Developing New Materials. *Adv. Funct. Mater.* **2013**, *23* (36), 4467–4482.

(138) Kluge, J. A.; Rabotyagova, O.; Leisk, G. G.; Kaplan, D. L. Spider Silks and Their Applications. *Trends Biotechnol.* **2008**, *26* (5), 244–251.

(139) Giesa, T.; Arslan, M.; Pugno, N. M.; Buehler, M. J. Nanoconfinement of Spider Silk Fibrils Begets Superior Strength, Extensibility, and Toughness. *Nano Lett.* **2011**, *11* (11), 5038–5046.

(140) Xu, M.; Lewis, R. V. Structure of a Protein Superfiber: Spider Dragline Silk. *Proc. NatI. Acad. Sci. USA* **1990**, *87* (18), 7120–7124.

(141) Hardy, J. G.; Römer, L. M.; Scheibel, T. R. Polymeric Materials Based on Silk Proteins. *Polymer* **2008**, *49* (20), 4309–4327.

(142) Simmons, A. H.; Michal, C. A.; Jelinski, L. W. Molecular Orientation and Two-Component Nature of the Crystalline Fraction of Spider Dragline Silk. *Science* **1996**, *271* (5245), 84–87.

(143) Lefèvre, T.; Rousseau, M.-E.; Pézolet, M. Protein Secondary Structure and Orientation in Silk as Revealed by Raman Spectromicroscopy. *Biophys. J.* **2007**, *92* (8), 2885–2895.

(144) Tian, L.; Croisier, E.; Frauenrath, H. Materials Taking a Lesson From Nature. *CHIMIA* **2013**, *67* (11), 782–787.

(145) Becker, N.; Oroudjev, E.; Mutz, S.; Cleveland, J. P.; Hansma, P. K.; Hayashi, C. Y.; Makarov, D. E.; Hansma, H. G. Molecular Nanosprings in Spider Capture-Silk Threads. *Nat. Mater.* **2003**, *2* (4), 278–283.

(146) Du, N.; Yang, Z.; Liu, X. Y.; Li, Y.; Xu, H. Y. Structural Origin of the Strain-Hardening of Spider Silk. *Adv. Funct. Mater.* **2011**, *21* (4), 772–778.

(147) O'Brien, J. P.; Fahnestock, S. R.; Termonia, Y.; Gardner, K. H. Nylons From Nature: Synthetic Analogs to Spider Silk. *Adv. Mater.* **1998**, *10* (15), 1185–1195.

(148) Jelinski, L. W. Establishing the Relationship Between Structure and Mechanical Function in Silks. *Curr. Opin. Solid State Mater. Sci.* **1998**, *3* (3), 237–245.

(149) Eisoldt, L.; Smith, A.; Scheibel, T. Decoding the Secrets of Spider Silk. *Mater. Today* **2011**, *14* (3), 80–86.

(150) Blackledge, T. A. Silken Toolkits: Biomechanics of Silk Fibers Spun by the Orb Web Spider Argiope Argentata (Fabricius 1775). *Journal of Experimental Biology* **2006**, *209* (13), 2452–2461.

(151) Sibanda, B. L.; Thornton, J. M. β-Hairpin Families in Globular Proteins. *Nature* **1985**, *316* (6024), 170–174.

(152) Milner-White, E. J.; Poet, R. Four Classes of β-Hairpins in Proteins. *Biochem. J.* **1986**, *240* (1), 289–292.

(153) Roche, D. B.; Do Viet, P.; Bakulina, A.; Hirsh, L.; Tosatto, S. C. E.; Kajava, A. V. Classification of β-Hairpin Repeat Proteins. *J. Struct. Biol.* **2018**, *201* (2), 130–138.

(154) Kajava, A. V.; Baxa, U.; Wickner, R. B.; Steven, A. C. A Model for Ure2p Prion Filaments and Other Amyloids: the Parallel Superpleated β-Structure. *Proc. NatI. Acad. Sci. USA* **2004**, *101* (21), 7885–7890.

(155) Kajava, A. V.; Aebi, U.; Steven, A. C. The Parallel Superpleated Beta-Structure as a Model for Amyloid Fibrils of Human Amylin. *J. Mol. Biol.* **2005**, *348* (2), 247–252.

(156) Tycko, R. Progress Towards a Molecular-Level Structural Understanding of Amyloid Fibrils. *Curr. Opin. Struct. Biol.* **2004**, *14* (1), 96–103.

(157) Selkoe, D. J. Folding Proteins in Fatal Ways. *Nature* **2003**, *426* (6968), 900–904.

(158) Makin, O. S.; Serpell, L. C. Structures for Amyloid Fibrils. *FEBS J.* **2005**, *272* (23), 5950–5961.

(159) Blanco, F. J.; Rivas, G.; Serrano, L. A Short Linear Peptide That Folds Into a Native Stable β-Hairpin in Aqueous Solution. *Nat. Struct. Mol. Biol.* **1994**, *1* (9), 584–590.

(160) Smeenk, J. M.; Otten, M. B. J.; Thies, J.; Tirrell, D. A.; Stunnenberg, H. G.; van Hest, J. C. M. Controlled Assembly of Macromolecular β-Sheet Fibrils. *Angew. Chem.* **2005**, *117* (13), 2004–2007.

(161) Dong, S.-L.; Löweneck, M.; Schrader, T. E.; Schreier, W. J.; Zinth, W.; Moroder, L.; Renner, C. A Photocontrolled β-Hairpin Peptide. *Chem. Eur. J.* **2006**, *12* (4), 1114–1120.

(162) Lashuel, H. A.; LaBrenz, S. R.; Woo, L.; Serpell, L. C.; Kelly, J. W. Protofilaments, Filaments, Ribbons, and Fibrils From Peptidomimetic Self-Assembly: Implications for Amyloid Fibril Formation and Materials Science. *J. Am. Chem. Soc.* **2000**, *122* (22), 5262–5277.

(163) Eckhardt, D.; Groenewolt, M.; Krause, E.; Börner, H. G. Rational Design of Oligopeptide Organizers for the Formation of Poly(Ethylene Oxide) Nanofibers. *Chem. Commun.* **2005**, *8* (22), 2814–2816.

(164) Winningham, M. J.; Sogah, D. Y. Evidence for Intramolecular Hydrogen Bonding in Beta-Alanine Derivatives of 2,8-Dimethylphenoxathiin 4,6-Dicarboxylic Acid. Model Studies for Nucleation of Parallel Beta-Sheets. *J. Am. Chem. Soc.* **1994**, *116* (24), 11173–11174.

(165) Winningham, M. J.; Sogah, D. Y. A Modular Approach to Polymer Architecture Control via Catenation of Prefabricated Biomolecular Segments: Polymers Containing Parallel β-Sheets Templated by a Phenoxathiin-Based Reverse Turn Mimic. *Macromolecules* **1997**, *30* (4), 862–876.

(166) Rathore, O.; Winningham, M. J.; Sogah, D. Y. A Novel Silk-Based Segmented Block Copolymer Containing GlyAlaGlyAla β-Sheets Templated by Phenoxathiin. *J. Polym. Sci. A* **2000**, *38* (2), 352–366.

(167) Rathore, O.; Sogah, D. Y. Nanostructure Formation Through β-Sheet Self-Assembly in Silk-Based Materials. *Macromolecules* **2001**, *34* (5), 1477–1486.

(168) Wagner, G.; Feigel, M. Parallel B-Sheet Conformation in Macrocycles. *Tetrahedron* **1993**, *49* (47), 10831–10842.

(169) Scobbo, J. J., Jr; Goettler, L. A. Applications of Polymer Alloys and Blends. In *Polymer Blends Handbook*; Utracki, L. A., Ed.; Springer Netherlands: Dordrecht, 2003; pp 951–976.

(170) Xanthos, M. Interfacial Agents for Multiphase Polymer Systems: Recent Advances. *Polym. Eng. Sci.* **1988**, *28* (21), 1392–1400.

(171) Utracki, L. A. Compatibilization of Polymer Blends. *Can. J. Chem.* **2002**, *80*, 1008–1016.

(172) Cigana, P.; Favis, B. D.; Jerome, R. Diblock Copolymers as Emulsifying Agents in Polymer Blends: Influence of Molecular Weight, Architecture, and Chemical Composition. *J. Polym. Sci. B* **1996**, *34*, 1691–1700.

(173) Horak, Z.; Hlavata, D.; Fortelny, I.; Lednicky, F. Effect of Styrene-Butadiene Triblock Copolymer Structure on Its Compatibilization Efficiency in PS/PB and PS/PP Blends. *Polym. Eng. Sci.* **2002**, *42* (10), 2042–2047.

(174) Novitsky, T. F.; Lange, C. A.; Mathias, L. J.; Osborn, S.; Ayotte, R.; Manning, S. Eutectic Melting Behavior of Polyamide 10,T-*co*-6,T and 12,T-*co*-6,T Copolyterephthalamides. *Polymer* **2010**, *51* (11), 2417–2425.

(175) Edgar, O. B.; Hill, R. The P-Phenylene Linkage in Linear High Polymers: Some Structure–Property Relationships. *J. Polym. Sci. A* **1952**, *8* (1), 1–22.

(176) Harvey, E. D.; Hybart, F. J. The Melting and Crystallization of Copolymers of Nylon-6,6 and

Nylon-6,10 with Poly(Hexamethylene Terephthalamide) (Nylon-6T). *Polymer* **1971**, *12* (11), 711–716.

(177) Rwei, S.-P.; Tseng, Y.-C.; Chiu, K.-C.; Chang, S.-M.; Chen, Y.-M. The Crystallization Kinetics of Nylon 6/6T and Nylon 66/6T Copolymers. *Thermochim. Acta* **2013**, *555*, 37–45.

(178) Guan, X. Crystallization of Polyamide 66 Copolymers at High Supercoolings, University of Tennessee: Knoxville, 2004.

(179) Khoury, F. The Formation of Negatively Birefringent Spherulites in Polyhexamethylene Adipamide (Nylon 66). *J. Polym. Sci. A* **1958**, *33* (126), 389–403.

(180) Bunn, C. W.; Garner, E. V. The Crystal Structures of Two Polyamides ('Nylons'). *Proc. R. Soc. London, Ser. A* **1947**, *189* (1016), 39–68.

(181) Deshmukh, Y. S.; Wilsens, C. H. R. M.; Verhoef, R.; Hansen, M. R.; Dudenko, D.; Graf, R.; Klop, E. A.; Rastogi, S. Conformational and Structural Changes with Increasing Methylene Segment Length in Aromatic–Aliphatic Polyamides. *Macromolecules* **2016**, *49* (3), 950–962.

(182) Dasgupta, S.; Hammond, W. B.; Goddard, W. A., III. Crystal Structures and Properties of Nylon Polymers From Theory. *J. Am. Chem. Soc.* **1996**, *118* (49), 12291–12301.

(183) Lee, S. S.; Phillips, P. J. Melt Crystallized Polyamide 6.6 and Its Copolymers, Part I. Melting Point – Lamellar Thickness Relations in the Homopolymer. *Eur. Polym. J.* **2007**, *43* (5), 1933–1951.

(184) Harvey, E. D.; Hybart, F. J. The Melting and Crystallization of Copolymers of Nylon-6,6 and Nylon-6,10 with Poly(Hexamethylene Terephthalamide) (Nylon-6T). *Polymer* **1971**, *12* (11), 711–716.

(185) Brekner, M. J.; Schneider, H. A.; Cantow, H. J. Approach to the Composition Dependence of the Glass Transition Temperature of Compatible Polymer Blends: 1. *Polymer* **1988**, *29* (1), 78–85.

(186) Wunderlich, B. *Thermal Analysis of Polymeric Materials*; Springer-Verlag Berlin Heidelberg: Berlin, 2005.

(187) Cousin, T.; Galy, J.; Dupuy, J. Molecular Modelling of Polyphthalamides Thermal Properties: Comparison Between Modelling and Experimental Results. *Polymer* **2012**, *53* (15), 3203–3210.

(188) Duxbury, P. M.; Rzepniewski, E.; Moukarzel, C. Structure-Sensitive Properties of Materials. In *IUTAM Symposium on Nonlinear Analysis of Fracture. Solid Mechanics and its Applications, vol 49*; Willis, J. R., Ed.; Dordrecht, 1997; pp 257–264.

(189) Zhang, G.; Zhou, Y.-X.; Kong, Y.; Li, Z.-M.; Long, S.-R.; Yang, J. Semiaromatic Polyamides Containing Ether and Different Numbers of Methylene (2–10) Units: Synthesis and Properties. *RSC Adv.* **2014**, *4*, 63006–63015.

(190) Zhang, C.; Huang, X.; Zeng, X.; Cao, M.; Cai, T.; Jiang, S.; Yi, Q. Fluidity Improvement of Semiaromatic Polyamides: Modification with Oligomers. *J. Appl. Polym. Sci.* **2013**, *131* (7), 40058.

(191) Novitsky, T. F.; Lange, C. A.; Mathias, L. J.; Osborn, S.; Ayotte, R.; Manning, S. Eutectic Melting Behavior of Polyamide 10,T-*co*-6,T and 12,T-*co*-6,T Copolyterephthalamides. *Polymer* **2010**, *51* (11), 2417–2425.

(192) Garcia, J. M.; Garcia, F. C.; Serna, F.; la Pena, de, J. L. High-Performance Aromatic Polyamides. *Prog. Polym. Sci.* **2010**, *35* (5), 623–686.

(193) Ahmed, D.; Hongpeng, Z.; Haijuan, K.; Jing, L.; Yu, M.; Muhuo, Y. Microstructural Developments of Poly (*p*-Phenylene Terephthalamide) Fibers During Heat Treatment Process: a Review. *Mat. Res.* **2014**, *17* (5), 1180–1200.

(194) Banerjee, S.; Maji, S. High-Performance Processable Aromatic Polyamides. In *High Performance Polymers and Engineering Plastics*; Mittal, V., Ed.; Hoboken, New Jersey & Salem, Massachussets, 2011; pp 111–166.

(195) Alger, M. S. M. High-Temperature and Fire-Resistant Polymers. In *Specialty Polymers*; Dyson, R. W., Ed.; Springer US: Glasgow and London, 1987; pp 38–64.

(196) Minemawari, H.; Yamada, T.; Matsui, H.; Tsutsumi, J.; Haas, S.; Chiba, R.; Kumai, R.; Hasegawa, T. Inkjet Printing of Single-Crystal Films. *Nature* **2011**, *475* (7356), 364–367.

(197) Yuan, Y.; Giri, G.; Ayzner, A. L.; Zoombelt, A. P.; Mannsfeld, S. C. B.; Chen, J.; Nordlund, D.; Toney, M. F.; Huang, J.; Bao, Z. Ultra-High Mobility Transparent Organic Thin Film Transistors Grown by an Off-Centre Spin-Coating Method. *Nat. Commun.* **2014**, *5*, 1–9.

(198) Takimiya, K.; Osaka, I.; Mori, T.; Nakano, M. Organic Semiconductors Based on [1]Benzothieno[3,2-*b*][1]Benzothiophene Substructure. *Accounts Chem. Res.* **2014**, *47* (5), 1493–1502.

(199) Takimiya, K.; Shinamura, S.; Osaka, I.; Miyazaki, E. Thienoacene-Based Organic Semiconductors. *Adv. Mater.* **2011**, *23* (38), 4347–4370.

(200) Schweicher, G.; Lemaur, V.; Niebel, C.; Ruzié, C.; Diao, Y.; Goto, O.; Lee, W.-Y.; Kim, Y.; Arlin, J.-B.; Karpinska, J.; Kennedy, A. R.; Parkin, S. R.; Olivier, Y.; Mannsfeld, S. C. B.; Cornil, J.; Geerts, Y. H.; Bao, Z. Bulky End-Capped [1]Benzothieno[3,2-*b*]Benzothiophenes: Reaching High-Mobility Organic Semiconductors by Fine Tuning of the Crystalline Solid-State Order. *Adv. Mater.* **2015**, *27* (19), 3066–3072.

(201) Tsutsui, Y.; Schweicher, G.; Chattopadhyay, B.; Sakurai, T.; Arlin, J.-B.; Ruzié, C.; Aliev, A.; Ciesielski, A.; Colella, S.; Kennedy, A. R.; Lemaur, V.; Olivier, Y.; Hadji, R.; Sanguinet, L.; Castet, F.; Osella, S.; Dudenko, D.; Beljonne, D.; Cornil, J.; Samorì, P.; Seki, S.; Geerts, Y. H. Unraveling Unprecedented Charge Carrier Mobility Through Structure Property Relationship of Four Isomers of Didodecyl[1]Benzothieno[3,2-*b*][1]Benzothiophene. *Adv. Mater.* **2016**, *28* (33), 7106–7114.

(202) Nair, V. S.; Sun, J.; Qi, P.; Yang, S.; Liu, Z.; Zhang, D.; Ajayaghosh, A. Conjugated Random Donor–Acceptor Copolymers of [1]Benzothieno[3,2-*b*]Benzothiophene and Diketopyrrolopyrrole Units for High Performance Polymeric Semiconductor Applications. *Macromolecules* **2016**, *49* (17), 6334–6342.

(203) Mitsui, C.; Tanaka, Y.; Tanaka, S.; Yamagishi, M.; Nakahara, K.; Yano, M.; Sato, H.; Yamano, A.; Matsui, H.; Takeya, J.; Okamoto, T. High Performance Oxygen-Bridged N-Shaped Semiconductors with a Stabilized Crystal Phase and Blue Luminescence. *RSC Adv.* **2016**, *6*, 28966–28969.

(204) Nakahara, K.; Mitsui, C.; Okamoto, T.; Yamagishi, M.; Matsui, H.; Ueno, T.; Tanaka, Y.; Yano, M.; Matsushita, T.; Soeda, J.; Hirose, Y.; Sato, H.; Yamano, A.; Takeya, J. Furan Fused v-Shaped Organic Semiconducting Materials with High Emission and High Mobility. *Chem. Commun.* **2014**, *50* (40), 5342–5344.

(205) Dischendorfer, O. Über Die Kondensation Von Glyoxal Und β-Naphthol. *Monatsh.* **1939**, *73* (1), 45–56.

(206) Rosenthal, A.; Zaionchkovsky, A. The Condensation of Glyoxal with *p*-Cresol. *Can. J. Chem.* **1960**, *38* (11), 2277–2278.

(207) Coxworth, E. C. M. Reaction of Glyoxal at the Ortho Position of Phenols. Synthesis of 5*a*,10*b*-Dihydrobenzofuro[2,3-*b*]Benzofurans and 2-(3-Benzofuranyl)Phenols. *Can. J. Chem.* **1967**, *45* (15), 1777–1784.

(208) Banihashemi, A.; Pourabbas, B. Synthesis of Benzofuro(2,3-*b*)Benzofuran-2,9-Dicarboxylic Acid. a Potential Monomer. *Iran. Polym. J.* **1996**, *5*, 145–151.

(209) Pourabas, B.; Banihashemi, A. Polymers with Benzofuro-Benzofuran Structures. *Polym. Int.* **2002**, *51* (10), 1086–1099.

(210) Banihashemi, A.; Firoozifar, H. Synthesis and Characterization of Novel Aromatic Polyamides Derived From Two Heterocyclic Diamines. *Eur. Polym. J.* **2003**, *39* (2), 281–289.

(211) Rahmatpour, A. 5a,10b-Dihydrobenzofuro[2,3-*b*]Benzofuran Type Compounds and Related Products From *P*-Substituted Phenols and Glyoxal. *J. Heterocyclic Chem.* **2010**, *47* (5), 1011–1016.

(212) Krebs, F. C.; Faldt, A.; Thorup, N.; Bechgaard, K. Arrested Handedness and Disordered Stacking in Crystals of the Pre-Helical Molecule 7,8-Dioxa[6]Helicene. *CrystEngComm* **1999**, *1* (6), 21–23.

(213) Eskildsen, J.; Krebs, F. C.; Faldt, A.; Sommer-Larsen, P.; Bechgaard, K. Preparation and Structural Properties of 7,8-Dioxa[6]Helicenes and 7a,14c-Dihydro-7,8-Dioxa[6]Helicenes. *J. Org. Chem.* **2001**, *66* (1), 200–205.

(214) Hasan, M.; Pandey, A. D.; Khose, V. N.; Mirgane, N. A.; Karnik, A. V. Sterically Congested Chiral 7,8-Dioxa[6]Helicene and Its Dihydro Analogues: Synthesis, Regioselective Functionalization, and Unexpected Domino Prins Reaction. *Eur. J. Org. Chem.* **2015**, *2015* (17), 3702–3712.

(215) Nanbu, M.; Momonoi, K.; Oguro, S.; Kawase, Y. The Synthesis of the Benzofuro[2,3-*b*]Benzofuran Derivative. *B. Chem. Soc. Jpn.* **1975**, *48* (11), 3421–3422.

(216) Vera, W. J.; Laya, M. S.; Poon, P. S.; Banerjee, A. K.; Cabrera, E. V. Reagents for the Synthesis of Alkenes From Carbonyl Compounds: Applications in the Synthesis of Terpenoid Compounds. *ARKIVOC* **2013**, 396–417.

(217) Andreetti, G. D.; Bocelli, G.; Sgarabotto, P. *Gazz. Chim. Ital.* **1974**, *104*, 1127.

(218) Kawecki, R.; Mazurek, A. P.; Kozerski, L.; Maurin, J. K. Synthesis of Benzofuro[2,3-*b*]Benzofuran Derivatives Under Hoesch Reaction Conditions. *Synthesis* **1999**, *1999* (05), 751–753.

(219) Goldberg, I.; Shmueli, U. Crystal and Molecular Structure of [1]Benzothieno[2,3-*b*][1]Benzothiophene ($C_{14}H_8S_2$). *Acta Cryst. B* **1971**, *27* (11), 2164–2173.

(220) Gidron, O.; Diskin-Posner, Y.; Bendikov, M. α-Oligofurans. *J. Am. Chem. Soc.* **2010**, *132* (7), 2148–2150.

(221) Skrovanek, D. J.; Painter, P. C.; Coleman, M. M. Hydrogen Bonding in Polymers. 2. Infrared Temperature Studies of Nylon 11. *Macromolecules* **1986**, *19* (3), 699–705.

(222) Van Krevelen, D. W. *Properties of Polymers*, Third Edition. Elsevier Science B. V.: Amsterdam, The Netherlands, 1990.

(223) Kemmish, D. J. Semi-Aromatic Polyamides (Polyphthalamides). In *Practical Guide to High Performance Engineering Plastics*; Shawbury, Shrewsbury, Shropshire, United Kingdom, 2011; pp 47–56.

(224) Klauk, H. Organic Thin-Film Transistors. *Chem. Soc. Rev.* **2010**, *39* (7), 2643–25.

(225) Fu, C.; Lin, H.-P.; Macleod, J. M.; Krayev, A.; Rosei, F.; Perepichka, D. F. Unravelling the Self-Assembly of Hydrogen Bonded NDI Semiconductors in 2D and 3D. *Chem. Mater.* **2016**, *28* (3), 951–961.

(226) Głowacki, E. D.; Romanazzi, G.; Yumusak, C.; Coskun, H.; Monkowius, U.; Voss, G.; Burian, M.; Lechner, R. T.; Demitri, N.; Redhammer, G. J.; Sünger, N.; Suranna, G. P.; Sariciftci, S. Epindolidiones-Versatile and Stable Hydrogen-Bonded Pigments for Organic Field-Effect Transistors and Light-Emitting Diodes. *Adv. Funct. Mater.* **2014**, *25* (5), 776–787.

(227) Głowacki, E. D.; Irimia-Vladu, M.; Kaltenbrunner, M.; Gsiorowski, J.; White, M. S.; Monkowius, U.; Romanazzi, G.; Suranna, G. P.; Mastrorilli, P.; Sekitani, T.; Bauer, S.; Someya, T.; Torsi, L.; Sariciftci, N. S. Hydrogen-Bonded Semiconducting Pigments for Air-Stable Field-Effect Transistors. *Adv. Mater.* **2012**, *25* (11), 1563–1569.

(228) Marty, R.; Szilluweit, R.; Sánchez-Ferrer, A.; Bolisetty, S.; Adamcik, J.; Mezzenga, R.; Spitzner, E.-C.; Feifer, M.; Steinmann, S. N.; Corminboeuf, C.; Frauenrath, H. Hierarchically Structured Microfibers of "Single Stack" Perylene Bisimide and Quaterthiophene Nanowires. *ACS Nano* **2013**, *7* (10), 8498–8508.

(229) Wall, B. D.; Diegelmann, S. R.; Zhang, S.; Dawidczyk, T. J.; Wilson, W. L.; Katz, H. E.; Mao, H.-Q.; Tovar, J. D. Aligned Macroscopic Domains of Optoelectronic Nanostructures Prepared via Shear-Flow Assembly of Peptide Hydrogels. *Adv. Mater.* **2011**, *23* (43), 5009–5014.

(230) Yagai, S.; Seki, T.; Murayama, H.; Wakikawa, Y.; Ikoma, T.; Kikkawa, Y.; Karatsu, T.; Kitamura, A.; Honsho, Y.; Seki, S. Structural and Electronic Properties of Extremely Long Perylene Bisimide Nanofibers Formed Through a Stoichiometrically Mismatched, Hydrogen-Bonded Complexation. *Small* **2010**, *6* (23), 2731–2740.

(231) Yao, J.; Yu, C.; Liu, Z.; Luo, H.; Yang, Y.; Zhang, G.; Zhang, D. Significant Improvement of Semiconducting Performance of the Diketopyrrolopyrrole–Quaterthiophene Conjugated Polymer Through Side-Chain Engineering via Hydrogen-Bonding. *J. Am. Chem. Soc.* **2016**, *138* (1), 173–185.

(232) Chiron, J.; Galy, J.-P. Reactivity of the Acridine Ring: One-Pot Regioselective Single and Double Bromomethylation of Acridine and Some Derivatives. *Synlett* **2003**, *2003* (15), 2349–2350.

(233) Park, D. H.; Kang, S. O.; Lee, H.-J.; Nam, K. C.; Jeon, S. Synthesis and Electrochemistry of Diester-Anthraquinone as Lithium-Ion Selective Receptor. *Bull. Korean Chem. Soc.* **2001**, *22* (6), 638–640.

(234) Sharghi, H.; Khoshnood, A.; Doroodmand, M. M.; Khalifeh, R. Rapid, Eco-Friendly, and One-Pot Synthesis of New Lariat Ethers Based on Anthraquinone by Using ZnO Nanoparticles via"Mannich" Reaction Under Solvent-Free Condition. *J. Heterocyclic Chem.* **2015**, *53* (1), 164–174.

(235) Ghosh, K.; Kar, D. Anthraquinone Coupled Benzothiazole-Based Receptor for Selective

Sensing of Cu^{2+}. *J. Incl. Phenom. Macrocycl. Chem.* **2012**, *77* (1-4), 67–74.

(236) Desiraju, G. R.; Gavezzotti, A.; IUCr. Crystal Structures of Polynuclear Aromatic Hydrocarbons. Classification, Rationalization and Prediction From Molecular Structure. *Acta Crystallogr. B* **1989**, *45* (5), 473–482.

(237) Gellman, S. H.; Dado, G. P.; Liang, G. B.; Adams, B. R. Conformation-Directing Effects of a Single Intramolecular Amide-Amide Hydrogen Bond: Variable-Temperature NMR and IR Studies on a Homologous Diamide Series. *J. Am. Chem. Soc.* **1991**, *113* (4), 1164–1173.

(238) Gung, B. W.; Zhu, Z.; Zou, D.; Everingham, B.; Oyeamalu, A.; Crist, R. M.; Baudlier, J. Requirement for Hydrogen-Bonding Cooperativity in Small Polyamides: a Combined VT-NMR and VT-IR Investigation. *J. Org. Chem.* **1998**, *63* (17), 5750–5761.

(239) Gung, B. W.; MacKay, J. A.; Zou, D. Substituent Effect on Intramolecular Hydrogen Bonding in β-Amino Acid-Containing Polyamides. *J. Org. Chem.* **1999**, *64* (3), 700–706.

(240) Frey, B. L.; Corn, R. M. Covalent Attachment and Derivatization of Poly(L-Lysine) Monolayers on Gold Surfaces as Characterized by Polarization–Modulation FT-IR Spectroscopy. *Anal. Chem.* **1996**, *68* (18), 3187–3193.

(241) Lim, C. Y.; Owens, N. A.; Wampler, R. D.; Ying, Y.; Granger, J. H.; Porter, M. D.; Takahashi, M.; Shimazu, K. Succinimidyl Ester Surface Chemistry: Implications of the Competition Between Aminolysis and Hydrolysis on Covalent Protein Immobilization. *Langmuir* **2014**, *30* (43), 12868–12878.

(242) Kasama, K.; Kikuchi, K.; Nishida, Y.; Kokubun, H. Deactivation Mechanism of Excited Acridine and 9-Substituted Acridines in Water. *J. Phys. Chem.* **1981**, *85* (26), 4148–4153.

(243) Kellmann, A. Intersystem Crossing and Internal Conversion Quantum Yields of Acridine in Polar and Nonpolar Solvents. *J. Phys. Chem.* **1977**, *81* (12), 1195–1198.

(244) Ryan, E. T.; Xiang, T.; Johnston, K. P.; Fox, M. A. Absorption and Fluorescence Studies of Acridine in Subcritical and Supercritical Water. *J. Phys. Chem. A* **1997**, *101* (10), 1827–1835.

(245) Negrón-Encarnación, I.; Arce, R.; Jiménez, M. Characterization of Acridine Species Adsorbed on $(NH_4)_2SO_4$, SiO_2, Al_2O_3, and MgO by Steady-State and Time-Resolved Fluorescence and Diffuse Reflectance Techniques. *J. Phys. Chem. A* **2005**, *109* (5), 787–797.

(246) Becker, H. D. Unimolecular Photochemistry of Anthracenes. *Chem. Rev.* **1993**, *93* (1), 145–172.

(247) Bouas-Laurent, H.; Desvergne, J.-P.; Castellan, A.; Lapouyade, R. Photodimerization of Anthracenes in Fluid Solution: Structural Aspects. *Chem. Soc. Rev.* **2000**, *29* (1), 43–55.

(248) Bouas-Laurent, H.; Desvergne, J.-P.; Castellan, A.; Lapouyade, R. Photodimerization of Anthracenes in Fluid Solutions: (Part 2) Mechanistic Aspects of the Photocycloaddition and of the Photochemical and Thermal Cleavage. *Chem. Soc. Rev.* **2001**, *30* (4), 248–263.

(249) Lamm, J.-H.; Glatthor, J.; Weddeling, J.-H.; Mix, A.; Chmiel, J.; Neumann, B.; Stammler, H.-G.; Mitzel, N. W. Polyalkynylanthracenes – Syntheses, Structures and Their Behaviour Towards UV Irradiation. *Org. Biomol. Chem.* **2014**, *12* (37), 7355–7365.

(250) Abrahamsson, S.; Dahlen, B.; Löfgren, H.; Pascher, I. Lateral Packing of Hydrocarbon Chains. *Prog. Chem. Fats Other Lipids* **1978**, *16*, 125–143.

(251) Mayo, S. L.; Olafson, B. D.; Goddard, W. A. DREIDING: a Generic Force Field for Molecular

Simulations. *J. Phys. Chem.* **1990**, *94* (26), 8897–8909.

(252) CrysAlis PRO. Rigaku Oxford Diffraction 2015.

(253) Sheldrick, G. M. SHELXT – Integrated Space-Group and Crystal- Structure Determination. *Acta Cryst. A* **2015**, *71*, 1–6.

(254) Sheldrick, G. M. Crystal Structure Refinement with SHELXL. *Acta Cryst. C* **2015**, *71*, 1–6.

(255) Sheldrick, G. M.; IUCr. A Short History of SHELX. *Acta Cryst. A* **2008**, *64* (1), 112–122.

(256) Furche, F.; Ahlrichs, R.; Hättig, C.; Klopper, W.; Sierka, M.; Weigend, F. Turbomole. *WIREs Comput. Mol. Sci.* **2013**, *4* (2), 91–100.

(257) Perdew, J. P.; Burke, K.; Ernzerhof, M. Generalized Gradient Approximation Made Simple. *Phys. Rev. Lett.* **1996**, *77* (18), 3865–3868.

(258) Weigend, F.; Ahlrichs, R. Balanced Basis Sets of Split Valence, Triple Zeta Valence and Quadruple Zeta Valence Quality for H to Rn: Design and Assessment of Accuracy. *Phys. Chem. Chem. Phys.* **2005**, *7* (18), 3297–3299.

(259) Weigend, F. Accurate Coulomb-Fitting Basis Sets for H to Rn. *Phys. Chem. Chem. Phys.* **2006**, *8* (9), 1057–1059.

(260) Trofimov, A. B.; Schirmer, J. An Efficient Polarization Propagator Approach to Valence Electron Excitation Spectra. *J. Phys. B: At. Mol. Opt. Phys.* **1995**, *28*, 2299–2324.

(261) Dreuw, A.; Wormit, M. The Algebraic Diagrammatic Construction Scheme for the Polarization Propagator for the Calculation of Excited States. *WIREs Comput. Mol. Sci.* **2014**, *5* (1), 82–95.

(262) Adamo, C.; Barone, V. Toward Reliable Density Functional Methods Without Adjustable Parameters: the PBE0 Model. *J. Chem. Phys.* **1999**, *110* (13), 6158–6170.

(263) Hanwell, M. D.; Curtis, D. E.; Lonie, D. C.; Vandermeersch, T.; Zurek, E.; Hutchison, G. R. Avogadro: an Advanced Semantic Chemical Editor, Visualization, and Analysis Platform. *J. Cheminf.* **2012**, *4*, 17.

(264) Chai, J.-D.; Head-Gordon, M. Long-Range Corrected Hybrid Density Functionals with Damped Atom–Atom Dispersion Corrections. *Phys. Chem. Chem. Phys.* **2008**, *10* (44), 6615–6620.

(265) Weigend, F.; Ahlrichs, R. Balanced Basis Sets of Split Valence, Triple Zeta Valence and Quadruple Zeta Valence Quality for H to Rn: Design and Assessment of Accuracy. *Phys. Chem. Chem. Phys.* **2005**, *7* (18), 3297–3305.

(266) Marenich, A. V.; Cramer, C. J.; Truhlar, D. G. Universal Solvation Model Based on Solute Electron Density and on a Continuum Model of the Solvent Defined by the Bulk Dielectric Constant and Atomic Surface Tensions. *J. Phys. Chem. B* **2009**, *113* (18), 6378–6396.

Appendix

9 Appendix

9.1 Spectral Data for Synthesized Compounds

^{1}H NMR spectrum (DMSO-d^6, 400 MHz) of **2**

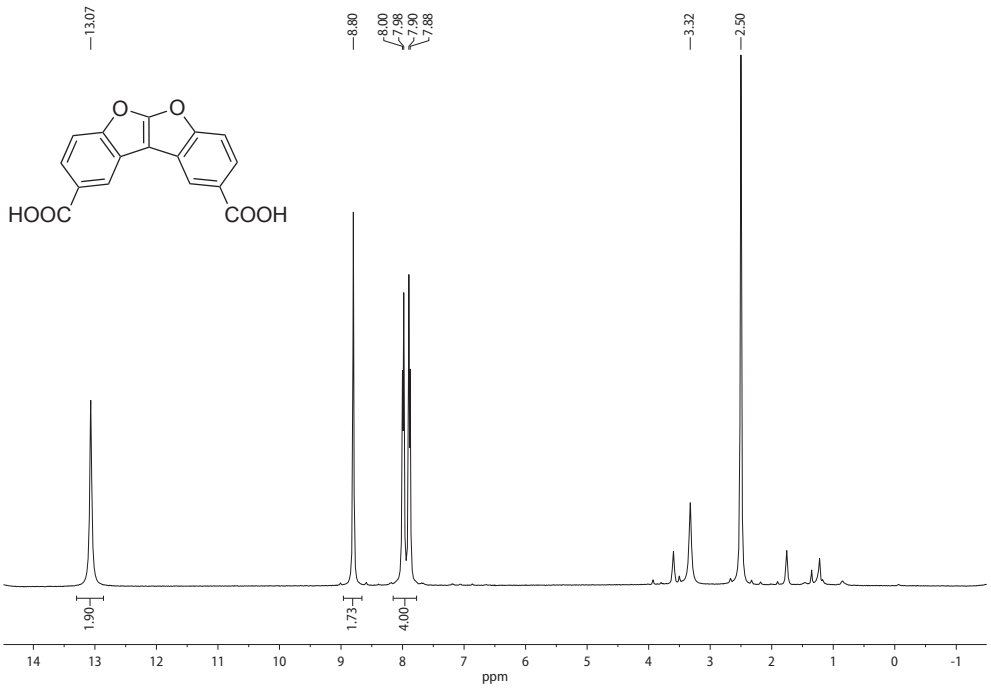

^{13}C NMR spectrum (DMSO-d^6, 101 MHz) of **2**

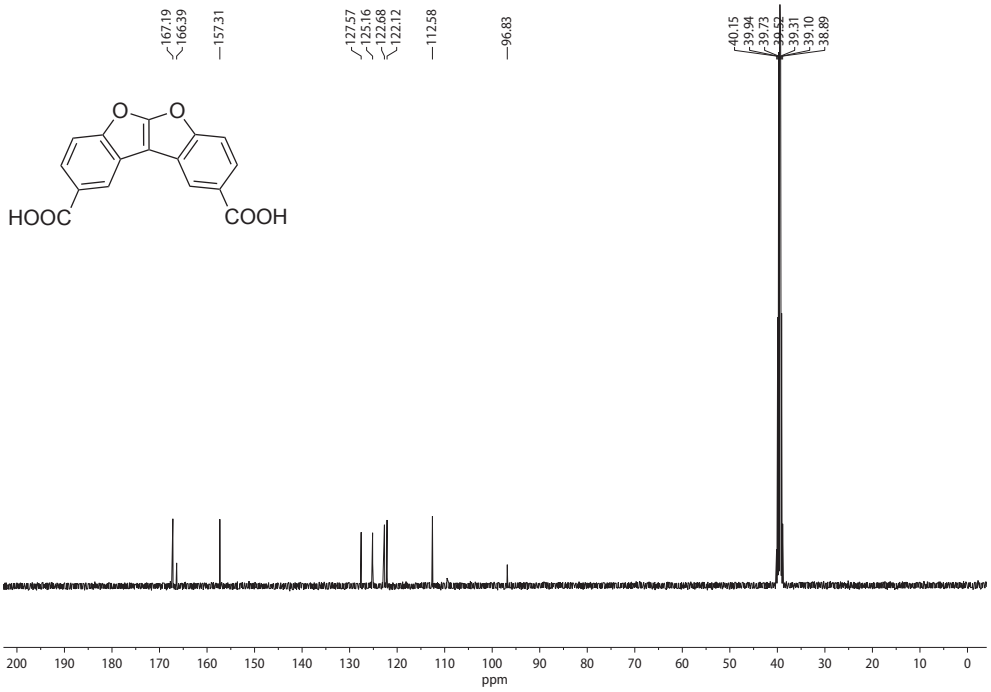

High-resolution mass spectrum (MALDI-TOF, negative-mode) of **2**

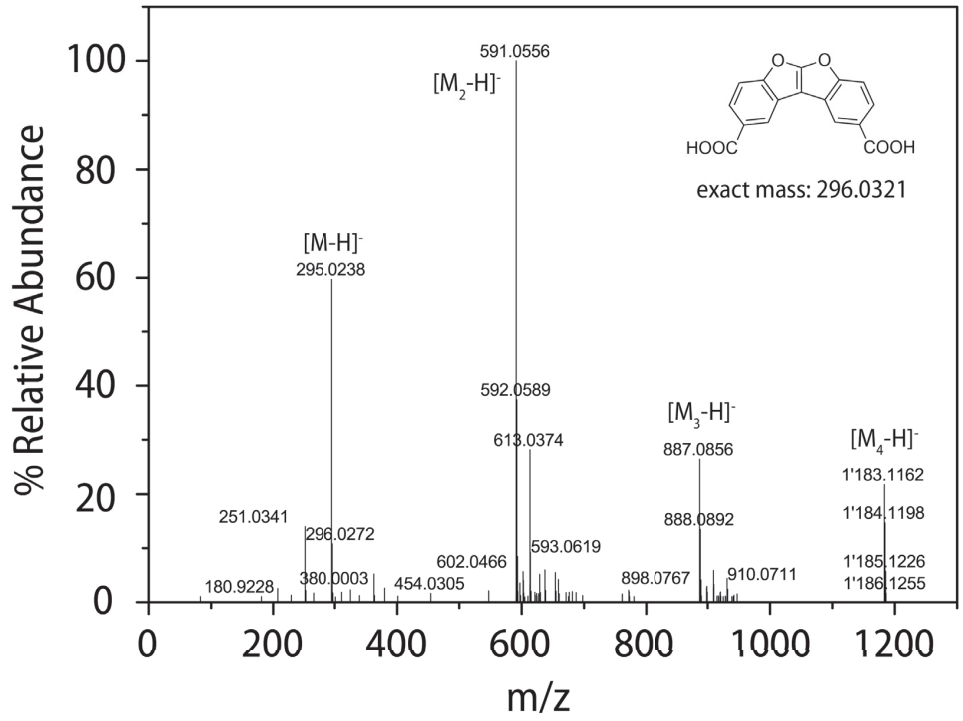

^{1}H NMR spectrum (DMSO-d^{6}, 400 MHz) of **3**

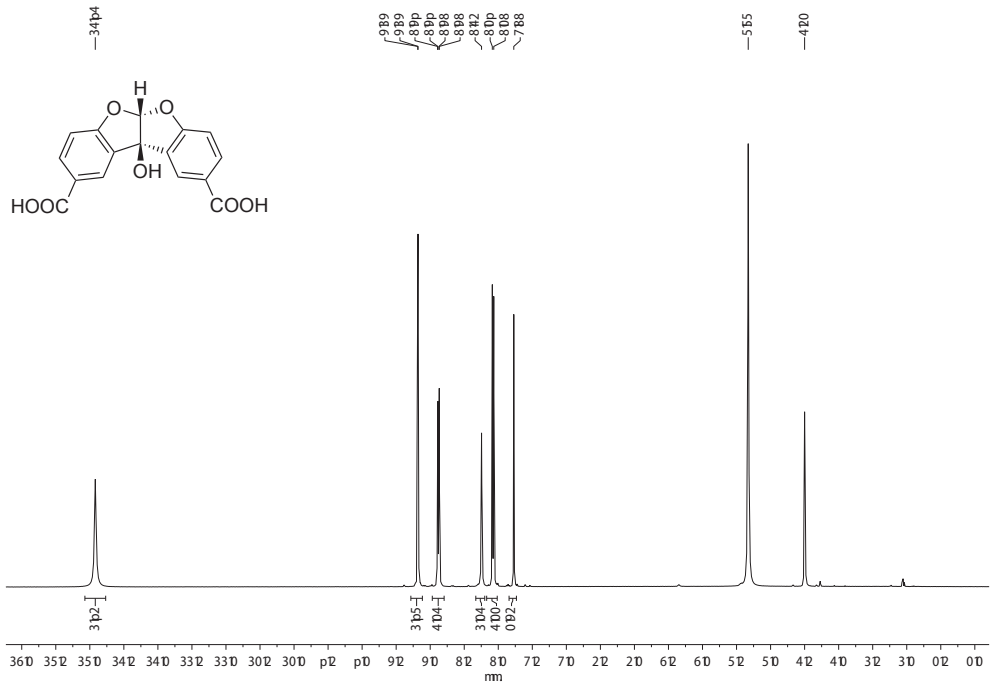

^{1}H-^{1}H COSY NMR spectrum (DMSO-*d*^{6}) of **3**

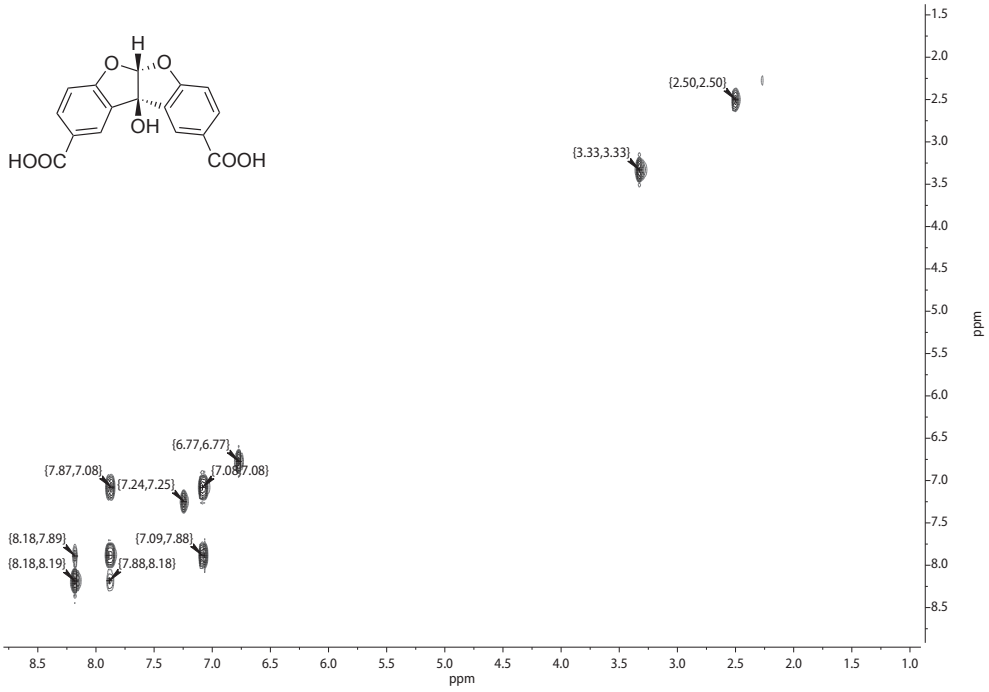

^{13}C NMR spectrum (DMSO-*d*^{6}, 101 MHz) of **3**

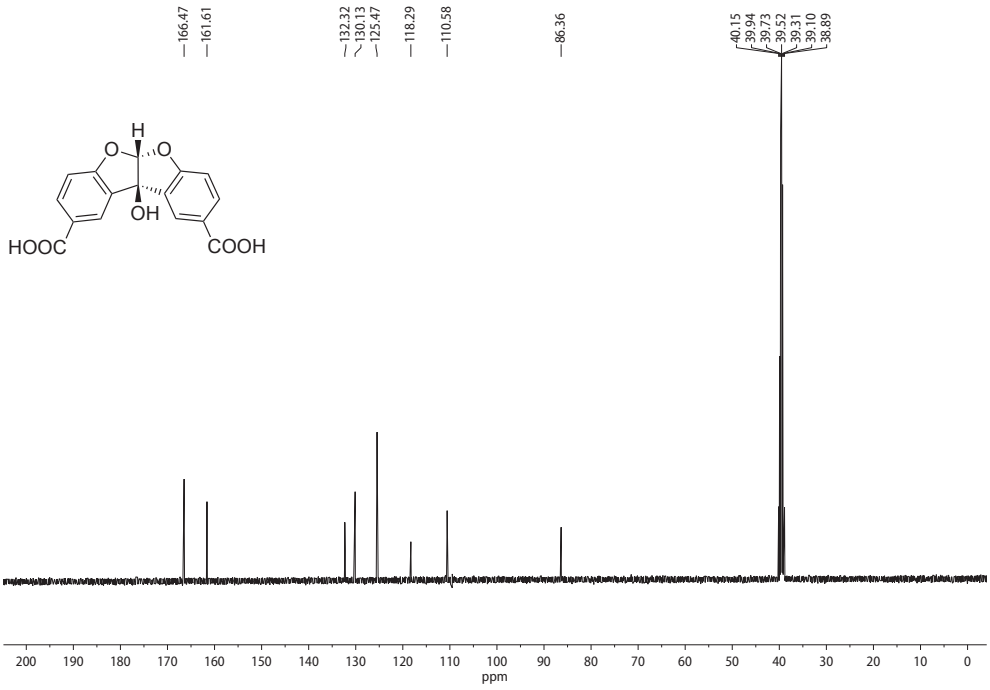

^{1}H-^{13}C HSQC NMR spectrum (DMSO-d_6) of **3**

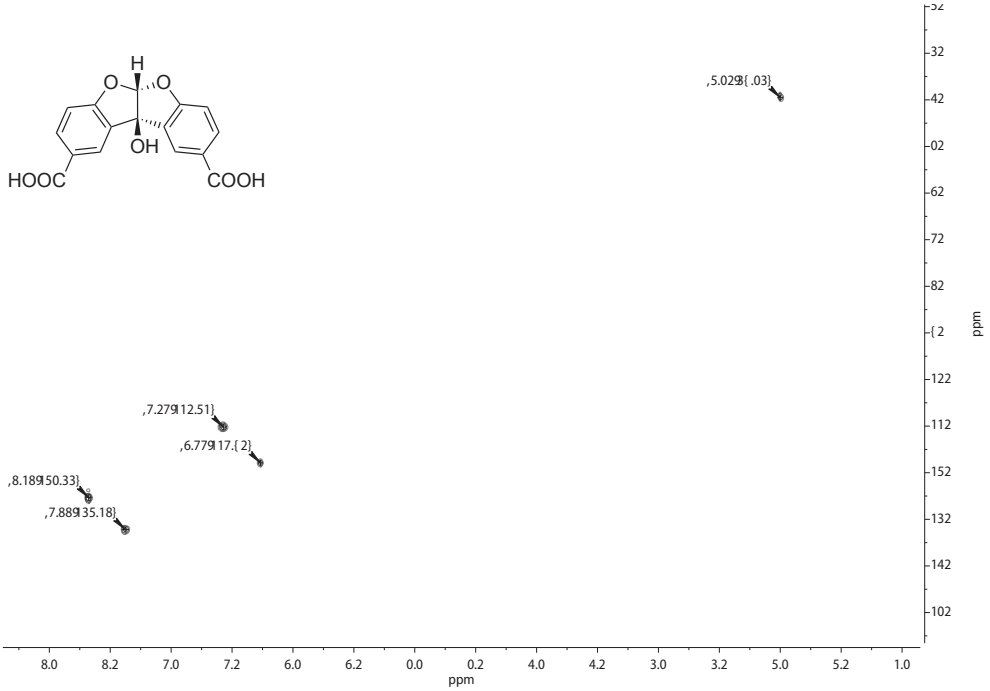

High-resolution mass spectrum (MALDI-TOF, negative-mode) of **3**

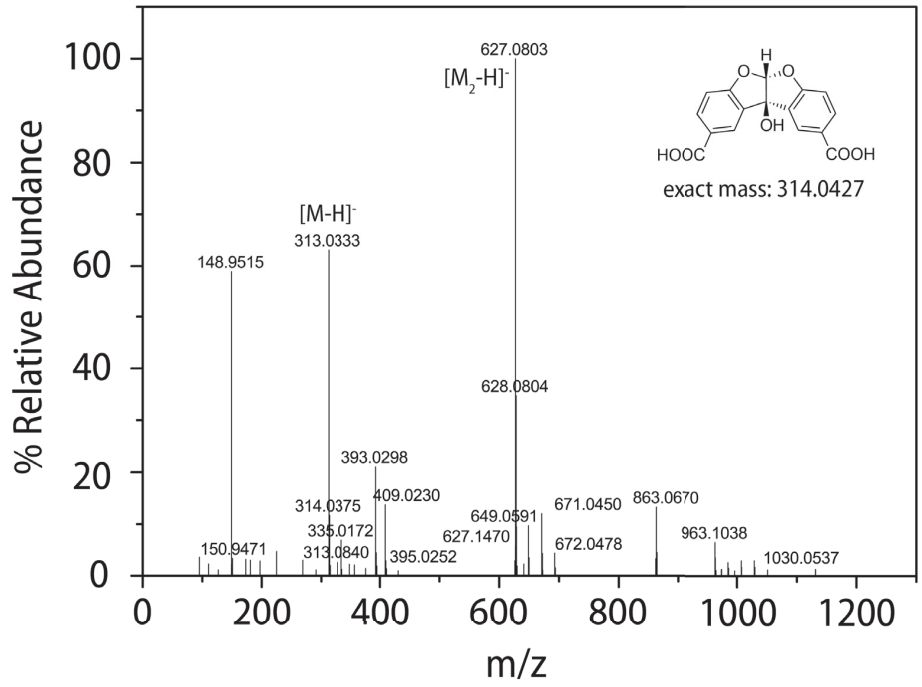

^{1}H NMR spectrum (DMSO-*d*^{6}, 400 MHz) of **4**

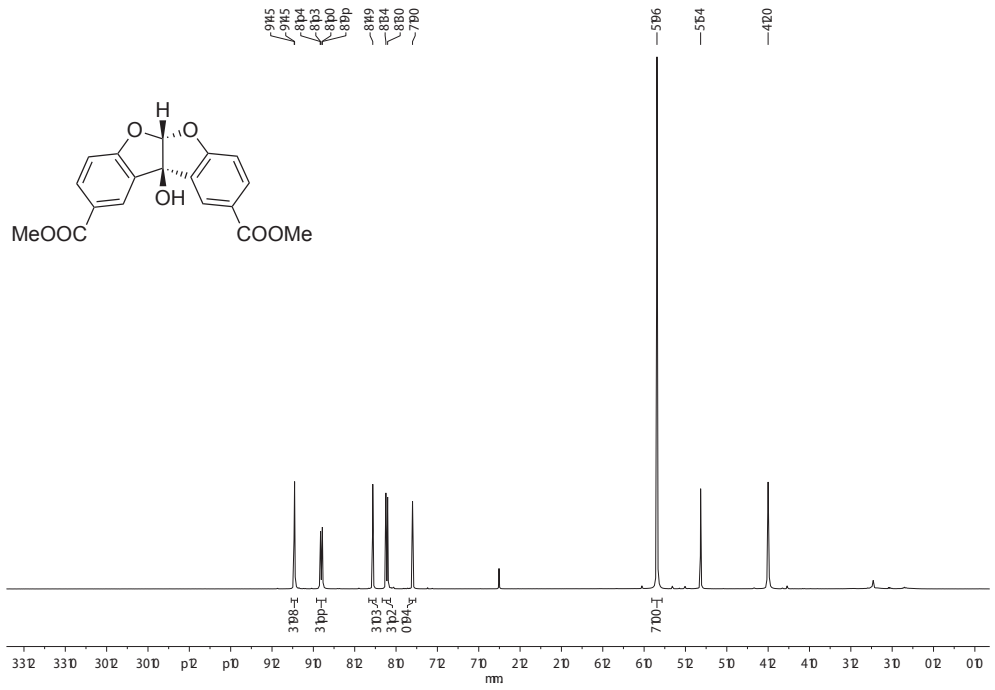

^{13}C NMR spectrum (DMSO-*d*^{6}, 101 MHz) of **4**

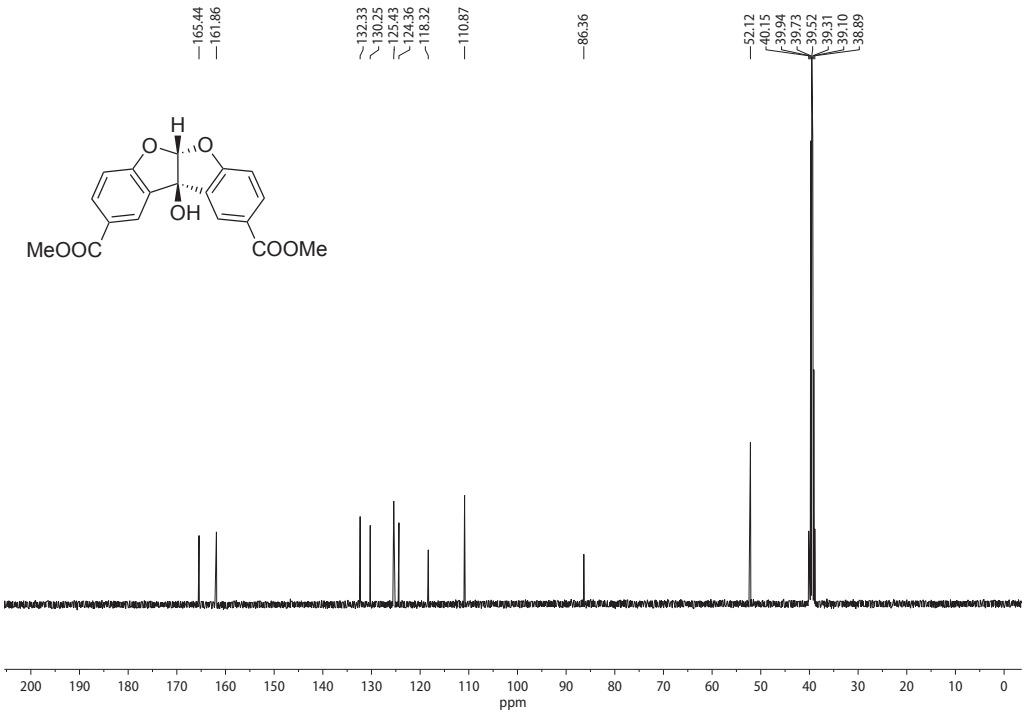

^{1}H NMR spectrum ($CDCl_3$, 400 MHz) of **5**

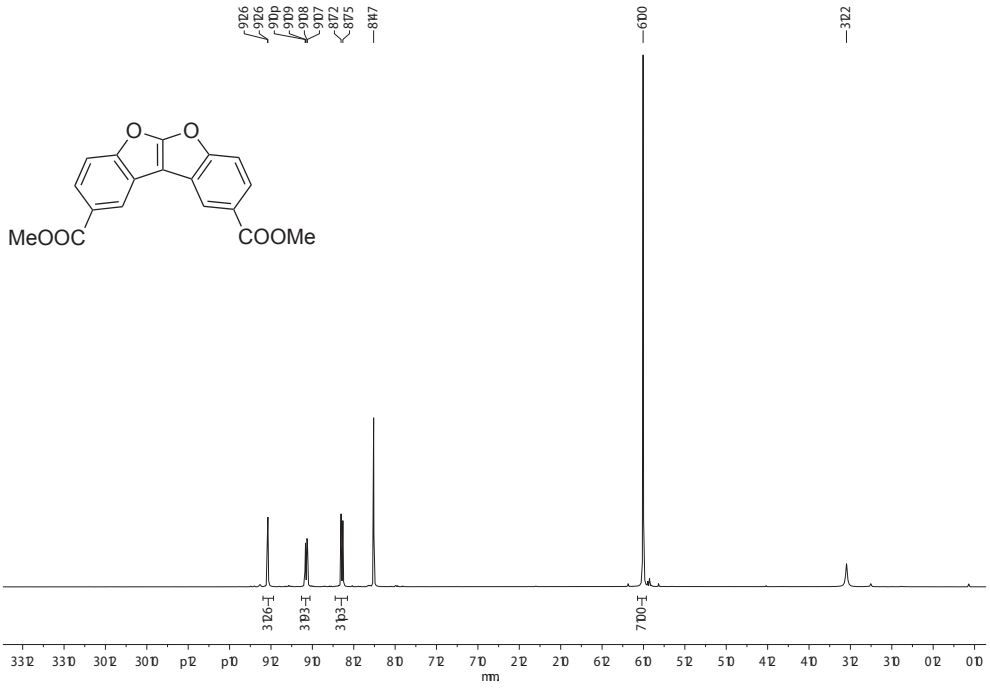

^{1}H NMR spectrum (DMSO-*d*^{6}, 400 MHz) of **5**

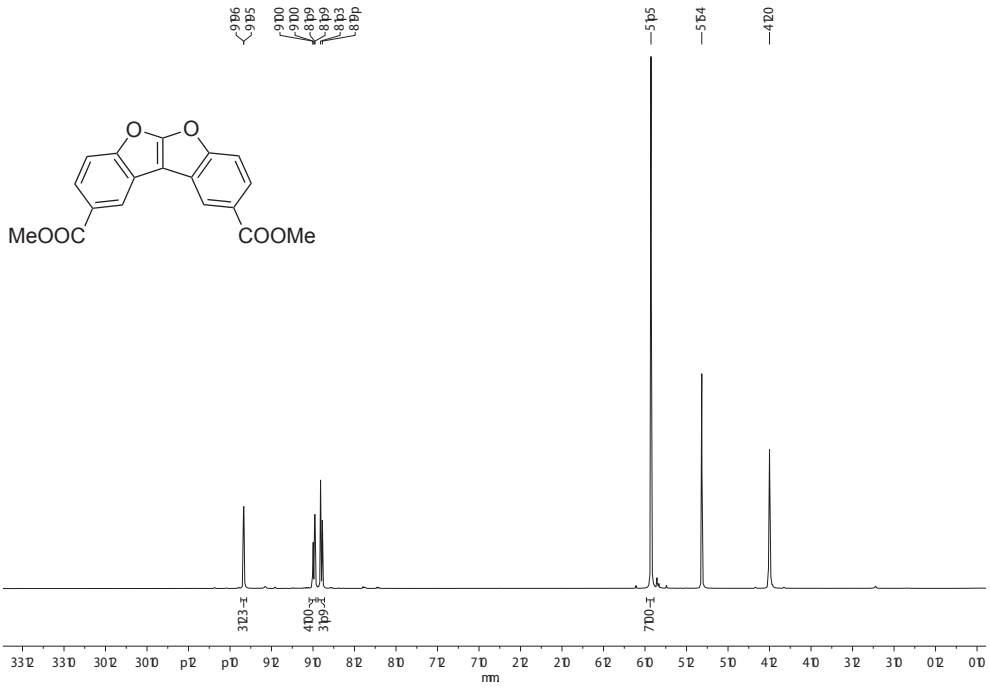

^{13}C NMR spectrum ($CDCl_3$, 101 MHz) of **5**

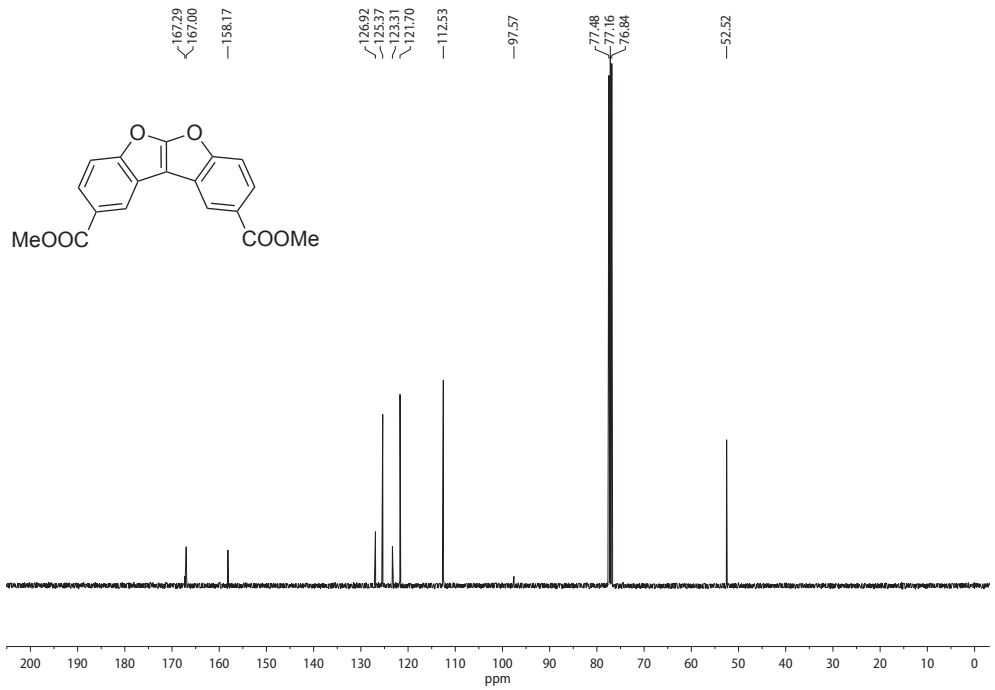

^{13}C NMR spectrum (DMSO-d^6, 101 MHz) of **5**

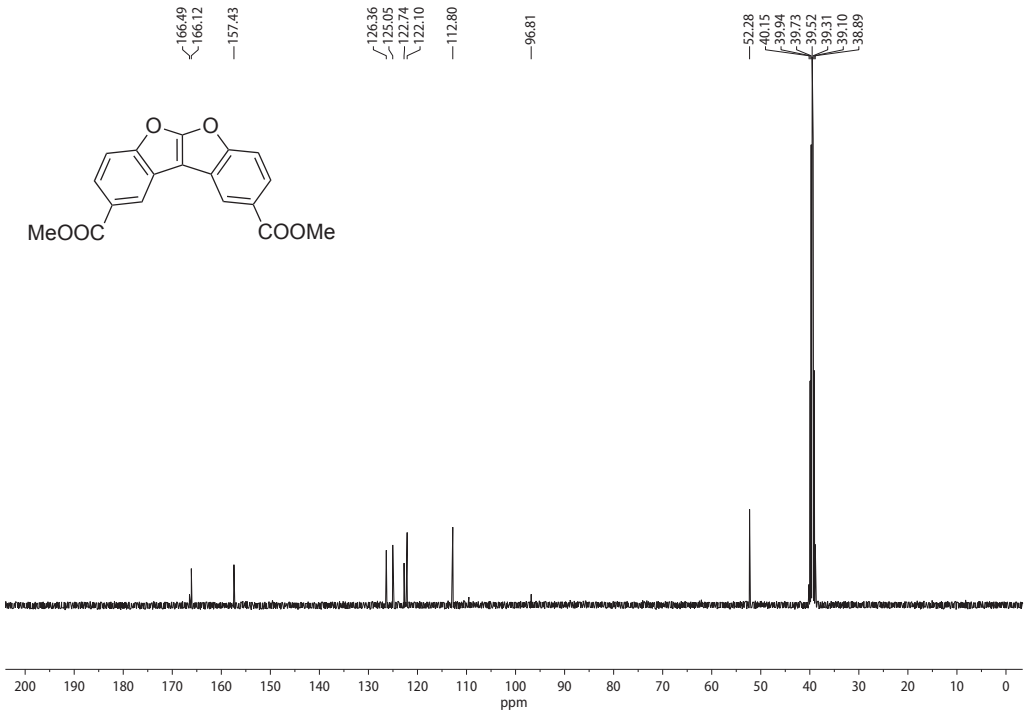

^{1}H NMR spectrum (DMSO-*d*^{6}, 400 MHz) of model compound **6** (co-crystals with EtOH)

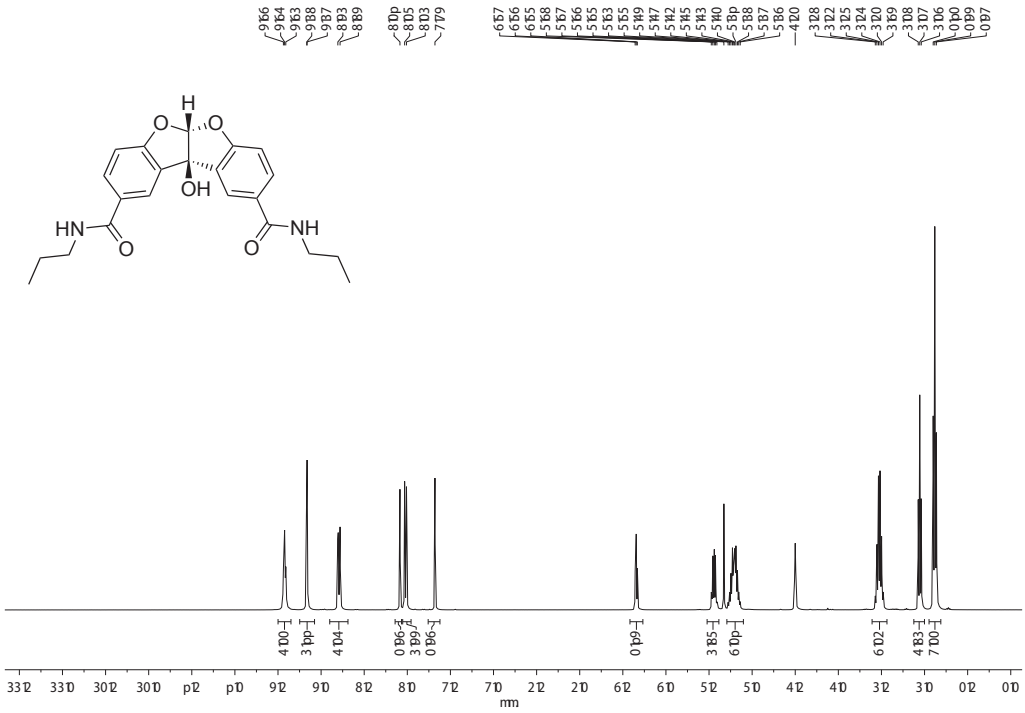

^{13}C NMR spectrum (DMSO-*d*^{6}, 101 MHz) of model compound **6** (co-crystals with EtOH)

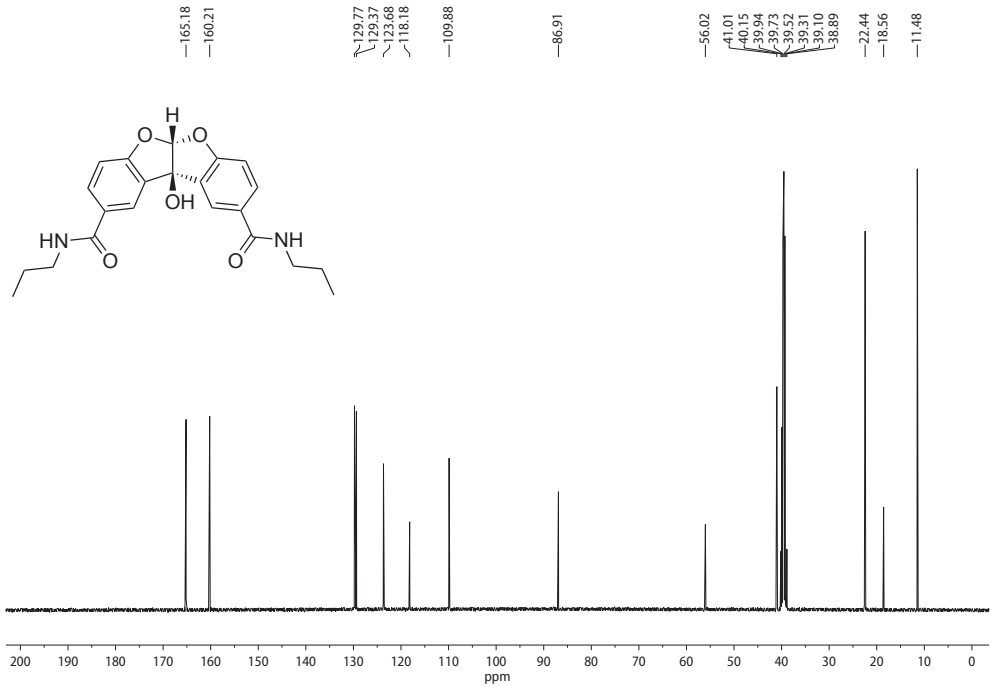

^{1}H NMR spectrum ($CDCl_3$, 400 MHz) of model compound **7**

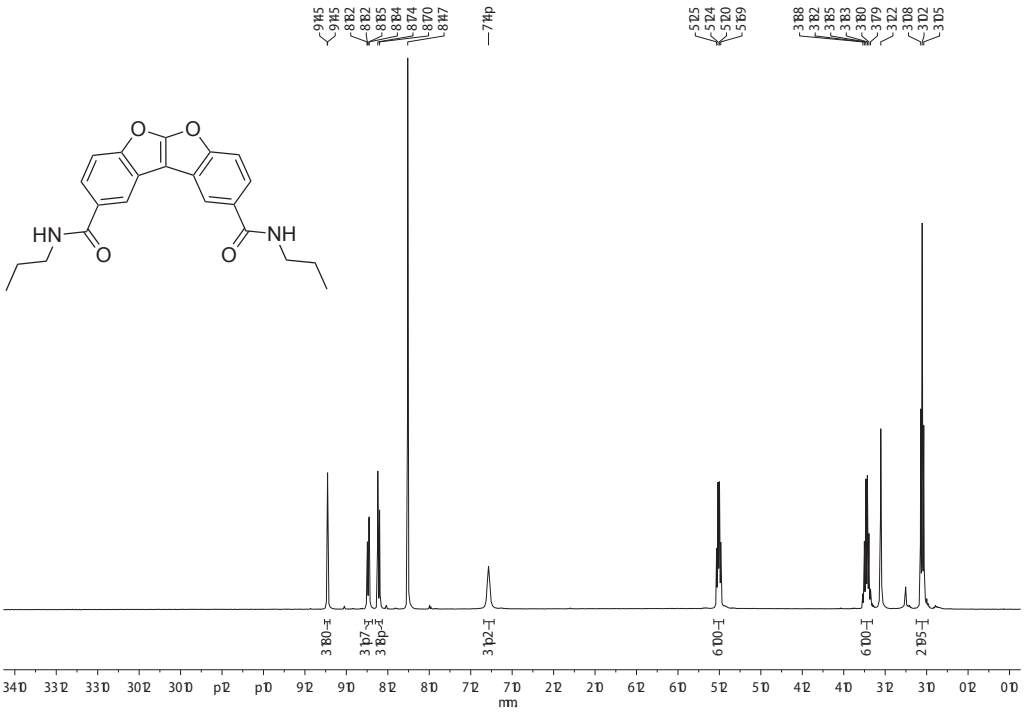

^{13}C NMR spectrum (DMSO-*d*^{6}, 101 MHz) of model compound **7**

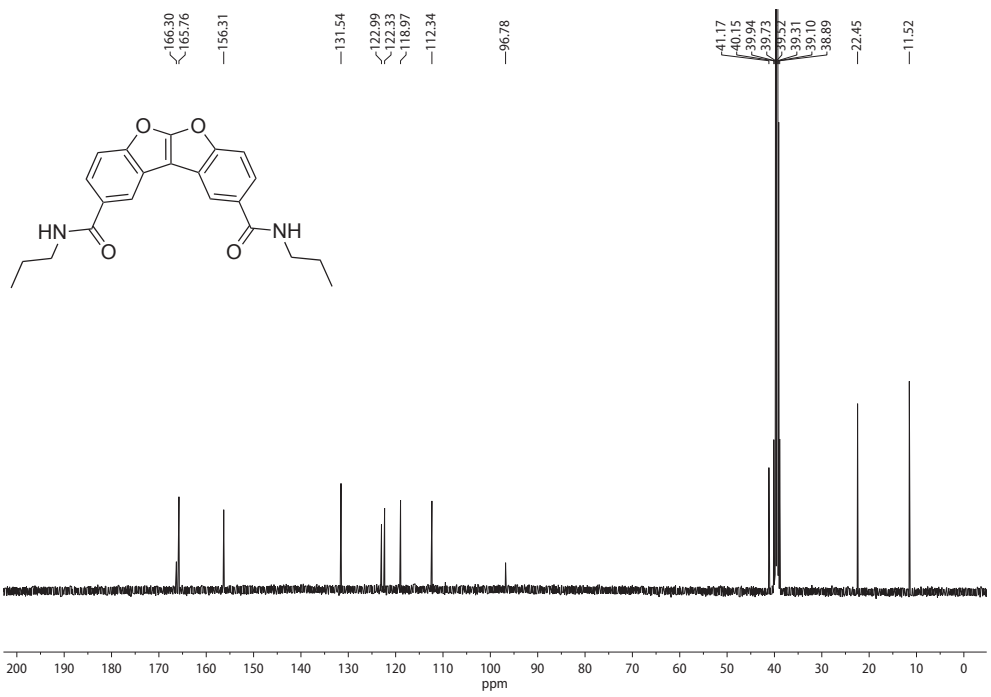

^{1}H NMR spectrum ($CDCl_3$, 400 MHz) of model compound **8**

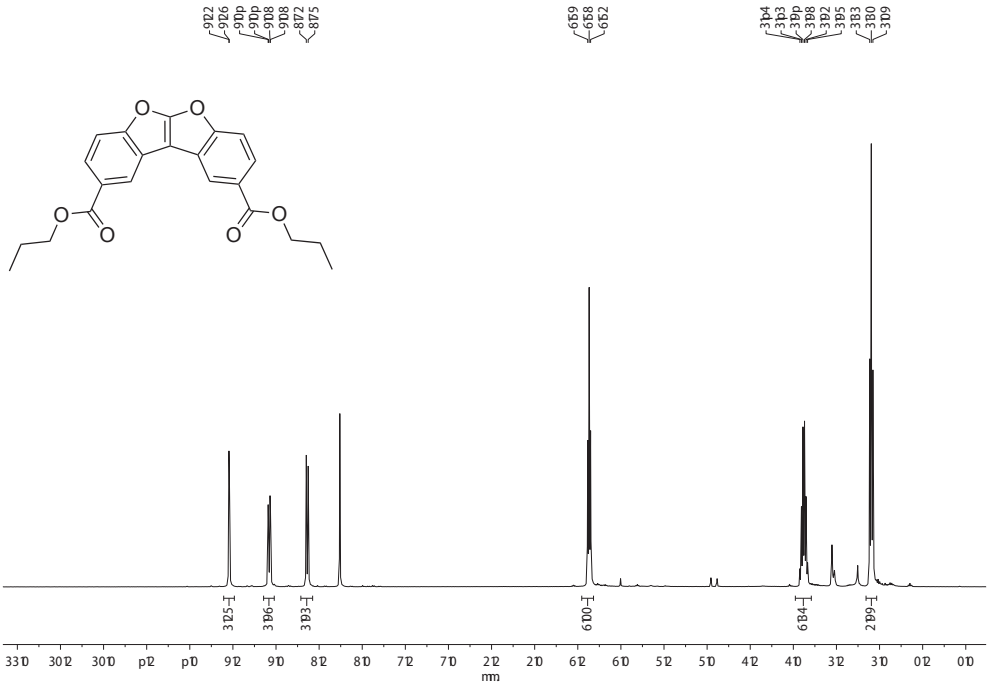

^{13}C NMR spectrum (DMSO-d^6, 101 MHz) of model compound **8**

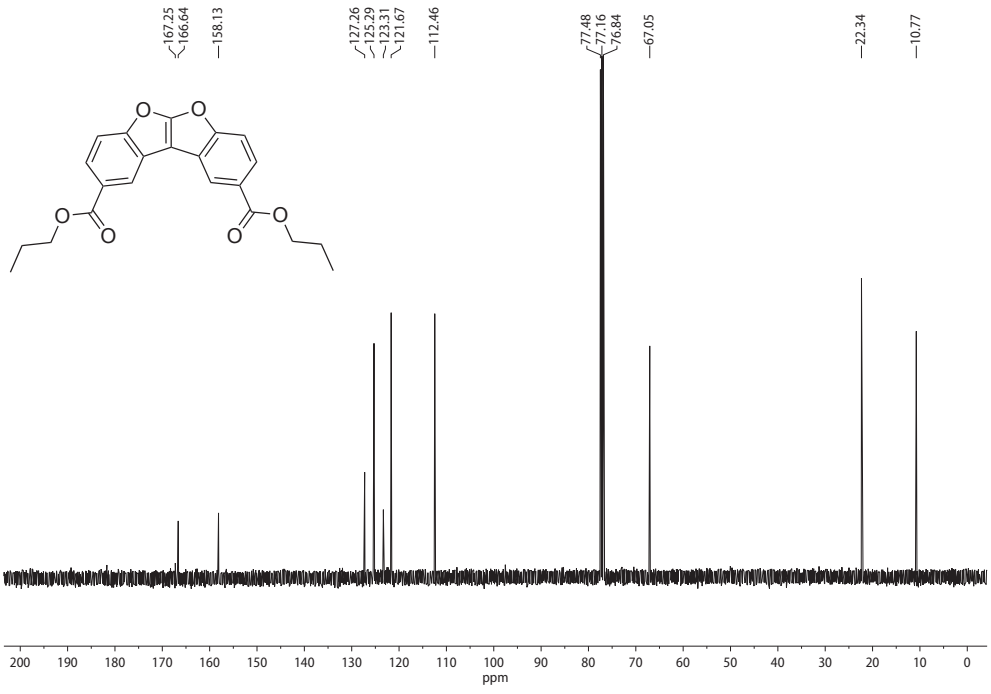

^{1}H NMR spectrum ($CDCl_3$, 400 MHz) of **10**

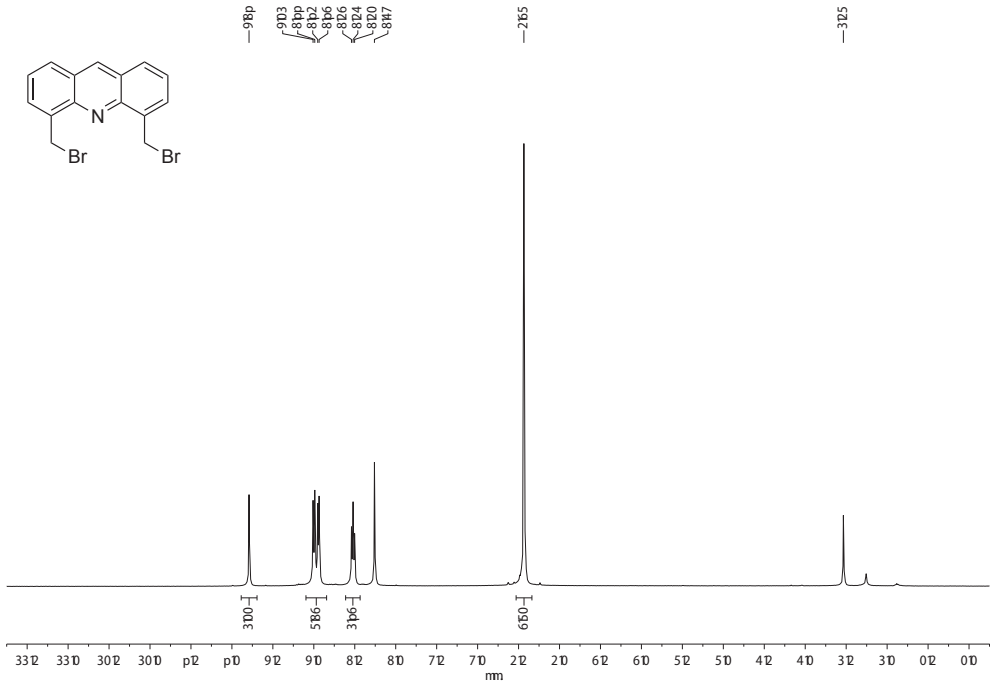

^{13}C NMR spectrum ($CDCl_3$, 101 MHz) of **10**

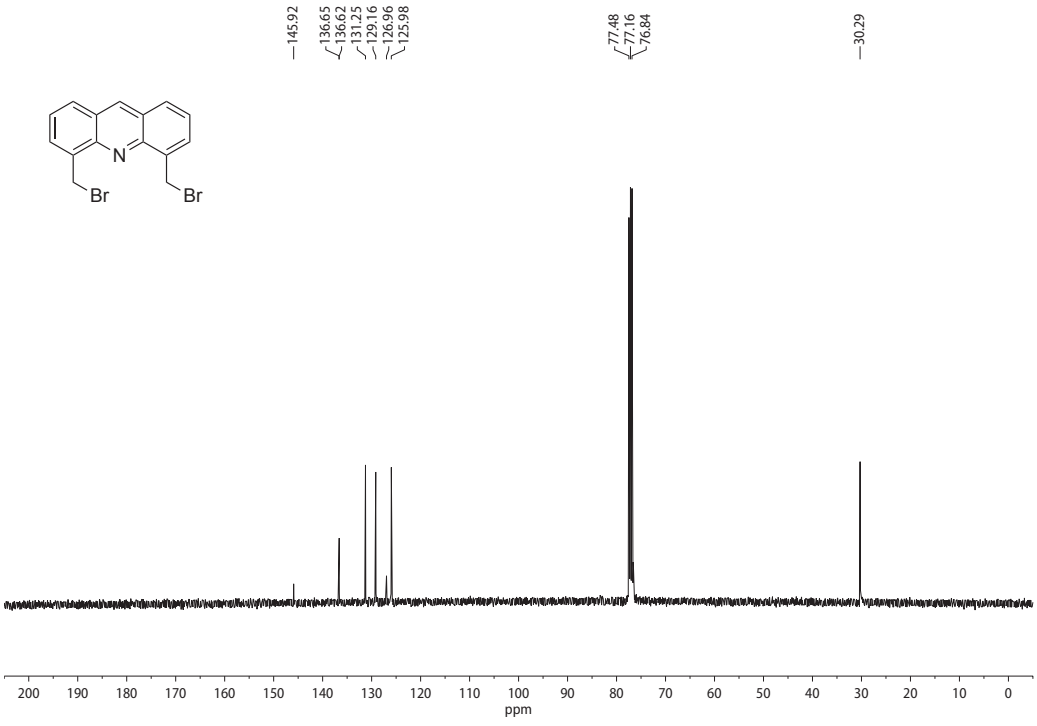

^{1}H NMR spectrum ($CDCl_3$, 400 MHz) of **11**

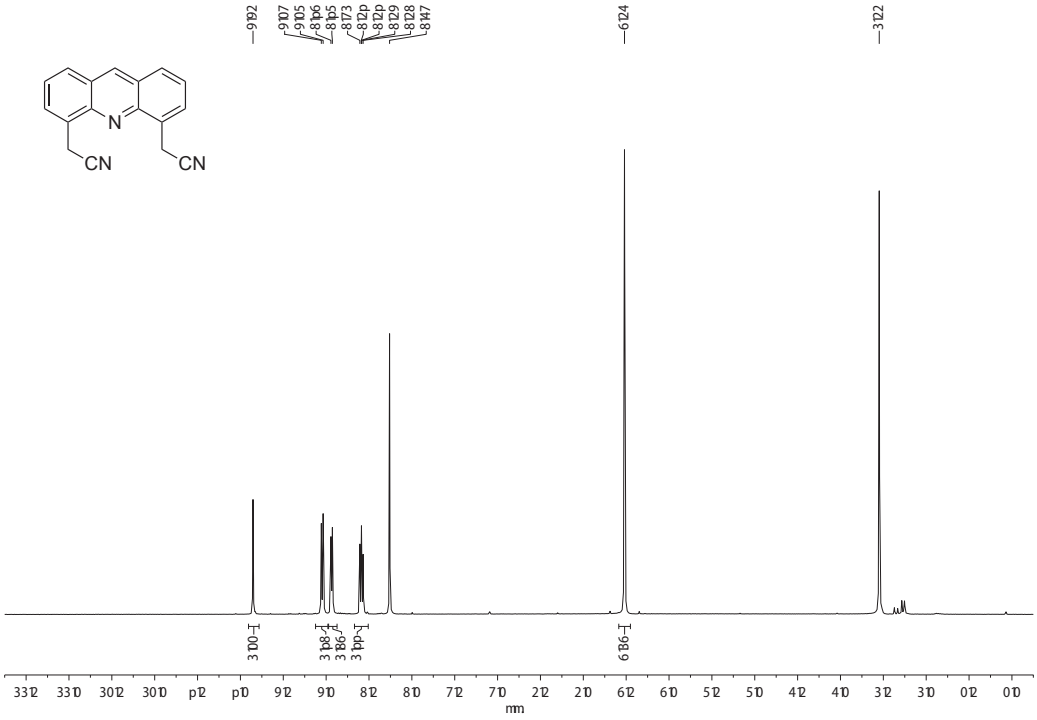

^{13}C NMR spectrum ($CDCl_3$, 101 MHz) of **11**

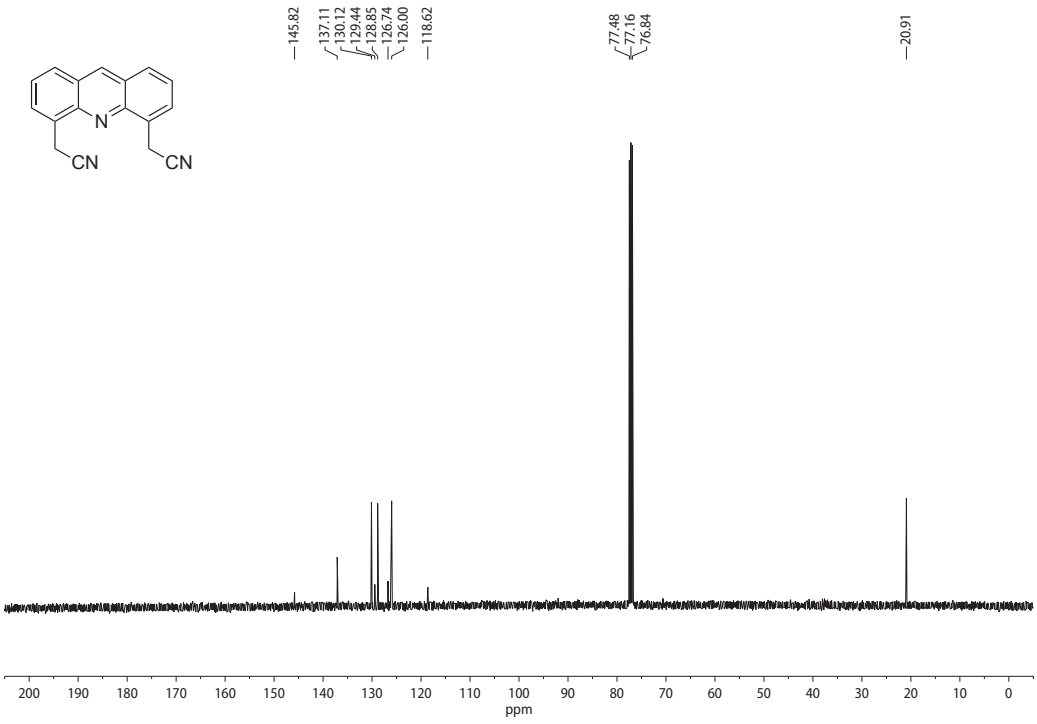

^{1}H NMR spectrum (DMSO-d^6, 400 MHz) of **12·xHCl**

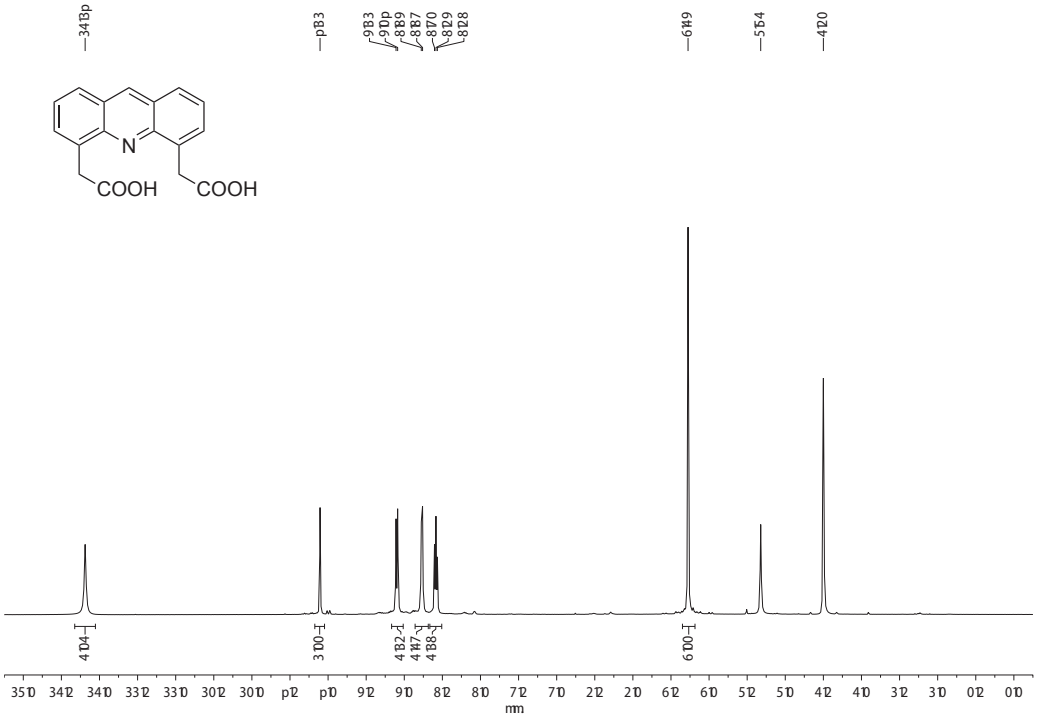

^{13}C NMR spectrum (DMSO-d^6, 101 MHz) of **12·xHCl**

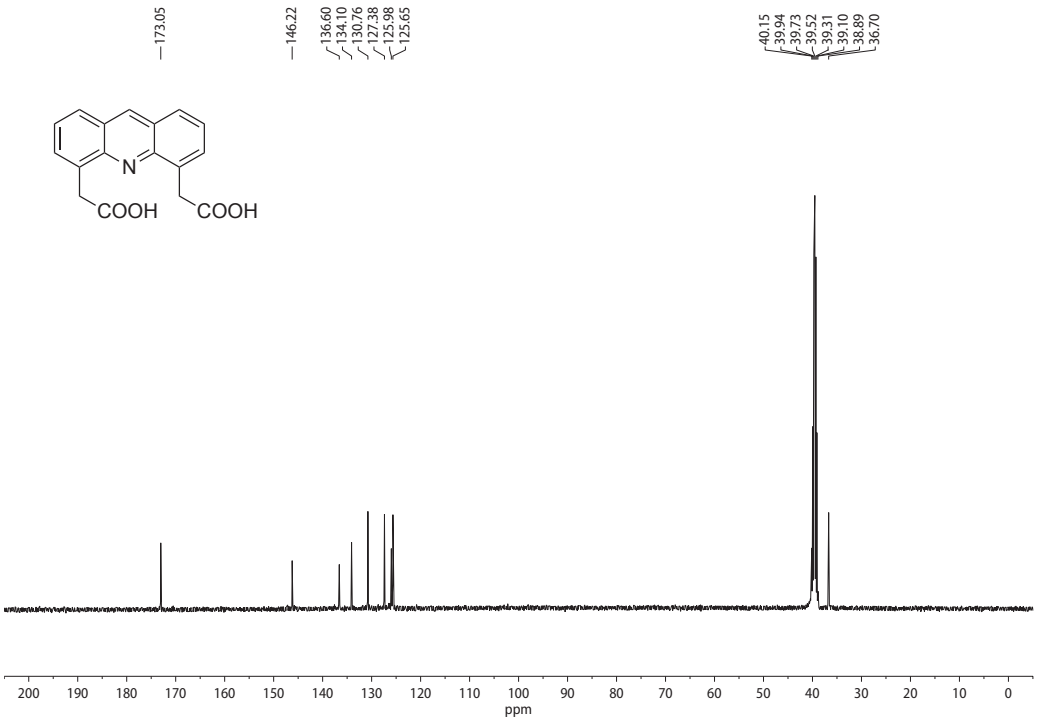

^{1}H NMR spectrum ($CDCl_3$, 400 MHz) of **13**

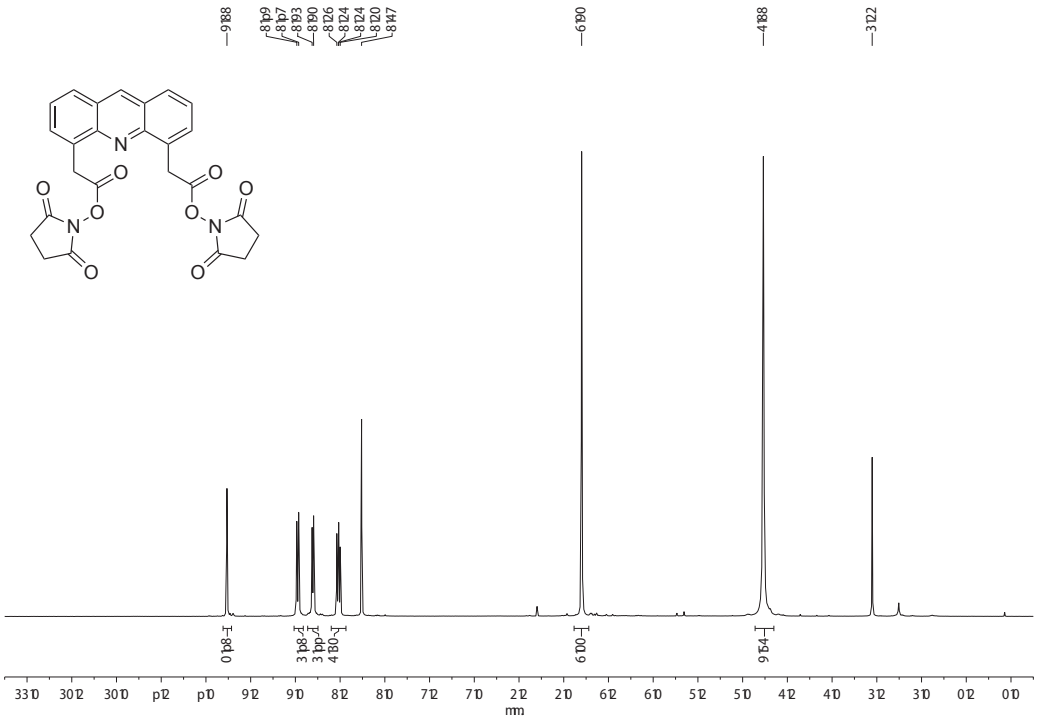

^{1}H NMR spectrum ($CDCl_3$, 400 MHz) of **13**

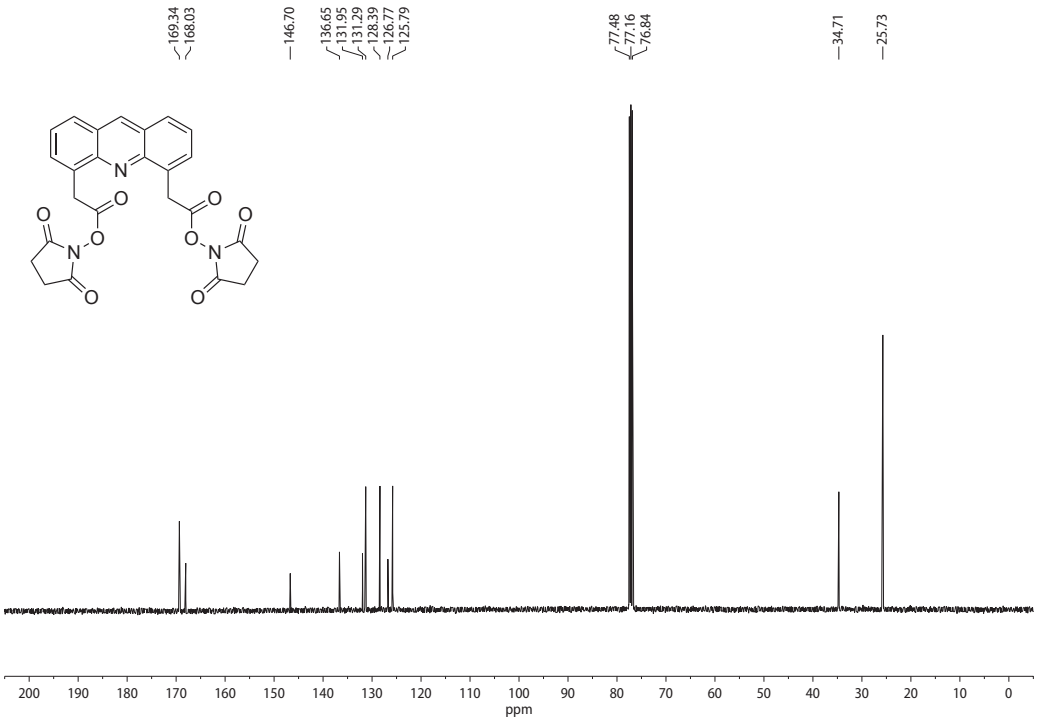

^{1}H NMR spectrum (DMSO-d^6, 400 MHz) of **14**

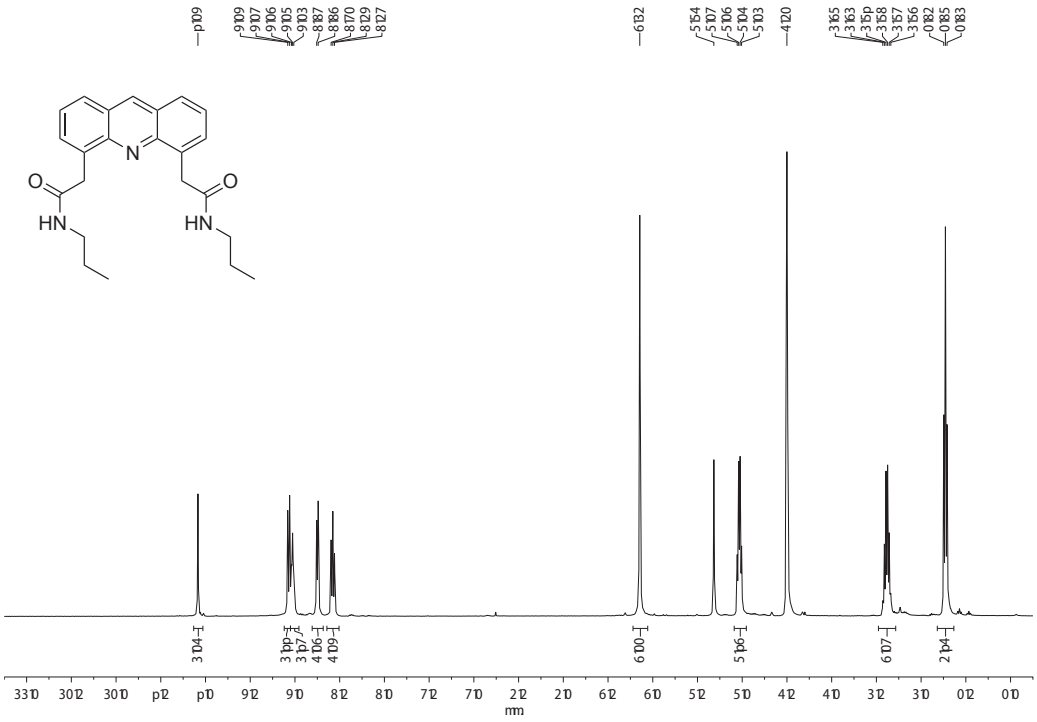

^{13}C NMR spectrum (DMSO-d^6, 101 MHz) of **14**

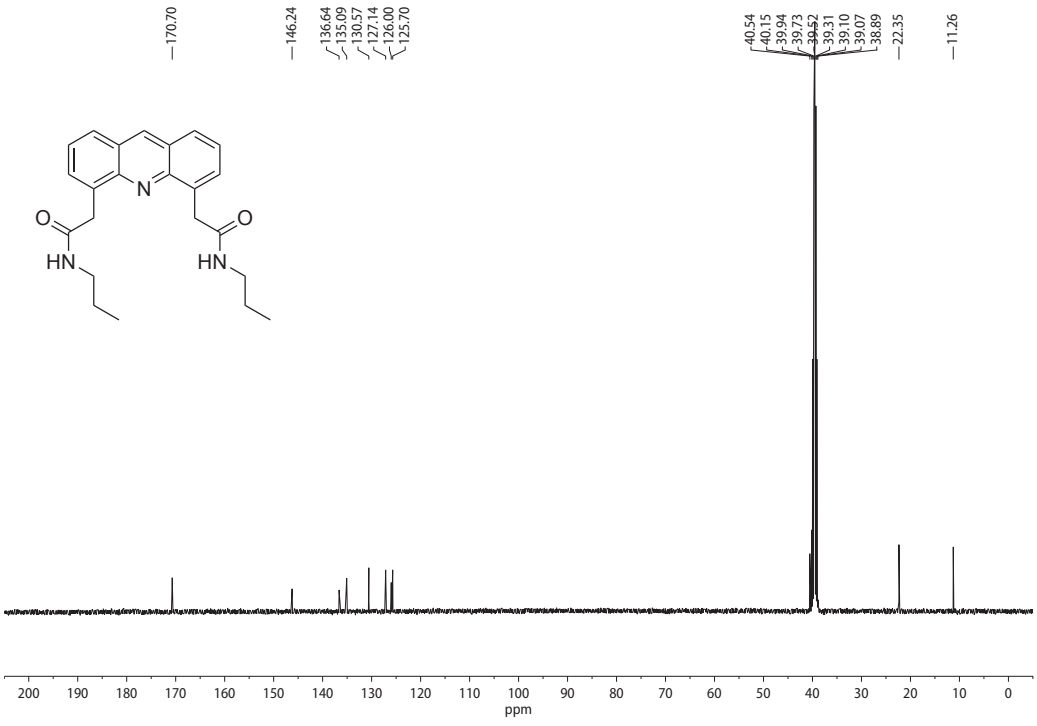

^{1}H NMR spectrum (DMSO-*d*^{6}, 400 MHz) of **15**

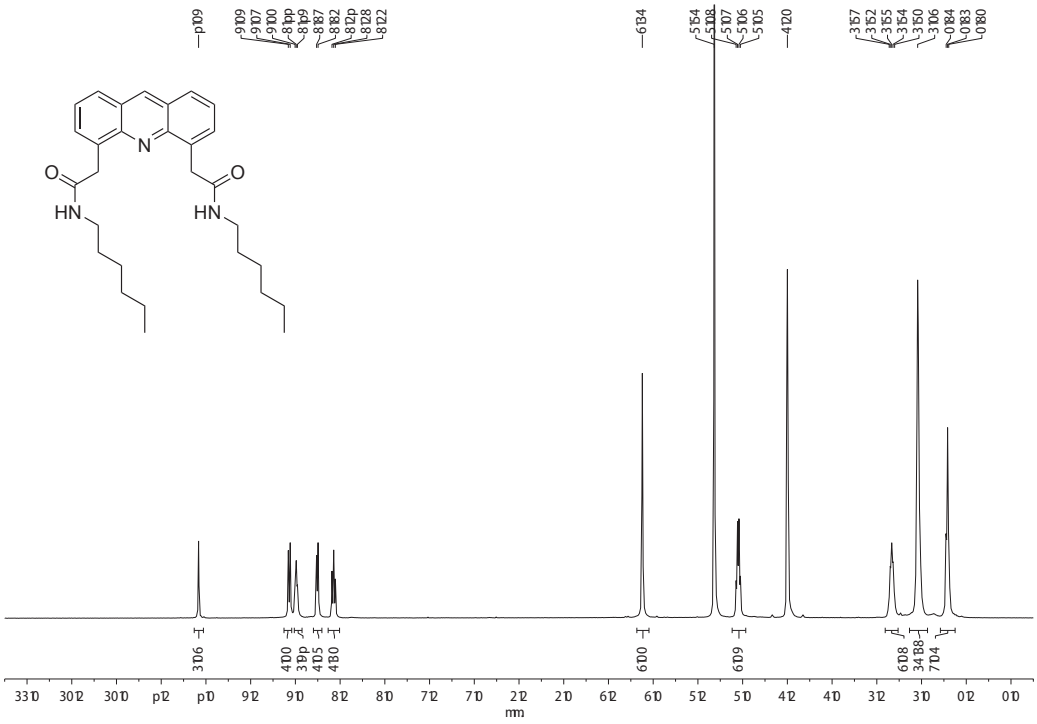

^{13}C NMR spectrum (DMSO-*d*^{6}, 101 MHz) of **15**

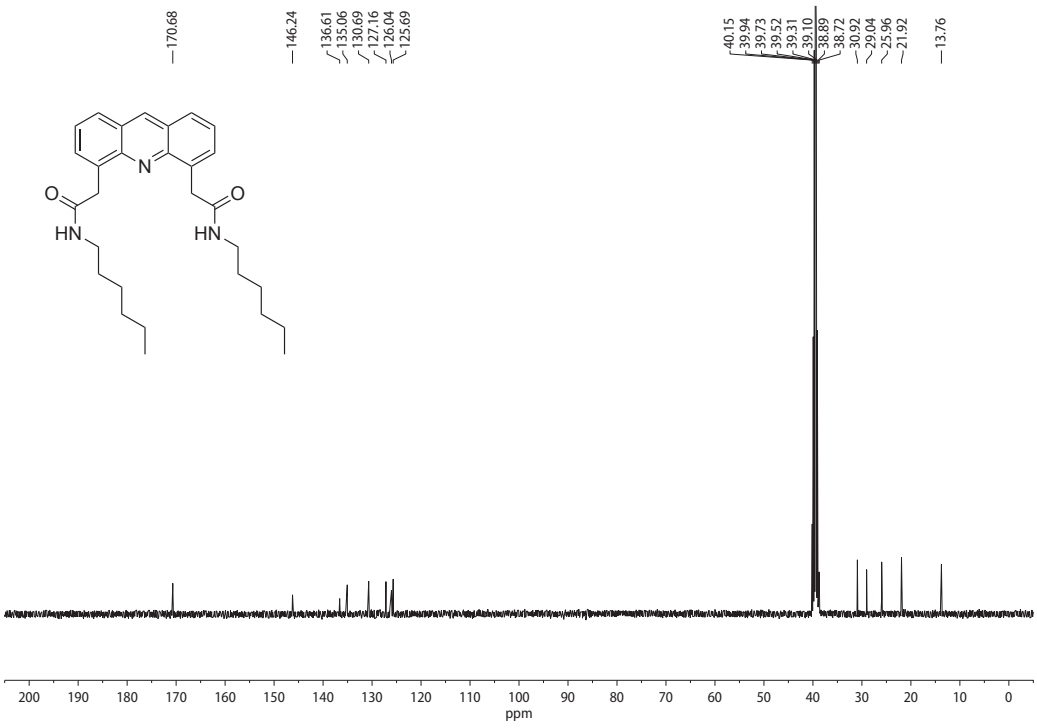

^{1}H NMR spectrum (CD_2Cl_2, 400 MHz) of **16**

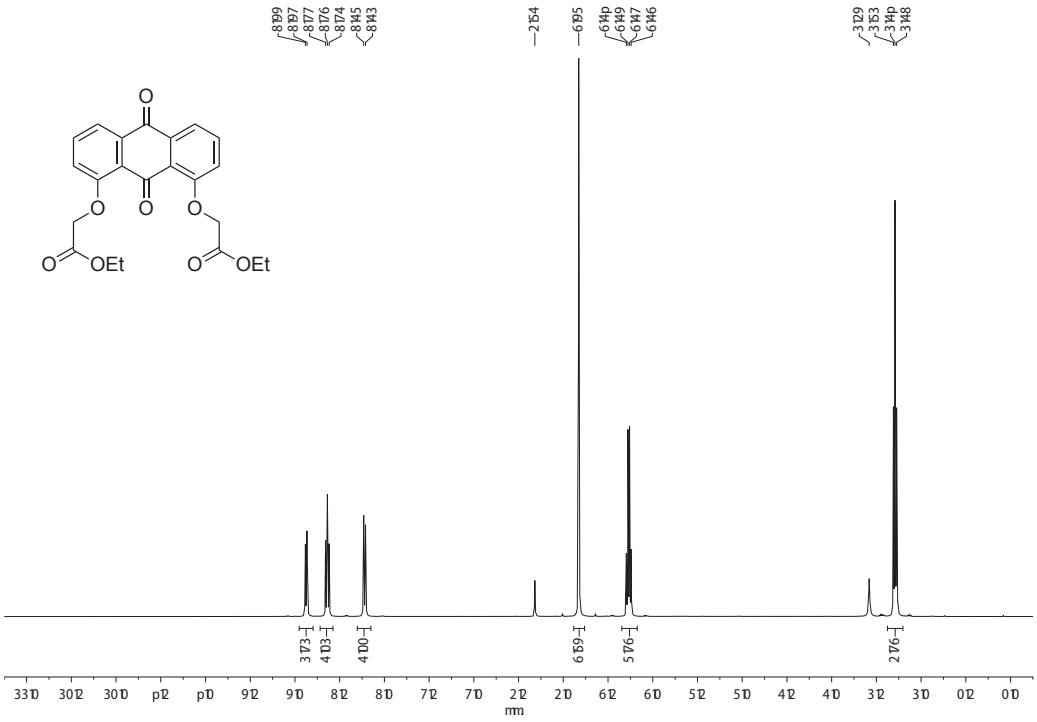

^{13}C NMR spectrum (CD_2Cl_2, 151 MHz) of **16**

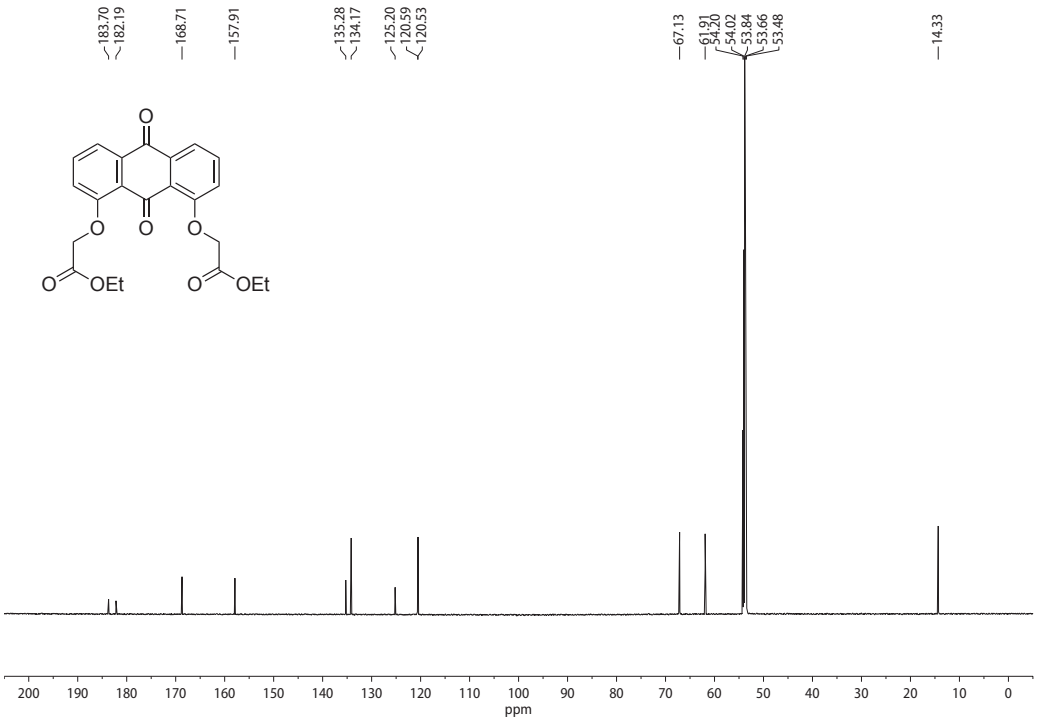

^{1}H NMR spectrum (DMSO-d^6, 400 MHz) of **17**

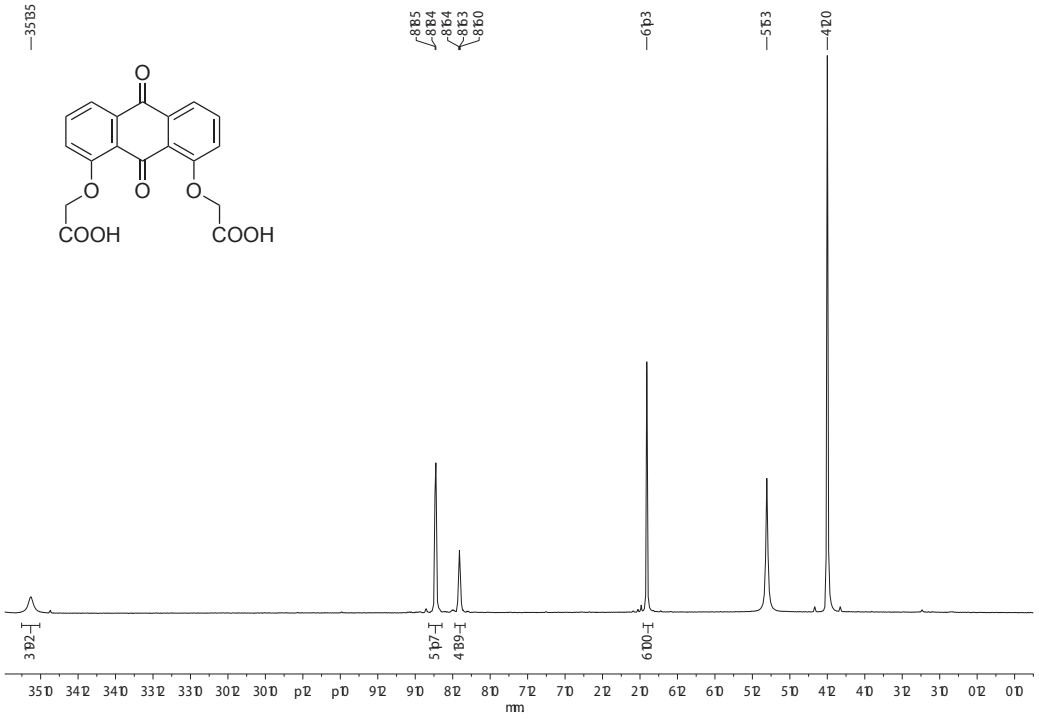

^{13}C NMR spectrum (DMSO-d^6, 101 MHz) of **17**

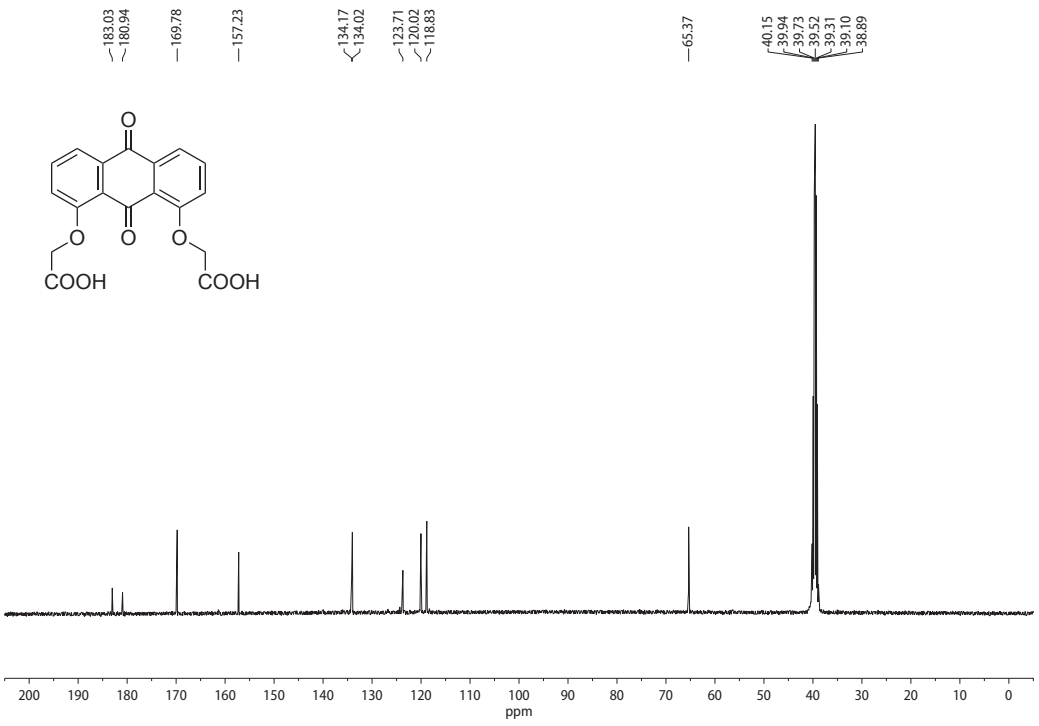

^{1}H NMR spectrum (DMSO-d^6, 400 MHz) of **18**

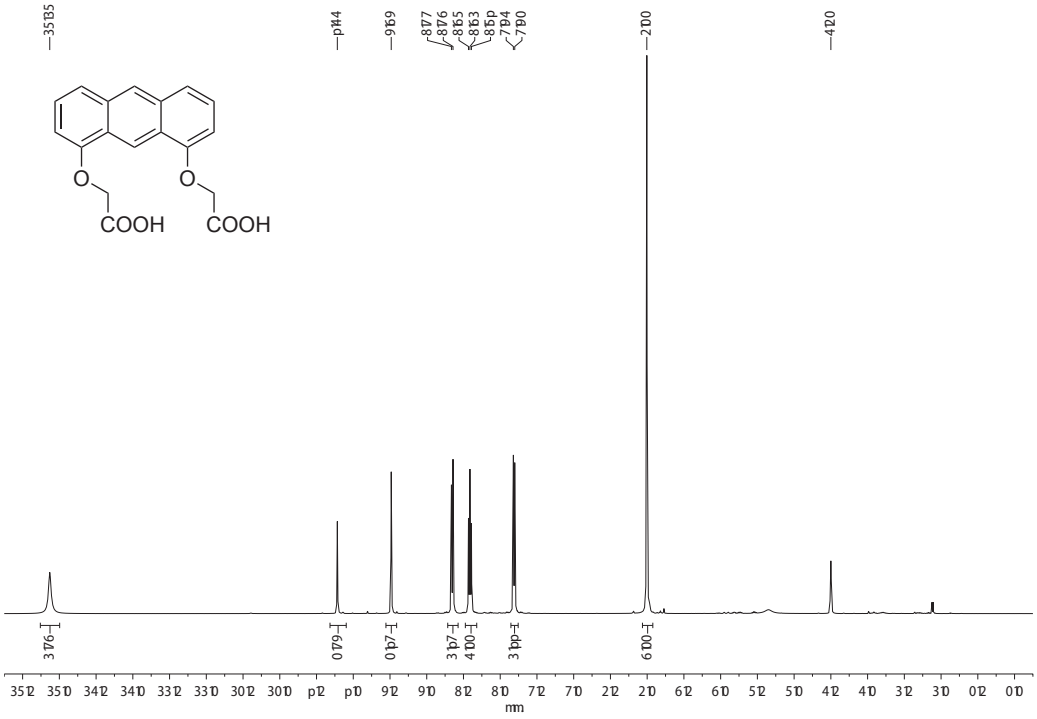

^{13}C NMR spectrum (DMSO-d^6, 101 MHz) of **18**

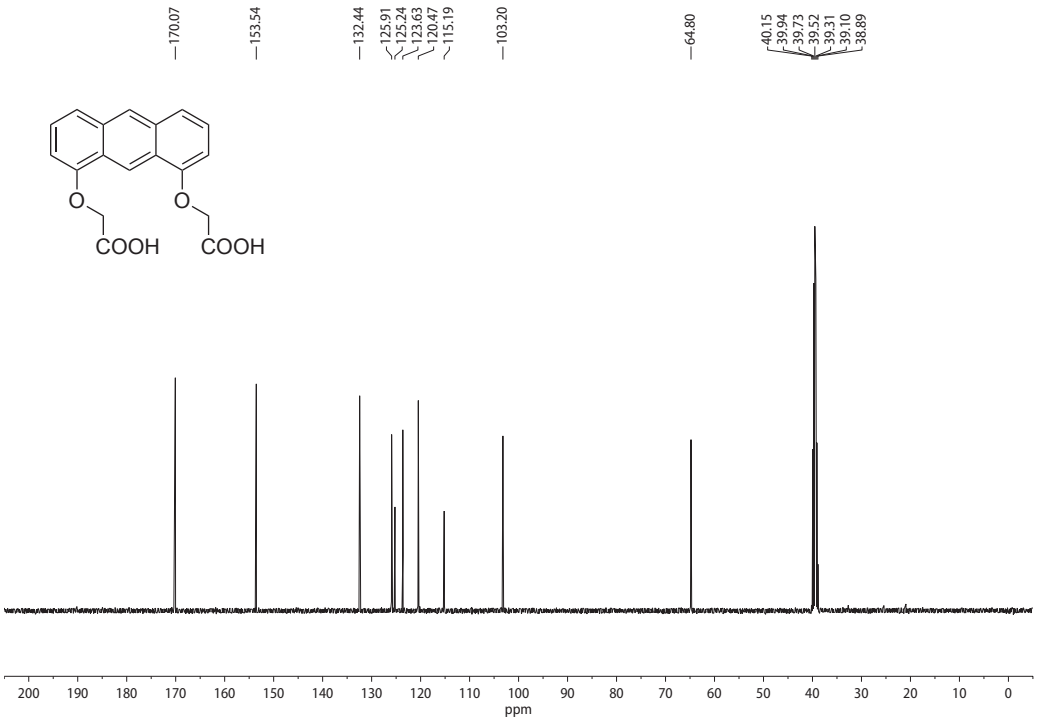

^{1}H NMR spectrum ($CDCl_3$, 400 MHz) of **19**

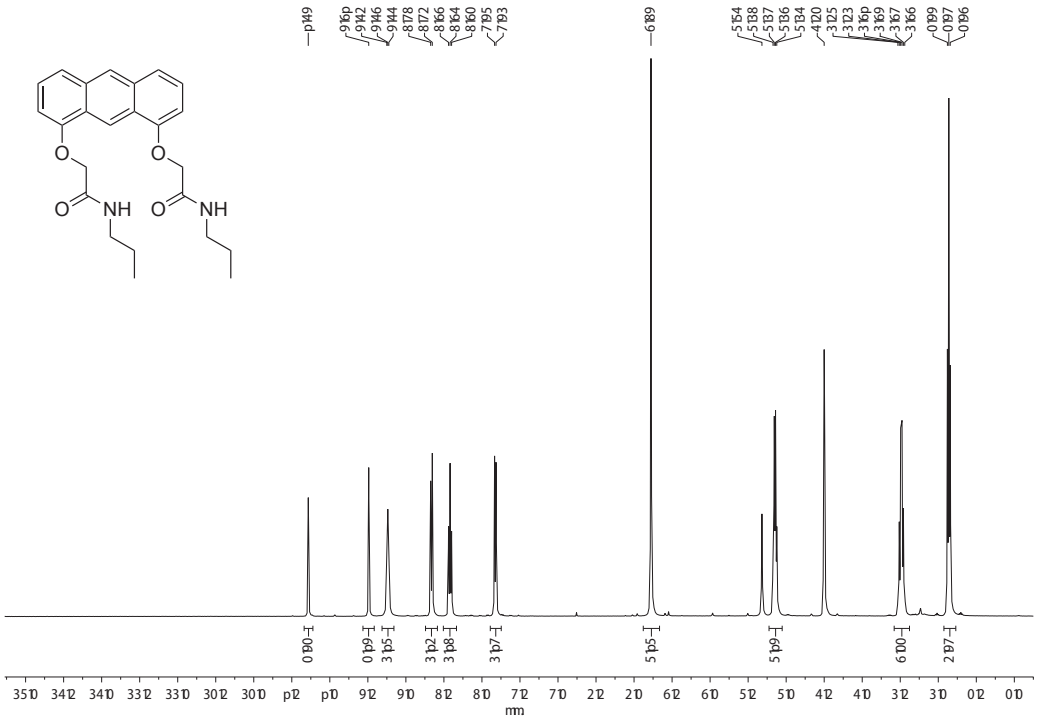

^{13}C NMR spectrum (DMSO-d^6, 101 MHz) of **19**

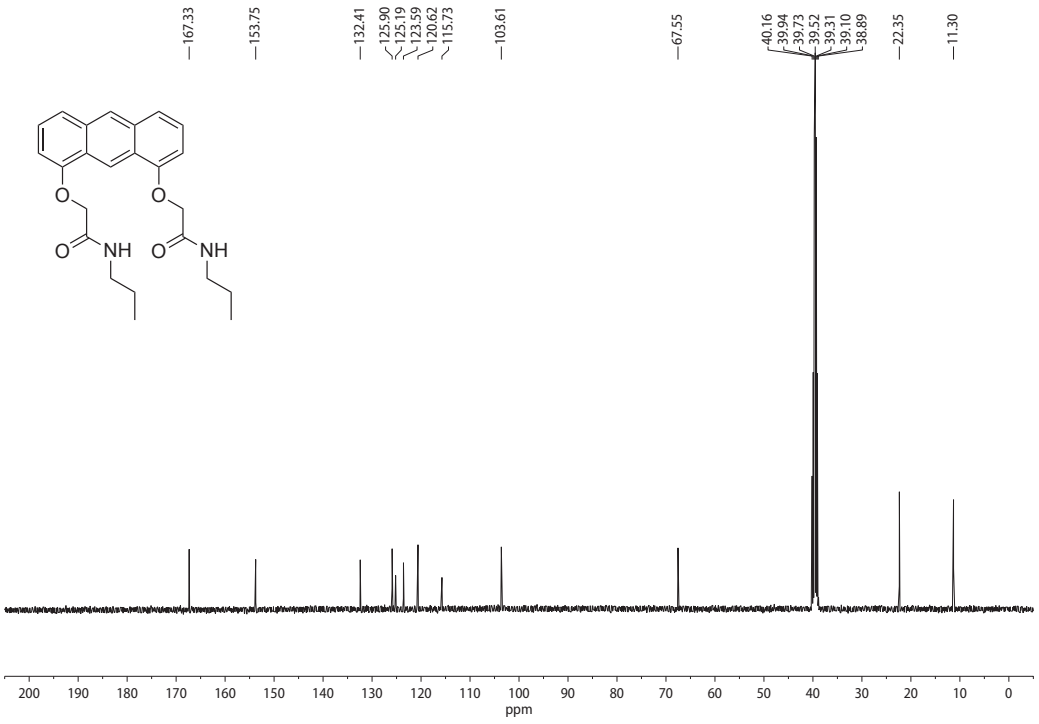

^{1}H NMR spectrum ($CDCl_3$:HFIP-d^2 90:10, 400 MHz) of **PA6Ac**

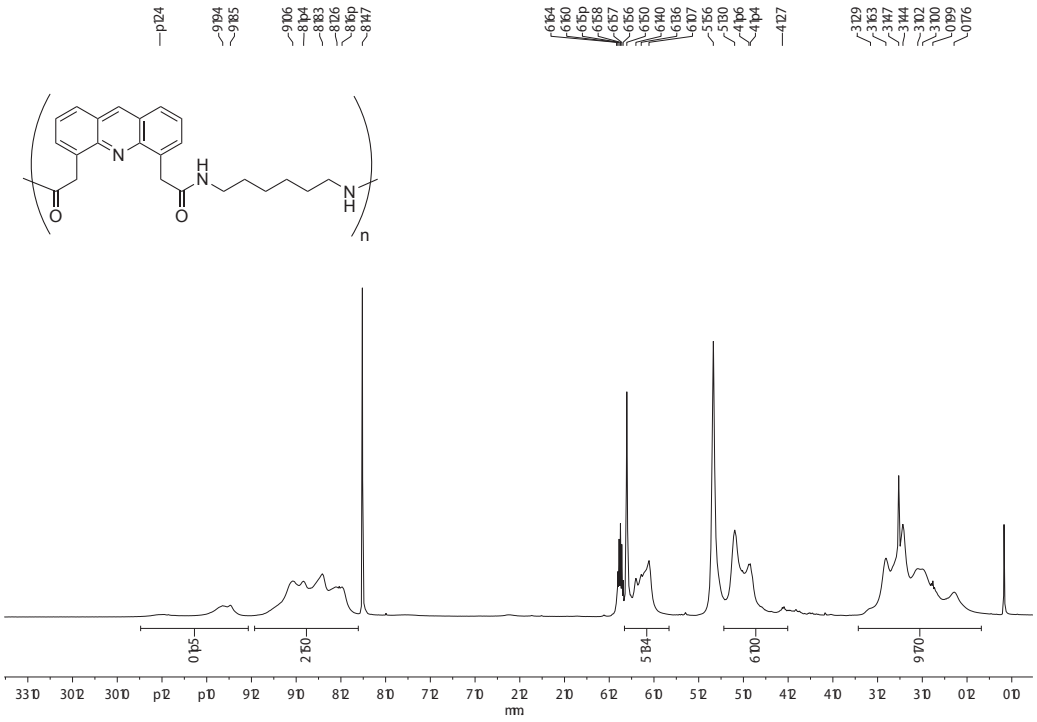

^{1}H NMR spectrum ($CDCl_3$:HFIP-d^2 90:10, 400 MHz) of **PA8Ac**

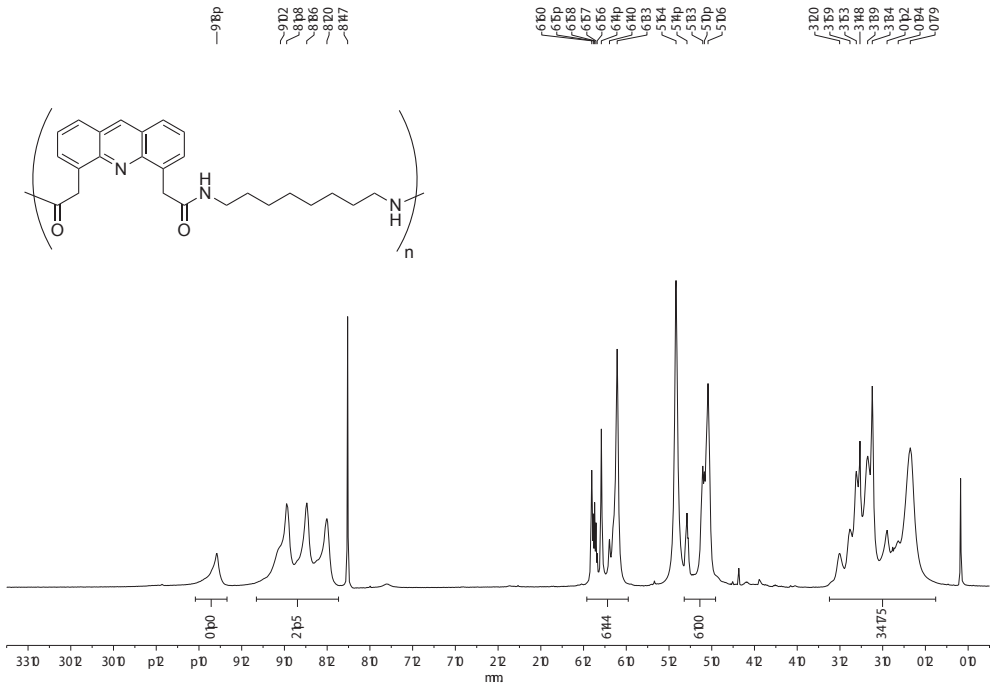

^{1}H NMR spectrum ($CDCl_3$:HFIP-d^2 90:10, 400 MHz) of **PA10Ac**

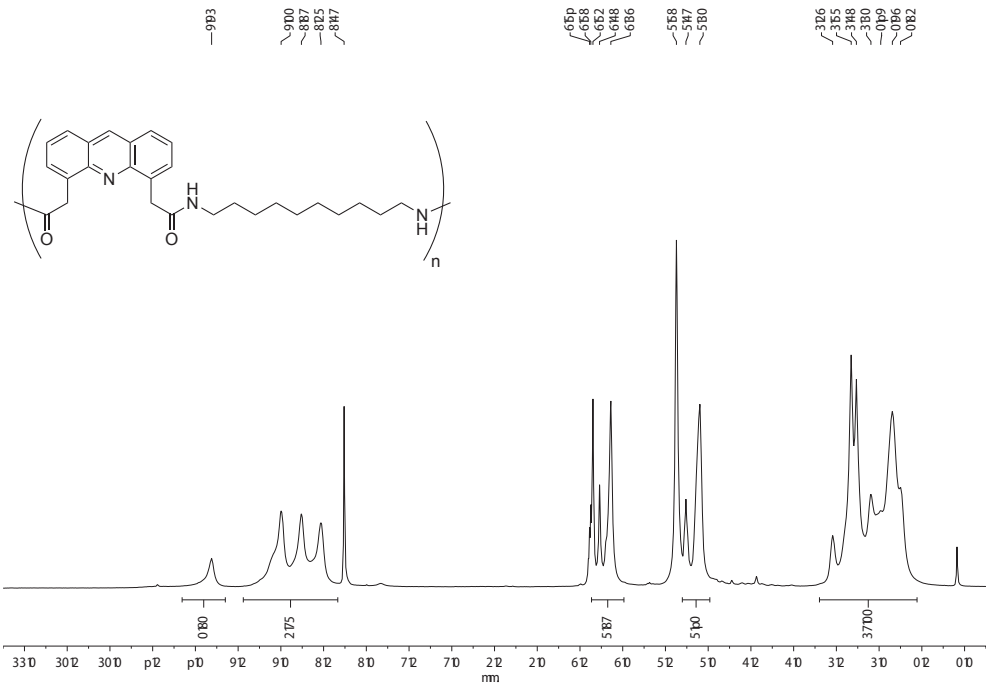

^{1}H NMR spectrum ($CDCl_3$:HFIP-d^2 90:10, 400 MHz) of **PA12Ac**

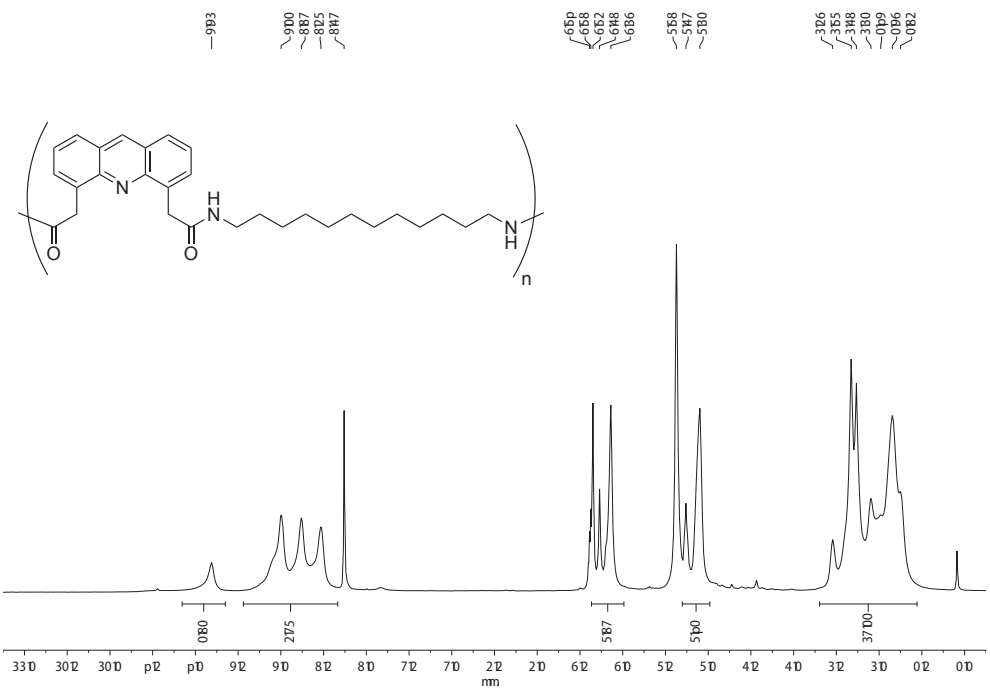

^{1}H NMR spectrum ($CDCl_3$:HFIP-d^2 90:10, 400 MHz) of **PA6Ant**

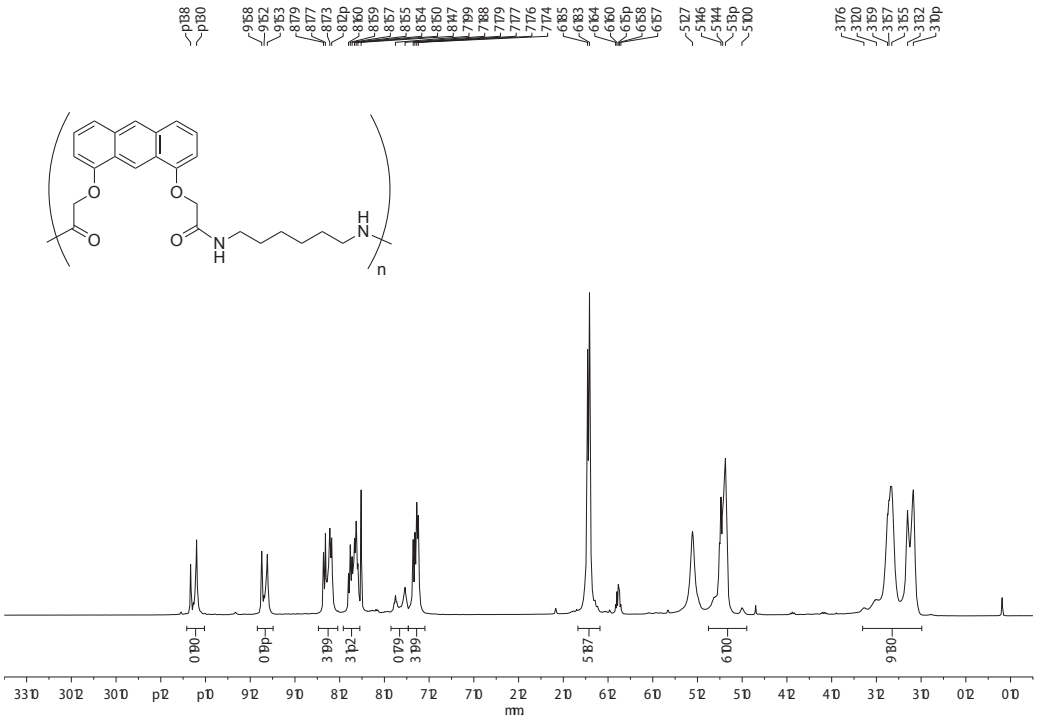

^{1}H NMR spectrum ($CDCl_3$:HFIP-d^2 90:10, 400 MHz) of **PA8Ant**

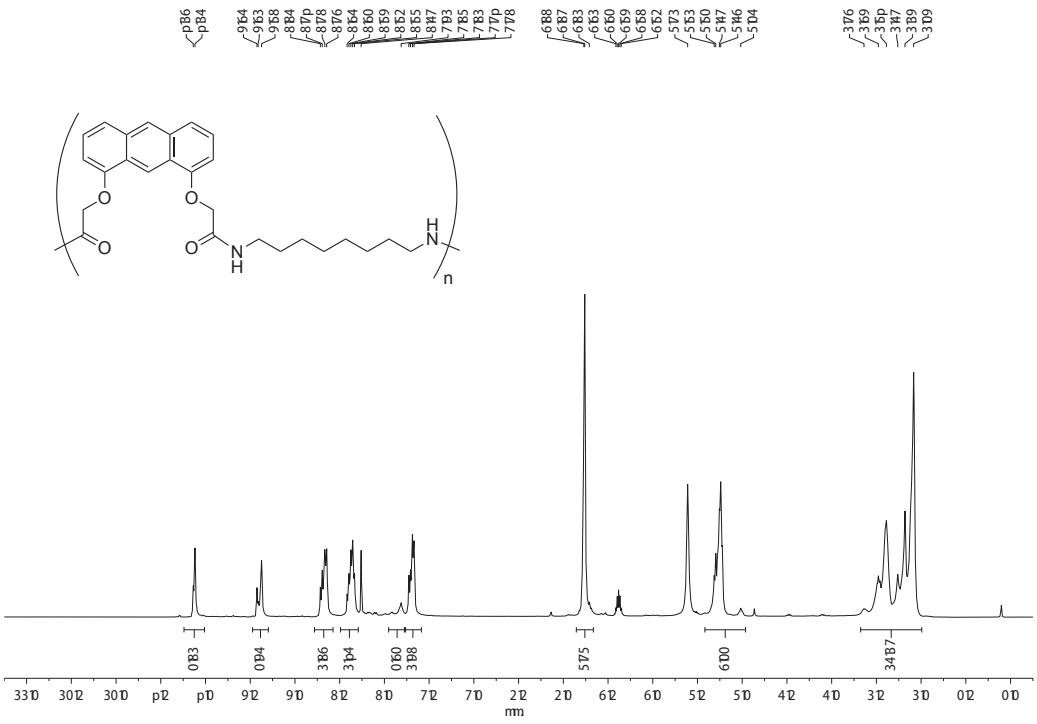

^{1}H NMR spectrum ($CDCl_3$:HFIP-d^2 90:10, 400 MHz) of **PA10Ant**

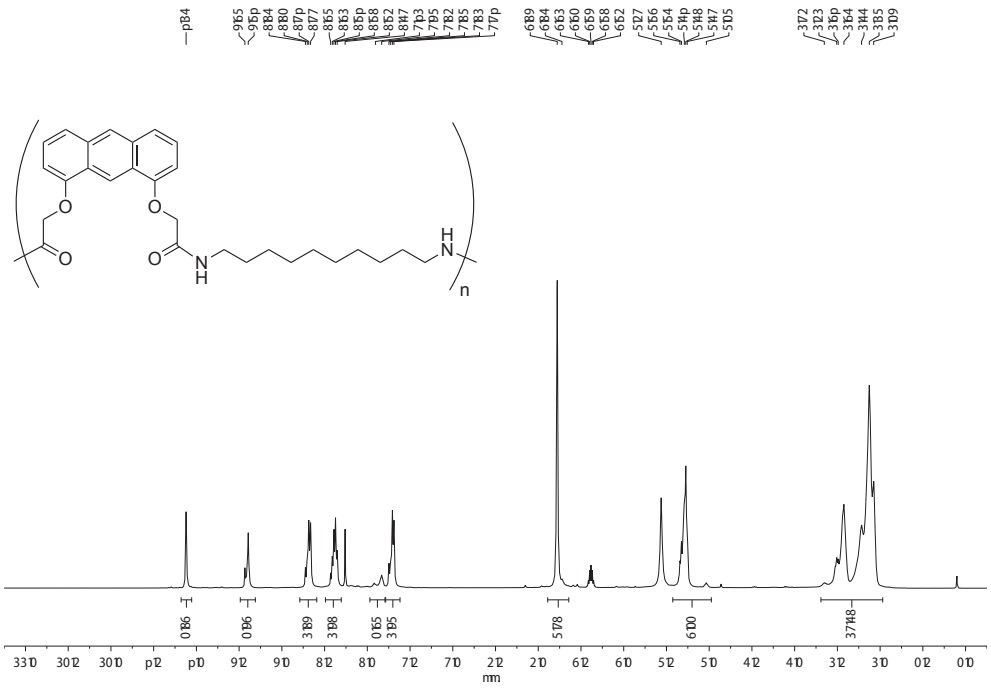

^{1}H NMR spectrum ($CDCl_3$:HFIP-d^2 90:10, 400 MHz) of **PA12Ant**

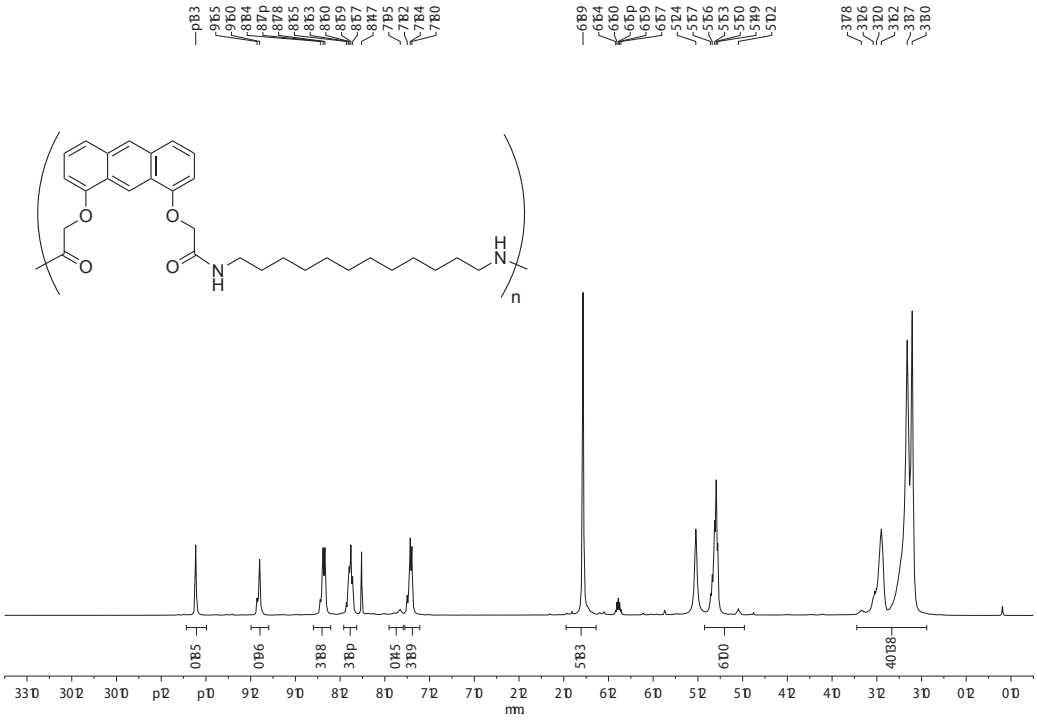

9.2 Curriculum Vitae

Education

2013 – 2018	**Doctorate (PhD)** in Material Science Ecole Polytechnique Fédérale de Lausanne (EPFL), Switzerland Laboratory of Macromolecular and Organic Materials (LMOM)
2008 – 2013	**Bachelor of Science (BSc.)** and **Master of Science (MSc.)** in Chemistry Ecole Polytechnique Fédérale de Lausanne (EPFL), Switzerland

Research and Professional Experience

2012 – 2013	Internship (Master thesis, 6 months): *"Extrusion and product characterization of whole wheat flours from different cultivars"* Nestlé Product Technology Center, Orbe, Switzerland Supervised by Dr. H. Chanvrier and Dr. J.-C. Gumy
2012	Internship (Master project, 14 weeks): *"Identification and quantification by gas chromatography of various sterols occurring in food products"* Service de la Consommation et des Affaires Vétérinaires, Switzerland Supervised by Dr. Y. Berger and Dr. B. Klein

Teaching Experience

2016 – 2017	Supervision of practical work sessions for the Bachelor course "Organic Chemistry for Material Scientists" given by Prof. H. Frauenrath at EPFL.
2013 – 2017	Animation and supervision of multiple synthesis workshops in the frame of the "Journées des Gymnasiens"
2013 – 2016	Teaching assistant for the exercises of the Bachelor course "Milieux Continus" given by Dr. J.-M. Drezet at EPFL.

Language Skills

- **French** Mother tongue
- **English** Fluent written and spoken level
- **German** B1

List of Publications

Publications (peer-reviewed)

"High Temperature Copolyamides by Efficient Transamidation of Crystalline-Crystalline Polyamide Blends", Cretenoud, J.; Galland, S.; Plummer, C. J. G.; Michaud, V.; Bayer, A.; Lamberts, N.; Hoffmann, B.; Frauenrath, H. *J. Appl. Polym. Sci.*, **2017**, *134*, 44349.

"Synthesis and Characterization of Semiaromatic Polyamides Comprising Benezofurobenzofuran Repeating Units", Cretenoud, J.; Özen, B.; Schmaltz, T.; Görl, D.; Fabrizio, A.; Corminboeuf, C.; Fadaei Tirani, F.; Scopelliti, R.; Frauenrath, H. *Polym. Chem.*, **2017**, *8*, 2197.

Publications (in preparation)

"Synthesis and Characterization of Semiaromatic Polyamides with U-Turn Repeating Units", Cretenoud, J.; Plummer, C. J. G.; Özen, B.; Baudat, E.; Fadaei Tirani, F.; Scopelliti, R.; Frauenrath, H. *To be submitted.*

"*Engineering Order and Disorder at the Nanoscale: High Performance Polyamides with Exceptional Ductility*" Galland, S.; Cretenoud, J.; Candau, N.; Gasparotto, P.; Ceriotti, M.; Balog, S.; Michaud, V.; Plummer, C. J. G; Frauenrath, H. *To be submitted.*

Talks and Poster Presentations

"High Temperature Copolyamides by Efficient Transamidation of Crystalline-Crystalline Polyamide Blends", Cretenoud, J.; Galland, S.; Plummer, C. J. G.; Frauenrath, H., **2017**, poster presentations at the EPF 2017 conference, Lyon, France; and at the EDMX Research Day, EPF Lausanne, Switzerland.

"High Temperature Copolyamides by Efficient Transamidation of Crystalline-Crystalline Polyamide Blends", Cretenoud, J.; Galland, S.; Plummer, C. J. G.; Frauenrath, H., **2017**, oral contribution at the SCS Fall meeting, Bern, Switzerland.